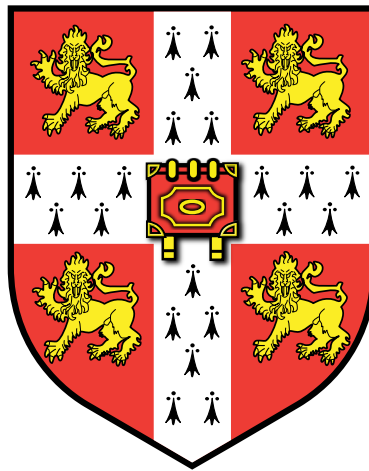


How to build a chordate:
Multiscale decomposition of axial
morphogenesis in the amphioxus, *Branchiostoma
lanceolatum*



Toby Gabriel Rufus Andrews

Hughes Hall
University of Cambridge

This dissertation is submitted for the degree of
Doctor of Philosophy

December, 2020

Declaration

This thesis is the result of my own work and includes nothing which is the outcome of work done in collaboration except as declared in the Preface and specified in the text. It is not substantially the same as any that I have submitted, or, is being concurrently submitted for a degree or diploma or other qualification at the University of Cambridge or any other University or similar institution except as declared in the Preface and specified in the text. I further state that no substantial part of my thesis has already been submitted, or, is being concurrently submitted for any such degree, diploma or other qualification at the University of Cambridge or any other University or similar institution except as declared in the Preface and specified in the text. It does not exceed the prescribed word limit for the Biology Degree Committee

Toby Andrews

December, 2020

Summary

How to build a chordate: Multiscale decomposition of axial morphogenesis in the amphioxus, *Branchiostoma lanceolatum*

Toby. G. R. Andrews

All members of the chordate phylum are united by a shared body plan – a stereotypical composition and topology of tissues that emerges in the wake of gastrulation and defines the major anatomical patterns emerging in later development. For this reason, although there is remarkable anatomical diversity between adult chordates, they are all united by a common set of design principles. The epicentre of the body plan is the notochord, located at the axial midline, which is flanked dorsally by a neural tube, bilaterally by a metameric pattern of somites, and ventrally by a primitive gut tube. If we are to understand how chordates emerged in evolution, and have subsequently diverged, it is therefore pertinent to ask how these traits are assembled in the embryo. However, here lies a paradox. The conservation of form emerging in the wake of gastrulation is matched by diversity in the morphogenetic processes that put it together. Therefore, if we are to understand chordate evolution, we must take a comparative approach to body plan morphogenesis. In this case, we can infer ancestral principles of development by comparing vertebrates with the most basally-branching member of the chordate phylum – the cephalochordate, amphioxus.

In this PhD thesis, I present a decomposition of body plan morphogenesis in the amphioxus embryo at three primary scales of observation. First, I identify the major changes in tissue shape and cellular architecture involved in body plan assembly, using a fusion of classical embryological approaches and three-dimensional morphometrics. This exposes the amphioxus embryo as a largely growth-free system, in which axial development primarily depends on tissue-specific programmes of convergent extension behaviour. Within this, volumetrically-reductive cell division acts to regulate tissue complexity via focal regulation of cell size and number, and is required in axial progenitor cells of the

tailbud for full elongation of the body axis. Second, I reconstruct patterns of cell shape change underpinning notochord development using single-cell morphometrics and morphospacial embedding. Despite its superficial simplicity, I show the amphioxus notochord to be remarkably complex, with evidence of region-specific behaviours, and an interplay between growth and cell rearrangement that generates axial length. Finally, I study the diversity of axial progenitor cell types in amphioxus using quantitative *in situ* imaging of gene expression, and a bespoke *in silico* pipeline for cell state classification and spatial mapping. Here, aided also by *in vivo* signalling perturbations, I locate a population of vertebrate-like neuromesodermal progenitors that generate the posterior spinal cord.

The results I present in this thesis reveal remarkable complexity in amphioxus axial development, and a developmental programme replete with morphogenetic principles shared with vertebrates. For this reason, we can infer a basic repertoire of developmental innovations required for body plan formation in the first chordates, as relatively simple structural perturbations of the gastrula. From this foundation, I use my findings to propose that the radiation of chordates has depended more on tweaks in the magnitude of processes already present in the ancestral chordate, than the innovation of new processes *de novo*. This thesis therefore contributes new understanding in chordate development and evolution. It also offers a suite of techniques suitable for studying and integrating morphogenesis a diversity of research organisms.

Acknowledgements

An important lesson I've learned during my PhD is that novelty is an illusion, both in the evolution of form and the evolution of ideas. It's less about eureka moments in the bathtub, and more about piecing together old ideas in new ways, and examining them under a different light. For that reason, science is (and has to be) a social endeavour. The ideas I'm able to present in this thesis have evolved thanks to innumerable conversations, lab meetings, Slack messages, cups of coffee and trips to the pub with the creative and excitable community of researchers I've been lucky enough to work with over the last four years, who have supported me both intellectually and emotionally during this whirlwind journey.

I thank Elia Benito-Gutierrez for hosting me in her lab, for her energy and encouragement, and for offering me the intellectual freedom to pursue my big questions. I am also grateful to all members of the Benito-Gutierrez lab, past and present, who have made the lab a friendly, supportive and creative working environment. I'd especially like to thank the founding members of *Toby's Mice*, Giacomo Gattoni, Michael Schwimmer, Lara Busby and Dan Keitley, who have always had incredible confidence in me as a scientist, and have kept me going through thick and thin. I will miss sketching out half-baked ideas with them, and inarticulately raving about evolution over too many glasses of wine. Then again, I've no doubt this will continue. I also thank my former students, Dillan Saunders, Sophie Kraunsoe and Anna Malkowska for their contributions to development of the ideas presented in this thesis, and for helping me to become a better mentor.

Outside of the lab, I am also thankful for the unshakable support of Olivia Tidswell, Matt Benton, Aleksandra Marconi and Eva Higgenbotham from the Department of Zoology, and Berta Verd from the Department of Genetics. They have always been there to talk, laugh or rant at a moment's notice. I am indebted to my advisors Andrew Gillis and Matthias Landgraaf who have had unwavering faith and confidence in me from day one, and have gone well beyond the call of duty in supporting me and my work. I have also gained immensely from their knowledge and endless enthusiasm for fate mapping. I thank Ben Steventon for numerous impassioned conversations about embryology, and for always

being a wise mentor on science and how to do it. Similarly, I thank Michael Akam and Alfonso Martinez-Arias who have both supported me immensely in my studies and career to date, and nurtured my interests in development and evolution.

I thank Chris Klingenberg, Jesus Marugan-Lobon and Soledad D'Esteban Trivigno for getting me lost in morphospace. In turn, I thank Wolfram Pönisch for his time and energy helping me to make my silly dreams of a notochord morphospace a reality. I'm also grateful to Marketa Kaucka-Peterson for her enthusiasm and support for the project.

I owe a special thanks to Marek Ziebart for guiding me through the daunting task of thesis writing, for his encouragement and advice on career progression, and for many a motivational Zoom call.

I thank the wonderful friends I've made over the years in Cambridge for their love, positivity and tolerance, with special thanks to Zoe Lederman, Jack Sardeson, Tom Latham, Alex Randall, Marieke Bigg, Celia Bell, Naomi Sirrs, Darren Peterson, Emma Sylvester, Molly James and Paulina Librizzi.

I thank my family for encouraging me to pursue my passion in science, for cheering me on all the way, and for propping me up when the going got tough.

Finally, I thank Georgia, for always being the best.

Declaration of collaborative work

The work presented in this thesis has benefited from collaborations with others, both in experimental practice and conceptual development. These are all stated here, and additionally highlighted in the footnotes where applicable in each results chapter. All data presented in this thesis were generated and analysed by the author.

- Sections 4. 3. 1 – 4. 3. 5: Dr Wolfram Pönisch (Department of Physiology, Development and Neuroscience, University of Cambridge) advised on pseudotemporal inference and assisted in formalising equations for geometric modelling. Drs Wolfram Pönisch, Ewa Paluch (Department of Physiology, Development and Neuroscience, University of Cambridge) and Ben Steventon (Department of Genetics, University of Cambridge) contributed to conceptual development of this project.
- Section 5. 2. 1: Optimisation of the Hybridisation Chain Reaction protocol for use in amphioxus was assisted by Lara Busby (Department of Genetics, University of Cambridge), Giacomo Gattoni and Michael Schwimmer (Department of Zoology, University of Cambridge).
- Section 5. 4. 5: Sophie Kraunsoe (now Wellcome/MRC Cambridge Stem Cell Institute) performed a trial analysis on the DAPT phenotype using the ASCRIBE pipeline. The data presented in this thesis were generated and analysed by the author.

Publications

The work in this thesis has contributed to two publications, which can be found attached in the appendices:

Andrews, T. G. R., Gattoni, G., Busby, L., Schwimmer, M. A., and Benito-Gutierrez, E. (2020). Hybridization Chain Reaction for Quantitative and Multiplex Imaging of Gene Expression in *Amphioxus* Embryos and Adult Tissues. In: Nielsen B., Jones J. (eds) *In Situ Hybridization Protocols. Methods in Molecular Biology*, vol 2148. Humana, New York, NY

Andrews, T. G. R., Pönisch, W., Paluch, E. K., Steventon, B. J., and Benito-Gutierrez, E. (2020). Single-cell morphometrics reveals ancestral principles of notochord development. *Biorxiv, in review*

Table of Contents

<i>Declaration</i>	<i>iii</i>
<i>Summary</i>	<i>iv</i>
<i>Acknowledgements</i>	<i>vi</i>
<i>Declaration of collaborative work</i>	<i>ix</i>
<i>Publications</i>	<i>xi</i>
<i>Table of Contents</i>	<i>xiii</i>
<i>Chapter I: Introduction</i>	<i>1</i>
1. 1 The embryo as a substrate for evolutionary transitions	1
1. 2 A morphogenetic paradox: conserved morphology, divergent morphogenesis	5
1. 3 The amphioxus: ‘flesh of our flesh and blood of our blood’	9
1. 4 Aims of this thesis	13
<i>Chapter II: Materials and Methods</i>	<i>15</i>
2. 1 Wet lab approaches	15
2. 1. 1 Animal husbandry, spawning and fixation	15
2. 1. 2 Immunohistochemistry	15
2. 1. 3 EdU labelling and detection	16
2. 1. 4 DiI labelling	17
2. 1. 5 Blastomere splitting	18
2. 1. 6 Hybridisation chain reaction (HCR)	19
2. 1. 7 Pharmacological perturbations	21
2. 1. 8 UVB irradiation	21
2. 1. 8 Confocal imaging	22
2. 2 Dry lab approaches	22
2. 2. 1 Cell position mapping (EdU landscapes and pulse-chase analysis)	22
2. 2. 2 Tissue segmentation and nuclear detection	23
2. 2. 3 Cell segmentation and shape quantification	26
2. 2. 4 Principal component analysis	28
2. 2. 5 Morphogenetic trajectory inference	28
2. 2. 6 Cell colour-coding for geometric variables	29
2. 2. 7 Morphospacial embedding	29
2. 2. 8 Geometric modelling	29
2. 2. 9 Cell state definition (further information)	29



Chapter III: Definition of tissue behaviours underpinning amphioxus axial elongation33

3.1	Introduction	33
3.1.1	Global principles of vertebrate body plan morphogenesis.....	33
3.1.2	Diverse strategies of body plan morphogenesis in vertebrate models.....	35
3.1.3	Specific aims of this chapter.....	38
3.2	Major morphological transitions during amphioxus axial development	40
3.2.1	Termination of gastrulation and internalisation of the neural plate.....	40
3.2.2	The tailbud <i>sensu stricto</i> forms at the completion of neural tube closure	43
3.2.3	Involution and convergence expand the dorsal mesoderm after invagination	44
3.2.4	Archenteron remodelling I: Emergence and maturation of the somites	50
3.2.5	Archenteron remodelling II: Emergence and maturation of the notochord	53
3.3	Morphometric decomposition of axial tissue elongation	56
3.3.1	Rates of axial elongation and somitogenesis	57
3.3.2	Collection of 3D morphometric datasets.....	59
3.3.3	Axial elongation occurs in a largely growth-free system	60
3.3.4	Elongation is mediated by tissue-specific programmes of convergent extension	63
3.4	Deciphering the role of cell division in growth-free morphogenesis	66
3.4.1	A spatiotemporal map of cell cycle progression	66
3.4.2	Pulse-chase identifies axial progenitors derived from the late blastopore lip	68
3.4.3	Cell division is required for full elongation of the larval body.....	73
3.4.4	Cell division is required for axial tissue geometry but dispensible for patterning.....	76
3.4.5	Volumetrically-reductive division scales cell size to total embryo size	77
3.5	Discussion	81
3.5.1	Emerging principles and open questions	83
3.5.2	Implications for chordate body plan evolution.....	87
3.5.3	Conclusion.....	91

Chapter IV: Unravelling notochord morphogenesis with single-cell morphometrics 93

4.1	Introduction	93
4.1.1	The notochord and its developmental functions.....	93
4.1.2	Formation and folding of the notochordal plate.....	96
4.1.3	A variable role for posterior addition in elongation of the notochord rudiment.....	98
4.1.4	Mechanisms of notochord elongation through convergent extension.....	100
4.1.5	Mechanisms of notochord elongation through cellular growth	102
4.1.6	Knowns and unknowns in amphioxus notochord morphogenesis	104
4.1.7	Specific aims of this chapter.....	107
4.2	Collection and visualisation of notochord cell shape data	108
4.2.1	Cell segmentation approaches.....	108
4.2.2	Morphospacial embedding of notochord cell shape data	110
4.2.3	Geometric parameterisation and morphospacial embedding	114
4.3	Morphospace exploration	118
4.3.1	Single-cell morphometrics highlights two major shape transitions in central notochord cells	118
4.3.2	Geometric modelling reveals a requirement for growth in coupling convergence and extension.....	122
4.3.3	Spatial mapping reveals bidirectional gradients of shape maturation.....	126
4.3.4	Spatial variants in trajectory structure demonstrate divergent and convergent paths to specific cell morphologies.....	129
4.3.5	Can cell shape trajectories explain tissue-scale dynamics?	132

4. 4 Discussion	133
4. 4. 1 What morphometrics can and cannot tell us about development	134
4. 4. 2 Implications for notochord development and evolution	136
4. 4. 3 Conclusion.....	139
<i>Chapter V: Defining axial progenitor cell state diversity with multiplex gene expression analysis</i>	<i>143</i>
5. 1 Introduction	143
5. 1. 1 Evolution through cell type innovation	143
5. 1. 2 The neuromesodermal progenitor (NMp).....	145
5. 1. 3 Specific aims of this chapter	151
5. 2 Quantitative and multiplex imaging of amphioxus gene expression	153
5. 2. 1 Optimisation of hybridisation chain reaction (HCR) for amphioxus embryos.....	153
5. 2. 2 Multiplex HCR imaging of posterior axial markers	154
5. 3 Methods for cell type classification <i>in situ</i>	163
5. 3. 1 Nuclear spheroids (Imaris).....	164
5. 3. 2 Nuclear segmentation (Imaris)	167
5. 3. 3 Nuclear boosting (Ilastik/Imaris).....	169
5. 3. 4 ASCRIBE I: Dispersal of nuclei in gene expression space	171
5. 3. 5 ASCRIBE II: Spatial mapping of putative cell states.....	173
5. 4 Location, fate and potency of neuromesodermal cell states	176
5. 4. 1 Isolation of neuromesodermal cells with gene expression thresholding.....	176
5. 4. 2 Spatial mapping of neuromesodermal cells	178
5. 4. 3 Temporal transitions in neuromesodermal cell number and diversity.....	181
5. 4. 4 Neuromesodermal cells in the late blastopore lip are neurally fated.....	184
5. 4. 5 Neuromesodermal cells require pro-neural signalling for germ layer commitment	185
5. 5 Discussion.....	189
5. 5. 1 Strategies for cell state definition: current options and future prospects.....	191
5. 5. 2 Maintenance of the NM transition state is a conserved motif in chordate development.....	192
5. 5. 3 Conclusion.....	196
<i>Chapter VI: On the evolution of morphogenesis</i>	<i>197</i>
6.1 How to build a chordate.....	197
6. 2 Future directions	203
6. 3 Conclusion	206
<i>Bibliography.....</i>	<i>208</i>
<i>Appendix I: Supplementary figures relevant to Chapter III.....</i>	<i>227</i>
<i>Appendix II: Supplementary figures relevant to Chapter IV</i>	<i>231</i>
<i>Appendix III: Mathematical modelling of notochord cell shape transitions</i>	<i>239</i>
<i>Appendix IV: Supplementary figures relevant to Chapter V.....</i>	<i>245</i>
<i>Appendix V: Amphioxus HCR optimisation chapter (Andrews et al, 2020a)</i>	<i>249</i>
<i>Appendix VI: Notochord cell shape trajectory inference preprint (Andrews et al, 2020b).....</i>	<i>267</i>

Some excuse, or at least some explanation, seems to be needed for the publication of another paper on such a well-worked subject as the embryology of Amphioxus

Edwin. G. Conklin, 1932

Chapter I

Introduction

1.1 The embryo as a substrate for evolutionary transitions

Theories of evolution are frameworks to explain the structure and origins of organismal diversity. The Modern Evolutionary Synthesis, formulated in the early 20th century, drew together Darwinian and Mendelian principles into a unifying theory of evolutionary change (Huxley, 1942). It has since endured as the conceptual lens through which evolutionary transitions are explained, between the binary scales of genotype and phenotype (Dawkins, 1976; Müller, 2017; summarised in Gilbert, 2000). Resting variation in the gene pool of a population generates a corresponding variation of phenotypic form, in which some individuals are fitter, with traits that enhance their survival and reproductive fitness, and others are weaker. As a result, the fitter pass on their genetic information to the next generation at higher frequency. Considered together, this process leads to the exaggeration of successful traits, thereby enabling organisms to adapt gradually, over the course of numerous generations, to face the unique challenges of their environment. This framework of differential survival, resting on random genetic variation as a substrate, confers evolution with a momentum, which has permeated life into the diverse ecological niches of Planet Earth.

However, evolution exhibits dynamics that evade explanation by the principles summated in the Modern Evolutionary Synthesis. If a genetic mutation is to affect the structure and function of a living organism, it must alter how that organism is assembled during its embryonic development, and this physical process of building a body offers a series of constraints, or rules, for how evolution can modulate form. As a result, the embryo plays an integral role in models of evolutionary change. This notion was initially formalised in the early 19th century by Karl Ernst von Baer in his rules of embryology (von Baer, 1828). von Baer posited that general characteristics emerge in development prior to the specific and, in turn, the characters shared by a broader diversity of organisms emerge

prior to the species-specific. When compiled from different organisms, this depicts developmental programmes in an arboreal network, united at a common trunk and branching to divergent terminal forms. For the most part, von Baer's laws have been robust to almost two centuries of embryological research (discussed in Abzhanov, 2013). The branching scheme he proposed for development differs from Haeckel's later recapitulation theory, in which Haeckel proposed that evolution acts by adding new processes to the terminal ends of existing developmental programmes, thereby leading to the progressive emergence of increasingly complex organisms (Haeckel, 1866). Mirroring the *scala naturae*, this culminates in the emergence of human beings as the 'highest' of organisms. In this model, Haeckel argued that phylogeny is embedded within ontogeny, such that humans resemble the adult forms of less complex species during their development (Haeckel 1866, discussed in Hopwood, 2015b). While Haeckel is often dismissed as a popularist and a fraud (Hopwood, 2015a; Hopwood, 2015b), some cases of Haeckelian recapitulation have been described, for example in development of the vertebrate jaw and pharyngeal apparatus (Anthwal et al., 2020; Graham and Richardson, 2012). The early postulations of von Baer and Haeckel have not necessarily stood the test of time, but were pioneering in identifying the embryo as the substrate for evolutionary transitions in form.

The field of Evolutionary Developmental Biology (Evo-Devo) emerged in the 1980s with the fusion of molecular biology and comparative embryology. The remit of the Evo-Devo research programme is essentially to formalise comparative embryology as a mechanistic science; one that goes beyond describing evolutionary transitions and relationships, and seeks to identify the underlying causal processes (Hall, 2012; Müller, 2007; Sommer, 2009; Willmore, 2012a). In other words, it marks a shift from asking *what* to asking *how*. This brief is generally interpreted as an attempt to discern how genetic information is used to construct organisms, and how morphological novelty can arise from changes in the DNA sequence (Carroll, 2008). In this manner, it builds upon the foundation laid by von Baer and Haeckel, by asking how molecular information is translated into differences in the structures of developmental programmes and the organisms they construct, and in doing so shifts the field of focus to the genetic code. Evo-Devo is sometimes considered derivative with regard to the basic principles of the Modern Evolutionary Synthesis. However, it has succeeded in identifying rules and logic to the evolutionary process that emerge from developmental principles, and therefore expands upon the principles summated in the Modern Evolutionary Synthesis (Müller, 2007).

Complexity in organismal form arises through the differential deployment of a limited, and highly conserved, ‘toolbox’ of developmental genes. Many of these are conserved across the major animal phyla, despite radical morphological variation. This includes genes encoding transcription factors (famously including the *Hox* genes) (Duboule, 2007; Graham et al., 1989; Krumlauf et al., 1987; Lewis, 1978), intercellular signalling ligands (Baker, 1987; Echelard et al., 1993; Nüsslein-Volhard and Wieschaus, 1980; Rijsewijk et al., 1987) and signal transduction pathway components (reviewed in Croce and McClay, 2008; Gazave et al., 2009; Hausmann et al., 2009). Given this conservation, a major source of evolutionary variation is in the *cis*-regulatory information associated with protein coding genes (Signor and Nuzhdin, 2018). Changes in the DNA sequence of genetic enhancers can change, for example, the timing (heterochrony), magnitude (heterometry), and position (heterotopy) of gene expression (Arthur, 2004; summarised in Fabrezi et al., 2016). For example, the extreme elongation of bat limbs is attributable to changes in the limb-specific transcriptional enhancer of *Prx1*, as shown by enhanced limb elongation in mice when the endogenous enhancer is replaced by that of the bat (Cretokos et al., 2008). Meanwhile, the relative abundance of limbs and feeding appendages in crustaceans has been shown to derive from changes in the spatial expression domains of the *Hox* genes, *Ultrabithorax* and *Abdominal-A*, which govern homeotic transitions in the limb primordia (Averof and Patel, 1997). An alternative to *cis*-regulatory evolution is changes in the sequence of protein coding genes – evolution ‘in trans’. Through the emergence of novel binding sites, transcription factors can acquire novel functionality, that propagate into morphological novelty. For example, loss of abdominal limbs in insects, within the phylum arthropoda, seems to have arisen by virtue of a mutation in the *Ultrabithorax* nucleotide sequence, leading to *de novo* repression of *Distal-less* expression (Galant and Carroll, 2002; Ronshaugen et al., 2002). Increasingly, the consequence of such aberrations is considered in the context of gene regulatory network topology and dynamics (eg. Clark and Akam, 2016; Verd et al., 2018), and cell type identity as defined by combinatorial expression of different transcription factors (Arendt et al., 2016; Marioni and Arendt, 2017).

In these respects, research in Evo-Devo has been very successful in identifying axes of evolutionary variation at the molecular level, and corresponding variations in form. However, the physical problem of how an embryo is built has often been neglected in Evo-Devo, and eclipsed by the rapid advance of experimental approaches for studying gene expression dynamics and genomic architecture. Nonetheless, if evolution is to act on organismal form, it must ultimately alter the

behaviours of cells and tissues at play during embryonic development. These processes, summated in the umbrella term of ‘morphogenesis’, are the link between genotype and phenotype. For this reason, there has been a call for reintegration of comparative morphology into the study of Evo-Devo (Wanninger, 2015). The study of morphogenesis has accelerated tremendously with the advent of novel imaging approaches and their increased accessibility, quantitative image analysis approaches, *in vitro* embryonic models (Warmflash et al., 2014; van Den Brink et al., 2015; Fulton et al., 2020), computational modelling (Sharpe, 2017), and methods to measure and perturb molecular and mechanical processes during development (eg. Choudhary et al., 2019; Campàs, 2016). With the emergence of this neo-experimental embryology, it has become possible to both map out patterns of cell and tissue behaviour at high resolution, and test how they are controlled. It has become increasingly apparent that form is not a linear readout of molecular patterning information (reviewed in Gilmour et al., 2017; Smith et al., 2018; Lenne et al., 2020). Rather, cell and tissue behaviour is an integrated output of processes acting across multiple scales, whose nature may be molecular, geometric (Guignard et al., 2020), mechanical (Fulton et al., 2020; Godard et al., 2020; Priya et al., 2020; Xiong et al., 2020), metabolic (O’Farrell, 2015; Oginuma et al., 2017), physiological (Dietrich et al., 2014; Huycke et al., 2019) and even bioelectrical (Levin, 2012). Collectively, such interactions compose a complex multi-scale system, whose dynamics are read out in morphogenesis and, ultimately, the forms it produces. In systems of this nature, the effects of genetic mutations – the substrate for natural selection – may be cryptic and non-intuitive.

For Evo-Devo, which seeks to understand the mechanistic basis of morphological innovation, a detailed understanding of the composition of morphogenetic systems, and their dynamics, is therefore essential; only with a deep understanding of the cell and tissue behaviours that generate form can we infer how they have been tuned to generate novelty and diversity over evolutionary time. And, by understanding the interplay between processes operating on multiple scales, we can better define how genetic mutations are translated into morphological variants. For this reason, I propose that research approaches in Evo-Devo need to reflect the multi-scale nature of morphogenetic systems. Methods are required to image and quantitatively map out morphogenesis across scales of observation, from tissue-scale geometry, to cell shape and behaviour, signalling interactions and cell state diversity. These approaches should be broadly applicable in both established model organisms and non-model systems for which experimental traction is limited. By acquiring a quantitative portrait of morphogenesis in different organisms, these can be organised in a phylogenetic

framework to discern the conservation of specific processes, and along which axes evolution has altered morphogenetic programmes to generate morphological diversity and novelty. This will facilitate correlation with environmental factors, that will in turn inform of why certain morphological transitions have been favourable. Ultimately, experimental embryological approaches are needed to infer interactions between processes acting on diverse scales of observation. Computational modelling is then instrumental to integrate complex and dynamic information from multiple scales, and infer how these steer morphogenetic events, likely including both intuitive dynamics and emergent properties. From this standpoint, the plasticity of morphogenetic programmes, and their range of morphological outcomes, can be both simulated computationally and experimentally tested. In sum, Evo-Devo has the potential for a renaissance as an interdisciplinary science, integrating classical comparative morphology with advanced imaging, experimental embryology and systems biology. This returns to the classical discipline of comparative embryology with a mechanistic lens.

1.2 A morphogenetic paradox: conserved morphology, divergent morphogenesis

In my possession are two little embryos in spirit, whose names I have omitted to attach, and at present I am quite unable to say to what class they belong. They may be lizards or small birds, or very young mammalia, so complete is the similarity in the mode of formation of the head and trunk in these animals.

Karl Ernst von Baer, 1828

While von Baer posited that general characters emerge before the specific during embryonic development, later comparative studies revised this hypothesis by noting a diversity in the morphologies of early chordate embryos. This applies to cleavage modes (Hasley et al., 2017), the distribution of maternal yolk (O'Farrell, 2015), patterns of gastrulation (Waddington, 1952) and axial elongation (Bénazéraf, 2019; Steventon and Martinez Arias, 2017; Steventon et al., 2016); the spherical frog gastrula contrasts with the disc-like chick and the cup-shaped mouse. Nonetheless, this diversity is reconciled at a mid-developmental phase, emerging in the wake of gastrulation, in which all chordates exhibit a common composition and topology of tissues that define the so-called body plan (Bertrand and Escriva, 2011; Willmore, 2012b). Given its appearance in the development of all chordates, this period has been defined as the 'phylotypic' stage (Sander, 1983). At the phylotypic stage, the embryo possesses a midline notochord, a dorsal hollow neural tube, bilateral pairs of

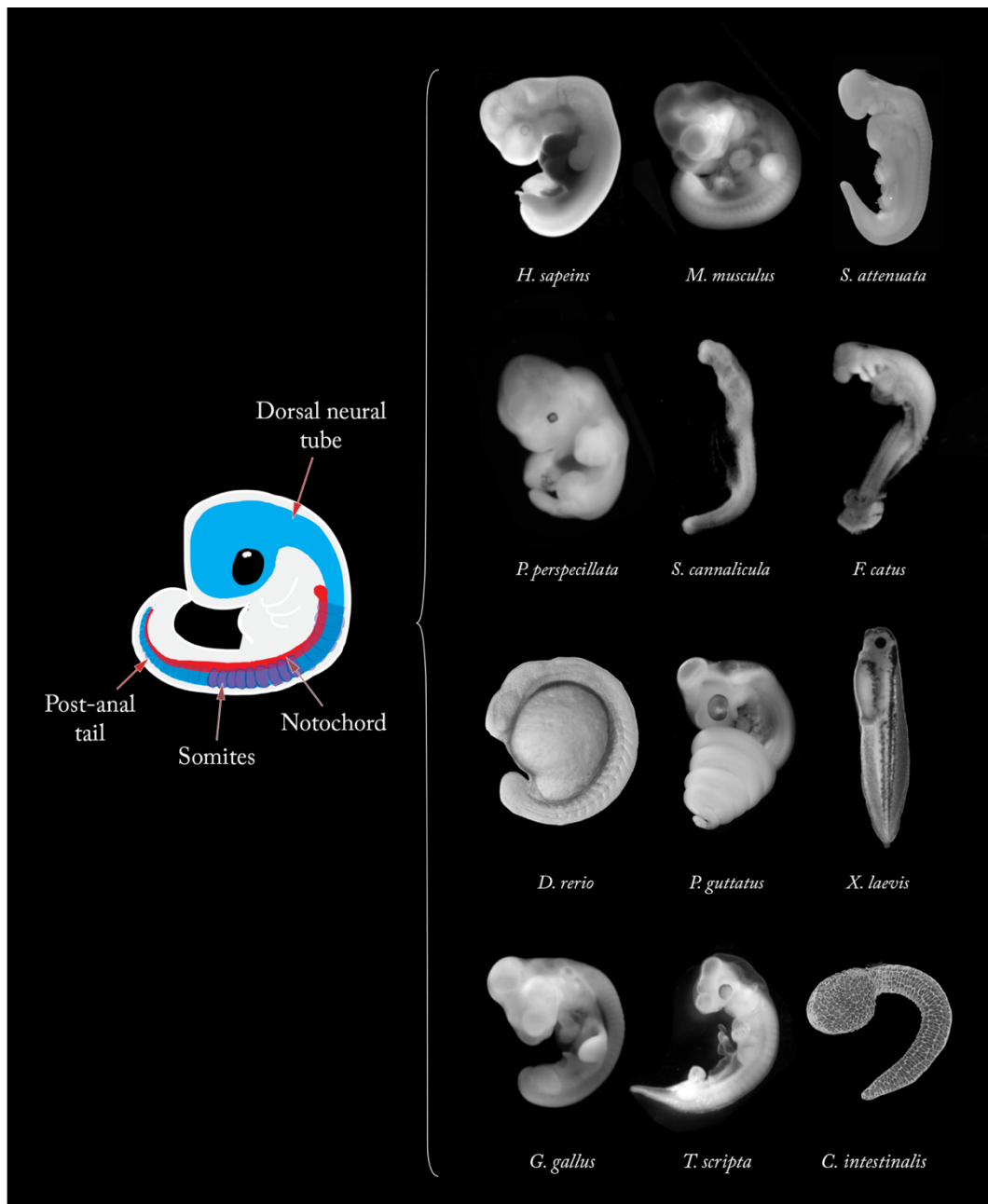


Figure. 1.1. The chordate phylotypic stage. All chordates converge on a ‘phylotypic’ stage of development, characterised by a stereotypical composition and topology of axial tissues; a notochord, dorsal neural tube, post-anal tail and metameric pattern of somites (schematised on left). The general patterns of the body plan manifest at the phylotypic stage are common in all chordates, although variation in conspicuous in axial tissue geometry, size, scale, and time of formation. A diverse selection of chordates at the phylotypic stage are shown on the right, not to scale. Human embryo, Brad Smith, The Multidimensional Human Embryo Project; Mouse embryo, Erica Watson, University of Cambridge; Dolphin embryo (Thewissen et al., 2018); Bat embryo, Richard Behringer; Frog embryo (Santos et al., 2016); Snake embryo, Patrick Tschopp. Zebrafish embryo, Thomas Braunbeck; Ascidian embryo (Lemaire, 2011); Turtle embryo, Abby Lawton; Chick embryo (Blom and Lilja, 2005); Dogfish and cat embryos (Richardson et al., 1997)

metameric somites, a ventral endoderm and a post-anal tail (*Fig. 1.1*). This basic framework of tissues defines the broad anatomical patterns of all chordates, leading to a conspicuous unity of form in adulthood despite extensive diversity in species-specific traits emerging later in development. The extent to which embryos are indistinguishable at the phylotypic stage has been hotly contested since von Baer initially made the claim in 1828, and the artistic license taken with some illustrations has led to some discredit (Bininda-Emonds et al., 2003; Richardson et al., 1997, Hopwood, 2015b). Phylotypic stage embryos are not identical, given conspicuous variation in the size and geometry of axial tissues and their timing of formation, and differences in the spatial context of the embryo, especially in their mode of attachment to large nutritional sources. Nonetheless, in all chordates studied, the product of early development is an embryo of common tissue composition and topology – one in which the body plan manifests (*Fig. 1.1*).

With a period of morphological conservation flanked by diversity, chordate developmental programmes have been described as fitting the contour of an hourglass (Duboule, 1994). Interestingly, transient morphological convergence at the phylotypic stage in vertebrates is also mirrored by an increased similarity in gene expression profiles (Irie and Kuratani, 2011; Irie and Kuratani, 2014), although this fails to account for common transitions in cephalochordate and ascidian embryos (Conklin, 1932; Hatschek, 1893). The prevailing thinking with regard to morphological convergence is that the phylotypic stage marks a period of developmental constraint, with hypotheses relating to transcriptional transitions (Drost et al., 2017), signalling pathway integration (Raff, 1996), resistance of highly conserved patterning processes to evolutionary variation, including spatially colinear expression of *Hox* genes for axial patterning (Duboule, 1994; Slack et al., 1993), and a rise in embryonic lethality in response to molecular and environmental perturbations (Uchida et al., 2018). In this context, flaring of the hourglass either side of the phylotypic stage is considered the product of a lack of constraint, enabling evolution to explore a greater range of morphologies. However, the structure and source of variation leading up to the phylotypic stage has received little research attention.

In the base of the hourglass, a common set of biological patterns, that defines the embryonic body plan (Slack et al., 1993), is mapped onto a diversity of cellular substrates. Since the original formulation of the hourglass model (Duboule, 1994), studies of early morphogenesis in vertebrates and ascidians have highlighted extensive diversity in cell and tissue behaviours, representing

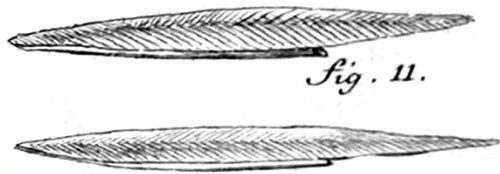
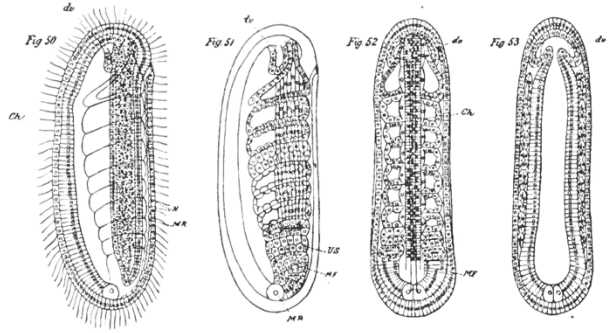
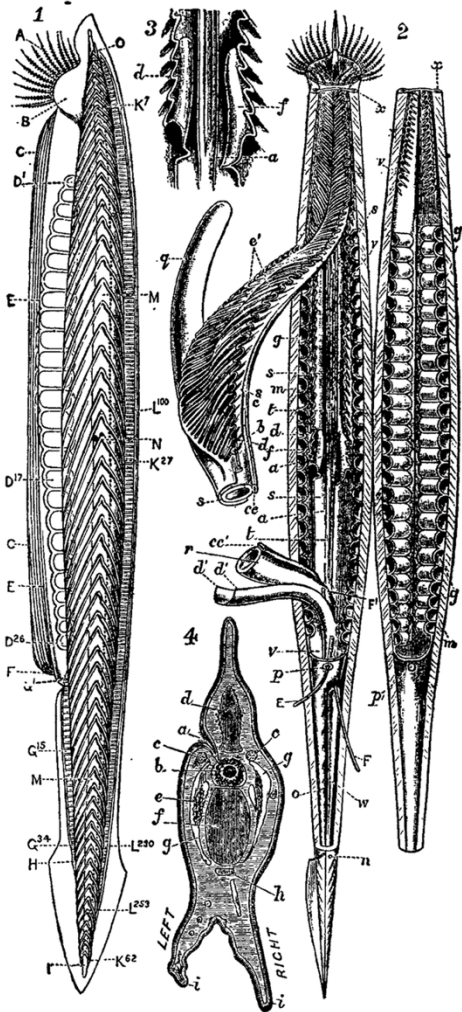


Fig. 11.

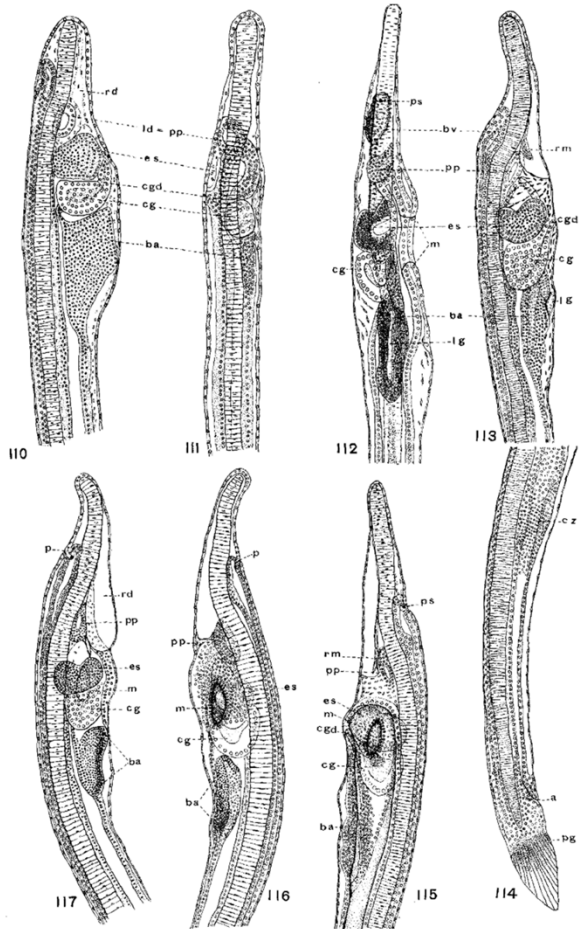
Pallas, 1774



Hatschek, 1894



Lankester, 1889



Conklin, 1932

Figure. 1.2. A first look at amphioxus. Sketches of amphioxus adults and embryos in the golden age of comparative morphology. (top left) The first known illustration of an adult amphioxus, by Peter Pallas (1774). (Bottom left) Adult amphioxus anatomy as depicted by Lankester (1889). (Top right) Amphioxus embryos depicted by Hatschek (1894). (Bottom right) Larval amphioxus as depicted by Conklin (1932). Not to scale.

trajectories of morphological change from the base to the centre of the hourglass. In fact, despite there being a premium on identifying common rules in developmental processes, that encourages generalisations, these morphogenetic events exhibit incredible interspecies variation, which can be categorised on different scales of observation; a) tissue behaviour and growth dynamics, b) the behaviours of single cells and multi-cellular neighbourhoods, and c) cell state diversity, defined by the differential expression of transcription factors. Taken at face value, such differences seem difficult to reconcile. On the other hand, such diversity may be explained by putting morphogenesis in a phylogenetic framework. By understanding the evolutionary distance between morphogenetic programmes, we may uncover order within apparent noise, and a logic to evolutionary transitions that isn't apparent at face value. In turn, we can ask how conserved morphogenetic processes are in early chordate development, along which axes evolutionary transitions are possible, and in what conditions those transitions have been favourable.

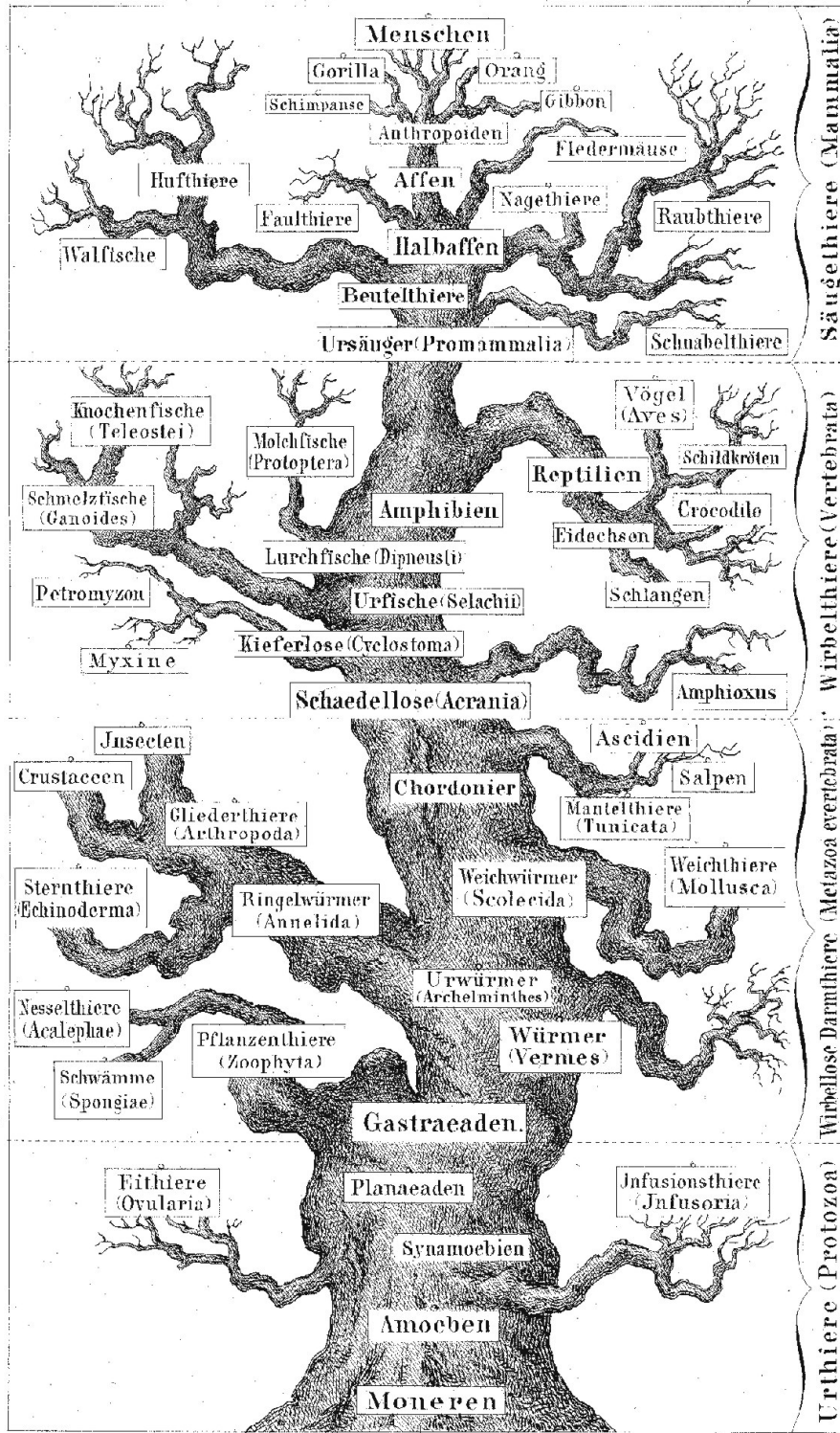
1.3 The amphioxus: 'flesh of our flesh and blood of our blood'

In order to discern which morphogenetic processes are conserved in early chordate development, and how evolution has acted upon them to generate diversity, it is imperative to develop a clear understanding of the ancestral chordate developmental programme. For this reason, a comparative approach is required to infer ancestral qualities based on those exhibited in extant species. With such approaches, the most parsimonious explanation – that requiring the fewest number of character changes – is considered the most likely, although the more convoluted path can never be fully dismissed (Steel and Penny, 2000). For example, if a trait appears uniquely in two sister clades, we infer that it most likely evolved once, in their common ancestor. If however, from a sampling of six clades, the trait appears in two distantly-related clades, the convergent evolution of the same trait twice in these two clades requires fewer transitions than its secondary loss four times after appearing in the common ancestor of organisms in all clades, and so is considered more likely. To infer the ancestral chordate condition, we need to seek shared characteristics in each of the two major subdivisions of the chordate phylum – the vertebrates and ascidians (collectively known as the 'olfactores'), and the cephalochordates.

The amphioxus ('sharp at both ends') was discovered by Peter Simon Pallas in 1774 and initially classified as a sea slug, *Limax lanceolatum* (Pallas, 1774) (*Fig. 1.2*). Subsequent morphological

Stammbaum des Menschen.

Taf. XII.



E. Haeckel del.

1871. Nach J. G. Beck, Leipzig.

Figure. 1.3. Haeckel's pedigree of man. Ernst Haeckel's illustration of animal evolution in the form of a branching tree, culminating in the emergence of man (*menschen*) at its highest tip. Other animals emerge as more proximal branches, in his view representing lesser states of complexity, and lesser states of embryonic development. The branch leading to amphioxus is the first within the vertebrates (*wirbeltiere*), appearing as the only member of the acrania – vertebrate lacking a head. From Haeckel's Pedigree of Man, 1874.

studies by Gabrielle Costa (1834) and William Yarrell (1836) motivated its reclassification as a primitive vertebrate, and allocation to a new genus, *Branchiostoma*. Indeed, like early vertebrate embryos, the amphioxus has a notochord, dorsal neural tube, somite pairs, gills slits and a post-anal tail. The centrality of the amphioxus in evolutionary studies, however, emerged from the seminal descriptive work of Alexander Kowalevsky, who described both vertebrate-like and invertebrate-like features during its embryonic development, thereby implicating it as a transitional form (Kowalevsky, 1867). This view was largely popularised by Ernst Haeckel (of recapitulation theory), who boldly claimed that amphioxus was not just an early vertebrate, it was the *first* vertebrate. Despite its invertebrate-like appearance, the amphioxus was ‘flesh of our flesh and blood of our blood’. Haeckel described the amphioxus as the last surviving member of an early division within the vertebrates, yielding on one side the lineage leading to humans, and the other a group of headless vertebrates represented only by the amphioxus (*Fig. 1.3*) (Hopwood, 2015). These claims were subsequently supported by further comparative morphological studies (Maisey, 1986; Schaeffer, 1987), and comparison of ribosomal RNA sequences (Winchell et al., 2002). Within the chordates, this left ascidians (sea squirts) the most basal branch, inferred from their divergent adult morphologies, in which the larval body undergoes a catastrophic morphogenesis and forms a new vase-like body with an often colourful cellulose tunic (Lemaire, 2011). However, a paradigm shift arose in 2006, in which comparison of 146 gene sequences between chordates established ascidians, not amphioxus, as the vertebrate sister group (Delsuc et al., 2006). In turn, the amphioxus was established as representative of the most basally-branching of the chordate subphyla – the cephalochordata (*Fig. 1.4*).

In its prime position as sister group to all other chordates, the amphioxus plays a unique role in evolutionary studies for reconstruction of the ancestral chordate condition; any traits shared by both olfactores and amphioxus are likely ancestral qualities, while unique traits are probably derived. It is important to avoid the assumption here that amphioxus is a proxy for the ancestral chordate, given that it too features a number of derived characters. This includes extensive tandem duplication at some gene loci (Holland et al., 1995; Louis et al., 2012; Meulemans and Bronner-Fraser, 2007; Minguillón et al., 2003), a single frontal ‘eye’ (Lacalli, 2018), profound asymmetry of gills and somites in the larva (Soukup et al., 2015), and secondary loss of vertebrate-like neural organisers in the embryo (Albuixech-Crespo et al., 2017; Lowe et al., 2003). Indeed, it too has experienced 550 million years of evolution since the emergence of the common chordate ancestor in the Cambrian explosion (Chen, 2009). However, amphioxus early morphogenesis, like that of vertebrates, culminates in formation of

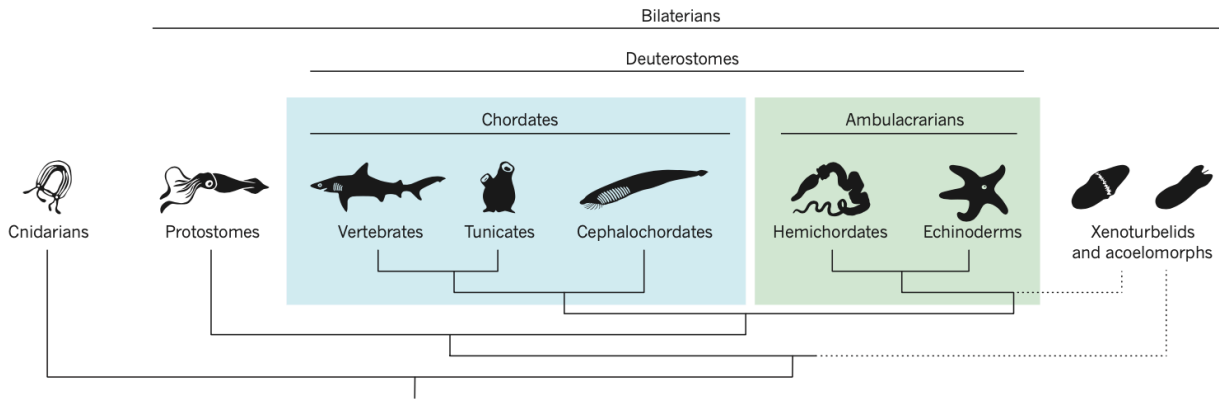


Figure. 1.4. **A simple deuterostome phylogeny.** A consensus cladogram illustrating the relatedness of the major deuterostome clades. The deuterostome super-phylum is made up of the chordate, hemichordate and echinoderm phyla, each defined by a unique body plan. The chordate phylum contains three subphyla. The cephalochordates, which includes amphioxus, is the most basally-branching. Its sister group, collectively termed the ‘olfactores’ includes the tunicates and the vertebrates. Figure taken from Lowe et al, 2015.

a phylotypic chordate anatomy. Therefore, studies in amphioxus development are a critical node for comparison in establishing ancestral mechanisms of development. In the last 30 years, the amphioxus has largely been a workhorse for developmental genetic studies based on *in situ* hybridisation, often in combination with experimental perturbations with small molecule inhibitors to infer signalling pathway function. Major findings based on studies in amphioxus have included; conserved patterning networks specifying the embryonic organiser, which induces dorsal structures (Le Petillon et al., 2017; Yu et al., 2007); a conserved single *Hox* gene cluster expressed across the AP axis with partial spatial and temporal collinearity (Pascual-Anaya et al., 2012); and, recently, evidence for a conserved telencephalic region in the brain, emerging with a temporal delay in amphioxus (Benito-Gutierrez et al., 2018).

Despite this progress in elucidating principles of gene expression and genomic organisation in amphioxus, still extremely little is known about the cell and tissue behaviours responsible for axial development. As a result, the most comprehensive descriptions date back to the late 19th and early 20th centuries, notably by Alexander Kowalevsky (1867), Berthold Hatschek (1893), Edwin Conklin (1932), Thomas Hunt Morgan and Annah Putnam Hazen (1900). These seminal texts, and accompanying sketches, offer great insight into major transitions in embryonic form occurring in early

development, but inevitably lack detail on the specific geometric transitions at play, cell behaviours, clonal dynamics, and cell state diversity. This means that existing descriptions of amphioxus development cannot easily be reconciled with modern, often quantitative, studies on vertebrate and ascidian morphogenesis. Despite this, these early descriptions offer a promising groundwork for future investigations, by identifying many familiar motifs in amphioxus morphogenesis: a stereotypical pattern of radial holoblastic cleavage events that generate a dense array of blastomeres; a process of compaction and cavitation that generates a hollow spherical blastula; gastrulation involving flattening and invagination of the vegetal hemisphere, followed by narrowing and closure of the blastopore; neurulation through separation of neural and epidermal ectoderm, following by folding to generate a tubular morphology; emergence of a notochord and bands of paraxial mesoderm from the dorsal roof of the archenteron; formation of a tailbud; and extensive elongation along the anteroposterior axis. With the benefit of modern imaging approaches and analytical tools, there is now an opportunity to define amphioxus morphogenesis in quantitative detail, and across multiple scales of observation.

1.4 Aims of this thesis

In order to infer ancestral principles of body plan morphogenesis in chordates, in this thesis I present a multi-scale deconstruction of amphioxus morphogenesis, focussing on the emergence and maturation of its axial tissues; the notochord, neural tube, somites and ventral endoderm. In the process, I have sought to apply and develop quantitative approaches for the study morphogenesis in non-model systems, where experimental traction is limited. A comprehensive understanding of amphioxus morphogenesis is a long-term research programme, which I hope only to initiate in this study. In turn, each chapter of this thesis is a case study, in which I seek to define morphogenesis on each of three scales of observation. When put in a comparative context, the data presented offers novel insight into the ancestral chordate morphogenetic programme, and along which axes of variation evolution has acted upon it generate morphological novelty. This also lays the groundwork for follow up studies, with the further development of imaging and experimental approaches in amphioxus, and conceptual advances in the study of the evolution of morphogenesis. My main aims in this thesis are as follows, each of which will be further decomposed into specific experimental aims in each chapter:

1. To describe major morphological transitions in amphioxus axial development, and define the constituent tissue behaviours using 3D morphometrics and embryological perturbations (Chapter III)
2. To infer cell behaviours responsible for elongation of a single axial tissue by imaging cell shape transitions (Chapter IV)
3. To define axial progenitor cell state diversity using molecular and embryological definitions defined in vertebrate systems (Chapter V)

Chapter II

Materials and Methods

2. 1 Wet lab approaches

2. 1. 1 Animal husbandry, spawning and fixation

Wild catch collections of amphioxus, *B. lanceolatum*, were made in Banyuls-sur-Mer, France, and transported to a custom-made amphioxus facility in Cambridge, UK. Adult amphioxus were maintained, bred and the progeny raised as described in Benito-Gutierrez et al (2013). All embryos were raised at 21°C, and fixed in 3.7% (w/v) PFA + 50% (v/v) MOPS (3-(N-morpholino)propanesulfonic acid; Sigma, M1254) buffer for 12 hours, then stored in either a) sodium phosphate buffered saline (PBS) + 0.1% (v/v) sodium azide at 4°C, if to be phalloidin stained, or b) 100% (v/v) methanol at -20°C.

2. 1. 2 Immunohistochemistry

Embryos were first permeabilised overnight in PBS + 1% (v/v) dimethylsulfoxide (DMSO; Sigma, 276855) + 1% (v/v) Triton X-100 (Sigma, T8787). They were then incubated in a bleaching solution of 3% (v/v) H₂O₂ (Sigma, H1009) + 3% (v/v) formamide (Sigma, F9037) in 0.2X SSC (Invitrogen, 15557044) diluted in nuclease-free H₂O (Sigma, W4502), resting on a sheet of aluminium foil under a bright desk lamp. Embryos were then washed from the bleaching solution in PBS + 0.1% (v/v) Triton X-100, and blocked in PBS + 0.1% (v/v) Triton X-100 + 0.1% (w/v) bovine serum albumin (BSA; Sigma, A9056) + 5% (w/v) normal goat serum (NGS, Sigma, 566380) for 3 hours at room temperature. The blocking solution was then replenished, this time to also include primary antibodies as described in Table 1. Primary antibody incubations were performed overnight at 4°C to ensure strong labelling with minimal non-specific binding. The next morning, primary

antibody washes were performed in PBS + 0.1% (v/v) Triton X-100 + 0.1% (w/v) BSA, repeating every 30 minutes for 2 hours, with all incubations at 4°C. Embryos were then transferred to a secondary block of PBS + 0.1% (v/v) Triton X-100 + 0.1% (w/v) BSA + 5% (w/v) NGS for 3 hours, again at 4°C. The secondary block was then replenished, to also include secondary bodies as defined in Table 1. Secondary antibody incubations were performed overnight, in the dark, at 4°C. Where necessary, staining with DAPI (Roche, D9542) at 1:500, and/or Rhodamine phalloidin (Abcam, 235138) at 1:250 was combined with the secondary antibody incubation. After the secondary incubation, embryos were washed thoroughly with PBS + 0.1% (v/v) Triton X-100, and this was repeated every 15 minutes for at least 1 hour, then every hour for at least 2 hours. After the secondary incubation, all incubation steps were performed in the dark at 4°C. Where laminin and PhH3 were performed together, both primary antibodies were detected by a single goat anti-rabbit secondary antibody, and the two channels were computationally resolved, using the DAPI signal to resolve nuclear PhH3 and non-nuclear laminin signal.

Table 1: Table of antibodies applied for immunohistochemistry

Epitope	Raised in	Supplier	Catalogue no.	Concentration
Laminin	Rabbit	Sigma	L9393	1:50
Acetylated tubulin	Mouse	Sigma	T6793	1:250
Phosphorylated histone H3	Mouse	Abcam	ab5176	1:500
Rabbit IgG	Goat	Abcam	150083	1:250
Mouse IgG	Goat	Invitrogen	84540	1:250

2. 1. 3 EdU labelling and detection

For EdU (5-ethynyl-2'-deoxyuridine) pulse analyses, EdU (Invitrogen, A10044) was applied to live embryos in fresh filtered seawater at a final concentration of 20µM for 2 hours prior to fixation, in a total volume of approximately 30ml. For pulse-chase analyses, EdU was diluted after 2 hours of incubation by transferring embryos to a 30µm pluriStrainer® filter (pluriSelect, 43-50030-03) and passing through an excess (>50ml) of

fresh filtered sea water. In this step, great care was taken not to allow the volume of water contained within the filter to fully deplete, which would cause the embryos to dry out and disintegrate. Embryos were then carefully removed from the filter using a p1000 pipette, and placed in a fresh petri dish containing fresh filtered sea water using a plastic 5ml transfer pipette. They were then returned to the 21°C incubator for the remainder of the incubation period.

Fluorescent detection of incorporated EdU was performed following the bleaching and permeabilisation steps of the immunohistochemistry protocol using a Click-it EdU Alexa Fluor 647 Imaging Kit (Invitrogen, C10634). This was performed at room temperature, with embryos protected from light. As advised in the protocol, for enhanced signal the Click-it copper reagent was replenished after 15 minutes, in a total incubation period of 30 minutes. The Click-it reaction was then terminated by two 15-minute washes in PBS + 3% (w/v) BSA, and at least 4 15-minute washes in PBS + 0.1% (v/v) Triton X-100.

2. 1. 4 DiI labelling

CellTracker CM-DiI (Invitrogen, C7001) was suspended in 100% (v/v) ethanol at a final concentration of 5µg/µl. A 2µl drop of DiI was then placed on a square of parafilm using a p10 micropipette. As the ethanol evaporated (taking 10-15 seconds at room temperature), the tip of a fine glass needle, mounted in a Drummond Nanoject II with MM33 micromanipulator, was submerged within the drop; needles for microinjection were prepared on a needle puller (Sutter Instrument Co.) with borosilicate glass capillary tubes of 1.00mm outer diameter and 0.58mm inner diameter. When the ethanol had evaporated, leaving a crust of crystals around the tip of the needle, the needle was withdrawn and set aside in the dark during embryo preparation. When labelling a large number of embryos, the needle was extended such that it flexed to lay flat on the surface of the parafilm. Care was needed here to gently manoeuvre the needle and avoid breakage.

Live amphioxus embryos were incubated to either 8hpf (for outer blastopore lip labelling) or 10hpf (posterior neural plate labelling), and then moved to a 12°C incubator

to slow further development. From this batch, a small sample of embryos was then transferred to a glass slide, with a single central concave depression, in a small volume of sea water. All following steps were performed using a Leica M165FC dissecting stereoscope, set to darkfield mode. Embryos were manually dechorionated using a pair of fine tungsten needles. For outer blastopore lip labelling, the DiI-coated needle, prepared previously, was then extended such that the tip lay beneath the surface of the water and lay flat against the base of the slide. With this in place, an eyelash wand was used to orient embryos with their blastopores facing down against the glass side, and push them against the side of the DiI-coated needle. Typically, embryos would stick to one or more patches of DiI on the needle tip, which kept them stationary for labelling. After approximately 1 minute, embryos were pulled away from the needle using the eyelash wand, and checked for positive DiI labelling using red epifluorescence. Positively-labelled embryos were imaged under darkfield conditions, and transferred to a large petri dish of fresh seawater for further incubation at 21°C. For posterior neural labelling at 10hpf, the eyelash wand was used to immobilise embryos against the base of the glass slide, with the dorsal side facing up. Meanwhile, using the other hand, the micromanipulator was adjusted to lower the needle tip against the posterior neural plate. After 1 minute, the needle was withdrawn and, as previous, positively-labelled embryos were incubated at 21°C. In both cases, fixed embryos were stored in sodium phosphate buffered saline (PBS) + 0.1% (v/v) sodium azide at 4°C to prevent fluorophore dehydration. After labelling, each needle was re-coated with DiI crystals for further use.

2. 1. 5 Blastomere splitting

Amphioxus embryos were fertilised as normal, and incubated for 1 hour at 21°C. They were then observed constantly under a dissecting light microscope until the first two blastomeres were resolved. At this stage, the plate of embryos was placed on an ice block, and a small batch was transferred to a glass slide with a single concave depression. These embryos were dechorionated using tungsten needles, and the blastomeres separated by gently rolling an eyelash wand forward and backward between them. Successfully-separated blastomeres were then transferred to a large petri dish containing fresh filtered sea water at low density, and incubated to 14ss at 21°C. Due to changes in temperature during the

blastomere splitting procedure, the moment for fixation was approximated 34hpf, but confirmed using morphological criteria, namely somite number and projection of the anterior notochord.

2. 1. 6 Hybridisation chain reaction (HCR)

mRNA sequences for genes of interest were located in the *B. lanceolatum* transcriptome published in Marlétaz et al (2018), and corresponding HCR probes (version 3) were ordered from Molecular Instruments. Probe sets used are itemised in Table. 2. Where possible, 20 probe pairs were ordered per transcript, as per the manufacturer's instructions. The only exception in this study was *Soxb1a*, for which the transcript was too short to accommodate 20 probe pairs (12 probe pairs designed). The required buffers were made in-house as per the published zebrafish protocol (Choi et al., 2018).

Table 2. Table of HCR probes used for quantitative gene expression analysis

Gene	Reference sequence	Hairpin initiator	No. of probe pairs
<i>Soxb1a</i>	BL16399	B5	12
<i>Soxb1c</i>	BL03503	B5	20
<i>Brachyury</i>	BL23557	B2	20
<i>Noto</i>	BL04895	B3	20
<i>Tbx6/16</i>	BL04677	B1	20
<i>Notch</i>	BL19990	B3	20
<i>Delta</i>	BL01694	B1	20

8-12 embryos per stage/condition of interest were selected from stocks stored in 100% (v/v) methanol at -20°C and sorted into 4-well plates. They were then iteratively rehydrated through a methanol/H₂O series in 20% (v/v) increments, separated by incubations of 20 minutes at room temperature. Care was taken not to take embryos up into the pipette during washes, given their propensity to stick to the inner side and become damaged. After the 20% (v/v) methanol wash, embryos were washed thoroughly in PBS + 0.1% (v/v) Triton X-100. As for immunostaining, they were then bleached for 30 minutes in 3% (v/v) H₂O₂ + 3% (v/v) formamide in 0.2X SSC diluted in nuclease-free H₂O, under

a bright desk lamp until transparent under a light microscope. The bleaching solution was removed with 3-4 washes in PBS + 0.1% (v/v) Triton X-100. Because the HCR buffers are based on 5X SSC rather than PBS, embryos were next washed into 5X SSC + 0.1% (v/v) Triton X-100 in H₂O.

The HCR hybridisation, wash and amplification buffers were prepared as per the Molecular Instruments protocol for zebrafish embryos (Choi et al., 2018). Hybridisation buffer was pre-warmed to 37°C in a hybridisation oven. Embryos were then transferred from 5X SSC + 0.1% (v/v) Triton X-100 into hybridisation buffer. Given the viscosity of the hybridisation buffer, it was imperative to mix the buffer with the residual 5X SSC + 0.1% (v/v) Triton X-100 through gentle pipetting. After two initial washes in hybridisation buffer, embryos were incubated in the hybridisation oven for 3 hours at 37°C. The hybridisation buffer was then replenished, to also include each HCR probe set at a final concentration of 40mM. After thorough mixing, the 4-well dish was wrapped in parafilm and left overnight at 37°C for probe hybridisation.

On the second day, embryos were washed 4 times in pre-warmed wash buffer, changing every 20 minutes. The first three washes were performed at 37°C, while the final was left to cool to room temperature. Great care was taken during the wash steps not to accidentally remove embryos, which become almost completely transparent in the hybridisation buffer. Embryos could be identified by changing the orientation of the light, due to their different refractive properties to the buffer. Waste was also always transferred to a separate well for inspection before disposal, and 5X SSC + 0.1% (v/v) Triton X-100 added to aid embryo location. After cooling to room temperature, embryos were washed into 5X SSC + 0.1% (v/v) Triton X-100 every 15 minutes for 1 hour, and then every hour for at least 4 hours to ensure thorough probe dilution. Embryos were then transferred into HCR amplification buffer, pre-warmed to room temperature. Meanwhile, 1µl of each HCR hairpin (purchased from Molecular Instruments) for use was transferred to a single 1.5ml Eppendorf tube and heated to 95°C for 90 seconds. The tube was then transferred to a cool block for 20 minutes, in a desk drawer to prevent undue light exposure. After snap cooling, the hairpin solution was increased to 80µl with fresh amplification buffer. All embryos were then collected in a total volume of 20µl and pipetted into the hairpin solution, leaving a total reaction volume of 100µm. Finally, the Eppendorf containing the embryos

in amplification buffer was wrapped in aluminium foil and left overnight on a shaker at room temperature.

On the final day, 400µl 5X SSC + 0.1% (v/v) Triton X-100 was added to the amplification solution in the Eppendorf tube, and the total volume of 500µl was transferred to the 4-well plate. The solution was then removed and discarded, and replaced with 500µl fresh 5X SSC + 0.1% (v/v) Triton X-100. Before adding to the plate, this was used to wash the 1.5ml Eppendorf and collect any trapped embryos. Embryos were washed in fresh 5X SSC + 0.1% (v/v) Triton X-100 every 30 minutes for 2 hours, and then every hour for at least 4 hours prior to imaging. Ideally, for best signal quality, embryos were left to wash overnight at 4°C prior to imaging.

2. 1. 7 Pharmacological perturbations

Hydroxyurea. Live amphioxus embryos were treated with 2µM hydroxyurea (Sigma, H8627) or an equal volume of dimethylsulfoxide (DMSO; Sigma, 276855). This was performed either between the 6-somite and 14-somite stages (18 - 34hpf at 21°C), or the cup-shaped gastrula and 14-somite stages (8 - 34hpf at 21°C).

DAPT. Live amphioxus embryos were treated with 20µM DAPT (Sigma, D5942) or an equal volume of dimethylsulfoxide (DMSO; Sigma, 276855). This was performed between the cup-shaped gastrula and 6-somite stages (8 - 18hpf at 21°C).

In each case, the total reaction volume was 20ml, in fresh filtered sea water. Embryos to be treated were transferred to a 50ml falcon tube using a 5ml plastic transfer pipette, in approximately 15ml sea water. The drug was then added and the volume made up to exactly 20ml with further sea water. This protocol ensured tight control of final drug concentration. After treatment, embryos were fixed in 3.7% (w/v) PFA + 50% (v/v) MOPS buffer and split for storage in both sodium phosphate buffered saline (PBS) + 0.1% (v/v) sodium azide at 4°C, and 100% (v/v) methanol at -20°C.

2. 1. 8 Pharmacological perturbations

Embryos were exposed to 305nm UV light in a BioDoc-It UVP Imaging System, sterilised with 100% ethanol, for 10 minutes at 18hpf (6-somite stage), and then returned

to a 21°C incubator prior to fixation as described previously (section 2. 1. 1) at 34hpf (14-somite stage). Control embryos were also briefly placed in the sterilised transilluminator, but the UV light was not turned on.

2. 1. 8 Confocal imaging

All imaging for the results presented was performed using inverted confocal microscopy. Embryos were equilibrated in 80% glycerol and mounted in 35mm glass bottomed dishes with a 10mm well diameter (CellVis, D35-10-1.5-N). An eyelash wand was used to position each embryo at the bottom of the dish, immediately against the glass slide, thereby falling within the working distance of most confocal objectives. For the cup-shaped gastrula, embryos were oriented blastopore-down against the slide. Thereafter, up to the 4-somite stage, embryos were oriented dorsal-down. And finally, embryos between 6ss and 14ss were oriented with one lateral side down, against the glass slide. These orientations were the least conducive to embryos rolling during imaging, and kept the whole embryo within the working distance of the objective. When imaging a large number of embryos, they were mounted in a single dish in a lattice pattern, with rows and columns corresponding to stages and conditions. Before imaging, the plates were incubated for at least 2 hours at 4°C to stabilise embryo positions. For the work presented, embryos were either imaged using a Leica SP5 inverted confocal microscope at 40X optical magnification (sections 3. 2. 1 - 3. 2. 2 | 3. 2. 5 | 3. 4. 1 – 3. 4. 2), or an Olympus V3000 inverted confocal microscope at 30X optical magnification (all other sections).

2. 2 Dry lab approaches

2. 2. 1 Cell position mapping (EdU landscapes and pulse-chase analysis)

The point selection tool in FIJI was used to identify a coordinate position for each nucleus positive for EdU or PHH3, plus the most anterior and posterior nuclei in the embryo. The position for each labelled nucleus was then quantified across a normalised AP axis, delineated by the distance between the most anterior and posterior points. Data was then pooled for embryos at each somite stage, and normalised length was scaled to the

mean length per stage. The mean frequency of EdU+/PhH3+ nuclei per embryo was then plotted using the ggridges package in R. In the proliferation landscapes, the peak height represents the *mean* frequency per bin, across all embryos. In the pulse-chase quantification, peak height represents the *total* frequency across all specimens, and each layer represents the contribution of a single embryo.

2. 2. 2 Tissue segmentation and nuclear detection

Z-stacks for embryos immunostained for laminin and acetylated tubulin, and stained with DAPI, were imported into Imaris (Bitplane, 9. 2. 1) for tissue-scale morphometrics. The embryonic anteroposterior (AP), mediolateral (ML) and dorsoventral (DV) axes were aligned with the x, y, z axis of the image using the free rotate tool. Axial tissues were then segmented using the manual surfaces function, in which a 2D spline was drawn around the tissue of interest, with a point spacing of 0.5µm for high resolution segmentation. Splines were drawn every 3-5 slices in transverse reslice of the embryo and automatically assembled into 3D triangle meshes by Imaris. Axial tissues were defined as stated in Table 3.

Table 3: Morphological definitions used for segmentation of axial tissues

Axial tissue	Definition
Trunk notochord	All cells of the notochord between the most anterior and posterior somitic boundaries. The notochord is initially continuous, ventrally, with the endoderm, but from the 6-somite stage is separated from it by a basal lamina. In transverse sections, this defines a ring around the notochord that can be used for unambiguous segmentation.
Trunk somites	All somites aside from the most anterior pair. The nascent somite is the last unequivocally resolved somite, with a complete posterior intersomitic boundary. The presomitic mesoderm, posterior to the nascent intersomitic boundary, is included in the unsegmented region/tailbud. During maturation, somites flatten and extend ventral protrusions, subsequently collapse/become separated. Where visible, these protrusions are included in my definition.

Neural plate/tube	All cells of the neural primordium between the most anterior and posterior intersomitic boundaries. Throughout its development, the neural plate is separated from more ventral mesodermal structures by a basal lamina. In the stages used for segmentation, it is also clearly delineated from the surface ectoderm, and submerged beneath it.
Ventral endoderm	All cells of the ventral endoderm between the most anterior and posterior intersomitic boundaries. The endoderm is initially continuous with the notochord, but within the window of quantitative analysis is separated from it and defined by a circumferential basal lamina, which was used for unequivocal segmentation.
Unsegmented region/tailbud	All cells located posterior to the nascent intersomitic boundary, excluding the surface ectoderm. The unsegmented region acquires morphological hallmarks of a tailbud between the 6-somite and 10-somite stages.

Measurements of tissue length, and volume were acquired directly from Imaris. Mean cross-sectional area was calculated externally as:

$$Area (\mu m^2) = \frac{Volume (\mu m^3)}{Length (\mu m)}$$

Mean diameter was calculated as:

$$Diameter (\mu m) = \sqrt{\frac{4V}{Length (\mu m) \pi}}$$

And the elongation coefficient α was calculated as:

$$\alpha_{(tissue)} = \frac{Length (\mu m)}{Diameter (\mu m)}$$

Nuclear number and positions were defined using the Imaris Spots function, with tissue-specific predictions of mean nuclear diameter, varying based on nuclear size and density. Invariably, under-estimation of nuclear diameter resulted in higher fidelity detection, and fewer false-negatives and false-positives. The prediction diameters were: notochord, 3.5 μm ; neural tube, 3.5 μm ; somites, 3.8 μm ; ventral endoderm; 3.2 μm ; unsegmented region 3.5 μm . In each case, nuclear detection was validated by false-colouring the contents of each spot using a masking function, and confirming the presence of a single spot per nucleus in 2D sections. Having located nuclei, the number was quantified using Imaris. Mean nuclear density was calculated externally as:

$$\text{Density (nuclei}/\mu\text{m}^3) = \frac{\text{Number of nuclei}}{\text{Tissue volume } (\mu\text{m}^3)}$$

Neighbourhood-scale α values were calculated using the same rationale as for the tissue-scale values. For each nucleus, the nearest 19 neighbours along the anteroposterior axis were identified, thereby delineating a neighbourhood of 20 total nuclei. AP dispersal was calculated as:

$$\text{AP dispersal } (\mu\text{m}) = \max(\text{AP}) (\mu\text{m}) - \min(\text{AP}) (\mu\text{m})$$

Mean lateral dispersal was calculated as:

$$\text{Lat dispersal } (\mu\text{m}) = \frac{(\max(DV) - \min(DV)) + (\max(ML) - \min(ML))}{2}$$

Neighbourhood elongation was then calculated as:

$$\alpha_{(\text{neighbourhood})} = \frac{\text{AP dispersal } (\mu\text{m})}{\text{Lat dispersal } (\mu\text{m})}$$

2. 2. 3 Cell segmentation and shape quantification

Z-stacks of embryos immunostained for laminin and tubulin, and stained for actin with phalloidin, were imported to Imaris (Bitplane, 9. 2. 1) for cell segmentation. Cells were segmented manually, using phalloidin staining to delineate cell outlines. Splines were drawn around each cell every 2 slices (equating to 1.58 μ m) in parasagittal section. Cell surfaces were validated by false colouring the contents of each object, using the masking function, and checking its faithful fit to the phalloidin stain in 2D sections. Cells were excluded if contours could not confidently be drawn using the phalloidin stain. The anterior tip, 25%, 50% and posterior tip were densely sampled in all notochords, and in one notochord for the 8 – 14 somite stages, all cells were segmented.

Most shape metrics were obtained directly from Imaris (raw xyz position for centre of surface homogenous mass, 3D orientation of the ellipsoid axes, area, axis-aligned/object-oriented bounding box dimensions, oblate ellipticity, prolate ellipticity, centre of homogenous mass for the DAPI channel masked within each surface, number of triangles, volume). The remainder were calculated manually as stated in Table 4, where l represents AP cell length, x , y , and z represent positions in space, bb refers to bounding box-derived metrics, and $cell$ refers to cell-derived metrics. Position along the AP axis was also recorded for all cells.

Table 4: Equations used for notochord cell shape quantification

Geometric parameter	Calculation
AP:DV ratio	$l_{AP}^{(bb)} / l_{DV}^{(bb)}$
AP:ML ratio	$l_{AP}^{(bb)} / l_{ML}^{(bb)}$
DV:ML ratio	$l_{DV}^{(bb)} / l_{ML}^{(bb)}$
Mean cell diameter $d^{(cell)}$	$\frac{l_{DV}^{(bb)} + l_{ML}^{(bb)}}{2}$

AP anisotropy	$\frac{l_{AP}^{(bb)}}{d^{(cell)}}$
Transverse spreading area	$l_{DV}^{(bb)} \times l_{ML}^{(bb)}$
Cross-sectional area $A^{(cell)}$	$\frac{V^{(cell)}}{l_{AP}^{(bb)}}$
Cuboidness	$Vol / (l_{AP}^{(cell)} \times l_{DV}^{(cell)} \times l_{ML}^{(cell)})$
Sphericity	$\frac{\frac{1}{\pi^{\frac{1}{3}}} (6V^{(cell)})^{\frac{2}{3}}}{A^{(cell)}}$
Flatness	$\frac{l_{max}^{(cell)}}{l_{min}^{(cell)}}$
Nuclear displacement from centre of homogenous mass (x, y, z)	$ABS(x^{(cell)} - x^{(DAPI)})$ $ABS(y^{(cell)} - y^{(DAPI)})$ $ABS(z^{(cell)} - z^{(DAPI)})$
Transverse surface convolution	$\frac{A^{(cell)}}{l_{DV}^{(cell)} \times l_{ML}^{(cell)}}$

In addition to each calculation stated above, categorical variables were defined for position along the AP axis in four sampled regions - anterior (0 – 15% AP length), pharynx (15 – 40% AP length), trunk (40 – 60% AP length), posterior (60 – 100% AP length) – and cell layer across the dorsoventral axis. With prior knowledge of the resolution of different cell shapes across the DV axis, in the dorsal and ventral rows of Müller cells and the central layer in the stack-of-coins organisation, the most dorsal and ventral layer of cells at each stage was categorised as dorsal and ventral Müller respectively, and the remainder were categorised as central layer. These categories were not included in the principal component analysis, which was only applied to geometric variables.

2. 2. 4 Principal component analysis

Principal component analysis (PCA) was performed using the *Factoextra* package in R on the following variables, having excluded those with a correlation greater than 0.9. True dimensions were also removed in favour of relative dimensions in order to isolate shape variation. Within the *Factoextra* package, the 'scale' function was used to standardise the data across all cells, giving them a standard deviation of 1 and mean of 0. After PCA, the PC coordinates were merged with the raw dataset using the `cbind()` function to allow colour-coding and filtering for specific groups.

- o Angle of major ellipsoid axis relative to x, y, z coordinate system
- o Number of triangles
- o Volume
- o Relative AP, DV, ML dimensions
- o AP anisotropy
- o Nuclear displacement from centre of homogenous mass on x, y and z planes
- o Cuboidness
- o Flatness
- o Sphericity

2. 2. 5 Morphogenetic trajectory inference

Trajectory inference was performed using the *Slingshot* package in R (Street et al., 2018), which uses clustering information to build a minimum spanning tree and identify one or more principal curves. The data input to *Slingshot* was the coordinates of the first three principal components, and somite stage was used as a clustering input to guide assembly of the minimum spanning tree. The start and end points of the trajectory were also defined as the first and final somite stages included in the analysis. To study spatial variation, the coordinates for each region were passed to *Slingshot* individually, and the resulting principal curves were compared. The directionality of the trajectory, as marked with an arrow in relevant figures, was inferred from prior information on transitions between somite stages.

2. 2. 6 Cell colour-coding for geometric variables

Colour-coding of cells for the values of specific geometric variables was generally performed using the statistics coding aesthetic in Imaris (Bitplane, 9. 2. 1). For externally derived metrics, for example the principal components and pseudotime, values were imported to Imaris as a new signal channel. In R, *ggplot2* was used to make scatter plots corresponding to each slice of the corresponding Z-stack, in which each point had a grey value scaled to the metric of interest. This information was encoded using the alpha variable. The series of outputted .tiffs was then imported to FIJI as a Z-stack, inverted, converted to 16-bit, and ascribed the same pixel dimensions as the corresponding raw data file. The resulting .tiff file was then imported to Imaris as a new channel, and used to colour-code cells via the statistics coding aesthetic.

2. 2. 7 Morphospacial embedding

All morphospace plots were generated using *ggplot2*, unless otherwise stated, and the *viridis* package was used to colour-scale the datapoints, using the *viridis*, *magma* or *inferno* options depending on the metric. To map datapoints in morphospace back to individual segmented cells, a live annotation function was employed in the *Plotly* package.

2. 2. 8 Geometric modelling

All geometric modelling was performed in Microsoft Excel. The logic and equations employed are explained fully in *Appendix III*.

2. 2. 9 Cell state definition (further information)

The methodology for cell state definition is mostly explained in section 5. 3. Any further details required to perform similar analyses are offered here.

Spheroids. Nuclear spheroids were defined in Imaris using the Spots function, which was applied to the DAPI channel with a predicted nuclear diameter of 3.5 μ m. Before

spot detection, a gaussian blur was applied to the DAPI channel to deplete intranuclear signal heterogeneity. A quality filter was used to fine-tune spot detection, and increase nuclear number until a spot was located in the majority of nuclei. Nuclear detection was validated by setting the grey values within each spheroid to 1000, and confirming in 2D sections that most nuclei contained a single spot. This was never possible across an entire embryo due to heterogeneity in nuclear size and density. Nuclei were dispersed in pairwise coexpression scatter plots in Imaris surpass mode. Background values were calculated for each gene by measuring the mean voxel intensity for each channel in spheroids containing no visible HCR signal. Both the quality filter value and channel-specific background values varied depending on the stage of the embryo in question, and the exact imaging parameters used. Spheroids were plotted in their correct spatial arrangement by uniquely colour-coding each cell state in the aesthetics menu, and returning to the vantage mode.

Imaris nuclear segmentation. The automated Imaris surfaces function was applied for nuclear segmentation. No ‘smoothing’ was performed, to avoid loss of surface detail. The absolute intensity threshold was increased until the surface filled all nuclei, and raw signal remained visible only at the extreme periphery. The success of nuclear segmentation was determined by false-colouring nuclei with a ‘random’ colour spectrum, and by examining a histogram of object volumes – correctly segmented nuclei appear in a strong spike in the histogram, whereas low and high outliers represent merged or over-segmented nuclei. Binary thresholds were calculated for each HCR channel using a Huang methodology, to resolve signal from background. Groups of nuclei expressing each possible combination of genes were then isolated into unique groups. In each group, the corresponding nuclear surfaces were used to isolate constituent DAPI and HCR signal. This enabled construction of a ven diagram of cell states, colour-coding of nuclei by cell state within a single rendering, and validating presence of fluorescent punctae for each HCR channel.

Ilastik and ASCRIBE. An auto-context pipeline in Ilastik was applied for nuclear segmentation against raw DAPI signal. Hysteresis thresholding was used to resolve adjacent objects and generate a label image, using a high threshold of 0.9 and a low threshold of 0.6. The label image was imported to FIJI, where mean fluorescence intensities

for each HCR channel were measured using the 3D ROI manager (Ollion et al., 2013), and stored with raw x, y, z position and volume values in .csv files for each embryo. Before dispersal in gene expression space, objects were filtered by size to remove over- and under-segmented nuclei, with a lower threshold of $50\mu\text{m}^3$ and an upper threshold of $300\mu\text{m}^3$. Signal intensities for each HCR channel were then normalised between 0 and 0.95. Nuclei were then dispersed in pairwise coexpression scatter plots using *ggplot2*, and candidate cell states were isolated using the freehand selection tool in the *gatepoints* R package. Average embryos were made in *ggplot2*, using *statdensity2d()* across all superimposed nuclear positions to define a mean embryo shape for each stage, and *geom_point()* to overlay points corresponding to the selected cell state. These points were ordered and colour-coded for Z-position. For isolation of NM cells, thresholds of 0.05 (low), 0.1 (medium) and 0.2 (high) were applied for normalised intensities of *Soxb1a/c* and *Brachyury1/2* expression.

Spatial mapping into single embryos. The dataframe for the cell state of interest, isolated using *gatepoints*, was filtered for a specific embryo. In the main .csv file for this embryo, these points were given a value of '1' in a new column called 'State'. All other points were given a value of '0'. This modified .csv file was then exported and loaded as a new results table in FIJI. The *Assign measure to label* function in the *MorphoLibJ* package (Legland et al., 2016) was used to colour-code objects in the label image for the embryo of interest by their 'State' value. This isolated nuclei corresponding to the state of interest in binary format. This binary image was used as a mask to isolate the DAPI and HCR signal for the corresponding nuclei, thereby enabling their identification and validation within the raw data.

Quantification of cell state number and area. The mean number of cells per embryo for each state isolated using *gatepoints* was calculated using the *aggregate()* function in R. The potential 2D area of spatial occupancy was calculated using the *chull()* function, applied to all cells regardless of embryo of origin, using ML (x) and DV (y) coordinates.

Chapter III

Definition of tissue behaviours underpinning amphioxus axial elongation

3.1 Introduction

In this first chapter, I seek to define processes underpinning amphioxus axial elongation on a tissue scale. This is motivated by a need for rigorous and quantitative description of morphogenesis in a diversity of research organisms, as a means to reconstruct paths of evolutionary change. In characterising these paths, we stand to infer nodes of plasticity within developmental programmes, and sources of constraint that limit morphological diversity. On more general terms, the structure of this chapter is composed to highlight analytical and experimental strategies to study morphogenesis in organisms where experimental traction is limited or absent, the density of information encoded in embryonic morphology, and the essential role of morphogenesis in the study of evolution and development.

3.1.1 Global principles of vertebrate body plan morphogenesis

Gastrulation refers to a large-scale topological reorganisation of the blastula, that culminates in morphological resolution of the three primary germ layers – the ectoderm, mesoderm and endoderm. The product of gastrulation is a trilaminar structure, that is organised along the major orthogonal embryonic axes, and possesses the early primordia for the core body plan tissues (Bardot et al., 2020; Martinez Arias and Steventon, 2018). The resulting embryo consists of a central endodermal layer, composing the future embryonic gut, an external ectodermal layer, containing the neural plate and future epidermis, and an intervening mesodermal layer that will generate the notochord, musculature, bone, vasculature and blood. In this respect, gastrulation manifests a

founding diversity and pattern of tissue primordia, which will be readout morphologically through subsequent tissue-specific programmes of organogenesis.

Although there are superficial differences in the dynamics of gastrulation between vertebrate species, these appear to emerge from conserved patterns of collective cell behaviour that drive common topological transitions in embryos of different shape and spatial context. These behaviours include convergent extension, invagination, involution, ingression and epiboly (Solnica-Krezel, 2005). The balance of each process is variable, but they collectively satisfy a shared challenge of internalising the prospective mesoderm and endoderm within a continuous layer of surface ectoderm. In amphibians, which have spherical embryos, gastrulation is mediated by the blastopore. This emerges as a small indentation on the future dorsal side of the embryo, generated by focal apical constriction in resident cells (Hardin and Keller, 1988), through which mesodermal and endodermal cells enter the embryo through invagination and extensive involution (Keller, 1975; Keller, 1976). The chick embryo, in contrast, develops on the surface of a large yolk supply, and so has a flat discoidal structure. In this case, the mediator of gastrulation is the primitive streak, which is a longitudinal groove at the axial midline, culminating anteriorly in the node (Bénazéraf and Pourquié, 2013). During gastrulation, epiblast cells converge on the primitive streak and ingress through it, undergoing an epithelial-mesenchymal transition, to assemble the deep layers of the embryo (Rozbicki et al., 2015; Voiculescu et al., 2007; Voiculescu et al., 2014). The situation in zebrafish lies between these two states, in that the embryo develops around, and in this case comes to envelope, a small central spherical yolk sac (Kimmel et al., 1995). While the embryo is initially concentrated at the animal pole, it spreads towards the vegetal pole during gastrulation, wrapping around the lateral margins of the yolk (Behrndt et al., 2012; Morita et al., 2017; Petridou et al., 2019). In the process, mesendodermal precursors converge on the future dorsal side of the gastrula, where they involute, and elongate along the anteroposterior axis, while the ectoderm proceeds to cover the embryo through epiboly (Warga and Kimmel, 1990). Finally, the mouse embryo is cup-shaped, with an inner layer of ectoderm and outer layer of visceral endoderm, and burrowed within the uterine wall (Bardot et al., 2020; Tam and Behringer, 1997). Like in the chick embryo, gastrulation occurs by ingression of cells through the primitive streak, which in this case invades a mesodermal layer between the ectoderm and visceral endoderm. The geometry is divergent, but the behaviours are conserved.

The collective cell behaviours that define gastrulation give rise to the most anterior territories of the embryo. More posterior territories then emerge progressively through differentiation of the tailbud at the posterior tip, which is formed at the termination of gastrulation (Beck, 2015; Catala et al., 1995). In vertebrates, this occurs with closure of the posterior neuropore, which impairs further cellular flow between the superficial and deep layers of the embryo (Catala et al., 1995). While the terms used to describe axial development imply a binary transition in developmental dynamics between gastrulation and tailbud formation, the processes are fundamentally continuous (Gont et al., 1993). The tailbud is framed around a lumen connecting the posterior neural tube to the posterior gut, termed the neurenteric canal. The anterior wall of the neurenteric canal is the chordoneural hinge, which is an interface between the posterior notochord and floor plate, while its posterior wall is an interface between the dorsolateral neural tube and paraxial mesoderm (Catala et al., 1995). Fate mapping studies in mouse and chick have revealed the chordoneural hinge to be the post-gastrulation derivative of the node (Cambray and Wilson, 2007; Catala et al., 1995), while similar studies in amphibians have identified it as the descendent of the dorsal blastopore lip (Gont et al., 1993). In both cases, the tailbud thus inherits organiser properties (Gont et al., 1993; Knezevic et al., 1998). Now, in their new positions, cells of the tailbud are progressively allocated to the trunk to extend the axial tissue primordia established during gastrulation, at a rate controlled by long-range signalling gradients across the anteroposterior axis (Bénazéraf and Pourquié, 2013). This includes oppositional gradients of fibroblast growth factor and retinoic acid, which regulate both the maintenance of resident progenitor cells, and their behaviours as they differentiate and passage into the trunk (Cunningham et al., 2015; Olivera-Martinez et al., 2012; Steventon et al., 2016; Yamamoto et al., 1998). Eventually, axial elongation ceases through exhaustion of tailbud cells, in some cases accelerated by apoptosis of residual progenitors (Sanders et al., 1986; Tenin et al., 2010).

3. 1. 2 Diverse strategies of body plan morphogenesis in vertebrate model systems

It is tempting to make generalisations between embryos of different species, but processual similarity at the macroscopic scale contrasts with diversity in the underlying morphogenetic programmes. In vertebrates, posterior elongation of the anteroposterior axis after gastrulation is widely attributed to ‘posterior growth’ - the addition of new tissue volume onto the posterior end of the embryo after gastrulation (Martin and Kimelman, 2009). This has been validated with 3D morphometrics in amniotes, specifically in mouse and quail embryos (Bénazéraf et al., 2017;

Steventon et al., 2016). Although more limited, 2D measurements of presomitic mesoderm length have identified an early phase of elongation followed by depletion in mouse, chick and cornsnake embryos, suggesting that they also expand in size before depleting (Gomez et al., 2008). However, posterior growth is not invariant in amniote species. Zebrafish and lamprey embryos lack a posterior growth phase, and form their body axes primarily through tissue reorganisation (Steventon et al., 2016). In these systems, the posterior unsegmented region is progressively depleted after gastrulation, without a conspicuous growth phase (Steventon et al., 2016). Dogfish (*S. canalicula*), on the other hand, which represent the sister group to boned vertebrates (the Chondrichthyes), do exhibit such a growth phase (Steventon et al., 2016). This variability has been reconciled by considering nutritional constraints on the developmental programme, and its spatial context (O'Farrell, 2015; Steventon et al., 2016). In most externally-developing amniotes, development is fuelled by a limited supply of extracellular yolk, which favours rapid and growth-limited developmental modes. In some cases, however, this constraint has been released, for example in the dogfish, which have a very large yolk supply, housed within a protective casing called a mermaid's purse (Cole and Currie, 2007; Steventon et al., 2016). Nutritional supplies have also expanded greatly in amniotes, with large yolks in avians and the placenta in mammals, corresponding with the increased dependence on posterior growth (O'Farrell, 2015). In a comparative context, it therefore seems that growth dynamics are very plastic in vertebrates, and have co-evolved with spatial and nutritional constraints on the developmental programme.

The amount of growth occurring during axis elongation also appears to correlate with the clonal dynamics of axial progenitor cells. This is summarised in the identification of Steventon and Martinez-Arias (2017) that the posterior neural tube is proportionally represented in fate maps of the late gastrula for zebrafish and amphibian embryos, but is grossly under-represented in corresponding fate maps for mouse and chick embryos (Steventon and Martinez Arias, 2017). This suggests that formation of the posterior body in amniotes requires a greater expansion of posterior neural progenitors than it does in amniotes, which, in turn, coincides with the prevalence of posterior growth. The same principle also seems to apply for the mesoderm. Fate mapping in the chick embryo has identified progenitors initially located in Hensen's node that contribute progeny across large stretches of the notochord and medial compartment of the somites (Selleck and Stern., 1991; Iimura et al., 2007). Meanwhile, recent DiO labelling in the E6.5 mouse gastrula beautifully confirmed that cells in the node-streak border and caudolateral epiblast generate large clones that occupy the entire post-

occipital body axis, in the notochord, floor plate, medial somite compartment and dorsolateral neural tube (Mugele et al., 2018). Previous studies have also demonstrated cells of the mouse chordoneural hinge to have stem cell properties, in so far as they survive multiple rounds of serial transplantation, and each time generate progeny appropriate to axial level (Cambray and Wilson, 2002; McGrew et al., 2008). These dynamics contrast with the smaller clones of amniote axial progenitors. For example, in zebrafish there is very little cell division in the tailbud, such that NMps, with their extensive contribution in amniotes (Cambray and Wilson, 2007; Mugele et al., 2018), only contribute to the extreme tip of the tail (Attardi et al., 2018). Together, these studies suggest that axial progenitor clonal dynamics are a node of evolutionary variation in vertebrate development, and may be linked to the emergence of posterior growth.

Cellular behaviours affecting the demand for posterior growth are not restricted to the tailbud, and here we need to revisit the collective behaviours of gastrulation. In the context of axial elongation, the proportion of the body axis generated by axial progenitors is influenced by the amount of cellular material that passages through the blastopore prior to its closure. Here, involution describes a flow of cells into the embryo, in effect permitting an expansion of the mesendoderm at the expense of the prospective ectoderm. Once this involuted cellular material has been consumed to form axial tissues, further length can only be generated (in so far as has been observed) through clonal expansion and growth of the posterior tip – the tailbud. As a result, involution is an important opportunity to alter the proportions of each embryonic compartment, and thus the cellular material available for later morphogenesis. Accordingly, involution makes a major contribution to axial length in externally-developing amniotes, where posterior cell division and growth is minimised. In zebrafish gastrulation, fate mapping has revealed that sufficient mesoderm is involuted during gastrulation to form 12 of 32 somites, constituting just under one-third of total axial length (Kanki and Ho, 1997; Steventon et al., 2016). In *Xenopus*, involution generates approximately half of the total body axis, as shown in striking loss of the posterior half through extirpation of the tail-forming region, and fate mapping of the blastopore lip (Gont et al., 1993; Keller, 1975; Keller, 1976; Tucker and Slack, 1995). Rather than simply a mode for effective cellular internalisation, involution is therefore an energy-efficient strategy to increase the cellular mass of mesendoderm in the absence of cell division or growth.

The dominant strategy of tissue elongation during gastrulation is convergent extension, which describes tissue elongation at the expense of cross-sectional area (Huebner and Wallingford, 2018; Keller et al., 1985; Wallingford et al., 2002). This change in tissue-scale geometry is typically mediated by active cell protrusion and intercalation, leading to the dispersal of cells across the perpendicular axis, as defined in seminal studies in explants of dorsal mesoderm in *X. laevis* (Shih and Keller, 1992a; Shih and Keller, 1992b). In amniotes, convergent extension makes a major contribution to elongation of the anterior body, whereas the posterior body extends with little further change in width (Bénazéraf and Pourquié, 2013). As such, gastrulation movements and posterior growth, through progenitor expansion, appear to make sequential contributions to axial length. However, this transition is much less defined in anamniotes. In zebrafish, intercalation and convergent extension continue in earnest within the tailbud after gastrulation, and are required for posterior elongation (Kanki and Ho, 1997; Lawton et al., 2013; Steventon et al., 2016). A contrary report from Mongera et al (2018), dismissing intercalation in the zebrafish tailbud, mistakenly assumed a mode of junctional exchange observed in the 2D drosophila blastoderm rather than 3D mesenchymal tissues (Mongera et al., 2018; Shindo, 2018). The zebrafish tailbud is also the site of other gastrulation movements, including epithelial-mesenchymal transitions to expand the presomitic mesoderm (Goto et al., 2017; Lawton et al., 2013). Ongoing convergent extension has also been identified in the posterior notochord of *Xenopus* embryos (Gont et al., 1993). Considered together, the protraction of gastrulation movements within the tailbud in these systems permits further elongation through tissue rearrangement, thus dampening the necessity for further length generation by axial progenitors and posterior growth.

3. 1. 4 Specific aims of this chapter

In this chapter, my aim is to infer morphogenetic processes contributing to axial development in the ancestral chordate condition, using the amphioxus as a laboratory research system. This is with a particular focus on the role of the gastrulation movements of involution and convergent extension, volumetric growth and proliferative axial progenitor cells. Current understanding of amphioxus morphogenesis derives primarily from classical embryological descriptions published in the late 19th and early 20th centuries (Conklin, 1932; Hatschek, 1893; Kowalevsky, 1867). These seminal texts offer detailed descriptions of macroscopic transitions in the shape of the embryo, and its major tissues, in the early phases of development, and in doing so reveal a conservation of form emerging in the

wake of gastrulation not just in all vertebrates, but all chordates. Despite differences in superficial appearance, the amphioxus embryo is remarkably similar in structure to ascidian and vertebrate embryos in the wake of gastrulation; the elongating neurula is composed of a midline notochord, flanked dorsally by a neural tube, ventrally by a primitive gut, and bilaterally by a metameric pattern of somites (Kowalevsky, 1867). However, modern studies of amphioxus development have focussed primarily on its genomic organisation and gene expression patterns, leaving morphogenesis largely unaddressed with modern imaging, analytical and experimental approaches. In response, the aims of this chapter crystallised as follows:

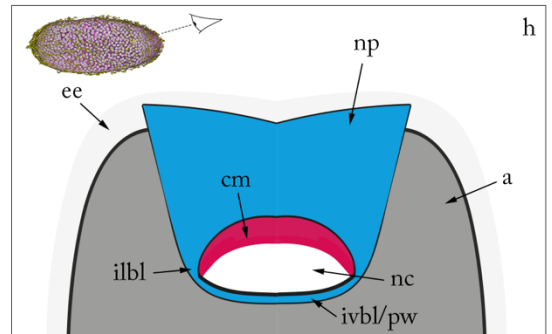
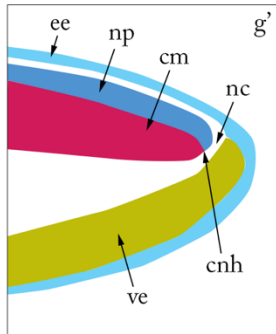
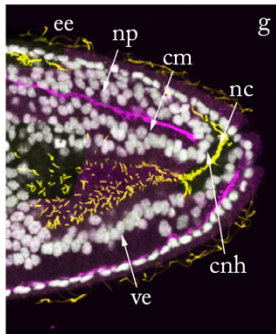
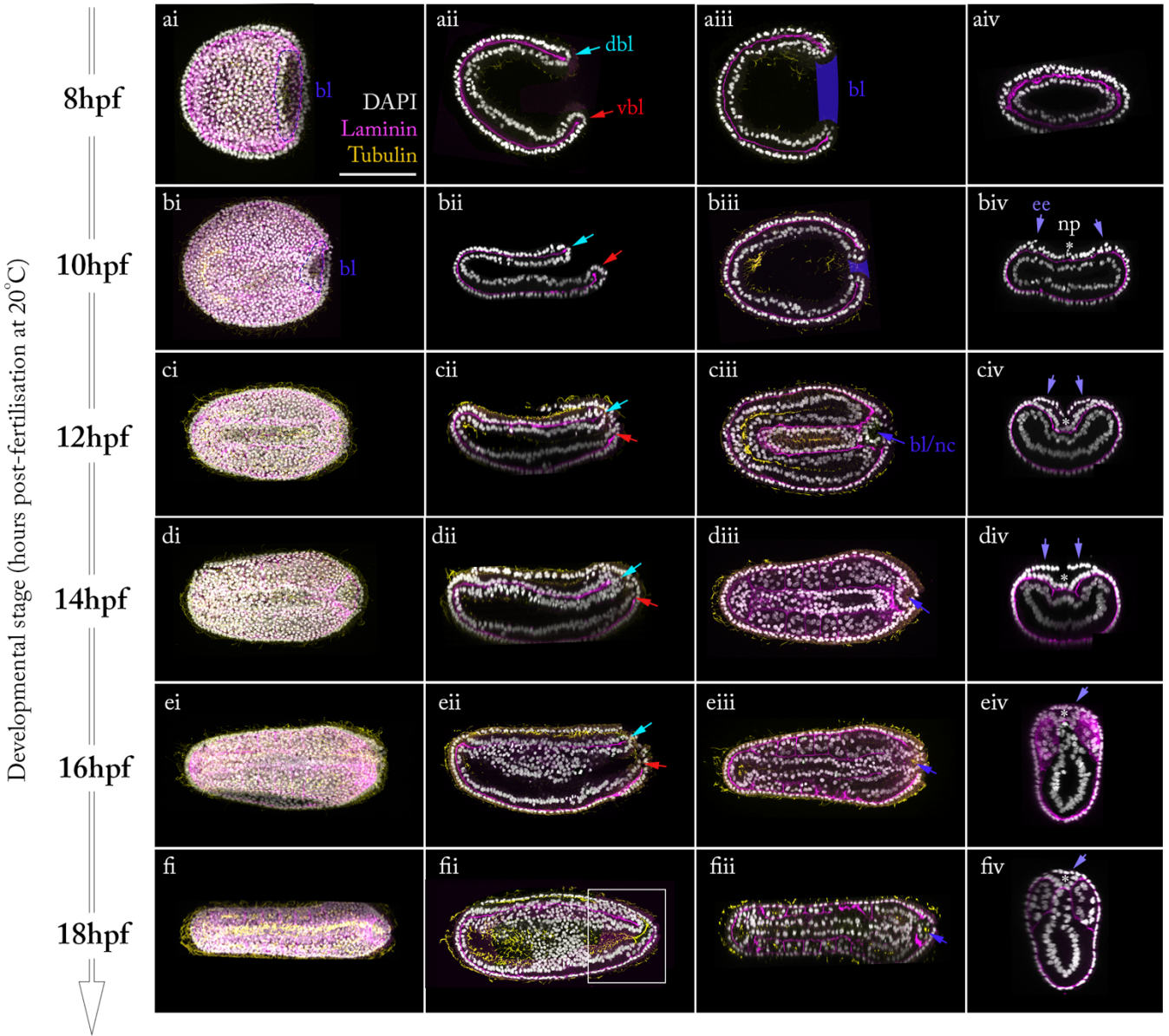
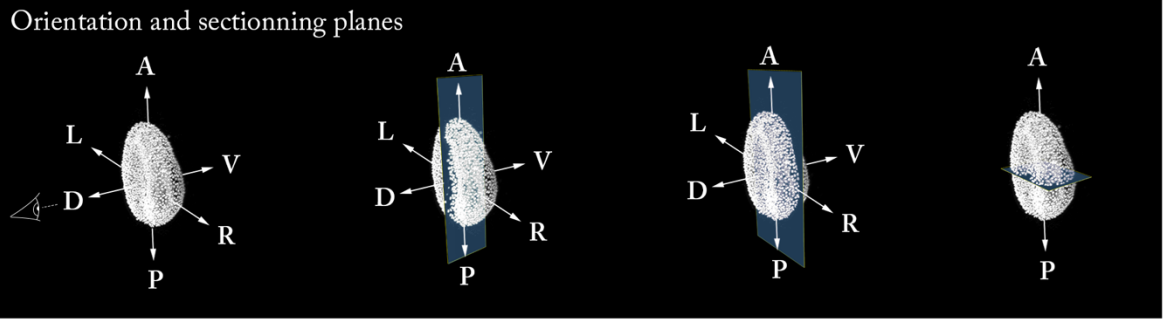
- I. To review major morphological transitions in amphioxus gastrulation and axial elongation using fluorescent confocal imaging at successive somite stages.
- II. To re-evaluate the presence of involution behaviour during amphioxus gastrulation using focal DiI labelling in the embryonic blastopore.
- III. To apply tissue-scale morphometric approaches to quantify changes in axial tissue size, shape and cellular architecture during axial elongation.
- IV. To define the dynamics of cell division in amphioxus axial elongation, and its contribution to embryo shape and size.

3.2 Major morphological transitions during amphioxus axial development

3.2.1 Termination of gastrulation and internalisation of the neural plate

Amphioxus gastrulation commences with invagination of the vegetal plate of the blastula, which generates a cup-shaped embryo with a wide blastopore connecting two juxtaposed epithelial layers; the epiblast (ectoderm) externally and the hypoblast (mesendoderm) internally (*Fig. 3.1. ai – 1iv*) (Hatschek, 1893, Kowalevsky, 1867). Now, both the animal pole and the former vegetal pole of the spherical blastula occupy an anterior position in the embryo, while the blastopore now occupies the posterior pole (*Fig. 3.1. ai – aiv*). The blastopore is a direct interface permitting cellular exchange between the epiblast and hypoblast, and so can be considered the physical mediator of gastrulation. Over the 2-hour period following mesendoderm invagination, the blastopore narrows extensively, to leave only a narrow persistent aperture lying at the posterior tip of the embryo (*compare 3.1ai – aiii with 3.1bi – biii*) (Morgan and Hazen, 1900). It also shifts to adopt a posterior-dorsal position (*Fig. 3.1. bii*). At the same time, the embryo elongates slightly along its anteroposterior axis, and flattens markedly across its dorsoventral axis (*compare Fig. 3.1ai, ii with bi, ii*). This gives the embryo a roughly circular shape when viewed from its dorsal side (*Fig. 3.1. bi*) and a flattened oval shape when visualised in transverse section (*Fig. 3.1. biv*). While this flattening has also been noted by other authors (Conklin, 1932; Hatschek, 1893), it should be considered that embryos are also flattened slightly when mounted for imaging, which may exaggerate the real phenomenon in living embryos. At this

Figure 3.1. Epidermal sealing results in neural plate internalisation and the termination of gastrulation (overleaf). Embryos at successive stages in hours post-fertilisation immunostained for laminin and acetylated tubulin; (i) dorsal views of 3D projections, (ii) sagittal sections, (iii) coronal sections, (iv) transverse views. Stages are separated by 2 hours post-fertilisation, from 8hpf (*ai – iv*) to 18hpf (*fi – iv*). In (ii) panels, cyan arrow indicates the dorsal blastopore lip/chordoneural hinge, and red arrow indicates ventral blastopore lip. In (iii) panels, blue area and arrow indicate the aperture of the blastopore/neurenteric canal. In (iv) panels, blue arrows mark the epidermal ectoderm, and the white asterisk sits above the neural plate. (g) Expanded view of box in (fii), with labelling for tissue subcompartments. (g') presents the same image in schematic form, with each axial tissue colour-coded. (h) Schematised 3D representation of the 6ss posterior body in posterior-dorsal view, showing the continuity of the open neural plate with the former lateral and ventral inner blastopore lips. ee, epidermal ectoderm; np, neural plate; cm, chordamesoderm; nc, neurenteric canal; cnh, chordoneural hinge; ve, ventral endoderm; a, archenteron; ilbl, inner lateral blastopore lip; ivbl, inner ventral blastopore lip; pw, posterior wall. Scale bar shows 50µm and applies to *ai – fiv*.



stage, appearing at 10hpf, there is little conspicuous morphological distinction between mesoderm and endoderm within the archenteron, and the blastopore remains open, thereby leaving the lumen of the archenteron continuous with the external environment (*Fig. 3.1. bi–biv*). Although the neural plate is molecularly-defined within the ectoderm on the dorsal side of the gastrula, expressing the neural marker *Soxb1a* (Holland et al., 2000; Meulemans and Bronner-Fraser, 2007; **Chapter V**), for now it remains continuous with the more lateral epidermal ectoderm (*Fig. 3.1. biv, outer layer*).

In the next two hours of development, between 10hpf and 12hpf, the prospective epidermal ectoderm detaches from the lateral margins of the neural plate and spreads across its apical surface in medial and anterior directions (Hatschek, 1893). At 12hpf, two arms of epidermal ectoderm can be identified in transverse sections, arching medially across the apical surface of the neural plate towards the dorsal midline of the embryo (*Fig. 3.1. civ*). Meanwhile, the neural plate itself is depressed ventrally into a midline concavity within the archenteron roof (*Fig. 3.1. civ*). This concavity lies between the bilateral bands of paraxial mesoderm, whose formation will be described in section 3. 2. 5; throughout axial development, the basal surfaces of the neural plate and archenteron roof remain juxtaposed (*Fig. 3.1. aiv – div*). At 12hpf, the epidermis has expanded to cover the posterior half of the neural plate (*Fig. 3.1. cii*). In the next two hours of development (12–14hpf), it expands further anteriorly to cover the entirety of the neural plate. Nonetheless, the left and right free edges of epidermis remain separated by a small midline deficiency, which is part of a longitudinal aperture spanning the length of the axial midline (*Fig. 3.1. div*). Finally, at 18hpf, this deficiency can no longer be identified, and the epidermis fully envelopes the embryo. The single exception is the anterior neuropore, which occupies an anterior-dorsal position in the embryo (*Fig. 3.1. dii – fii*). This is a persistent aperture connecting the lumen of the anterior neural tube – the future brain – to the external environment. In the posterior body, epidermal sealing involves a separation of the outer (epidermal) blastopore lip from its inner (mesendodermal) counterpart, and its closure across the blastopore aperture. This is best visualised in sagittal and coronal sections as a coherent cellular layer lying posterior and dorsal to the internalised inner blastopore lip (*Fig. 3.1. b–f, panels ii and iii*). As a result, the outer blastopore lip seals early in axial development, while the inner lip remains open.

Collectively, epidermal sealing of the embryo terminates gastrulation, and defines the morphology of the neurula. Even though the inner blastopore lip remains open after epidermal sealing, in so far as there is a persistent deficiency in the posterior wall of the archenteron, its

submergence beneath the surface ectoderm means it no longer represents an interface between the hypoblast and the epiblast (*compare Fig. 3.1. bii with cii – fii*). As such, gastrulation is physically arrested. The neural plate has now also been internalised as a flat epithelial sheet, which comes to lie between the surface ectoderm on its dorsal side, and the archenteron roof on its ventral side (*Fig. 3.1. biv – fiv*). Posteriorly, the neural plate remains continuous with the dorsal side of the archenteron via the internalised dorsal blastopore lip, whose post-gastrulation derivative is termed the chordoneural hinge (*Fig. 3.1. fii*). The chordoneural hinge is an interface between the neural plate dorsally and the chordamesoderm ventrally (*Fig. 3.1. g, g'*). Importantly, amphioxus neural plate internalisation is not coupled to its folding to form a neural tube, as is the case in many vertebrate systems (Lowery and Sive, 2004). *Fig. 3.1. g* and *g'* detail the structure of the posterior body at 6ss as observed in sagittal section, summarising the spatial relationships of the structures introduced in this section. Meanwhile, *Fig. 3.1h* schematises the same tissue topology in 3D, in a posterior-dorsal view, looking down on the posterior neural plate and chordoneural hinge. Note here that the lateral margins of the open neural plate are continuous posteriorly with the lateral and ventral lips of the internalised blastopore. This point is vital for understanding the relationship between neurulation and tailbud formation, which will now be addressed.

3. 2. 2 The tailbud *sensu stricto* forms at the completion of neural tube closure

Formation of the tailbud is a critical event in body plan formation in vertebrates, in which it acts as a niche for axial progenitor cells that fuel anteroposterior elongation of the body axis (Beck, 2015; Davis and Kirschner, 2000; Gont et al., 1993). The epicentre of the tailbud is the neurenteric canal, which is a continuous lumen connecting the posterior neural tube to the posterior archenteron. It is bounded anteriorly by the chordoneural hinge, as described above, and posteriorly by a continuity between the dorsolateral neural tube and archenteron termed the posterior wall (Catala et al, 1997; Gont et al, 1993). In vertebrates, where these terms have been established, all three components of the tailbud – the neurenteric canal, chordoneural hinge and posterior wall - form simultaneously. This is because gastrulation is terminated by neural tube closure. When the lateral margins of the posterior neural plate come together at the dorsal midline and fuse, the neural tube is submerged beneath the surface ectoderm. In the process, the lateral blastopore lips – which are continuous with the posterior neural folds – fuse at the midline to define the posterior wall. As a result, the dorsal blastopore lip (or node in amniotes) is internalised as the chordoneural hinge (Catala et al., 1995; Gont et al., 1993). In

this process, gastrulation and neurulation are completed, and the tailbud is fully assembled around a definitive neurenteric canal. The situation is complicated in amphioxus by a temporal delay of neurulation relative to gastrulation. When the epidermis seals across the embryo and the dorsal blastopore lip is internalised as the chordoneural hinge, the neural plate remains a flat sheet (*Fig. 3.1fv, g, h*). As a result, the neurenteric canal lacks a coherent posterior wall, and will do so until the neural tube closes. To identify the moment of tailbud formation and study its morphology, we must therefore also study the dynamics of neural tube closure.

At 6ss, the neural plate is open across its full length, with a 'U' shape in transverse section (*Fig. 3.1g, h; Fig. 3.2a - c*). From this stage onwards, the lateral margins fold dorsally and medially, and come together to fuse at the dorsal midline. This process is illustrated in the imaging data presented by the transition from neural plate nuclei occupying a 'U' shape, to a rosette-like appearance surrounding a common lumen (*Fig. 3.2a - c*). The latter is clearly marked by the luminal enrichment of acetylated tubulin, initially in apical cilia internalised from the surface of the embryo, and later in longitudinal axonal tracts. At 8ss, the neural tube has clearly sealed at its anterior and posterior tips (*Fig. 3.2bi, iii*), but remains open at its centre, level with the 4th somite boundary (*Fig. 3.2bii*). This region only acquires a tubular structure at the 10ss (*Fig. 3.2c ii*). Considered together, the neural tube commences folding after gastrulation, and seals progressively from the anterior and posterior tips towards the centre. Once this is completed, the ventral aspect of the neural plate is continuous with the posterior notochord via the chordoneural hinge. Meanwhile, the lateral margins of the posterior neural plate have sealed behind the chordoneural hinge, thereby conferring the tailbud with a coherent posterior wall (*Fig. 3.2d, d'*). The luminal structure of the neurenteric canal is explicit in transverse and coronal sections, in which nuclei surround the core of acetylated tubulin staining on all sides (*Fig. 3.2d, d'*). In 3D reconstructions, the neurenteric canal can also be identified as a posterior continuity between the neural tube lumen and the posterior archenteron (*Fig. 3.2e, e'*). A simplified schematic of the 10ss tailbud is provided in *Fig. 3.2f*, which highlights the tailbud as a persistent interface between neural, mesodermal and endodermal compartments of the trunk.

3. 2. 3 Involution and convergence expand the dorsal mesoderm after invagination

In the scheme of tissue folding, splitting and fusing events described thus far, the relative size of the ectoderm and mesendoderm at the end of gastrulation might appear to be determined by the

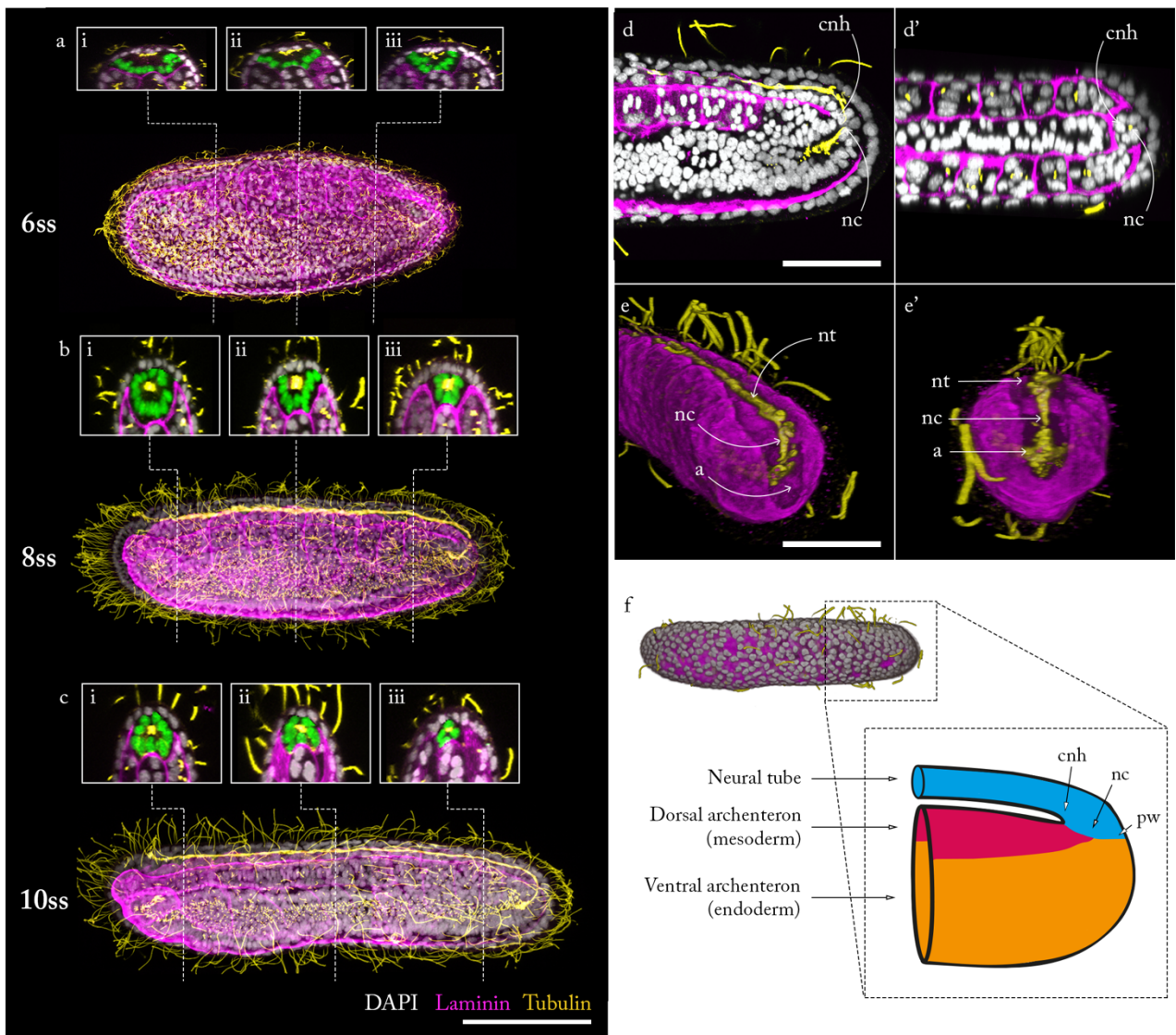


Figure 3.2. The pattern of neural plate folding, and formation of the definitive tailbud. (a – c) Embryos at 6ss (a), 8ss (b) and 10ss (c) in dorsal view, immunostained for laminin (magenta) and acetylated tubulin (yellow), and labelled with DAPI (grey). Transverse lines mark the positions of sections through the neural tube in corresponding inlays i, ii and iii from anterior to posterior. In each inlay, nuclei of the neural tube have been false-coloured green. Acetylated tubulin marks the neural tube lumen in a distinct central puncta. (d) Sagittal section through the 10ss tailbud, showing the neurenteric canal as a continuity between the posterior neural tube and archenteron, marked with acetylated tubulin. (d') Coronal section of 10ss tailbud, showing the presence of nuclei around the neurenteric canal lumen on all sides. (e) 3D projections of immunostaining for laminin and acetylated tubulin in a 10ss embryo, shown in postero-lateral (e) and posterior (e') views. (f) Simplified schematic of 10ss tailbud, showing the continuity between the lumen of the neural tube with that of the archenteron via the neurenteric canal. Folds in the archenteron roof have been collapsed, and the distance between neural tube and archenteron increased, for visualisation purposes. nc, neurenteric canal; cnh, chordoneural hinge; a, archenteron. Scale bars show 100 μ m (a) and 50 μ m (d, e).

proportion of the vegetal hemisphere of the blastula internalised during gastrulation. However, a still contentious issue in amphioxus gastrulation is whether involution - a flow of cells in a continuous sheet around the blastopore lip - further contributes to expansion of the archenteron (Conklin, 1932; Zhang et al., 1997). This is the case for amphibian gastrulation, in which mesodermal and endodermal cells of the marginal zone flow into the embryo through the blastopore lip. As such, labelled cells in the blastopore are internalised and displaced anteriorly (Gont et al., 1993; Krmeta-Stankic et al., 2010). Classical descriptions of amphioxus embryology vary in the amount of involution they report. Lwoff (1894) described the involution of epiblast after gastrulation, especially around the dorsal blastopore lip, based on an apparent morphological distinction between epiblast and hypoblast. This has been matched by similar descriptions from Cerfontaine (1906) and Klaatsch (1897). In contrast, other authors have challenged the presence of involution based on similar morphological criteria. This includes MacBride (1898), Morgan and Hazen (1900) and Conklin (1924). The problem with these descriptions is that cell morphology in fixed specimens is being used to infer movement, therefore resting on the assumption that cell morphology itself is lineage-specific and invariant over the same time course. In this respect, it suffers from the same pitfalls as attempts to predict lineage from gene expression patterns, as elegantly criticised by Stern (2019). Cell movement can only be reliably mapped by following changes in the locations of specific cells and their derivative clones in individual embryos, which can be achieved either through cell marking or live imaging analysis.

Zhang et al (1997) attempted to resolve the contribution of involution to amphioxus gastrulation using DiI labelling. Here, embryos were dechorionated at 4hpf, and immobilised on the bottom of plastic petri dishes, with their anterior pole adhered to the plate and the blastopore lip facing upwards. The authors then filled glass pipettes with Fast DiI-oil and submerged them in sea water, which led to the formation of DiI crystals on the needle tip. By holding these crystals against the surface of the embryo, a ring of eight spots was marked around the circumference of the blastopore lip. The distribution of the DiI spots was then analysed over the course of blastopore closure, up to formation of the cup-shaped gastrula at 8hpf. Over time, the authors noted that the DiI spots elongated towards the centre of the blastopore, but failed to internalise. This observation led to the interpretation that involution makes a negligible contribution to amphioxus gastrulation, instead rendering it a process of simple invagination. However, this study suffers from several major pitfalls. Most importantly, the authors did not follow the DiI spots for the full duration of gastrulation. In

fact, the blastopore remains wide at 8hpf, and continues to close for an additional 4 hours after the end of the Zhang et al (1997) experiments. This means that involution in the latter part of gastrulation remains untested. Furthermore, the potential for sticking embryos to the dish by their epiblast to impair cellular flow into the hypoblast by physical constraint cannot be excluded. Given these limitations, this methodology is therefore insufficient to fully address the role of involution in amphioxus gastrulation.

Given these pitfalls in the Zhang et al (1997) experiments, I sought to retest the presence and contribution of involution using a modified DiI labelling protocol. Surprisingly, I found that Fast DiI oil failed to crystallise in sea water in my hands (*data not shown*). However, I did have some success with DiI suspended in dimethylsulphoxide (DMSO), which crystallised slowly when ejected into sea water, and aggregated spontaneously on the needle tip. Nonetheless, this process generated crystals of highly variable size, which were only sufficient to mark a single spot, ranging from single cells to groups of ~30 (*data not shown*). In sum, I found this method far too variable and low-throughput for experimental use. In chick experiments, dimethylformamide is often used as a carrier for DiI (eg. Selleck and Stern, 1991), but I found this incredibly toxic, leading to rapid embryo death during labelling (*data not shown*). I instead applied a method for DiI crystal preparation described in Rickert et al, 2013 for labelling single neurons in the drosophila nervous system. Here, I suspended DiI in 100% ethanol, and pipetted a 10 μ l droplet onto a sheet of parafilm. I then dipped the tip of a fine glass needle into the drop as the ethanol evaporated (*Fig. 3.3a*). The result was a thin crust of very small DiI crystals coating the needle tip (visible in *Fig. 3.3b*). While each crystal contained sufficient DiI for only a single labelling experiment, I found that many DiI crystals would form along the length of a fine needle if dipped fully into the DiI droplet. This meant that many embryos could be labelled simultaneously along the needle length, thereby enabling experiments of reasonable throughput (*Fig. 3.3b*).

For this experiment, my aim was to test for involution in the latter part of gastrulation, in the window of blastopore closure following formation of the cup-shaped gastrula at 8hpf. This is the time window not covered in the Zhang et al (1997) experiments. To this end, I manually dechorionated embryos at 8hpf using two fine tungsten needles. This was performed on glass plates, which I found amphioxus embryos would not stick to in short incubation periods. I then used an eyelash wand to orient the dechorionated embryos blastopore-down against the glass slide, and push them against the

side of a glass needle coated with DiI crystals (*Fig. 3.3b*). After approximately 1 minute of contact, DiI on the needle surface was locally transferred to the embryo, thereby resulting in small and specific labels in the outer blastopore lip (*Fig. 3.3c, c'*). These contained between 3 and 6 labelled cells. Given the circular shape of the gastrula in this view (see *Fig. 3.3b* for experimenter's view), I found it impossible to discriminate the dorsoventral polarity of the embryo (*Fig. 3.3b, c, c'*). As a result, DiI in the immobilised crystals was locally transferred to the embryo in random positions around the blastopore circumference, depending on the orientation in which it first contacted the needle. After labelling, I gently pulled the labelled embryos away from the needle with an eyelash, verified successful labelling using epifluorescence, and transferred them to a large non-stick petri dish containing fresh sea water using a siliconised pipette tip. After labelling, I incubated embryos up to either 12hpf (the moment of blastopore closure), or 34hpf (formation of the larva) and fixed them in 3.7% (v/v) paraformaldehyde. The final distribution of labelled clones could then be analysed at high resolution with confocal microscopy.

If gastrulation involved only invagination, as reported by Zhang et al (1997), all labels should eventuate in the posterior surface ectoderm, having failed to internalise from the epiblast to the hypoblast during gastrulation. In contrast, I found that the majority of outer blastopore lip labels were internalised by 12hpf, and were therefore located in the posterior archenteron. In the embryo shown in *Fig. 3.3d* and *e*, the DiI label can be identified in the dorsal side of the archenteron, spreading anteriorly in the prospective chordamesoderm and right paraxial mesoderm. At 34hpf, while a small proportion of labels did give rise to patches of posterior ectoderm (2/27, *Fig. 3.3f*), the majority eventuated inside the embryo as posterior somites, and frequently adjacent notochord cells or neurons (25/27, *Fig. 3.3g, i*). In the internalised clones, cells that initially occupied a small localised cluster in the outer blastopore lip were dispersed across the anteroposterior axis, whilst typically remaining continuous with the neurenteric canal (*Fig. 3.3f–h*). As noted previously, the neurenteric canal is a post-gastrulation derivative of the blastopore. In this dispersal across the anteroposterior axis, labelled cells appeared to become intercalated with unlabelled cells, as opposed to only changing spatial distribution within clones (*Fig. 3.3h, i*).

These observations suggest that cells initially located in the outer blastopore lip in the cup-shaped gastrula are internalised into the posterior archenteron through a late phase of involution that follows invagination. Coupled to the Zhang et al (1997) experiments, we can infer that this burst of

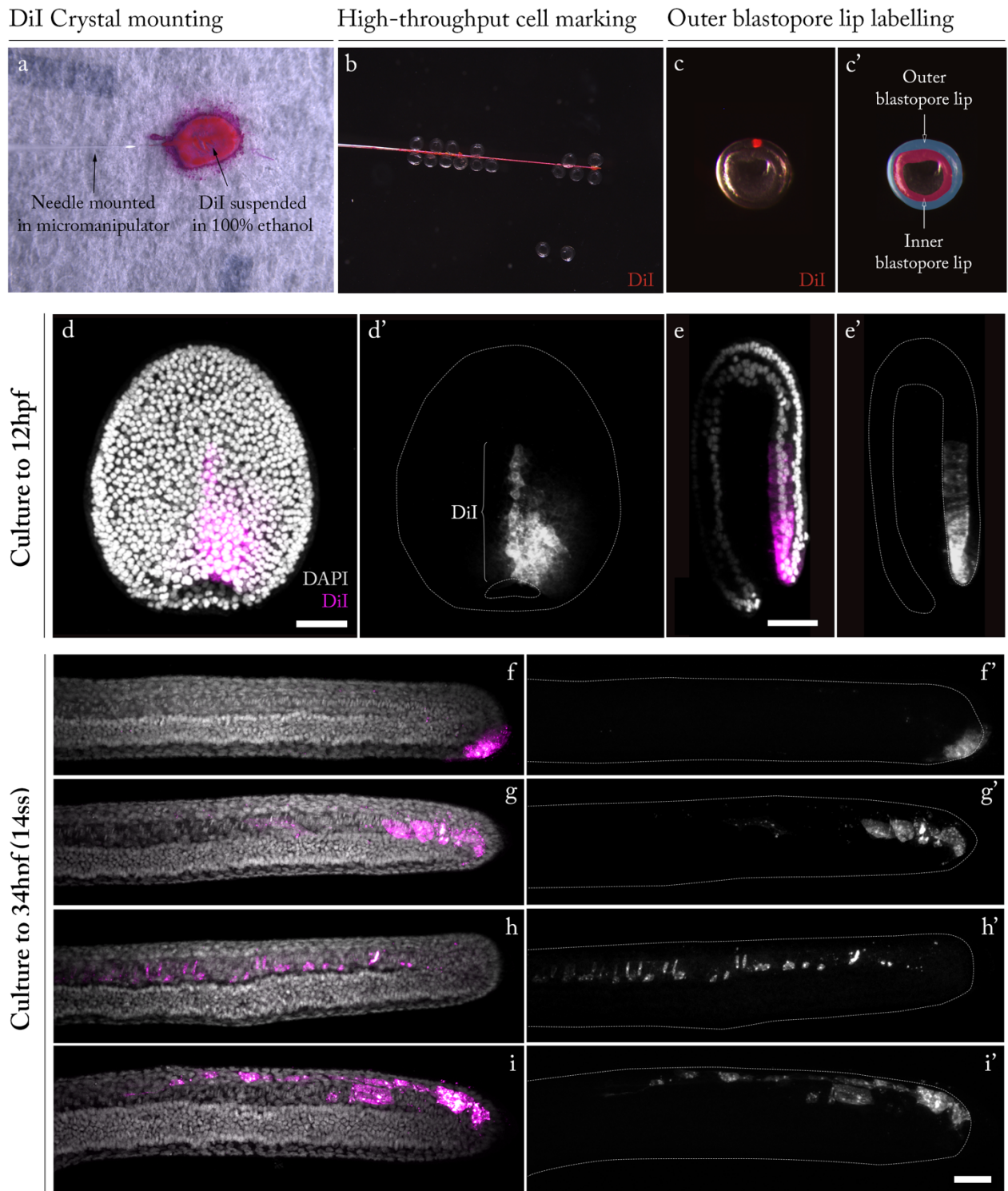


Figure 3.3. Blastopore closure involves involution and convergent extension in the dorsal mesoderm. (a) Mounting method for DiI crystals. A fine glass needle is held in a drop of DiI suspended in 100% ethanol. As the ethanol evaporates, a film of DiI crystals is left coating the needle surface. (b) High-throughput labelling of dechorionated cup-shaped gastrulas, pushed against the side of the DiI-coated needle in random orientations. (c) Representative DiI label in the outer blastopore lip. (c') Colour-coding of embryo in (c), demarcating the inner and outer blastopore lips. (d, d') Labeled embryo fixed at 12hpf, with an internalised DiI label spreading anteriorly in the dorsal mesoderm. (e, e') Embryo from (d, d') in sagittal section. (f–i) Distributions of labelled cells in the posterior body of 34hpf larvae, showing in enrichment in the posterior ectoderm (f), somites (g), notochord (h) and both somites and neurons (i). $n = 7$, 8hpf–12hpf; $n = 27$, 8hpf–34hpf. All scale bars show 50 μ m.

involution occurs between 8hpf and 12hpf, at which point the outer lip of the blastopore then seals over, resulting in physical arrest of further involution. A very unexpected additional finding was that an apparently unbiased labelling of cells around the blastopore margin resulted in a later biased distribution in the archenteron roof and its mesodermal derivatives; invariably, internalised DiI labels were located in its dorsal aspect. One explanation is that, unbeknownst to me, a geometric asymmetry of the gastrula at 8hpf led to a bias in labelling towards the dorsal side. The dorsal side could be slightly flatter, or possibly more adherent to the DiI crystals. However, this was not visible during the experiment. Instead, embryos touched the needle in the orientation of their approach without appearing to roll to a different surface of contact. A more likely possibility is that involution of cells is coupled to their convergence on the dorsal side of the archenteron and extension across it. This is congruent with the finding that internalised clones in the dorsal mesoderm are also dispersed across the anteroposterior axis, and intercalated with unlabelled cells. In this respect, convergent extension behaviour in the archenteron roof would withdraw cells from the blastopore lip, and potentially facilitate its closure. This type of interface between convergent extension, involution and blastopore closure is well documented in amphibians and zebrafish gastrulae (Keller et al., 1985). These proposed movements in amphioxus also map onto known changes in the expression pattern of the pan-mesodermal marker, *Brachyury1/2*, which transitions from a circumblastoporal to dorsal mesodermal distribution during blastopore closure (Holland et al., 1995; Terazawa and Satoh, 1997; Zhang et al., 1997, also see **Chapter V**).

3. 2. 4 Archenteron remodelling I: Emergence and maturation of the somites

In the wake of gastrulation, the archenteron undergoes a stereotypical morphogenesis to generate the notochord, paraxial mesoderm, and ventral endoderm of the trunk (Hatschek, 1893). Of these derivatives, the first to resolve is the paraxial mesoderm (PM). The PM first appears through the evagination of bilateral longitudinal folds in the roof of the archenteron, that project dorsally and laterally. These folds can be seen in transverse section at 2ss, lying to the left and right of the neural plate, which sits in the concavity between them (*compare Fig. 3.1. biv and civ; Fig. 3.4a*). At 2ss, each band of PM remains continuous with the lumen of the archenteron at all positions along the anteroposterior axis (*Fig. 3.4a, inlays*). However, in the anterior, there is evidence of the formation of a series of regularly-spaced transverse fissures that define a loose segmental pattern across the anteroposterior axis (*Fig. 3.4a*). Each transverse fissure emerges preferentially from the medial side of

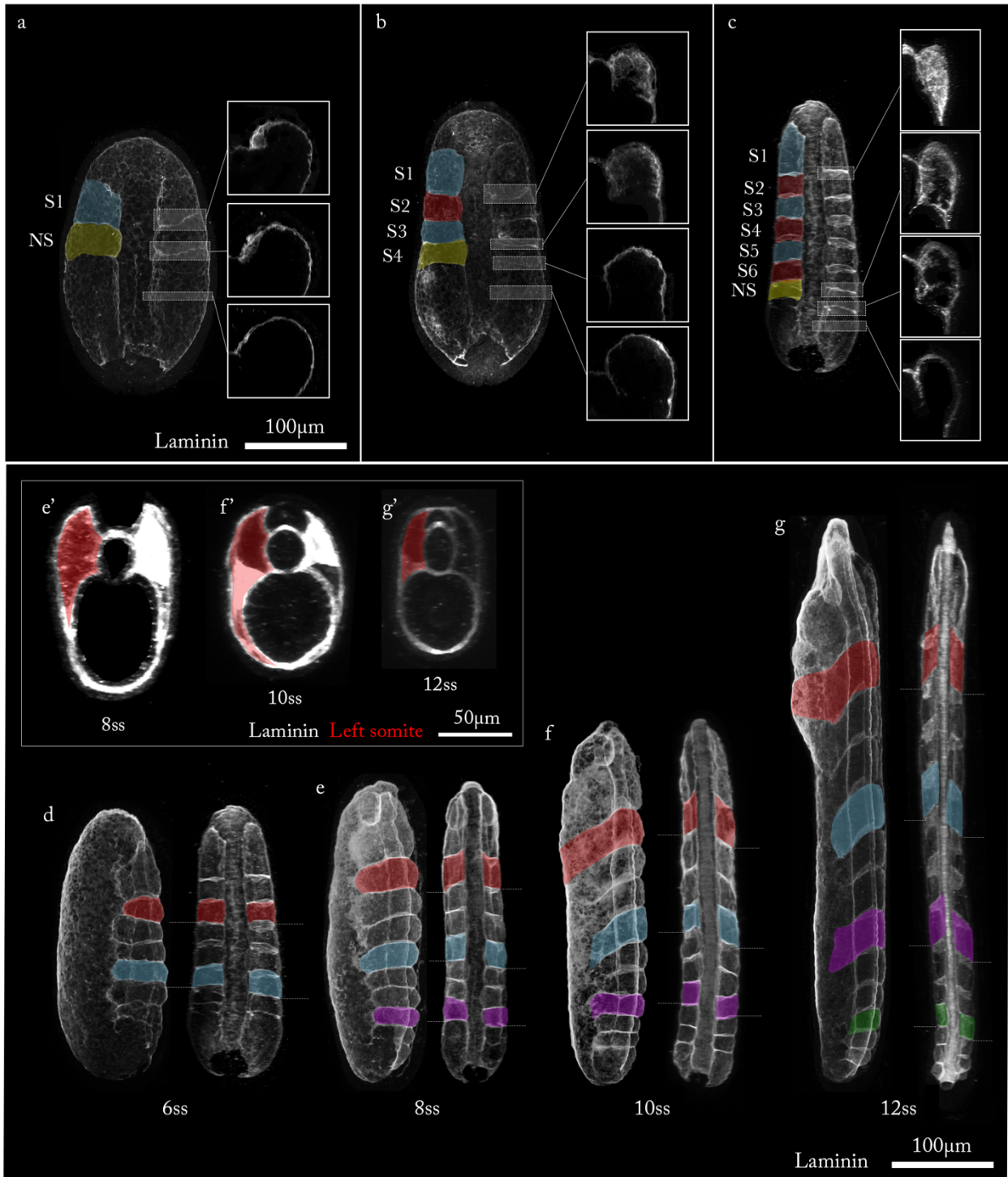


Figure 3.4. **Patterns of somite formation and maturation.** (a – c) Embryos at 2ss (a), 4ss (b) and 6ss (c), immunostained for laminin and shown in 3D projection from a dorsal view. Inlays show transverse sections through the paraxial mesoderm at the level of somite boundaries highlighted in the main projection. Cyan and red colouring marks prospective somites (S1 – S6) along the left side of the body. Yellow marks the nascent somite (NS). (d – g) Embryos at 6ss (d), 8ss (e), 10ss (f) and 14ss (g) immunostained for laminin and shown in 3D projection from a lateral (left) and dorsal (right) views. Highlighted somites mark equivalent somites across the stages shown. Dashed white lines mark the levels of equivalent somite boundaries on the left and right sides. (e' – g') Transverse sections of embryos in (e – g), with somite cross-sectional shape highlighted in red on the left side, including elongate ventral projections.

the PM, and progressively extends across it in a lateral direction to form a coherent boundary between segments. This temporal maturation process can be visualised in fixed specimens at 2ss and 4ss, using relative anteroposterior position as a readout of developmental maturity (*Fig. 3.4a, b inlays*). By 4ss, the anterior-most segments are fully circumscribed from the more posterior PM by coherent transverse fissures (*Fig. 3.4b, 'S1' inlay*). They have also fully budded from the archenteron, and are separated from it by an additional laminin-enriched boundary. As such, there is a temporal delay of approximately 4 somite periods between the first appearance of transverse intersomitic fissures, and the physical delineation of somites as discrete epithelial compartments. For this reason, the prospective somites defined by nascent transverse fissures are more aptly termed 'somitomeres', prior to their full morphological segmentation. From 6ss, all somites are fully separated from the archenteron, while the posterior unsegmented part – which we can term presomitic mesoderm (PSM) – remains continuous with it (*Fig. 3.4c, inlays*).

After gastrulation, the embryo commences elongation along the anteroposterior axis, and somites continue to form at the anterior end of the PSM through the enrichment of extracellular matrix in new transverse fissures. Unlike the early somites, these new fissures seem to emerge circumferentially around the nascent somite boundary in the PSM, and then stabilise inwards towards its centre (*Fig. 3.4c, inlays*). In the process, cells are segregated from the anterior end of the PSM into new somites, and in turn the PSM shortens towards the posterior tip of the embryo (*compare PSM length in Fig. 3.4d – g*). By 14ss, the PSM is entirely lost (*Fig. 3.4g*) (Hatschek, 1893). While each new somite appears similar in shape at their moment of formation, each undergoes a significant change in morphology during its subsequent maturation (*Fig. 3.4a – g*). First, somites elongate along the anteroposterior axis. At 6ss, all somites appear to be of similar length (*Fig. 3.4c*). However, as the axis elongates, a graded distribution of somite lengths emerges across the anteroposterior axis, from the longest in the anterior to the shortest in the posterior (*compare Fig. 3.4d – g*); at 14ss, somite 1 is approximately 5-times the length of somite 14 (*Fig. 3.4g*). In parallel, somites also extend projections towards the ventral midline, between the ventral endoderm and surface ectoderm, and narrow on the mediolateral plane (*compare Fig. 3.4d – g, and inlays e' – g'*). According to classical descriptions, these ventral projections are responsible for generating the lateral trunk musculature (Hatschek, 1893). Finally, somites transform from rectangular, in dorsal and lateral views, to rhomboid (*compare Fig. 3.4d – g*). Viewed dorsally, the somite boundaries rotate away from the axial midline by $\sim 45^\circ$, such that the medial side of each somite reaches further anterior than the lateral. Viewed laterally, the

boundaries also undergo a similar counter-clockwise rotation, such that the dorsal sides reach further anterior than the ventral. Each somite undergoes these morphological changes at a unique rate and magnitude, leading to a stereotypical pattern of somite shapes across the PM at the tissue-scale (*Fig. 3.4g*).

Another transition occurring at this scale is symmetry-breaking between the left and right sides of the embryo. At 14ss, the right somites boundaries are displaced posteriorly relative to the left somites, thereby rendering each column out of phase by one-half-somite (*Fig. 3.4g*). One source of asymmetry in amphioxus development is segmentation itself, in which new intersomitic boundaries form alternately from the left and right bands of PSM (see difference in left/right boundary maturation in *Fig. 3.4a – g*). From qualitative analysis, it appears that somites form preferentially on the right side, which therefore tends to be up to one somite advanced of the left at each stage of analysis (*Fig. 3.4a – g*). In turn, the right PSM also tends to be shorter than the left PSM (clear in *Fig. 3.4c – e*). Nonetheless, there is no conspicuous difference in the length of somites formed on either side of the embryo. Instead, the majority of asymmetry seems to emerge after segmentation. At 6ss, the left and right somites have a roughly symmetrical distribution (*Fig. 3.4c*), which is subsequently lost despite the PM remaining of equal length on either side (*Fig. 3.4g*). By comparing equivalent left-right somite pairs, it appears that somites on the right side elongate more than their left counterparts, thereby displacing the segmental pattern posteriorly (*Fig. 3.4d – g*). This is most apparent at the 10ss, midway through axial elongation (*Fig. 3.4f*). It may be the case that these differences in somite maturation are a consequence of the earlier asynchrony in somite formation – somites on the right are more developmentally advanced. However, this is difficult to reconcile with the right PM remaining the same length as the left (*Fig. 3.4g*). If some somites are longer than expected, others must be shorter. The patterning and morphogenesis underpinning axial asymmetry is an enduring unknown in amphioxus development.

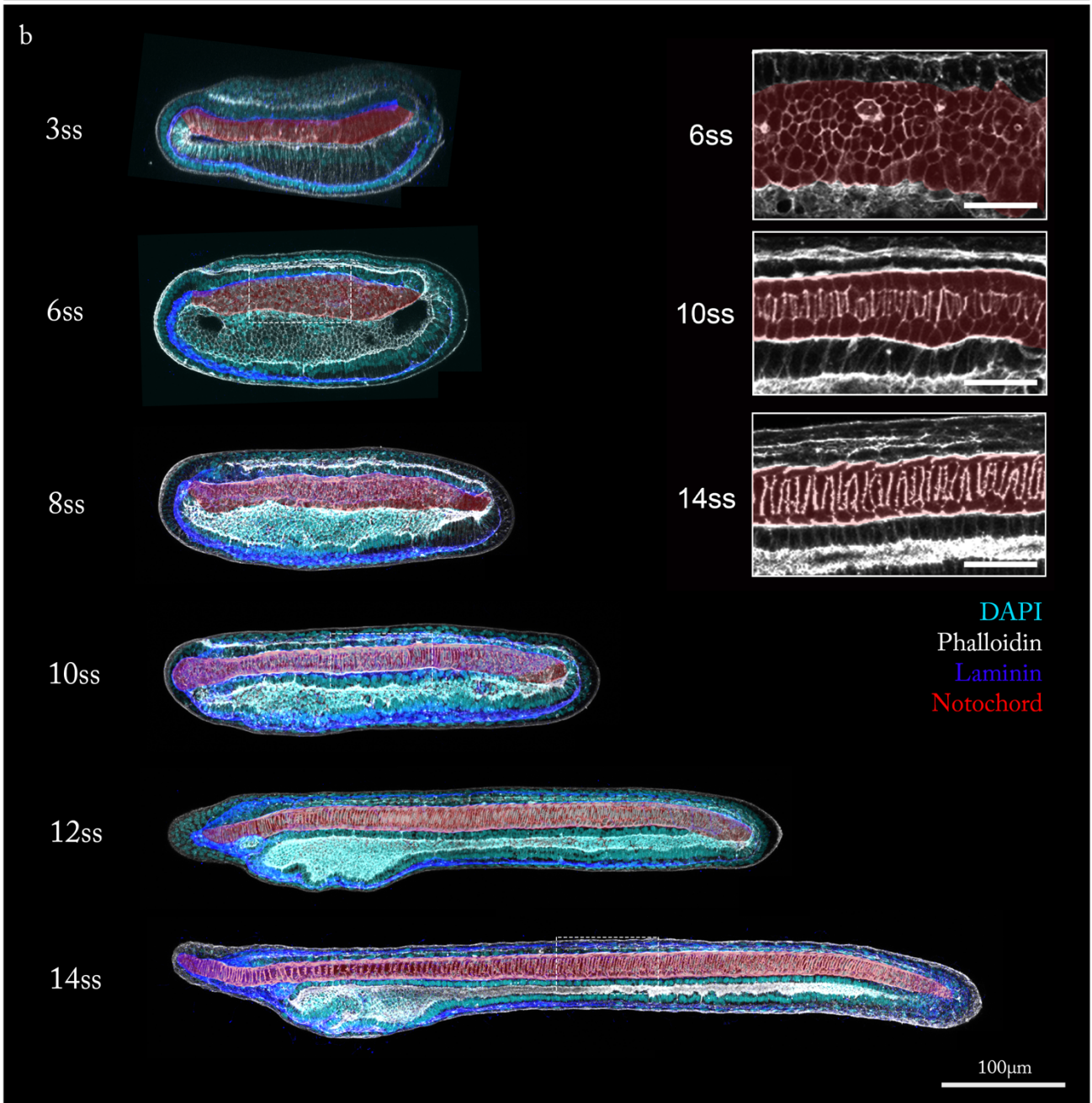
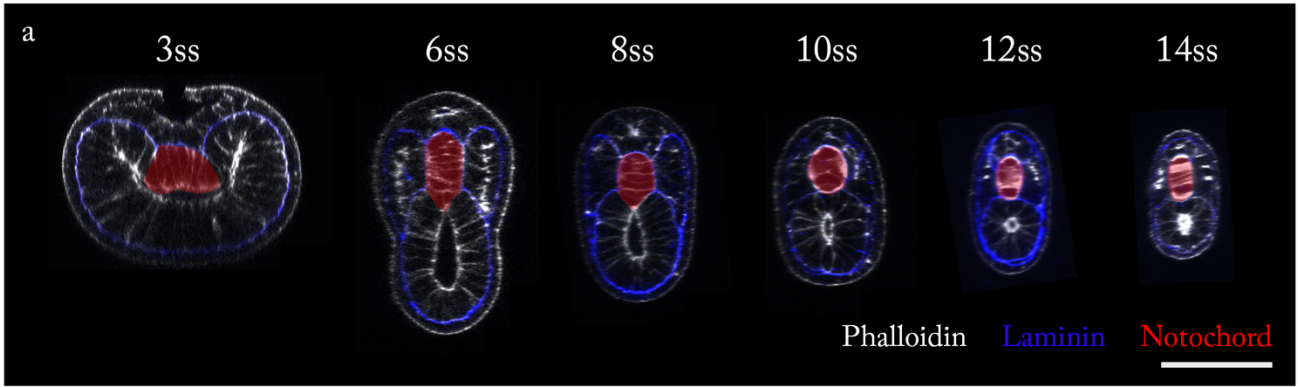
3. 2. 5 Archenteron remodelling II: Emergence and maturation of the notochord

The amphioxus notochord forms after the emergence of the paraxial mesoderm, and occupies a midline position, lying centrally between the somites and ventral to the neural plate. Unlike the neural tube and somites, we can also visualise cell outlines in the notochord through phalloidin staining, given the very strong enrichment of cortical F-actin in these cells (*Fig. 3.5*). At 3ss, the

chordamesoderm (the presumptive notochord) is a flat epithelial sheet, consisting of tall columnar cells in a dorsoventral orientation (*Fig. 3.5a, 3ss*). These lie in the same epithelial plane as the PM on the left and right sides. The chordamesoderm first becomes morphologically-resolved between 3ss and 6ss, when it evaginates from the dorsal roof of the archenteron as a longitudinal groove extending along the anteroposterior axis (*Fig. 3.5a, b 3ss*). In this process, constituent cells change their orientation (that of the longest axis) to extend across the midline, and each acquires bilateral contacts with the left and right sides of the tissue (*Fig. 3.5a, compare 3ss and 6ss*). Thus, by the end of gastrulation, the chordamesoderm can be identified as a multi-layered midline array of mediolaterally-elongated cells (*Fig. 3.5a, b 6ss*). Nonetheless, the chordamesoderm remains continuous with the remainder of the archenteron ventrally, which is known to be distinct in its endodermal fate (*Fig. 3.5a, 6ss*). As development proceeds and the body axis elongates, the length of the chordamesoderm along the dorsoventral axis seems to decrease until, at 10ss, it resolves into three single-file rows of cells (*Fig. 3.5a, b, 6ss-10ss*). The central cells have a conspicuous, and highly conserved, stack-of-coins pattern when visualised in a sagittal plane (*Fig. 3.5b, 10ss + inlay*). The flanking cells, that lie dorsally and ventrally with respect to the central row, are termed Müller cells. These are more rounded than the central row, and have a beads-on-a-string appearance across the anteroposterior axis (*Fig. 3.5b, 10ss-14ss + inlays*). While their function is unknown, roles for Müller cells been proposed in secretion of the notochord sheath and mechanical stabilisation of the anteroposterior axis (Bočina and Saraga-Babić, 2006; Holland and Holland, 1990; Flood, 1975).

Another important change in chordamesoderm morphology is apparent by the 10ss, in its separation from the ventral endoderm through formation of a circumferential sheath. This structure

Figure 3.5. Emergence and maturation of the notochord rudiment (overleaf). (a) Transverse cross-sections of embryos derived from somite stages between 3ss and 14ss, immunostained for laminin and stained with rhodamine phalloidin. The notochord rudiment is false-coloured in red. Between 3ss and 6ss, the notochord rudiment evaginates from the archenteron roof, and cells on either side of the evagination interdigitate across the midline. Between 6ss and 10ss, the number of cell layers in the notochord reduces to 3. (b) Sagittal sections of the same embryos, from 3ss to 14ss, showing elongation of the notochord rudiment. (inlays) Expanded view of boxes marked in (b), showing only phalloidin staining, which is enriched in the cell cortex. Between 6ss and 14ss, the notochord transitions from a seemingly disordered multi-layered array, to a more ordered trilaminar array across the dorsoventral axis.



wraps around all three rows of notochord cells and is roughly oval in transverse cross-section (*Fig. 3.5a, 10ss – 14ss*). It is enriched with both laminin and actin (*Fig. 3.5a*). The sheath is most clearly formed in the anterior region, where it is thickest and stains most strongly, whereas it dissipates towards the posterior end of the embryo where cells continue to compact into the distinctive three-tiered notochord topology (see laminin and phalloidin distribution in *Fig. 3.5b*). After formation of the sheath, the chordamesoderm is physically resolved as a distinct epithelial compartment – the notochord (*compare Fig. 3.5a, 10ss and 12ss*). It is no longer continuous with the paraxial mesoderm or ventral endoderm, apart from within the tailbud where these compartments become continuous (*Fig. 3.5b*). The notochord then proceeds to undergo its most rapid phase of AP elongation between 10ss and 14ss (*Fig. 3.5b*). During this process, the notochord appears to retain its basic cellular topology (*compare Fig. 3.5b, inlays, 10ss and 14ss*), although it does become progressively narrower on a mediolateral plane (*compare Fig. 3.5a, 10ss – 14ss*). In addition, cells of the middle layer – visualised with phalloidin staining – seem to become longer on the anteroposterior axis (*Fig. 3.5b + inlays*). In classical descriptions, elongation this has been linked to proliferation and cellular growth, mediated by vacuolation (Hatschek, 1894). I will return to notochord morphogenesis in **Chapter IV**.

3.3 Morphometric decomposition of axial tissue elongation

The morphological transitions detailed so far in this chapter describe the conversion of the simple cup-shaped gastrula into a multi-tissue system, complete with the primordia for each of the major axial tissues – the notochord, neural tube, paraxial mesoderm and ventral endoderm. Once these primordia have been established in the embryo, they then proceed to elongate in parallel along the anteroposterior axis. This transforms the late gastrula into a free-swimming voracious larva. Now, the amphioxus moves through contraction of axial muscle fibres, which flex the notochord laterally to drive undulatory movement, as opposed to earlier stages of development when embryos move by virtue of motile cilia on the apical surfaces of epidermal cells. As described, axial elongation is also coupled to further tissue-specific changes in structure that are visible at the macroscopic scale, most explicit in segmentation of the paraxial mesoderm to form somites, and stabilisation of a trilaminar cell topology in the notochord. However, the specific transformations in axial tissue geometry and cellular architecture responsible for their elongation have not been defined. The next step in my analysis was therefore to define these processes using quantitative approaches, with a specific focus on the contributions of tissue growth, shape change, and patterns of cell division.

3. 3. 1 Rates of axial elongation and somitogenesis

I first quantified change in axial length over time, and found the rate of axial elongation to be discontinuous (*Fig. 3.6a, b*). During gastrulation, whole embryo elongation progresses at a minimal rate of $5.73\mu\text{m}/\text{hour}$ (*Fig. 3.6a*). This accounts for a total 1.13-fold length change. After the 6ss, the rate of elongation increases sharply, and continues to do so during formation of the posterior 8 somites (*Fig. 3.6b*). In this latter phase, the embryo elongates by a total of 2.7-fold, at a constantly increasing rate. Between 6ss and 10ss, elongation occurs at a mean of $14.86\mu\text{m}/\text{hour}$. Then, between 10ss and 14ss, it accelerates to a mean of $45.87\mu\text{m}/\text{hour}$ (*Fig. 3.6b*). While somitogenesis offers a useful metric for developmental time, because it is reported in the morphology of the embryo itself, we cannot assume that its rate maps linearly onto real time. Indeed, another transition occurring at 6ss is a change in the rate of somitogenesis (compare point spacing in *Fig. 3.6b*). Prior to 6ss, somites form at a rate of 1 somite/hour, while after 6ss they form at a lower rate of 0.5 somites/hour (*Fig. 3.6b*). Collectively, these data reveal two sequential phases of axial development. The anterior six somites form in the latter part of gastrulation, when the surface ectoderm is expanding to cover the inner blastopore lip and internalise the neural plate. During this period, axial length remains relatively stable. The posterior 8 somites then form after gastrulation, at half the rate, and concomitant with an accelerating process of axial elongation.

The next question is where the cellular material for elongation of axial tissues comes from. Axial elongation in vertebrates tends to progress through the differentiation of cells in the embryonic tailbud, and ultimately this compartment tends towards depletion at late stages of axial development. In quail, 3D measurements of tissue volume have shown the prospective tailbud to undergo an early growth phase followed by a late depletion (Bénazéraf et al., 2017), while in zebrafish the tailbud has been shown to undergo a continual depletion without a growth phase (Steventon et al., 2016). A similar 2D approach has been applied in the milkweed bug, *Oncopeltus fasciatus*, highlighting potential growth within the posterior segment addition zone (Auman et al., 2017). Following this rationale in amphioxus, the body axis can be partitioned into broad equivalent domains (*Fig. 3.6c*). Here, I defined the segmented body as that lying between the most anterior and posterior intersomitic boundaries. Anterior to this, axial tissues exhibit an atypical morphogenesis associated with development of the brain and glandular derivatives of the anterior gut (Hatschek, 1893), so I have defined it as a distinct territory, here termed the rostrum. Posterior to the nascent intersomitic boundary, all axial tissues

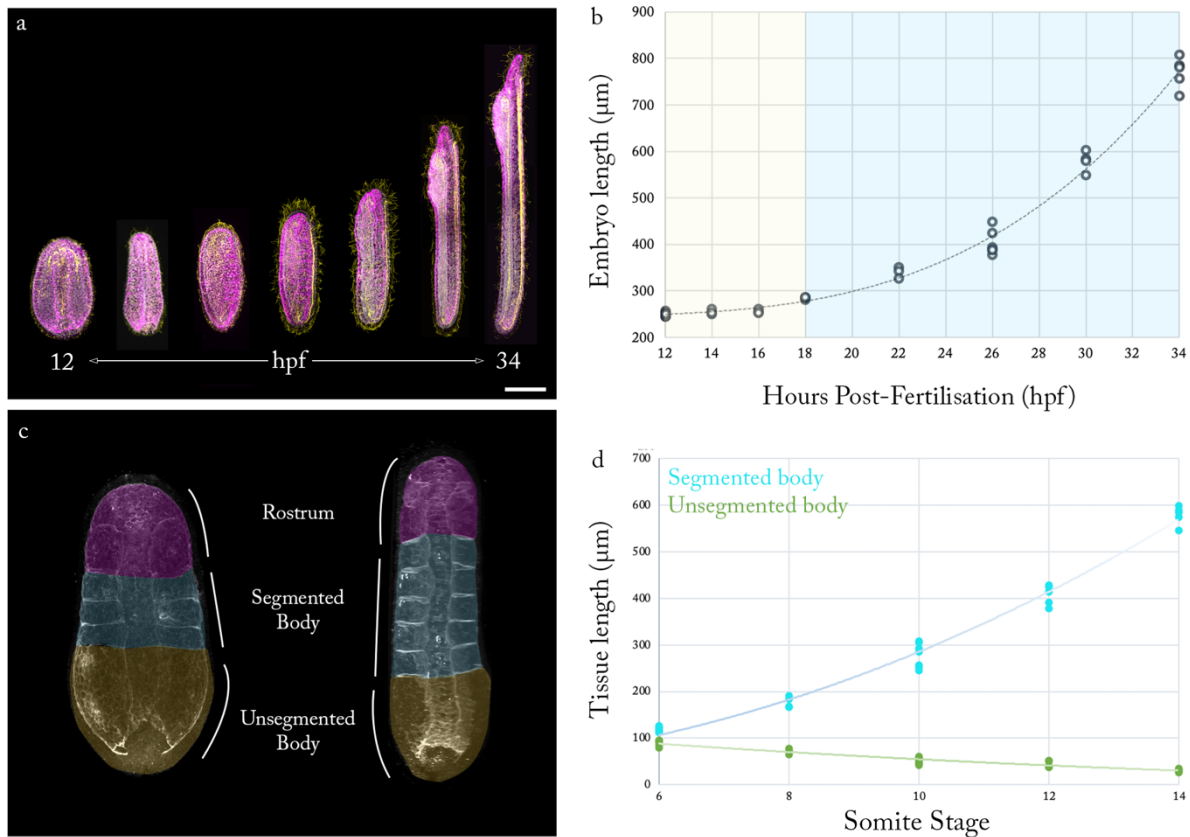


Figure. 3.6. Rates of elongation and somitogenesis in amphioxus. (a) Embryos at successive somite stages between 12hpf and 34hpf, shown as 3D projections in dorsal (12hpf and 14hpf) or lateral (18hpf– 34hpf) view. (b) Quantification of embryo length over time. Measurements are from embryos every two somite stages, and so the graph also shows a transition in rate from 1 somite/hour to 0.5 somites/hour at 18hpf, marked by yellow and blue shading respectively. (c) False-colouring in a 4ss (left) and 6ss (right) embryo showing the limits of the rostrum, segmented body and unsegmented body. The rostrum is anterior to the first intersomitic boundary, the segmented body lies between the first and last resolved intersomitic boundaries, and the unsegmented body lies posterior to the nascent intersomitic boundary. (d) Change in length of the segmented and unsegmented body during axial elongation. $n = 33$ embryos for tissue length quantifications. Scale bar in (a) shows 100µm.

become continuous and so can no longer be morphologically resolved. After 10ss, this region can be considered a tailbud, although for rigour, and the sake of continuity across axial development, I will here term it the ‘unsegmented body’. During axial elongation, the length of the segmented body increases progressively, while that of the unsegmented body decreases (*Fig. 3.6d*). These measurements reflect an anterior-to-posterior wave of differentiation in the paraxial mesoderm, that is punctuated by the progressive formation of intersomitic boundaries (*Fig. 3.6b*). However, the rate of elongation in the segmented body far exceeds that of depletion in the unsegmented body,

suggesting that tailbud differentiation alone is insufficient to explain axial elongation (*Fig. 3.6a*). This could be explained by posterior growth, dispersed growth throughout the body axis, or a driving role for tissue rearrangement. To resolve these possibilities, the full 3D structure of axial tissues must be considered.

3.3.2 Collection of 3D morphometric datasets

To infer the distribution and relative contributions of tissue growth and rearrangement to axial elongation, I used an image analysis pipeline in Imaris (9.2.1) to quantify changes in tissue shape, size and cellular organisation. This was performed at key developmental stages that span axial elongation; the 6ss embryo (18 hpf), 10ss embryo (24 hpf) and 14ss embryo (34 hpf). For tissue segmentation, two-dimensional splines with $0.5\mu\text{m}$ point spacing were drawn manually on every 3rd - 5th slice of the Z-stack (depending on the amount of shape fluctuation in the tissue surface) and these were assembled into 3D triangle meshes (*Fig. 3.7a-c*). To quantify cellular composition, nuclei were first isolated within each segmented tissue by applying a signal masking function to the DAPI channel. The Imaris spot detection algorithm was then used to locate centres of mass, using tissue-specific predictions of nuclear diameter (ranging from $3\mu\text{m}$ to $4\mu\text{m}$), and an adjustable quality filter (*Fig. 3.7d*). Nuclear detection was then manually verified by false-colouring the contents of each spot and confirming successful detection against DAPI staining in 2D sections. For each tissue analysed with this pipeline, I extracted metrics on tissue and cellular scales. At the tissue-scale, I exported values for tissue length and volume. I then used these to derive mean transverse cross-sectional area. On the cell scale, I exported values for cell number, and the position of every nucleus along the anteroposterior (x), dorsoventral (y) and mediolateral (z) axes. Combined with the tissue-scale measurements, I was then able to derive further measurements of nuclear density, and frequency distribution along the anteroposterior axis. By normalising axial length, I was then able to overlay all measurements from multiple embryos for specific developmental stages, and also compare mean changes in tissue structure over developmental time. In addition to allowing collection of morphometric data, building these tissue renderings in Imaris has enabled more intuitive visualisation of amphioxus morphology and morphogenesis. Each digital representation of the embryo can be constructed from a variable balance of raw imaging data and rendered surfaces, and, within this, tissues can be colour-coded based on identity, virtually dissected, and translated entirely into numerical datasets.

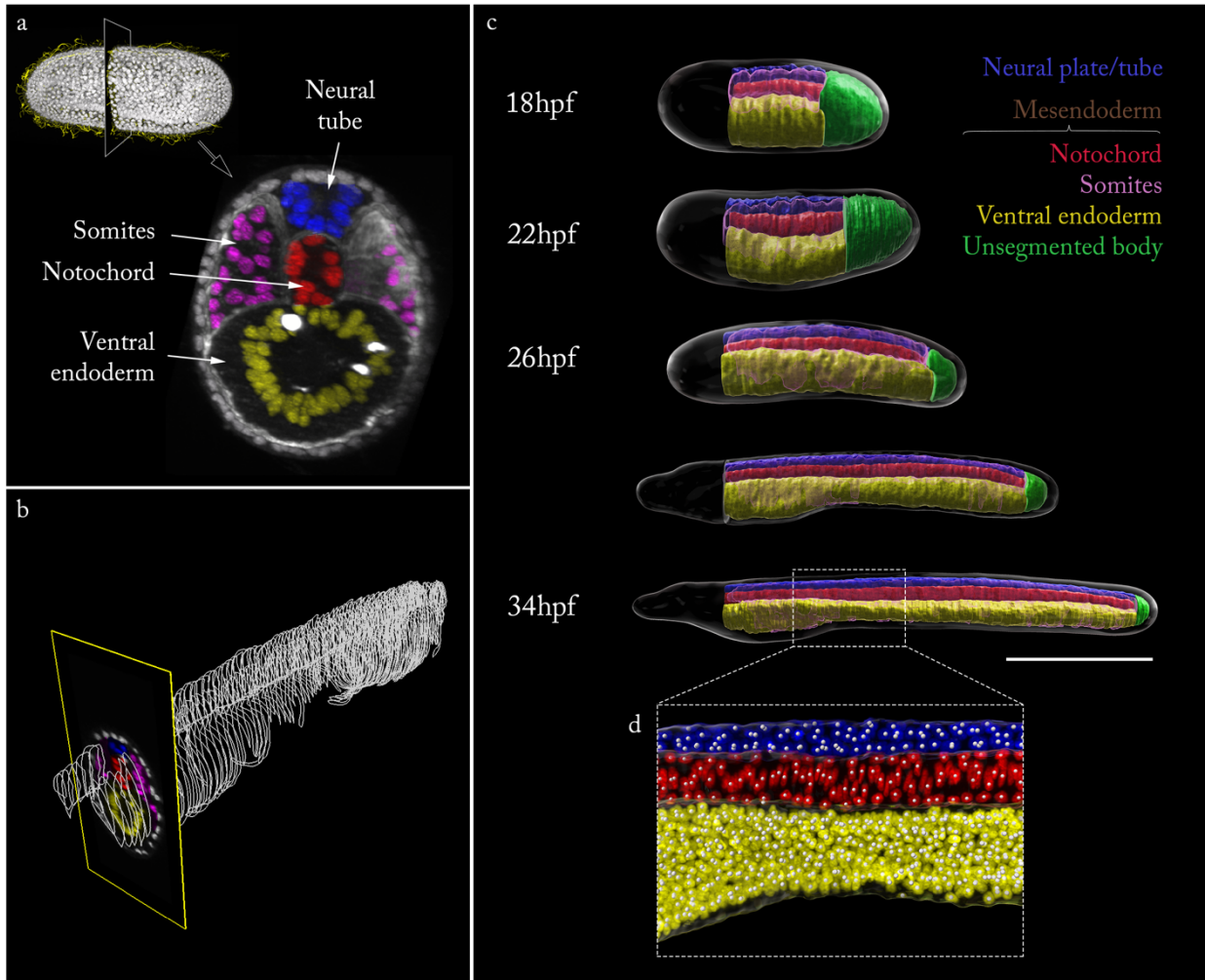


Figure. 3.7. **Collection of 3D morphometric datasets.** Quantitative renderings of amphioxus embryos were made through manual tissue segmentation in Imaris. (a) Transverse section of 6-somite stage embryo at the 50% AP level, immunostained for laminin, which resolves boundaries between adjacent axial tissues in the trunk – the notochord, neural tube, somites and endoderm – which are false-coloured. (b) All 2D splines for the paraxial mesoderm of an embryo at 12ss, prior to assembly into a 3D surface. (c) Sample of renderings for embryos at successive somite stages spanning axial elongation, shown in lateral view. Segmented tissues are colour-coded by identity. The paraxial mesoderm is transparent in these images, allowing midline tissues can be visualised. (d) Expanded view of region marked in (c), with masked DAPI staining within surfaces for the neural tube, notochord and somites, and spots used to quantify nuclear number and distribution. Scale bar in (c) shows 200 μ m.

3. 3. 3 Axial elongation occurs in a largely growth-free system

All trunk tissues undergo a net increase in volume during axial elongation, between 6ss and 14ss (*Fig. 3.8a*). However, this occurs in parallel with depletion of the unsegmented body, at the

posterior tip of the embryo, which experiences a 22.5-fold decrease in volume in the same time interval (*Fig. 3.8a, green bar + dotted line*). Considered together, this means that axis elongation does not involve a significant net increase in total trunk volume (*Fig. 3.8b*). If each trunk tissue received a common volume of new tissue from the unsegmented region during its depletion, we might hypothesise that each would grow by the same relative amount, based on variation in their starting volume. Instead, they expand by different amounts (*Fig. 3.8a*). The smallest volumetric changes were measured in the paraxial mesoderm (+1.38-fold) and neural tube (+1.36-fold), while the greatest were measured in the endoderm (+1.73-fold) and notochord (+1.94-fold). These measurements may suggest that the tissue volume of the unsegmented region is allocated unevenly between axial tissues during their maturation. On the other hand, trunk tissue volumes will also be altered by subsequent tissue growth, or loss of volume through cell death and shrinkage or ablation of cavities, and so further cell marking would be necessary to discern the relative contributions of the unsegmented region to each axial tissue. In sum, these volumetric measurements indicate that amphioxus axial elongation occurs primarily through the rearrangement of existing tissue volume established by the end of gastrulation.

While total body volume remains relatively constant during axial elongation (*Fig. 3.8b*), I measured an increase in cell number in all tissues (*Fig. 3.8c*), summing in a 2.6-fold net increase in total cell number in the trunk from 6ss to 14ss (*Fig. 3.8d*). The greatest increase occurred in the notochord, which expanded by 1.93-fold, followed by the ventral endoderm, which expanded by 1.73-fold (*Fig. 3.8c*). Given the maintenance of embryo volume, it follows that increases in cell number coincide with those in nuclear density. During axis elongation, nuclear density increased in all axial tissues (*Fig. 3.8e, f*). In the endoderm, I measured a 3.02-fold increase in nuclear density (*Fig. 3.8e, yellow bar*). Interestingly, in the notochord, despite exhibiting the greatest increase in cell number (*Fig. 3.8c, red bar*), there was only a 1.28-fold increase in nuclear density (*Fig. 3.8e, f*). This may reflect a requirement for some growth in the notochord for it to accommodate new cells with only a relatively minor increase in nuclear density. We can conclude from these morphometric data that cell division and growth are uncoupled during axial development, such that cell division acts to alter tissue architecture, without necessarily affecting their size, in tissues undergoing radical shape changes to establish total axial length. From these early conclusions, my next questions regarded the types of rearrangement active in each tissue of the body axis, and the role of cell division in regulating cell size and number.

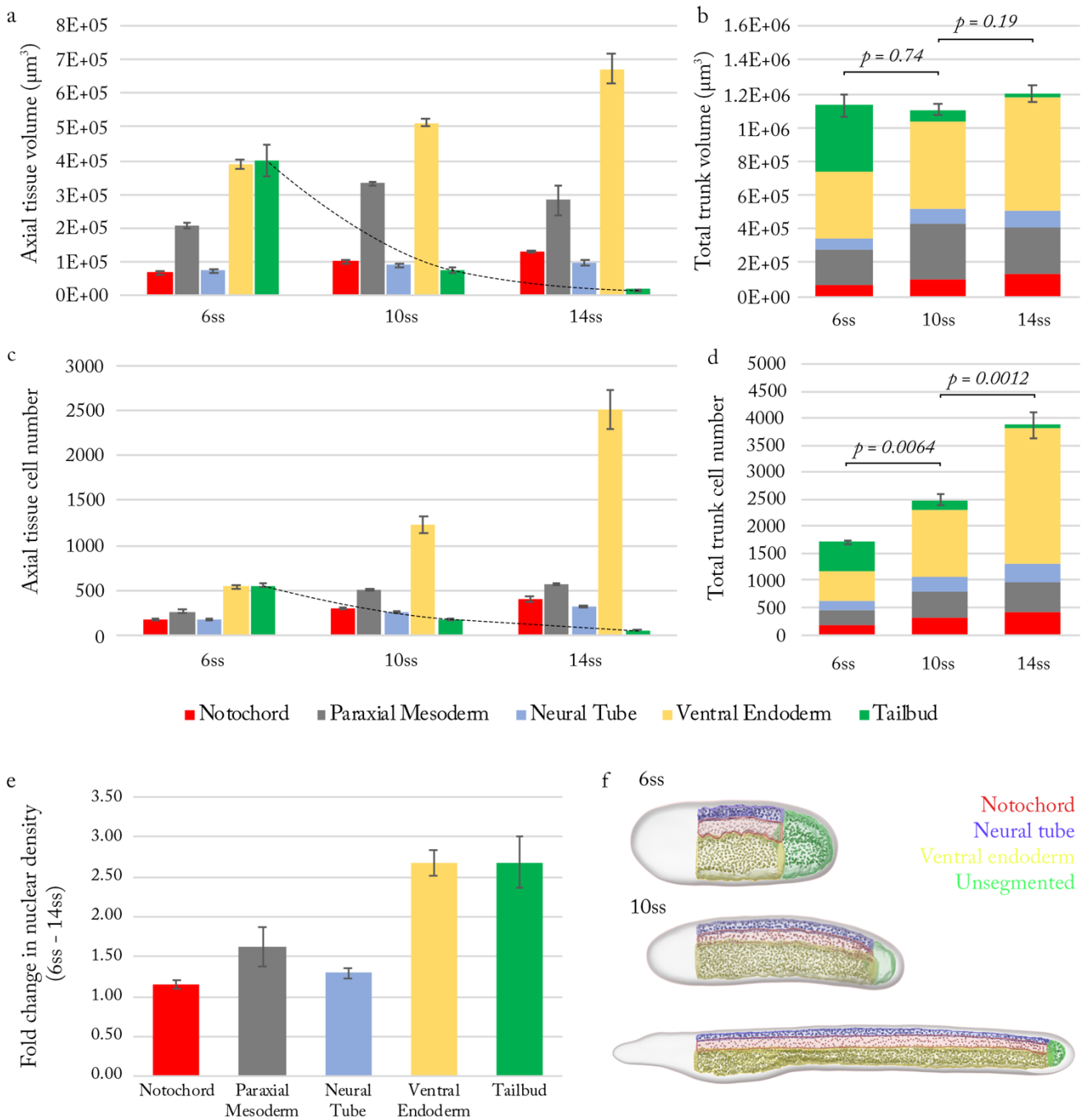


Figure 3.8. Elongation occurs rapidly with minimal volumetric growth. (a) Temporal changes in axial tissue volume between 6ss and 14ss. Dashed black line follows progressive depletion of the unsegmented region. (b) Stacked bar chart showing net change in trunk volume. (c) Temporal changes in axial tissue cell number between 6ss and 14ss. Dashed black line follows progressive depletion in the unsegmented region. (d) Stacked bar chart showing net change in trunk cell number over time. (e) Bar chart showing fold changes in tissue-specific nuclear density between 6ss and 14ss, calculated between each 14ss tissue and the mean value at 6ss. (f) Renderings of axial tissues with spots for constituent nuclei at 6ss, 10ss and 14ss, illustrating changes in tissue-specific nuclear density over time. All error bars show +/- 1 standard error of the mean. p values are the results of unpaired two-tailed Student's t -tests. All values shown are the mean for $n = 3$ embryos per stage.

3.3.4 Elongation is mediated by tissue-specific programmes of convergent extension

A widespread mechanism of tissue elongation through rearrangement is convergent extension – defined by an increase in tissue length at the expense of cross-sectional area. To test for convergent extension in the axial tissues of amphioxus, I devised a simple elongation coefficient termed α , as a ratio of tissue length to mean transverse diameter (*Fig. 3.9a*). Here, the longer and narrower the shape, the greater the α value. I calculated α for each tissue individually, and the entire trunk, every two somite stages between 4ss and 14ss, thereby spanning the transition from elongation-free (0ss-6ss) to elongation-coupled (6ss-14ss) somitogenesis. I also plotted relative changes in tissue-specific elongation coefficient values with a simulated ‘convergence-null’ condition in which a theoretical tissue elongates at the same rate, but experiences no narrowing of cross-sectional area (*Fig. 3.9b*). If measured values for amphioxus axial tissues exceed this simulation, a gain in length must be achieved at the expense of width. By plotting these values together, I found that all axial tissues closely aligned with the convergence-null simulation between 4ss and 8ss. Thereafter, all trunk tissues increased above the simulation, with the greatest deviation emerging between 10ss and 14ss. From this analysis, we can therefore infer that all axial tissues undergo a synchronous phase of widespread convergent extension late in axis elongation.

To learn more about the geometric constraints on convergent extension in each axial tissue, I projected them into a simple tissue morphospace; a plot describing possible variations on a given form, and the paths connecting different shape states. In this case, I considered each tissue a perfect cylinder of fixed volume, that is fluid in its relative length and cross-sectional area. These simplified forms can be depicted as curves on a graph of length against cross-sectional area, ranging from very long and narrow forms to the very short and wide (*Fig. 3.9c*). On each curve, I marked a point for the real measured geometry of each tissue at 14ss, and another for the position of a cylinder of the same volume but a cross-sectional area matching that measured at 6ss (*Fig. 3.9d*). The curve connecting each point now represents a theoretical shape trajectory connecting these two forms – a continuum of shapes the tissue must transition through if it is to passage directly between the two states by convergent extension. From this perspective, it is first apparent that the amount of tissue narrowing required for full elongation is dependent on the cross-sectional area of the tissue: i.e. a greater amount of narrowing is required in wider tissues (e.g. the endoderm) than narrower tissues (e.g. the neural tube and notochord) to generate the same net length change. In terms of axial development, this

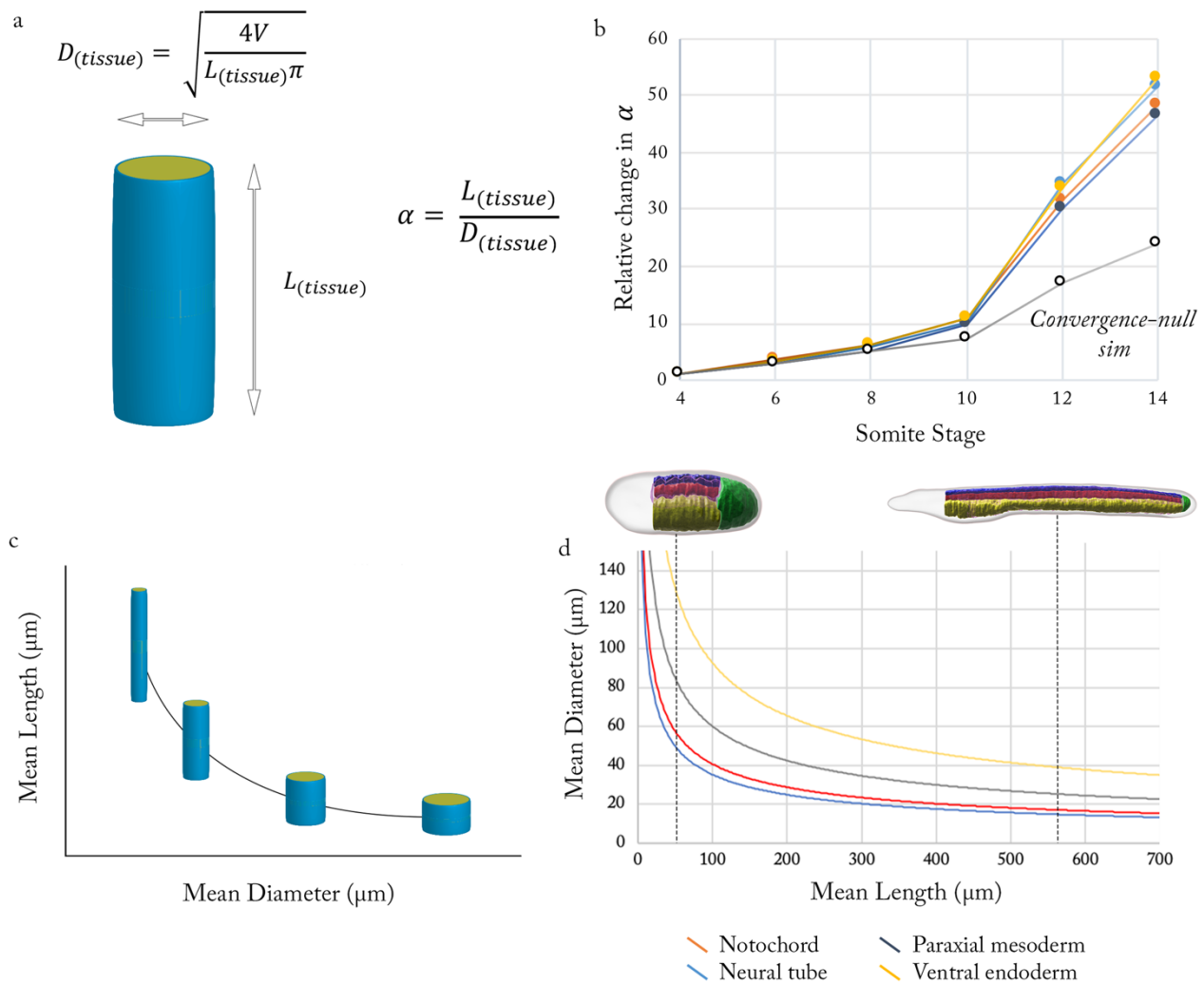


Figure. 3.9. Axial tissue elongation involves a late phase of multi-tissue convergent extension. (a) Shape parameterisation applied for tissue shape analysis. Axial tissues are simplified to perfect cylinders, with a known length $L_{(tissue)}$, and mean diameter $D_{(tissue)}$ calculated from $L_{(tissue)}$ and the measured tissue volume, $V_{(tissue)}$. The elongation coefficient, α is then derived as the ratio of $L_{(tissue)}$ to $D_{(tissue)}$. (b) Relative changes in α over successive somite stages, from the onset of elongation to 14ss. Changes in α for real axial tissues are plotted against a ‘convergence null simulation’, in which tissue length increases at the same rate but without any change in $D_{(tissue)}$. (c) Schematic showing the principle of morphospace embedding for axial tissue geometries. Axial tissues with volumes measured at 14ss are depicted as curves, describing a range of cylinders of that volume, defined by different lengths and mean diameters. Each curve connects short and wide shapes to tall and narrow shapes. (d) Amphioxus axial tissues from 14ss projected into morphospace, with dashed lines marking shapes with length measured at the start (6ss) and end (14ss) of elongation. Key applies to both (b) and (d). Values derived from $n = 3$ embryos per stage.

geometric property demands that the ventral endoderm reduces its cross-sectional area by a much greater amount than the neural tube if it is to generate the same length change; at 6ss, a 30 μ m decrease in mean diameter will generate over 10-times the length increase in the neural tube than it will in the endoderm (*Fig. 3.9d, compare yellow and blue curves*). In relative terms, however, each tissue must undergo a common 2.93-fold narrowing to achieve their dimensions at 14ss. A further interesting feature illustrated in this morphospace is that the paths between shapes of the same volume are non-linear. This means a cylinder that narrows at a constant rate will elongate at a continually increasing rate. In this theoretical study, we can therefore predict that cellular processes that mediate a constant rate of narrowing could propagate into exponential dynamics at the tissue scale.

This analysis raises the interesting possibility that each tissue of the embryonic trunk faces different geometrical demands to perform the same act of elongation, despite a common length change, occurring at the same time and rate. To further pursue this idea, I sought to question whether each tissue exhibits common changes in cellular organisation over time, but at different rates, or whether each employs different cellular strategies for convergent extension. To this end, I quantified variation in local cell neighbourhood organisation across the AP axis of each tissue, and across developmental time. For every cell, I identified its 20 adjacent neighbours along the AP axis and divided their total AP dispersal by their mean lateral dispersal to derive a neighbourhood-scale α value (*Fig. 3.10a*). I then plotted these values across normalised AP axes for each tissue, showing the mean values in a series of evenly-sized bins (*Fig. 3.10b* illustrates translation of form into a quantitative plot). For this analysis, I focussed on the neural tube and notochord, which are directly adjacent in the embryo, and have continuous cord-like morphologies. This contrasts with the tubular endoderm, and segmented paraxial mesoderm. In the trunk notochord, my approach revealed that cell neighbourhoods converge and extend preferentially in the anterior, followed by those in the posterior, manifesting as a conspicuous maturation gradient (*Fig. 3.10c*). This dynamic is matched by the tendency of more posterior transverse sections to bisect a greater number of notochord nuclei (*Fig. 3.10e, red nuclei*). Unexpectedly, I found a very different pattern of neighbourhood reorganisation in the neural tube. Here, convergence was more synchronous in neighbourhoods across the AP axis, but there emerged a clear bimodality between the anterior and posterior halves of the tissue, in which neighbourhoods in the posterior elongated and narrowed to a much greater extent (*Fig. 3.10d*). In turn, I found that the cross-sectional area of the posterior neural tube was significantly less than the anterior, and single transverse slices through it transected a lesser number of nuclei (*Fig. 3.10e, blue*

nuclei). In sum, these data suggest that while all axial tissues converge and extend in parallel and at a common rate, each faces different geometric demands, and employs distinct morphogenetic strategies.

3.4 Deciphering the role of cell division in growth-free morphogenesis

3.4.1 A spatiotemporal map of cell cycle progression

During tissue rearrangement, the cellular architecture of each axial tissue is also changing due to increases in cell number and density (*Fig. 3.8c-f*). This raises the question of where these new cells come from, at what time, and what effect they have on tissue structure. Accordingly, the next question I sought to address is how cell division is distributed during axial development. There is evidence from BrdU incorporation studies that cell division shifts from broad synchronous bursts to more specific domains after gastrulation (Holland & Holland, 2006). However, this is yet to be comprehensively mapped. To this end, I labelled embryos at successive somite stages with markers for nuclei in two cell cycle phases; 5-ethynyl-2-deoxyuridine (EdU), for those passing through S-phase in the time window of exposure, and immunostaining for phosphorylated histone 3 (PhH3), for those in mitosis at the moment of tissue fixation. Embryos were incubated in EdU for 2 hours before fixation, which corresponded to the temporal spacing between fixations (samples for each stage are shown in *Fig. S1, Appendix I*). In order to synthesise staining profiles from a large number of embryos into a single map, I calculated the mean frequency of labelled nuclei in evenly-sized bins of the anteroposterior axis at each somite-stage, and used these values to construct tissue-specific proliferation landscapes by plotting frequencies over time and mean axial length per stage. This is presented in *Fig. 3.11* for the notochord and neural tube. Each landscape illustrates spatiotemporal changes in the distribution of proliferation throughout the embryo as it passes through successive

Figure. 3.10. **Convergent extension in axial tissues rests on different changes in cell topology (overleaf).** (a) Parameterisation for neighbourhood elongation quantification. The elongation coefficient α is derived as a ratio of length $l_{AP}^{(nb)}$ to mean lateral dispersal $l_{lat}^{(nb)}$ of a neighbourhood of 20 cells oriented along the anteroposterior axis. (b) In a hypothetical tissue that progressively narrows across its length, local cell neighbourhoods are increasingly elongate. Through calculations of α , this tissue can be represented in graphical form. (c) Changes in local neighbourhood elongation across the notochord (*continued overleaf*)

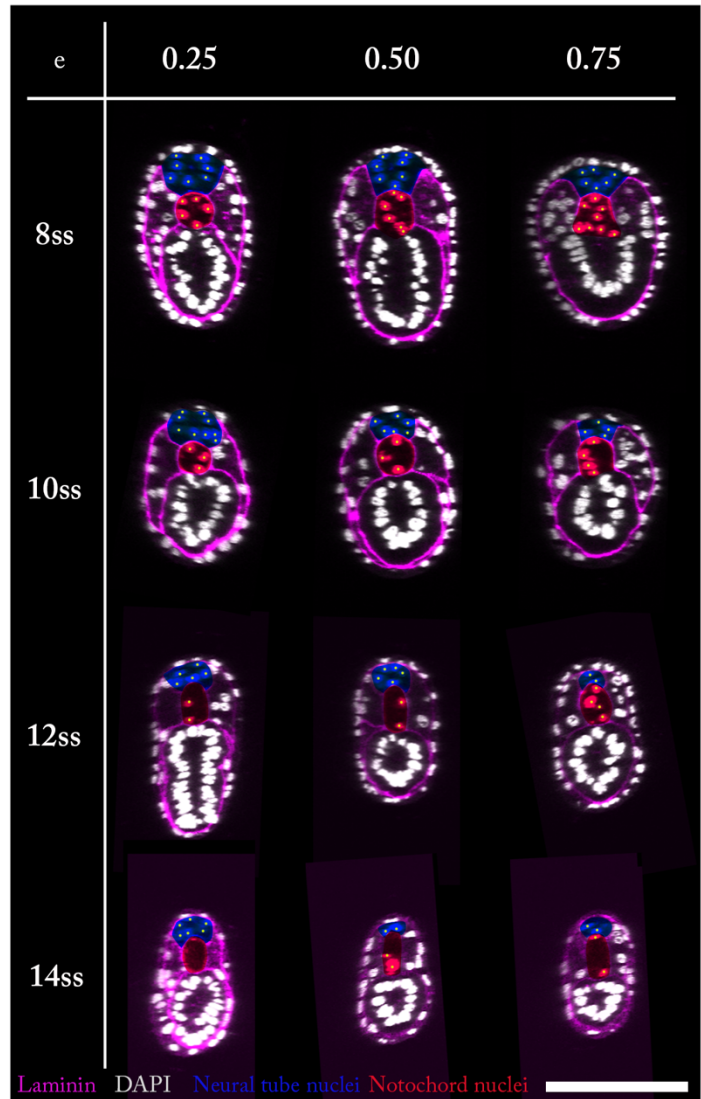
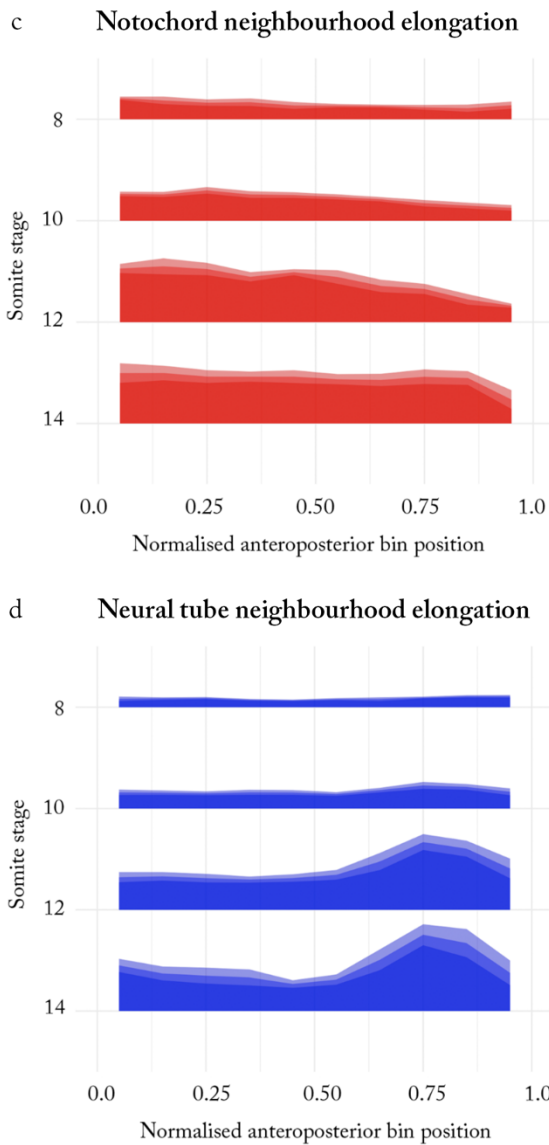
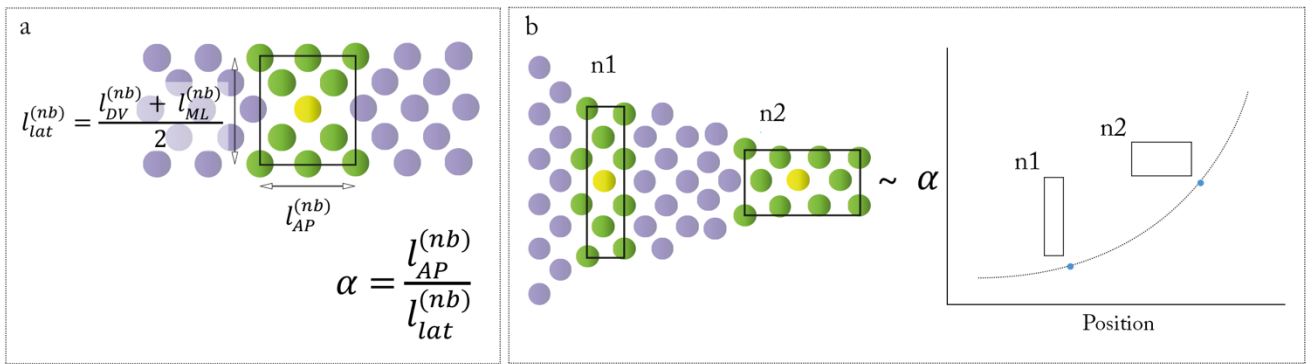


Figure. 3.10. (*continued*). in the most rapid phase of axial elongation, 8ss to 14ss, ± 1 standard deviation. Cells included are from the segmented body only, and the length of the segmented body is normalised at each stage between 0 (anterior intersomitic boundary) and 1 (posterior intersomitic boundary). (d) Same methodology in (c) now applied for the neural tube. (e) Transverse sections through the embryo at stages represented in (c, d), at axial levels indicated. Nuclei are false coloured to highlight the notochord (red) and neural tube (blue). Yellow spots mark single nuclei. Values derived from $n = 3$ embryos per stage. Scale bar in (e) shows $100\mu\text{m}$.

phases of elongation and segmentation. In addition, they offer temporal information on cell cycle dynamics, with cell populations passing progressively through EdU-/PhH3-, EdU+/PhH3-, EdU+/PhH3+ and EdU-/PhH3+ states.

While early phases of development in midline tissues involve dispersed intercalatory cell division across the anteroposterior axis, the proliferation landscapes for the notochord and neural tube highlight a transition at 6ss, to a polarised dynamic (*Fig. 3.11a, b*). From this stage onwards, proliferation is restricted to the posterior tip of the notochord, and the most anterior and posterior tips of the neural tube. Returning to the raw imaging data, sagittal sections reveal this localisation to correspond to labelling in the future brain and the chordoneural hinge of the tailbud (*Fig. 3.11c*). Importantly, this means that cell division is scarce or absent throughout the trunk region in the notochord and neural tube. I noted in the neural tube, at the 7-8 somite stage, that EdU labelling in the tailbud extends further anterior than PhH3 labelling, and initially assumed that the more anterior EdU+ nuclei were the progeny of the more posterior EdU+/PHH3+ nuclei (*Fig. 3.11a - c*). While this remains a possibility, the landscapes challenge a sufficiently high cell cycle rate for these cells to be born and displaced from the tailbud in a 2-hour time window – the duration of EdU exposure prior to fixation. In fact, there is a lag of 4-6 hours between the first emergence of EdU+ nuclei in the chordoneural hinge at 5ss, and the appearance of PhH3+ mitotic cells at 7ss (*Fig. 3.11a, b, posterior domains*). It therefore seems more likely that a broad field of cells around the chordoneural hinge undergoes a slow pulse of cell division at the onset of elongation, and the population passes sequentially through S-phase, followed by mitosis. An additional unexpected finding from this analysis was an apparent temporal alignment of cell cycle progression in the tailbud and the brain (*Fig. 3.11a, b*). This might suggest that axial development involves a series of globally-regulated bursts of volumetrically-reductive cell division, that become increasingly spatially restricted over time, and focally alter tissue architecture.

3.4.2 Pulse-chase identifies axial progenitors derived from the late blastopore lip

Having identified proliferative cells around the chordoneural hinge during axial elongation, I next sought to determine the contribution of their derivative clones to axial length. To this end, I first expanded the EdU staining protocol to a pulse-chase analysis. Here, embryos were incubated in EdU to label active proliferative domains, as described previously, then the EdU was washed out in fresh

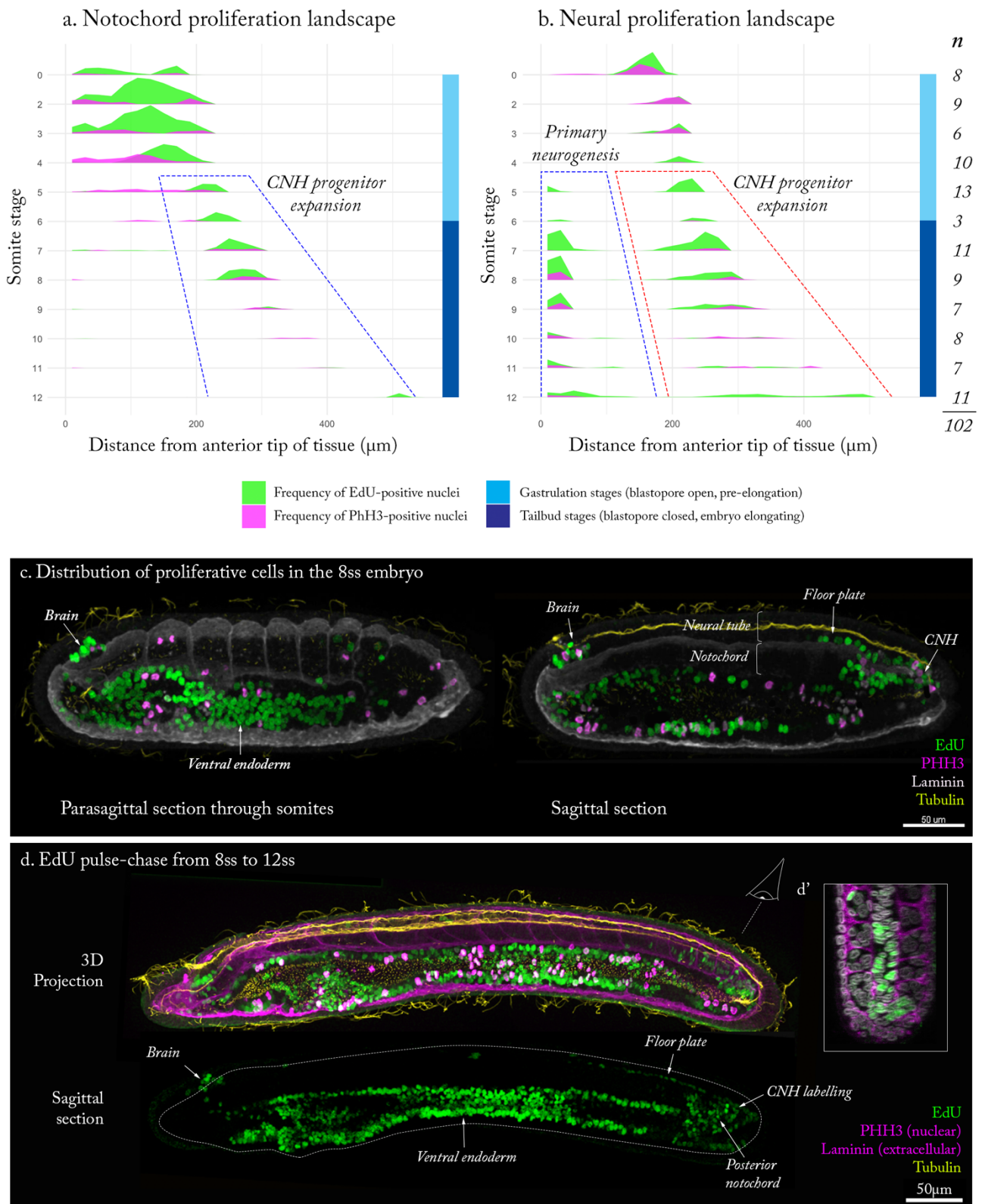


Figure 3.11. Elongation of dorsal structures involves proliferation in two distinct progenitor domains. (a, b) Proliferation landscapes for the notochord (a) and neural tube (b) showing the frequency of EdU- and PhH3-labelled nuclei in 20 evenly-sized bins of the anteroposterior axis across segmentation in the form of ridgeline plots. Just before the onset of axial elongation, proliferation becomes restricted to the brain and chordoneural hinge. (c) Imaging data for the 8-somite stage, highlighting the two progenitor domains in the brain and chordoneural hinge. (d) Pulse-chase fate mapping of 8-somite stage progenitor domains with EdU pulse-chase to the 12-somite stage. Labelled nuclei persist in the brain, and are enriched in the posterior floor plate and notochord. (d') Coronal section through tail showing specific contribution of chordoneural hinge progenitors to the notochord, not the somites. Representative of $n = 8$ embryos imaged.

sea water, and the embryos were allowed to develop to later stages at which the distribution of labelled nuclei was analysed. This method enabled me to map the size and distribution of clones derived from proliferative domains present during the first incubation step. Reliable pulse-chase analysis relies on two limiting criteria, which are assessed in *Fig. S2 (Appendix I)*. First, I had to ensure that positive EdU labelling would not be diluted during multiple rounds of cell division, to the extent that it is no longer detectable in fluorescent imaging. To test this, I performed a first pulse-chase experiment following incubation with EdU between 6hpf and 8hpf, thereby marking proliferative cells in the cup-shape gastrula. If cells labelled at this stage are still detectable at 14ss, then dilution could be dismissed as a problem for labelling experiments at later stages. At 14ss, I found that strong EdU labelling persisted throughout the embryo, including in the surface ectoderm, neural tube, somites, notochord and ventral endoderm. In the endoderm, which is the most proliferative tissue during axial development, I found that the signal was not diluted. Rather, it had acquired a punctate distribution in labelled nuclei. This suggests that the signal retained similar intensity but had been spatially dispersed through cell division. The second criterium is that residual EdU does not continue labelling new proliferative cells after the initial incubation window. Often exogenous nucleotides are applied to compete out the residual EdU in pulse-chase experiments. However, here I used only an excess of sea water to avoid toxic effects on gene expression. With this method, I found a non-overlapping distribution of EdU labels between stages, which supported an effective loss of EdU labelling during the chase step.

With the pulse-chase method validated, I chased cells labelled with EdU at the 8-somite stage (marked in a 20 - 22hpf incubation), when the chordoneural hinge is most strongly enriched with EdU+ nuclei (*Fig. 3.11c*), to their destinations in the 14ss embryo. The future brain and ventral endoderm were also strongly labelled in this EdU pulse, but were non-overlapping with cells labelled in the chordoneural hinge (*Fig. 3.11c*). The chordoneural hinge progenitor labelled at 8ss generated clones that expanded by 14ss to populate the posterior notochord and the floor plate of the neural tube (*Fig. 3.11d*), with no contributions to the posterior somites (*Fig. 3.11d*). Labelling in both tissues extended anterior from the dorsal (neural) and ventral (notochordal) sides of the chordoneural hinge into the more differentiated part of each tissue (most explicit in *Fig. 3.11d, bottom*). In both cases, labelled nuclei were most densely packed at the posterior tip, but were interspersed with unlabelled nuclei more anteriorly. Notochord labelling extended to occupy approximately 20% of the total tissue length, while floor plate labelling extended much further anterior to occupy 50% of the total tissue

length (*Fig. 3.11d, bottom*). Given that this discrepancy exceeds that in EdU pulses at 8ss (*Fig. 3.11c*), the greater dispersal of floor plate nuclei likely derived from the nature of cell rearrangement acting on these clones; the floor plate nuclei resolve into a single-file row, but the notochord nuclei remain multi-layered on the dorsoventral axis (*Fig. 3.11d, bottom*). In sum, this experiment suggests that proliferative progenitors present in the chordoneural hinge during axis elongation specifically contribute new cells to the posterior notochord and neural tube.

Fate mapping studies in vertebrates have revealed chordoneural hinge progenitors of the tailbud to derive from differentiation of the embryonic organiser (Catala et al., 1995; Gerhart, 2001; Gont et al., 1993). This motivated a hypothesis that proliferative chordoneural hinge progenitors in amphioxus derive from the dorsal blastopore lip of the late gastrula, which is established at the termination of involution. The proliferation landscapes revealed that proliferation is polarised in the amphioxus late gastrula, between distinct domains in the anterior archenteron, and the dorsal blastopore lip (*Fig. 3.11a, b*). Closer analysis of EdU incorporation in the blastopore at these stages revealed a temporal delay in cell cycle progression across the dorsoventral axis. Between 10hpf and 12hpf, EdU was strongly enriched in the dorsal and upper lateral blastopore lips (*Fig. 3.12a*). Over the following two hours, however, the staining shifts to become most strongly enriched in the ventral and lower lateral lips (*Fig. 3.12b*). Meanwhile, the archenteron labelling shifts posteriorly towards the centre of the chordamesoderm, and ventral endoderm labelling was diminished (*Fig. 3.12b*). From this observation, I reasoned that I could determine the derivatives of different blastopore subdomains through a series of semi-overlapping pulse-chase experiments that follow the sequential enrichment of EdU across the dorsoventral axis of the blastopore.

Figure 3.12. Characterisation of blastopore progenitor diversity with EdU pulse-chase (overleaf). (a) Distribution of EdU+ nuclei after a pulse between 10hpf and 12hpf shown in a sagittal section and a blastopore view, indicated by the eye. (b) Distribution of EdU+ nuclei after a pulse between 12hpf and 14hpf, again in sagittal section and a blastopore view. (c) Lateral view of an embryo labelled with EdU 10 – 12hpf as in (a), and fixed at 34hpf, showing gross morphology. (d) Projection through the sagittal midline of the embryo shown in (c), with only EdU staining shown. Transverse section (left) is through the posterior region marked with the white box. Annotations itemise tissue specificity of EdU labelling. (e) Similar projection for an embryo pulsed with EdU at 12 – 14hpf as in (b), with a transverse section highlighting changes in tissue-specificity of EdU labelling. (f) Schematic of approach used to quantify EdU labelling in pulse-chased (*continued overleaf*)

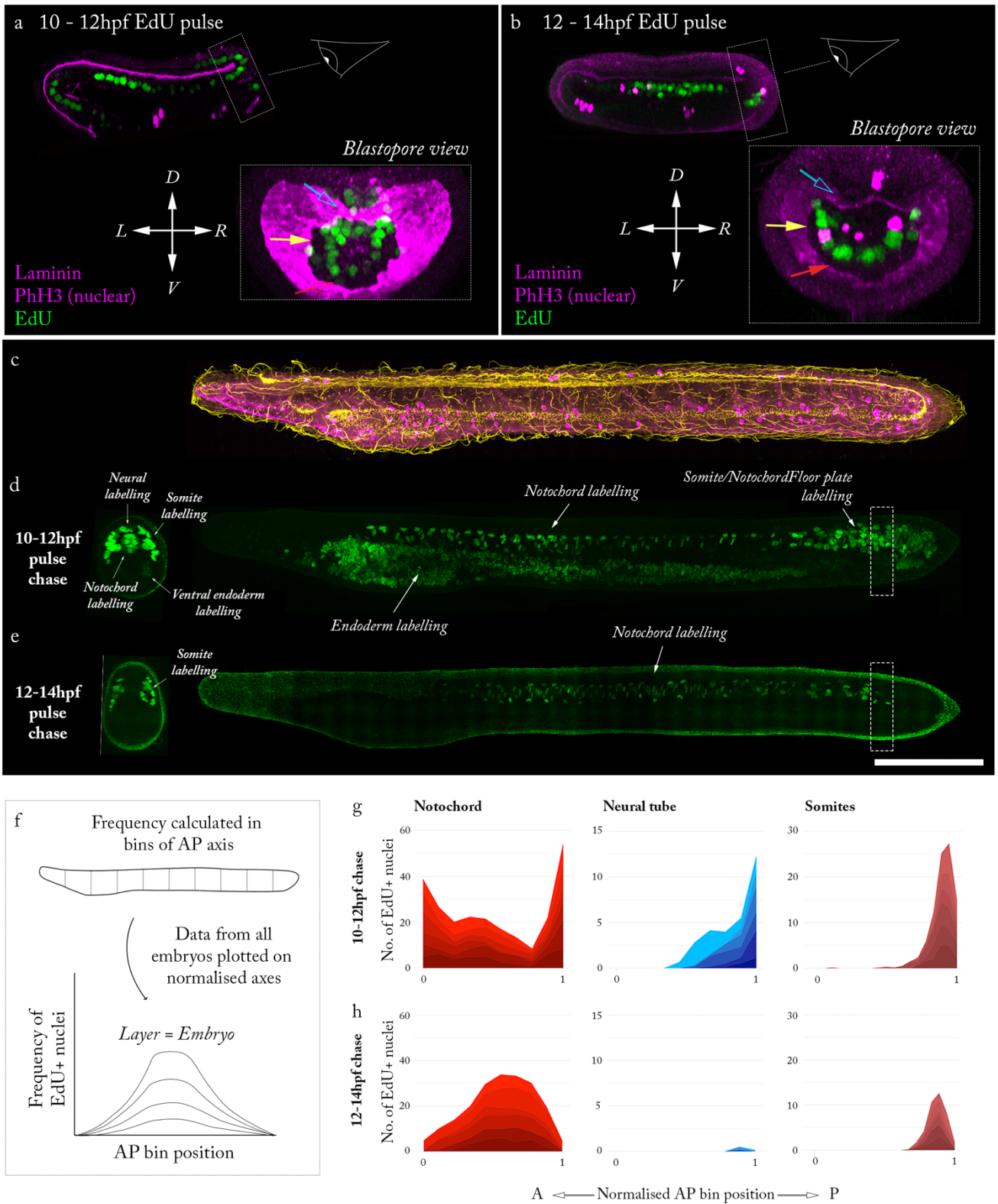


Figure. 3.12. (*continued*). specimens as a frequency curve across normalised AP length, following quantification in 10 evenly-sized bins. (g, h) Stacked area graphs for each pulse-chase condition and tissue, following rationale in (f). Each stratum represents an individual specimen contributing to a cumulative total value. N = 6 embryos quantified included for each pulse-chase experiment. Scale bar shows 50 μ m and applies to a – e, excluding inlays.

I therefore used EdU pulse-chase again, this time to define the fate of blastopore-derived clones in the larva and test if this included chordoneural hinge derivatives highlighted in the previous experiment. For each pulse-chase experiment, labelling is shown in individual embryos in *Fig. 3.12c, d* and *e*. The frequency of cells was also quantified along the anteroposterior axis *Fig. 3.12f*, and the results shown graphically in *Fig. 3.12f* and *g*. Labelled cells between 10hpf and 12hpf (*Fig. 3.12a*) became enriched in three domains in midline structures; the notochord in the pharyngeal region, posterior notochord and posterior neural tube, and their interface at the chordoneural hinge (*Fig. 3.12c, d, g*). The labelling of the chordoneural hinge and the adjacent floor plate and notochord in this experiment overlaps with results of the 22-34hpf pulse-chase experiment (*Fig. 3.11d*). This suggests that a portion of the late blastopore lip will give rise to axial progenitors of the chordoneural hinge that proliferate during axial elongation. However, EdU-labelled nuclei were also present in the posterior somites, which are not contributed to by the chordoneural hinge during its later proliferative phase (*Fig. 3.11d*). I therefore hypothesised that this early pulse of EdU had also marked a population of somite precursors that are not inherited by the chordoneural hinge. Interestingly, when EdU incorporation in the blastopore shifts ventrally, therefore predominantly marking the lateral and ventral lips (*Fig. 3.12b*), the chordoneural hinge, posterior notochord and floor plate are not labelled in pulse-chase experiments (*Fig. 3.12e*). In this case, only the somites are positively labelled (*Fig. 3.12e, b*). While the middle part of the notochord remains labelled (*Fig. 3.12e, b*), due to more anterior labelling in the archenteron in the EdU pulse (*Fig. 3.12b*), posterior labelling is absent (*Fig. 3.12e, b*). By taking advantage of temporal changes in blastopore proliferation dynamics, this experiment therefore exposes a spatial regionalisation of constituent progenitor subtypes, in which the dorsal lip is composed of posterior midline progenitors, and the lateral/ventral lips are composed of posterior somite progenitors.

3. 4. 3 Cell division is required for full elongation of the larval body

To functionally test the contribution of chordoneural hinge progenitors to axial elongation, I first exposed embryos to 305nm ultraviolet (UVB) light, which has been shown to block cell division by both activating a DNA damage response (Diffey, 1991; Sinha and Häder, 2002) and perturbing microtubule stability (Rowning et al., 1997; Veselská and Janisch, 2000). Embryos were exposed to 305nm UVB light in a sterilised UV transilluminator at the 6-somite stage, when elongation is commencing in earnest and cell division has become localised to the chordoneural hinge (see *Fig.*

3.6b, *Fig. 3.11a – c*). They were then removed and allowed to develop to the 14-somite stage in a 24-hour incubation. Following a 10-minute UV exposure at 6ss, embryos proceeded to elongate, but only reached 75% of the length of control embryos, which were placed in the transilluminator without turning on the UV light (*Fig. 3.13a, b*). Three representative UV treated embryos are shown in *Fig. 3.13a*. While this experiment offered promising preliminary data, due to extensive batch variation and the potential for replication-independent disruption of cell shape through microtubule collapse I instead treated embryos with hydroxyurea (HU) in a second iteration of the experiment (*Fig. 3.13c*). HU arrests the cell cycle in S-phase by inhibiting the ribonucleotide reductase enzyme required to synthesise deoxyribonucleotides (dNTPs), and therefore new DNA strands (Koç et al., 2004). In embryos treated with HU from 6ss to 14ss, elongation was also reduced, here to 81% of the expected length (*Fig. 3.13d*). In treated embryos, mitotic figures (PhH3+ cells) were also reduced in density, which offered a strong positive control for cell cycle arrest (*Fig. 3.13c*). Interestingly, phalloidin staining revealed a disorganisation of the posterior notochord in treated embryos, where chordoneural hinge progenitors are concentrated, which lost its regular stack-of-coins pattern (*Fig. 3.13c'*). In sum, while length is primarily generated by cell rearrangement in axial tissues, these data reveal an additional requirement for proliferative posterior progenitors in providing the cellular material to complete tissue elongation.

Despite loss of anteroposterior length in UV- and HU-mediated short-embryo phenotypes, the pattern of the body axis seemed to be largely unperturbed in each case (*Fig. 3.13a, c*). This was particularly striking in the stability of somite number (somite boundaries visible in *Fig. 3.13a, c*). On this foundation, I sought to ask whether the tissue-scale pattern of somite lengths was disrupted in the absence of elongation. Indeed, axial elongation is a critical regulator of somite shape and size in vertebrate embryos (Cunningham et al., 2015; Liao et al., 2016). To test this, I designed a strategy to

Figure. 3.13. Inhibition of cell division retards axial elongation, but leaves the somite pattern intact. (a) Embryos exposed to 305nm UVB light at 6ss (18hpf) for 0 mins or 10 mins, and raised to 14ss (34hpf). Embryos are shown in lateral view. (b) Quantification of anteroposterior axial length change following UVB exposure. (c) Embryos treated with DMSO or 2µM HU from 6ss to fixation at 14ss. (c') Sagittal sections through the tail of DMSO- and HU-treated embryos, showing only phalloidin staining to highlight changes in cellular structure. Notochord is false-coloured in red. (d) Quantification of axial length in DMSO- and HU-treated embryos. (e) Schematic showing rationale for pattern quantification in paraxial mesoderm. Curves are plotted as cumulative lengths from the most posterior to most anterior somite. A straight line will reflect an equal (*continued* overleaf)

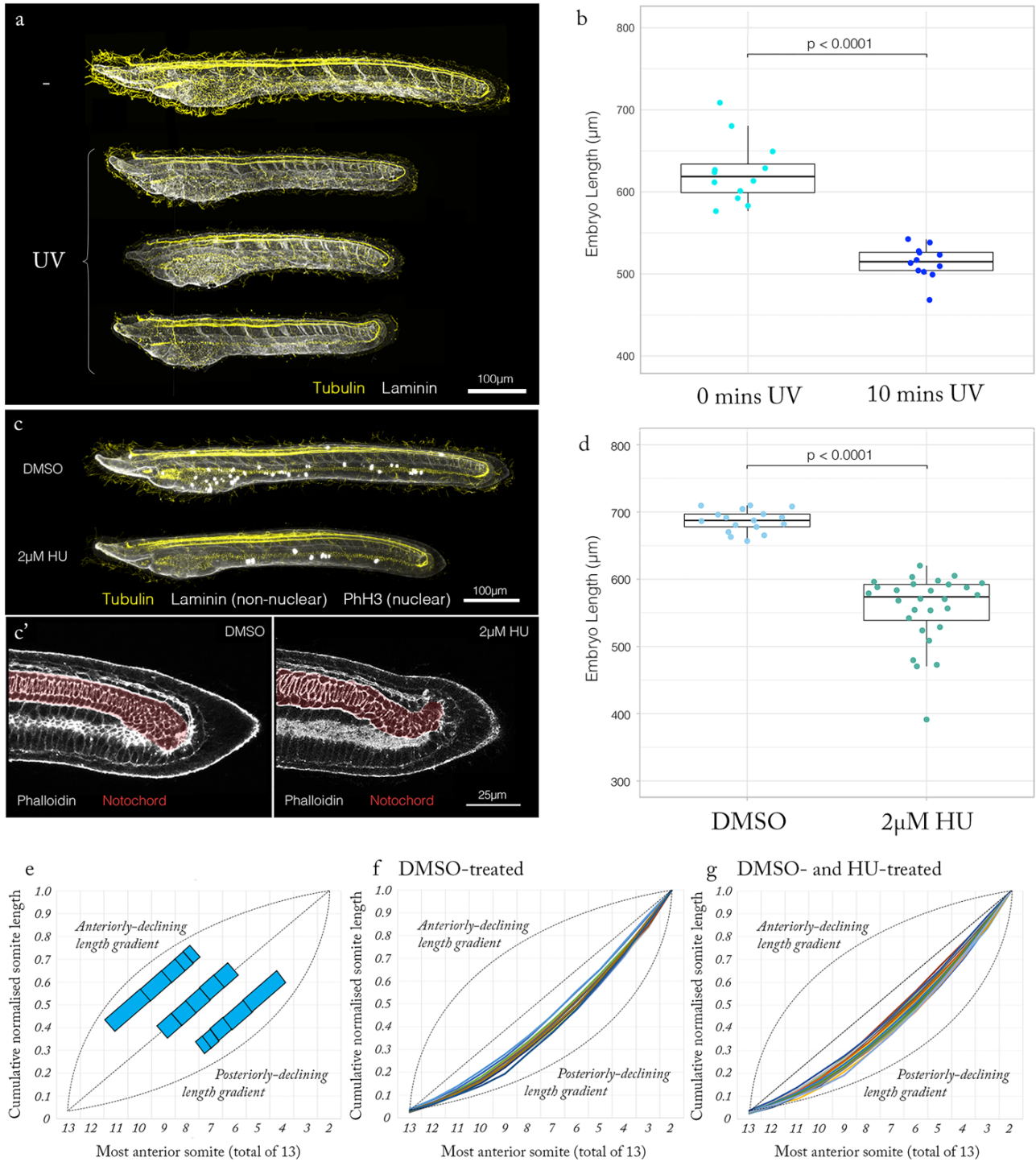


Figure 3.13. (*continued*). contribution of all somites to tissue length, while deviations will reflect heterogeneity across the anteroposterior axis. (f) Somite pattern curves for DMSO-treated embryos, showing displacement to the right of an equal-length curve. This reflects a greater contribution to length in anterior somites. (g) Somite pattern curves for DMSO- and HU-treated specimens, showing an overlap of pattern despite differences in axial length. $n = 12$ embryos per condition. p values are the results of unpaired two-tailed Students' t -tests.

describe the distribution of somite lengths in a pattern curve, expressing the relative contribution of somites at each AP level to total normalised tissue length (*Fig. 3.13e*). Herein, I plotted the cumulative length of the paraxial mesoderm, starting from the most posterior somite and adding each successively more anterior somite. If each somite were the same length, the curve should be a perfectly straight line. However, deviations to the left or right will reflect length inhomogeneity, revealing regional discrepancies in the contribution to total length (*Fig. 3.13e*). Somite pattern curves from control embryos were displaced to the right of a simulation of equal somite lengths, which reflects that the more anterior the somite, the greater the contribution to length – a posteriorly-declining gradient of stereotypical pitch (*Fig. 3.13f*). Remarkably, curves from shortened HU-treated specimens overlapped perfectly with the controls when length was normalised (*Fig. 3.13g*). This reflects the dispersal of an identical pattern across a shorter axial length. Together, these data hint that both somitogenesis and somite maturation occur independently of axial elongation, but are dependent on behaviours of neighbouring tissues to scale the somite pattern to stochastic variations in body length.

3. 4. 4 Cell division is required for axial tissue geometry but dispensible for patterning

Having identified a requirement for cell division in the chordoneural hinge for axial elongation, the final question I posed was *how* cell division generates this tissue length. In other words, how does it alter tissue architecture to increase anteroposterior dispersal. If cell division is volumetrically-reductive, then it acts to modulate two key cellular qualities; cell size and cell number. I therefore sought to test the robustness of body plan shape and pattern to extreme perturbations of each of these qualities. First, I applied HU at the cup-shape gastrula stage, when cell division is broad throughout the embryo, and is yet to restrict to spatially-specific mitotic domains (*see Fig. S2 a, and Holland and Holland, 2006*). This means that cells are both low in number and relatively homogenous in size. Long incubations in HU can have toxic effects (Singh and Xu, 2016). However, I found that HU-treated embryos remained viable until the 14ss (*Fig. 3.14a, b*). This included active swimming at the moment of fixation (*data not shown*). Cell death was widespread in HU-treated embryos, as indicated by numerous pyknotic DAPI-stained nuclei, while all others were abnormally large relative to the size of the embryo and appeared homogenous in size (*Fig. 3.14b, b'*). Nonetheless, the major patterns of the body axis were intact. The notochord was present at the axial midline, with a characteristic stack-of-coins pattern, the neural tube was internalised and axonal tracts were explicit in its anterior half, and a complete pattern of somites was present within the paraxial mesoderm (*Fig.*

3.14b[†]). These patterns were therefore robust to the deviation in cell number and size, but the shapes of each axial tissue were severely distorted; HU-treated embryos totally failed to elongate, leaving them less than half the anteroposterior length of DMSO-treated siblings (Fig. 3.14a, b). From this experiment, we can infer that regulation of cell shape and size may be dispensable in the broad patterning of the embryo, but remains required to confer tissues with the correct geometry.

3.4.5 Volumetrically-reductive division scales cell size to total embryo size

To discern whether the aberrant morphogenesis of HU-treated gastrulas was due to their cells being too large, or too similar, I next sought to disentangle the regulation of *true* cell size (the exact volume of the cell) and *relative* cell size (the relative differences in volume between cells in the same embryo, regardless of true volume). To achieve this, I strove to re-evaluate a size-reduced phenotype initially described by Wilson (1893), Conklin (1933) and Morgan (1896), generated by splitting the first two amphioxus blastomeres. It has been reported that isolated blastomeres at the 2-cell stage are capable of forming complete larval body axes, but these larvae are scaled down to approximately two-thirds the length of normal specimens. In the size-reduced embryos, I hypothesised that cell division should progress with its normal dynamics, and therefore act to introduce normal cell size heterogeneity, but act on a smaller volume of cellular material. As a result, the experiment should reduce true cell size, while leaving relative cell size intact. This hypothesis was challenged, however, by a report from Morgan (1896) who predicted from transverse sections that size-reduced larvae possess only two-thirds the cell number of normal larvae. He also reported that not all tissues are perfectly scaled with total body size. To gain a higher-resolution understanding of the size-reduced phenotype, I therefore sought to raise larvae from isolated blastomeres at the 2-cell stage.

In this experiment, I manually dechorionated 2-cell stage embryos using tungsten needles. This was performed on glass-bottomed dishes coated with 1% (w/v) agarose to protect blastomeres from sticking and becoming damaged. I then separated the two blastomeres by rolling an eyelash between them, while applying gentle pressure. In general, this led to blastomere separation without damage to the membrane. Isolated blastomeres were then transferred to a separate agarose-coated petri dish containing fresh sea water, and incubated for 34 hours through the entirety of axial development. This was a very slow-throughput method, and survival was low in part due to the

stickiness of the blastomeres, which often led them to fuse together during the incubation period. The resulting aggregates were necrotic and failed to pass through gastrulation (*data not shown*). Nonetheless, I collected a small number of 14ss embryos derived from separated blastomeres, and, in line with Morgan's observations, they appeared perfectly scaled-down to approximately two-thirds the length of unmanipulated larvae (*Fig. 3.14c*). I could also confirm that cell division was occurring normally, based on the presence of PhH3 immunostaining in a common pattern and density in size-reduced and normal larvae (compare *Fig. 3.14a* with *c*). From here on, size-reduce larvae will be termed $1/2$ larvae, and the controls $2/2$ larvae.

I next immunostained the $1/2$ larvae for laminin and tubulin, stained with phalloidin for cortical actin, and imaged them in 3D using confocal microscopy (*Fig. 3.14c*). With this resolution of imaging, I hoped to better assess the extent of successful scaling on tissue and cellular scales. At this resolution, my imaging data confirmed Morgan's observations (Morgan, 1896) that axial tissues were not scaled proportionally in all dimensions. In fact, the ventral endoderm seemed to be an exception in being both shorter in anteroposterior length and smaller in cross-sectional area (*Fig. 3.14c, c'*). As noted by Morgan, the cross-sectional areas of the notochord, neural tube and somites actually appeared unchanged in $1/2$ larvae compared to $2/2$ larvae (*Fig. 3.14c'*). This means they are *greater* in cross-sectional area than would be expected for a perfectly-scaled embryo of the same length; if the tissue is shortened by a third, it should also be reduced in cross-sectional area by a third. As a result, axial tissues in $1/2$ larvae have actually declined in their AP elongation, or α values.

In order to better understand these anisotropic perturbations in axial tissue geometry, I next analysed changes in their structure at the cellular scale. The best case study for comparison here was the notochord, in which the cell outline can be visualised with phalloidin. In the notochords of $1/2$ larvae, I found cells to exhibit the same trilaminar topology as that in $2/2$ larvae, with a central layer

Figure 3.14. Cell division is dispensible for patterning but required for normal tissue geometry. (a, b) Embryos treated between 8hpf (cup-shaped gastrula stage) and 14ss with DMSO (a) or 2 μ M HU (b). Embryos are immunostained for laminin, PhH3 and tubulin, and stained with rhodamine phalloidin. (b') Inlays highlight morphological landmarks in HU-treated specimens; a coherent tailbud and fully resolved axial tissues in the trunk, a full complement of somites, and a notochord with typical stack-of-coins organisation in its central layer. ph, pharynx; n, notochord; ve, ventral endoderm; pw, posterior wall; nc, neurenteric canal; cnh, (*continued overleaf*)

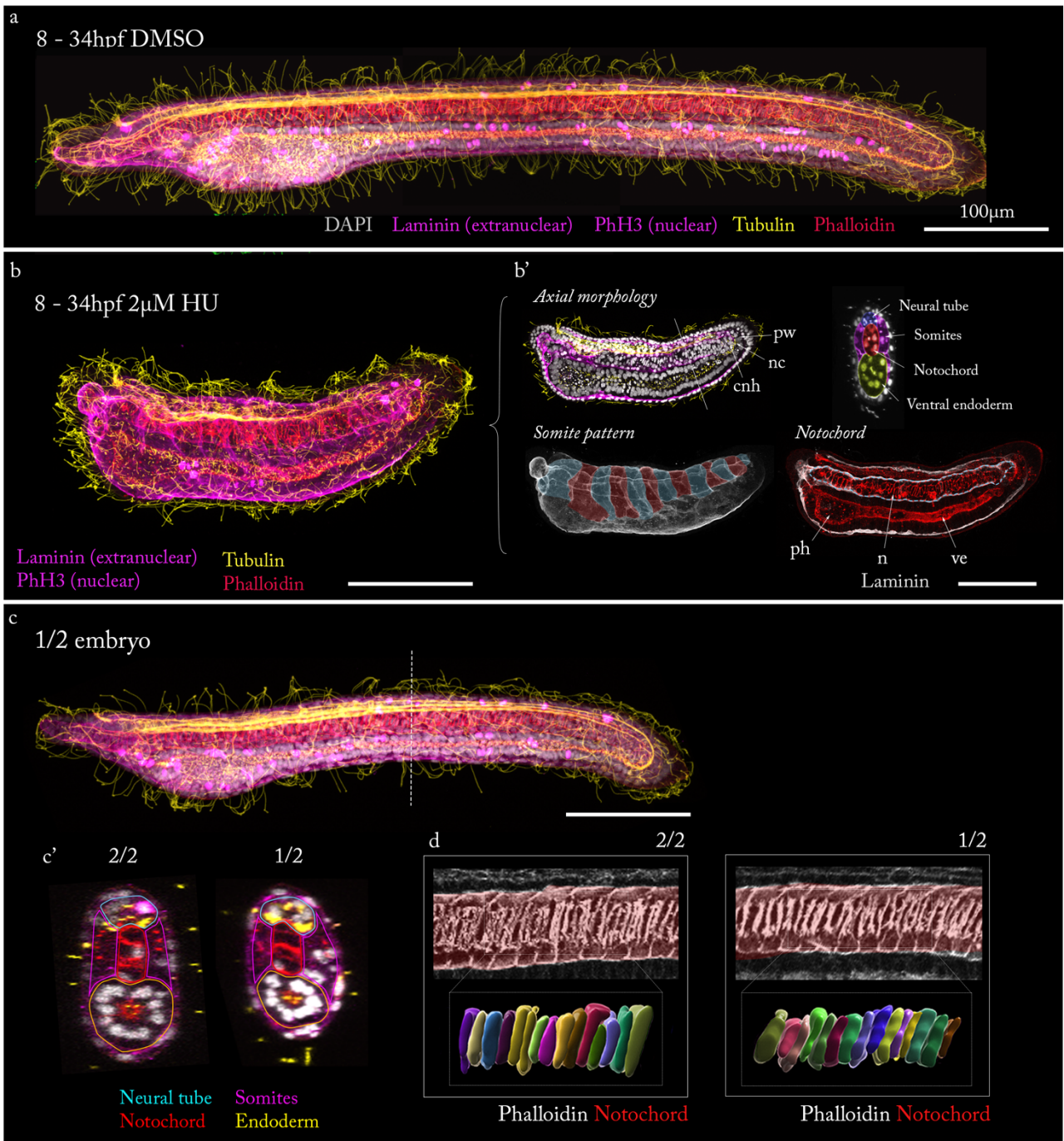


Figure 3.14. (*continued*). chordoneural hinge. 8hpf – 34hpf HU experiment representative of $n = 13$ imaged embryos. (c) A $\frac{1}{2}$ embryo derived from a single blastopore isolated at the 2-cell stage. (c') Comparison of axial tissue shape and size in a transverse section at the 50% AP level from the embryo shown in (a) and (c) with axial tissue identity marked. (d) Inlays show a Z-projection through the notochord at the 50% level of the embryos in (a) and (c) (top), with 15 cells manually segmented (bottom). Blastomere splitting experiment representative of $n = 3$ imaged embryos. All scale bars shown 100µm.

in a stack-of-coins pattern flanked dorsally and ventrally by two rows of more rounded Müller cells (*Fig. 3.14d*). More surprisingly, by segmenting groups of individual cells in $1/2$ and $2/2$, from the central layer, I found no difference in local cell size or packing density; a fixed number of cells occupied the same axial length in each case (*Fig. 3.14d, inlays*). In fact, when observed at the cellular scale, I could find no clear criterion to distinguish the $1/2$ and $2/2$ conditions. It therefore appeared that my initial hypothesis was wrong. Rather than having a normal number of size-reduced cells, the notochords of $1/2$ larvae had a reduced number of normally-sized cells. In turn, the local cellular structure is reiterated fewer times along the anteroposterior axis, and so to reach the full length of a $2/2$ notochord a greater number of cells would be required to extend the pattern. In this respect, tissue length has been cut short due to premature exhaustion of cellular material.

Considered together, it seems the defective tissue scaling manifest in $1/2$ larvae results from local tissue morphogenesis being falsely tuned to a larger amount of cellular material than is actually available in the embryo. In the notochord, this is shown in the local cellular structure being indistinguishable from that in $2/2$ larvae. This means that, for the total size of the embryo, each notochord cell is too large and occupies too great a cross-sectional area on the transverse plane. In turn, the notochord is too broad to reach its full elongation. For proper tissue scaling, we can hypothesise that the same behaviours should be exercised in cells of lower volume, but this is not adjusted for after blastomere separation in $1/2$ larvae. Returning to the problem of cell division, this experiment hints that formation of axial tissues with the correct geometry relies on regulation of cell size as a set *proportion* of total embryo size. When this is ensured, local cellular behaviours assemble tissues of a scale appropriate to the total cellular material available for morphogenesis. In amphioxus, this scaling between cell size and embryo size may be achieved by a set programme of volumetrically-reductive division that fractionates the available cellular material into a stereotypical diversity and abundance of cells.

3.5 Discussion

The results presented in this chapter form an account of amphioxus morphological development, covering the period in which it transforms from a cup-shaped gastrula to free-swimming larva. My analysis both adds resolution to previous descriptive accounts, and expands on them with fate mapping, quantitative analysis of tissue shape change, molecular staining, and functional perturbations. My primary experimental conclusions are as follows:

- Immunostaining and confocal microscopy reveals formation of the amphioxus body plan to involve a similar stepwise series of tissue-scale transitions to that observed in vertebrates. This includes circumblastoporal gastrulation, internalisation and folding of a neural plate derived from the dorsal ectoderm, formation of a *bona fide* tailbud, and formation of somites through sequential splitting of presomitic mesoderm. The description of these processes offered in this chapter satisfies Aim I.
- Internalisation and elongation of DiI labels in the outer blastopore lip of the cup-shaped gastrula reveals involution behaviour occurring after invagination of the vegetal hemisphere of the blastula. This challenges a current consensus that amphioxus gastrulation is a simple invagination process. In addition, convergence of DiI labels on the dorsal side of the gastrula hints at a coupling of involution with convergent extension behaviour, which would expand the dorsal mesoderm and contribute to blastopore narrowing. These experiments satisfy Aim II.
- By applying tissue-scale morphometric approaches at successive somite stages, I show that amphioxus axial elongation occurs in a net growth-free system, and depends on a synchronous burst of convergent extension behaviour occurring in all tissues, throughout the trunk – not restricted to the tailbud. Despite elongation of axial tissues in parallel, and at the same rate, quantification of changes in local cell neighbourhood topologies reveals tissue-specific programmes of neighbourhood reorganisation. A 3-fold increase in cell number in the absence of volumetric growth highlights a programme of volumetrically-reductive cell division occurring during axial elongation. These measurements satisfy Aim III.

- Using EdU incorporation and PhH3 immunostaining, I show that cell division becomes restricted to the chordoneural hinge and anterior neural plate during axial elongation. In this period, EdU pulse-chase shows that proliferative chordoneural hinge progenitors contribute to elongation of the posterior notochord and floor plate. Subsequent pulse-chase experiments in the gastrula show that chordoneural hinge progenitors derive from the late dorsal blastopore lip, once involution has ceased. In this position, they lie adjacent to somite precursors in the lateral blastopore lips that undergo earlier clonal expansion to elongate the posterior presomitic mesoderm. This descriptive account satisfies the first part of Aim IV.
- Inhibition of cell division at the onset of axial elongation using hydroxyurea revealed a requirement for cell division for full elongation of the body axis. This includes the proliferation of chordoneural hinge progenitors. Serendipitously, this experiment also revealed a robustness of somite number and pattern to perturbations of axial length. This experiment satisfies the second part of Aim IV.
- Treatment of embryos with hydroxyurea from gastrulation revealed a requirement for volumetrically-reductive cell division in defining tissue geometry, but a dispensability for patterning, given the maintenance of correct tissue diversity. In half embryos generated through blastomere splitting at the 2-cell stage, I found that embryo size is reduced, but cell size is unperturbed. Here, I show that local cell behaviours commence formation of a notochord that is too large in relation to the experimentally adjusted total embryo volume, and so cellular material is prematurely exhausted. In normal development, this experiment suggests that volumetrically-reductive cell division may register cell size to total embryo size, thereby aligning local tissue morphogenesis with the amount of cellular material available to build axial tissues. These experiments offer further detail and open questions relating to Aim IV.

3. 5. 1 Emerging principles and open questions

Amphioxus gastrulation commences through invagination of the vegetal hemisphere of the spherical blastula. In the next two hours of development, the blastopore narrows extensively, and the embryo flattens across its dorsoventral axis. The DiI labelling experiments detailed in this chapter suggest that the blastopore is, in fact, a dynamic population of cells during this period rather than a static landmark, and cells from the epiblast continue to flow through it into the early archenteron, via involution, during blastopore closure. This may allow for the reduction in cell number within the blastopore circumference that occurs as it narrows (Morgan and Hazen., 1900). In the process of involution, cells also converge on the dorsal side of the archenteron and extend across it along the anteroposterior axis, which could reflect mediolateral intercalation of cells within the archenteron roof. This act of convergence may actually facilitate blastopore closure by withdrawing cells from its circumference and focussing them towards the dorsal mesoderm, as described in *X. laevis* (Keller et al., 1985). Such a scheme of movement is supported by changes in the distribution of *Brachyury1/2+* cells during gastrulation, which shift from a circumferential distribution around the blastopore lip to residency only in the dorsal mesoderm (Terazawa and Satoh, 1997; Zhang et al., 1997; Chapter V). To follow up this study, it will be important to validate the random sampling of blastopore subdomains in the DiI labels. As noted previously, the experiment may suffer from an unknown user-bias. A more unsettling possibility is that DiI labelling itself affects the molecular patterning of the dorsoventral axis. For robust conclusions to be drawn, these scenarios need to be excluded. First, *in situ* hybridisation should be performed for markers of dorsoventral polarity immediately after DiI labelling to confirm the random placement of DiI spots. Then the presence of mediolateral intercalation should be tested directly by marking cells on opposite sides of the blastopore circumference with different lipophilic dyes, for example DiI and DiO. If mediolateral intercalation is present, cells marked by each label should come together and interdigitate at the dorsal midline.

Given the technical limitations of precise cell labelling during gastrulation, other approaches may become more effective for large-scale mapping of amphioxus gastrulation movements. At present, live imaging has only been successfully performed prior to formation of the cup-shaped gastrula, at which point the embryo starts to spin (Ben Steventon, personal communication). This makes cell tracking impossible. While in experiments not shown in this thesis I have found full embryo immobilisation to result in death, technological advances may circumvent this problem. For

example, embryos survive when embedded in agarose, which immobilises them but permits rotation. In this state, live imaging may be possible if corrected to remove the rotational movement. If scanned from anterior to posterior with single-plane illumination microscopy (SPIM), the embryo at each time point could be reconstructed using temporal registration, or by rotating each plane by the amount of rotation measured between each image acquisition event. This has been performed effectively for the beating zebrafish heart (Trivedi et al., 2015). Another more elaborate approach that has recently proved successful is acoustic trapping, in which the embryo is immobilised in an ultrasonic standing wave field (Yang et al., 2019). In each case, approaches would also need optimising for live nuclear and membrane labelling (Hirsinger et al., 2015). This is possible using transient transgenesis, via oocyte microinjection. Equally, commercial dyes are available for live imaging (Lukinavičius et al., 2015), although still face problems of toxic effects (Sen et al., 2018).

After the blastopore has narrowed, the epidermal ectoderm detaches from the lateral margins of the neural plate and blastopore, and spreads medially and anteriorly to envelope the embryo. At this point, gastrulation is terminated, because the hypoblast and epiblast become discontinuous. Now, the former dorsal blastopore lip is submerged as the chordoneural hinge, forming the anterior wall of the neurenteric canal. In vertebrates, epidermis also expands to cover the embryo during epiboly, which tends to involve an increase in surface area at the expense of its thickness through radial cell intercalation (Bensch et al., 2013; Szabó et al., 2016). However, in amphioxus the ectoderm is a single sheet of cells throughout gastrulation. Equally, sealing of the ectoderm across the neural plate in vertebrates tends to occur concomitantly with neural tube closure (Harrington et al., 2009). In these cases, active epithelial folding in the neural plate draws the epidermis towards the dorsal midline where each side detaches and fuses. While the description offered for amphioxus in this chapter highlights the functional importance of epidermal sealing, it does not address the cellular processes responsible. One interesting possibility is that a contractile actomyosin purse-string forms in the exposed margin of epidermis after its detachment from the neural plate, whose constriction would narrow the open aperture. This is observed in other cases of epithelial window closure (Jain et al., 2020), and is reminiscent of epithelial wound healing (Abreu-Blanco et al., 2012; Davidson et al., 2002). In principle, this could be tested through laser ablation at the epidermal margin (akin to Jain et al., 2020; Scarpa et al., 2018). However, a purse-string alone could not explain the pattern of epidermal sealing described here, in which the aperture first resolves to a long and narrow opening spanning the anteroposterior axis. Perhaps a purse-string mechanism is coupled to generation of

tension across the anteroposterior axis, thereby extending the aperture longitudinally and pulling its left and right lateral margins together. Alternatively, active protrusive activity in each lateral margin may result in their collective migration towards the midline, assuming a corresponding chemoattractive gradient, although the epidermis does not appear to be strongly adhered to the underlying neural plate. These scenarios could be resolved through imaging of the actomyosin network in cells of the epidermal margin, signalling perturbations against putative chemoattractants and, potentially, live imaging.

When neurulation is completed, between 6ss and 10ss, a definitive tailbud is formed at the posterior tip of the amphioxus embryo. Here, the notochord and floor plate unite at the chordoneural hinge, which is derived from the late dorsal blastopore lip. Importantly, the EdU pulse-chase analysis presented in this chapter reveals the chordoneural hinge to be a population of axial progenitor cells, whose proliferation during axial elongation fuels elongation of the notochord and floor plate. Given this continuity, it is important to recognise that although these progenitors reside at the posterior tip of the embryo throughout axial development, they only contribute to the most posterior tip. We can therefore infer that progenitors for the remainder of the notochord must be internalised during gastrulation, before the cellular composition of the blastopore lip stabilises. Meanwhile, the anterior floor plate should derive from cells within the neural plate internalised during epidermal sealing. By exploiting a wave of cell division across the dorsoventral axis of the blastopore, I showed that it also houses somite progenitors in its lateral or ventral lips, that undergo an earlier burst of cell division prior to axis elongation. These progenitors mark, approximately, the posterior 5 somites, while the anterior 9 must in turn derive from cells internalised during gastrulation. Considered collectively, we can use this experiment to define the limits of the amphioxus anterior and posterior body – that formed through remodelling of the late gastrula, and that conjugated onto the posterior end through differentiation of axial progenitor cells in the late blastopore lip.

While the cells identified in this study are reminiscent of vertebrate axial progenitors in their position and derivatives, the EdU pulse-chase approach employed in this study is very limited in its resolution. EdU incorporation identifies the posterior notochord as a proliferative domain during elongation, but it cannot resolve whether the domain is a homogenous field of cells with common dynamics, or a heterogenous population; the data presented would be consistent with both a broad field of cells undergoing one to two rounds of cell division, and a small population of long-term

potentially self-renewing resident progenitors generating large clones through multiple rounds of cell division. In the latter case, the majority of the labelled region could represent a field of transit amplifying progenitors. In this respect, the data presented will require further testing for robust comparison of progenitor dynamics on a cellular scale. One potential approach would be to apply sequential pulses of EdU and BrdU during the time window of chordoneural hinge proliferation prior to fixation. If labelled cells were mixed, it would hint at a homogenous population, whereas spatially resolved labelling along the anteroposterior axis might hint at a long-term progenitor continually adding progeny to the posterior tips of axial tissues. The problem with such an approach is the potentially toxic effects of high doses of thymidine analogues on gene expression. A complementary approach would be to focally laser ablate small regions of the chordoneural hinge, and test whether the effect on tissue elongation is equally affected regardless of the cells ablated. As noted previously, live imaging is a major challenge in amphioxus. However, a compromise could be the mosaic expression of photoconvertible dyes, like Kikume (see Attardi et al., 2018; Nowotschin and Hadjantonakis, 2009). Clonal analysis could then be performed by labelling cells in the chordoneural hinge and quantifying changes in their position and number in periodic imaging sessions.

Once the axial tissue primordia have been formed, through neural plate internalisation and evagination of the archenteron, they undergo a 3-fold elongation along the anteroposterior axis. By quantitatively measuring changes in axial tissue shape and size, I have shown that axial elongation is predominantly mediated by tissue rearrangement. In this case, axial tissues elongate through a late phase of convergent extension, in which they increase in length at the expense of their width. Because this occurs throughout the segmented body, length generating processes in amphioxus are not restricted to the tailbud. Although all axial tissues experience the same change in length, and at the same rate, I have shown that these common processes are underpinned by different transitions in cell topology. An interesting deduction from these results is that the division of labour for generating length is unevenly distributed across the anteroposterior axis, and this property differs between tissues. This may mean that a degree of slippage is required between closely opposed tissues for the body to remain straight. Here, consider that a high rate of elongation in the posterior neural tube, alongside a low rate of elongation in the notochord, should generate a ventral curvature in the embryo. Indeed, this type of mechanical coupling is critical for the generation of biological curvature, for instance in the formation of intestinal loops (Nerurkar et al., 2017; Savin et al., 2011). Looking forward, we must now also consider the role of each tissue in elongation of the body axis at large. In other words, which

tissues are required to generate the elongating force? To this end, it would be informative to compare tissue-specific stiffness at different stages using atomic force microscopy, or injection of ferrofluid oil droplets whose deformation reflects the amount and orientation of local tissue stiffness (Mongera et al., 2018; Serwane et al., 2017). If embryos are prohibitively small for this method, laser ablation could also be applied to arrest elongation in specific tissues and test their influence on total axial extension. Alternatively, a molecular approach could be applied to inhibit elongation in specific tissues, for example function blocking Dishevelled antibodies have been shown to inhibit amphioxus notochord elongation (Ben Steventon, personal communication).

3.5.2 Implications for chordate body plan evolution

When placed in the context of vertebrate literature, the data presented in this chapter on amphioxus development highlights putative ancestral strategies of axial morphogenesis in chordates. We can infer, based on their shared presence in vertebrates and cephalochordates, that involution and convergent extension were essential innovations for axial elongation in the first chordates, thereby enabling the restructuring of the embryo into novel patterns and a dramatic increase in anteroposterior length. This hypothesis challenges suggestions that such movements were instead vertebrate innovations, framed partly on incomplete experimental studies in amphioxus (Zhang et al., 1997). In amphioxus and externally-developing anamniotes, gastrulation movements establish most of the tissue volume required to assemble axial tissues. In zebrafish, they then continue within the tailbud (Goto et al., 2017; Kanki and Ho, 1997; Steventon et al., 2016), while in amphioxus they are protracted throughout the trunk; the amphioxus represents an extreme case of chordate body plan assembly almost entirely through tissue rearrangement. In turn, extensive volumetric growth appears to be missing from the ancestral chordate morphogenetic programme, and is therefore most likely a secondarily derived property explicit in some vertebrates, enabling elongation of the body beyond the limits of tissue rearrangement acting on the gastrula. This proposed scheme is congruent with the limited supply of intracellular yolk in amphioxus, ascidians, and non-chordate deuterostomes, and the externalisation and expansion of embryonic nutritional supplies in vertebrates (O'Farrell, 2015).

An interesting twist in the tail of axial elongation is the conspicuous role for posterior growth in the metamorphosis of indirectly developing deuterostomes. This is very explicit in the acorn worm, *S. kowalevskii*, whose metamorphosis involves extensive anteroposterior elongation, leading to the

addition of a *Hox*-patterned trunk onto the posterior end of the larva (Gonzalez et al., 2017). It is also the case in amphioxus (Schubert et al., 2001). The developmental events described in this chapter lead to formation of a voracious larva that can fuel further development through active feeding. Metamorphosis involves both extensive elongation and growth of the body axis, as well as the addition of new somites. Although not validated with lineage tracing, the amphioxus larva is also considered to give rise to the most anterior portion of the adult body, while the posterior (constituting the majority of the body axis) is thought to form through further budding of cells from the neurenteric canal (Holland et al., 2008; Schubert et al., 2001). Homology between the amphioxus neurula and vertebrate head is supported by similar nested domains of anterior Hox gene expression (Wada et al., 1999), and similar neuroanatomy (Wicht and Lacalli, 2005). In this respect, the adult amphioxus is very similar to the amniote embryo, in consisting of an anterior (pre-occipital) region that is formed through tissue rearrangement and extended gastrulation movements, and a posterior (post-occipital) region formed, in this case much later, through posterior growth. As a result, when post-embryonic development is also considered, posterior growth emerges as ancient process in deuterostome elongation rather than a true novelty in vertebrates. The apparent novelty of posterior growth in amniote embryogenesis can therefore be attributed to the precocious activation of processes normally occurring during metamorphosis, or simply the removal of a larval phase from the life cycle.

The identification and perturbation of reductive-cell division in this chapter support a critical role for cell division in converting the cellular material of the oocyte into a phylotypic stage embryo, without a necessary coupling with growth. Instead, reductive cell division divides the embryo into a large number of cells, and therefore an entity with greater morphogenetic potential through active programmes of cell rearrangement. If the process is blocked, as performed here using hydroxyurea to arrest DNA synthesis, embryos form many of the correct patterns but fail to acquire the correct geometries. This is congruent with the limited nutritional supply of amphioxus embryos, and places the onus on the mother to generate large eggs (O'Farrell, 2015). In amphioxus, we find an interesting case of reductive cell division occurring in cells of the chordoneural hinge, inherited from the dorsal blastopore lip, that contribute to elongation of the posterior notochord and floor plate, and somite precursors derived from the lateral blastopore lips. These populations are similar in position and tissue contributions to analogous progenitors identified in amniotes, that have very large clones and are associated with posterior growth (Catala et al., 1996; Selleck and Stern, 1991). This finding therefore suggests that axial progenitors initially emerged in evolution in a novel spatial pattern of

volumetrically-reductive cell division, to enhance the elongation of posterior tissues. In fact, this is very similar to the presence of cell division in the posterior zebrafish notochord in the absence of a posterior growth phase (Bouldin et al., 2014; Steventon et al., 2016; Sugiyama et al., 2009). Considered together, I propose here that proliferative posterior progenitors are likely a conserved motif in chordates, and have a conserved function in axial elongation, but how this is exercised – the specific cell behaviours – is divergent. Within this, a coupling with growth may represent a derived condition in vertebrates, through secondary changes in cell cycle dynamics.

Formation of the chordate body plan involves both axis elongation, and the emergence of a stereotypical tissue diversity and topology. One apparent innovation is the somites. In the current literature, the somites of the amphioxus larva are not considered homologous with vertebrate somites (Beaster-Jones et al., 2008; Holland et al., 2008). This was founded initially on their apparently distinct morphogenesis. As described here, somites form through enterocoely, which describes sequential outpouching of the archenteron roof. This contrasts with the more posterior somites, and vertebrate somites, that form through schizocoely – the splitting of an early tissue primordium (Schubert et al., 2001). In this manner, amphioxus larval somites are considered homologous to the coelomic cavities of ambulacrarian deuterostomes, that form through archenteric evagination (Green et al., 2013; Onai, 2018). Loss of enterocoelic segmentation, and head segmentation, in vertebrates is equated to loss of the underlying processes (Holland et al., 2008). Only the posterior, schizocoelic, somites of amphioxus are considered homologous to vertebrate somites (Schubert et al., 2001). And, given that they form without a presomitic intermediate, the presomitic mesoderm is considered a vertebrate innovation. This is further supported by lack of *Mesogenein* expression in amphioxus (Wang et al., 2012). From my analysis here, it is my contention that these studies are flawed by too literal a definition of homology. Amphioxus larval somites do not appear to be homologous to vertebrate somites based on molecular characterisations, but their mode of formation implies a homology of process. Despite forming as archenteric evaginations, amphioxus somites emerge through formation of bilateral bands of unsegmented paraxial mesoderm, that are segmented sequentially through the budding of cells from their anterior tips. As the somite number increases, the length of remaining unsegmented tissue depletes. Thus, in its common position and function, amphioxus enterocoelic somites emerge from a presomitic mesoderm. From this perspective (simply reiterating the work of Hatschek, 1893), amphioxus larval somitogenesis appears to reflect the

topological rearrangement of invertebrate coelomic pouch formation into a vertebrate-like somite patterning system.

Considered more broadly, modularisation of axial tissues may release constraint on morphogenesis. In amphioxus, the early archenteron is segregated into four discrete compartments – the notochord, somites and ventral endoderm. As shown in this chapter, each of these axial tissues exhibits a different maturation process on the cellular scale, despite their elongation in parallel and at a common rate. In this respect, morphological modularisation of the archenteron expands the number of morphogenetic processes that can act simultaneously, and may release constraint between them. Now, for example, length-generating processes are not constrained by the requirement of the archenteron to remain tubular for its gastrointestinal function. Instead, they can be outsourced to a new tissue, the notochord. Nonetheless, the tissues remain mechanically coupled within the body axis, such that they retain synergistic effects on axial length and pattern. This modularity may allow a greater diversity of morphogenetic processes, and, in the same breath, it may enhance morphological robustness because variation in one tissue will not collapse the whole system. The example given in this chapter shows that length-generating processes in the notochord, like cell division, can be modulated without distorting the segmental pattern of somites. Even when cell division is arrested from gastrulation throughout axial development, with a catastrophic impact on tissue geometry, a full complement of somites still forms. In the wild, where environmental conditions may be unpredictable in terms of, for example, temperature and nutrient supply, this may ensure embryo viability through scaling of axial patterns to stochastic variations in axial length. In turn, it may also enhance the evolvability of the system. Consider that, if the rate of axial elongation were critical for defining the number of somites, that rate would be constrained and not so free a node for evolutionary variation.

This line of thinking raises the question of how body shape is controlled. Does the system steer towards a set geometry that is stabilised by feedback, or is form instead simply an emergent property of earlier behaviours? If so, how do those behaviours map onto specific axes of geometric variation? This chapter offers some insight into these questions in the examination of a size-reduced phenotype generated through blastomere splitting at the 2-cell stage. The results presented for this experiment suggest that the size reduction is a consequence of a loss of cellular material with the removal of one blastomere, while the programme of cell divisions seems to generate cells of sizes similar to those in full-size embryos. In turn, the tissues assembled by local cell behaviours, here

examined in the notochord, are almost identical in their cellular architecture, but are shorter in total axial length. It seems that the developmental programme initiates a morphogenesis that is appropriate for a much larger amount of tissue than is actually available in the embryo. And so, in size-reduced specimens, the notochord is prematurely truncated through exhaustion of progenitors. My hypothesis emerging from this experiment is that volumetrically-reductive cell division acts to register embryo size and cell size; a starting mass of cellular material is fractionated into a set diversity of cell types, each of a size related to the number and symmetry of divisions in its lineage, therefore representing a set proportion of the embryo at large. This puts local tissue morphogenesis in phase with the amount of cellular material available to form an embryo. In addition, the formation of a stable body axis in size-reduced specimens tells us something about the control of body shape. Here, a functional larva is built around a notochord that is geometrically perturbed, containing far fewer cells than it should for their size and cross-sectional area, and occupying a disproportionately large amount of the trunk cross-section. Nonetheless, the patterns of the body axis are stable and functional. Considered together, form is revealed to be a robust and plastic quality, emerging from early regulation in cell size and number.

3.5.3 Conclusion

In conclusion, the work presented in this chapter offers a novel scheme for the evolution of chordate body plan morphogenesis and growth dynamics. In considering amphioxus axial morphogenesis, we find a remarkable conservation of morphogenetic processes throughout the chordates. This includes the conserved gastrulation movements of convergent extension and involution, the clonal dynamics of axial progenitors, and posterior growth. The apparently novel dynamics evident in vertebrates, most prominently in amniotes, therefore represent changes in the timing and magnitude of ancestral processes rather than those that are qualitatively new. In particular, this includes an increase in sizes of axial progenitor clones, and precocious activation of a posterior growth programme already common in post-embryonic metamorphic development. On this scale of observation, morphogenetic processes involved in chordate axial development appear to be highly conserved, but operating in the context of different environmental constraints through variations in timing and magnitude.

Chapter IV

Unravelling notochord morphogenesis with single-cell morphometrics

4. 1 Introduction

Chapter III offers a global view of morphogenetic processes contributing to amphioxus axial development at the tissue-scale. It also highlights the utility of morphometric approaches for defining and comparing patterns of tissue behaviour. Next, it must be considered that geometric transformations at the tissue-scale emerge from the behaviours of constituent cells, which in turn are tightly controlled in time and space by virtue of molecular and mechanical instructive cues, exercised in the context of local boundary conditions. These cell behaviours also exhibit variation between species, even if the resulting geometric transformations (eg. tissue elongation) at the tissue-scale are seemingly conserved. In considering the evolution of morphogenesis, methods are therefore required for both characterisation of patterns of cell behaviour in a diversity of organisms, and rigorous non-bias comparison of dynamics between species. Cell behaviour is the next important focus of analysis in this multi-scale decomposition of amphioxus axial development. In this chapter, I present a quantitative methodology to map out single-cell morphogenesis in an entire developing tissue, using the amphioxus notochord as a case study. In doing so, I seek to elucidate ancestral principles of notochord morphogenesis in chordates.

4. 1. 1 The notochord and its developmental functions

The notochord is an elongate and stiffened rod of mesodermal cells occupying the axial midline of all chordate embryos, and represents one of the core synapomorphic

(shared-derived) traits of the chordate body plan (Stemple, 2005; Willmore, 2012). In this position, the notochord acts as the structural core of the embryo. Once formed, it acts to mechanically stabilise the long body axis, and counterbalance its active bending during undulatory movement, driven by contraction of somite-derived axial muscle fibres (Annona et al., 2015; Stemple, 2005). While the notochord retains this structural function throughout embryonic and adult life in invertebrate chordates, it is instead inherited by the vertebral column in vertebrates (Linsenmayer et al., 1986; Gee, 1996). Here, the notochord acts as a scaffold for formation of the vertebral cartilages, which come to envelope and replace it (Newgreen et al., 1986; Renn et al., 2013; Ward et al., 2018). In amniotes, fate mapping studies have shown the notochord to only persist as the nucleus pulposus of the intervertebral discs (Choi et al., 2008; McCann et al., 2012).

During development, the notochord makes mechanical contributions to elongation of the embryonic anteroposterior axis. In ascidians, the notochord appears to provide the driving force for axial elongation, given that mosaic inhibition of mediolateral intercalation behaviour prevents full elongation of the body axis (Segade et al., 2016). In a similar vein, surgical excision of the notochord rudiment in *X. laevis* (Bijtel, 1958; Niewkoop, 1946; Mookerjee, 1953) and chick (Jacobson et al., 1981) leads to a shortening of axial length. However, these experiments are prone to misinterpretation and variable results, given the regulative potential of the embryo to adjust to surgical manipulation, and potential indirect contributions to elongation. A more systems view of axial elongation is now emerging, in which the notochord contributes via mechanical feedback with other tissues (Benazeraf, 2019). In chick embryos, for example, axial elongation has been attributed to a cell motility gradient across the paraxial mesoderm; greater motility in the posterior presomitic mesoderm focally reduces cell density, and inflates the tissue posteriorly and laterally (Bénazeraf et al., 2010). A similar gradient has also been identified in zebrafish (Mongera et al., 2018). In chick, inflation of the posterior presomitic mesoderm locally compresses the notochord and neural tube at the midline (Xiong et al., 2020). This promotes their convergence and extension along the anteroposterior axis, which, in turn, forces the entry of axial progenitors of the tailbud into the presomitic mesoderm, thereby fuelling its further expansion (Xiong et al., 2020). In this manner, the notochord completes a positive feedback

loop that maintains posterior growth in the presomitic mesoderm, and drives axial elongation.

As well as acting as a structural core for the developing embryo, the notochord has important patterning roles through the secretion of intercellular signalling ligands. The best characterised of these functions is dorsoventral patterning of the neural tube, which is mediated by secretion of the morphogen, Sonic hedgehog (Placzek et al., 1990; Yamada et al., 1993). In this case, notochord-derived Shh induces and maintains the floor plate at the ventral midline of the neural plate, which in turn also secretes Shh. Together, the notochord and floor plate contribute to a gradient of Shh pathway activation across the dorsoventral axis of the neural tube, which is read out as a stratified distribution of gene expression domains, and ultimately distinct motor neuron subtypes (Placzek and Briscoe, 2018). Beyond the neural tube, the notochord also has an important inductive role in somite patterning. Here, notochord-derived Shh specifies the schlerotome in the medial portion of the somites, which will generate the axial skeleton (Munsterberg and Lassar, 1995; Pourquié et al., 1993). More lateral somite cells, which are exposed to lower concentrations of Shh ligand, instead differentiate as myotome and dorsal dermis. Ongoing Shh signalling is then required for ventral schlerotome cells to envelope the notochord and generate the primordia of the vertebral bodies. Moreover, a Notch-dependent signalling relay between schlerotome and notochord is required to translate the segmental pattern of somites into a metameric pattern of vertebral bodies (Wopat et al., 2018). In its patterning functions, the notochord has also been implicated in left-right symmetry breaking (Compagnon et al., 2014), angiogenesis (Danos and Yost, 1995; Fouquet et al., 1997) and endoderm organogenesis (Amorim et al., 2020; Kim et al., 1997). Considered collectively, the notochord has diverse functions in establishing the tissue diversity of the body plan, their constituent cell types, and their proper geometries.

Given its diverse contributions to body plan development, the tweaks in the deuterostome developmental programme responsible for the emergence of the notochord in evolution, and how the morphogenetic programme has diversified in chordates, are of great interest. For morphogenetic studies, the notochord is also a compelling case study for morphological evolution given its very simple geometry and cellular structure; an elongate

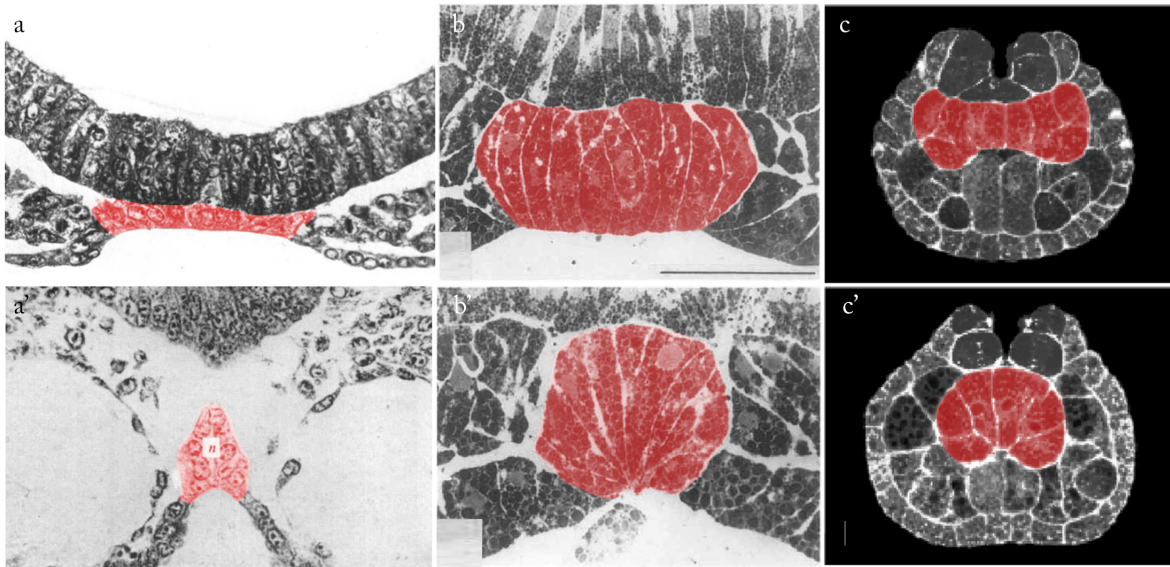


Figure. 4.1 **Longitudinal evagination is a conserved process in olfactoran notochord development.** The notochord plate before (top row) and after (bottom row) evagination of the notochord plate in mouse (a, a'), ribbed newt (b, b') and ascidian (c, c'), shown in transverse sections. In all panels, notochord cells (per definition in corresponding texts) is false-coloured in red. Mouse sections are from Jurand (1974). Newt sections are from Novoselev (1995). Ascidian sections are from Munro and Odel (2002). Images not to scale.

cord of coin-like cells extending along the axial midline. As shown in **Chapter III**, the amphioxus notochord can also be imaged in its entirety, at cellular resolution, due to the small size and optical transparency of the embryos. Now, before probing notochord morphogenesis in the amphioxus, I will first provide the necessary context by detailing principles of notochord formation in vertebrate and ascidian embryos.

4. 1. 2 Formation and folding of the notochordal plate

In vertebrates, notochord precursors are initially specified as a flat sheet of cells, termed the notochordal plate. The mouse notochordal plate can first be identified on the ventral surface of the embryo at E8 (8 days post-coitum) (Balmer et al., 2016; Jurand, 1974). During gastrulation, axial mesodermal cells ingress from the epiblast through the anterior part of the primitive streak, and intercalate between endodermal cells at the ventral midline of the embryo, undergoing a mesenchymal-to-epithelial transition (Tam and Beddington, 1987). Despite their lateral continuity with the endoderm, the notochordal

plate can be identified by its columnar monociliated cells, which are also tightly adherent to the ventral surface of the neural plate at their basal surfaces (*Fig. 4.1a*) (Sulik et al., 1994). As the notochordal plate matures, it invaginates to form a longitudinal groove, arching ventrally away from the plane of the endoderm (*Fig. 4.1a'*) (Sausedo and Schoenwolf, 1994). This occurs in a rostral-to-caudal direction. Ultimately, the notochord separates fully from the endoderm, and adopts a tubular structure that is submerged within the embryo between the neural plate dorsally, and endoderm ventrally. Eventually, the attachment between the notochord and the neural plate is also released through the penetrance of migratory mesenchymal cells (Jurand, 1974). A very similar process of notochordal plate maturation has recently been described in human embryos, which have a flat morphology, in contrast to the cup-shaped mouse gastrula (De Bree et al., 2018). Here the notochordal plate is again established at the ventral midline within the endoderm, in this case via a flow of cells through a node-endoderm interface termed the notochordal process. Once again, the notochordal plate then invaginates and is submerged within the embryo as an epithelial tube, in this case initiating at the centre and progressing both rostrally and caudally (De Bree et al., 2018).

A similar process has also been identified in amphibians, despite their circumblastoporal mode of gastrulation. The amphibian notochordal plate is specified in the dorsal roof of the archenteron, which is expanded through the involution of the dorsal marginal zone during gastrulation (Keller et al., 1985; Shih and Keller, 1992). It has been described in *X. laevis*, axolotl, ribbed newt and Mexican salamander that notochordal plate cells first become distinct in acquiring tall columnar morphologies, while remaining continuous with prospective paraxial mesoderm on the left and right sides (*Fig. 4.1b*) (Brun and Garson, 1984; Löfberg, 1974; Novoselov, 1995). In this process, cell height is increased at the expense of apical area, which has enabled the morphological identification of the notochord rudiment in scanning electron micrographs (Löfberg, 1974; Novoselov, 1995). Subsequently, cells of the notochordal plate undergo apical constriction, which gives the notochord plate a fan-shape in transverse section and draws together the lateral margins of the archenteron (*Fig. 4.1b'*) (Novoselov, 1995). The notochord plate then fully pinches off from the dorsal side of the archenteron, leading to the separation of the notochord *sensu stricto* as a discrete tissue compartment. The notochord now lies between the neural plate

on its dorsal side, and the primitive gut on its ventral side (Brun and Garson, 1984). The situation also appears somewhat similar in zebrafish, in which the notochord emerges at the dorsal midline of the involuting hypoblast during gastrulation (Glickman et al., 2003). However, the separation process of the notochord from the endoderm surrounding the yolk sack remains poorly characterised.

Finally, in ascidians, the notochordal plate occupies the inner aspect of the dorsal blastopore lip, within the embryonic archenteron (*Fig. 4.1c*) (Miyamoto and Crowther, 1985; Munro and Odell, 2002). Once again, the notochordal plate has been described evaginating from the archenteron roof shortly after gastrula, arching ventrally away from the archenteron lumen towards the ventral surface of the neural plate (*Fig. 4.1c'*) (Miyamoto and Crowther, 1985). Following evagination, the notochord rudiment is circular in transverse section, and is composed of multiple adjacent cells on the mediolateral and dorsoventral axes (Munro and Odell, 2002; Veeman and Smith, 2013). It is now flanked laterally by trunk mesoderm, and ventrally by trunk endoderm (*Fig. 4.1c'*). From these descriptions, it is clear that the initial appearance of the notochordal plate as a monolayered epithelial sheet continuous with the endoderm, and its later separation through evagination, are conserved transitions in Olfactoran notochord development (*Fig. 4.1*).

4. 1. 3 A variable role for posterior addition in elongation of the notochord rudiment

The size of the notochordal plate is the product of both the size of the primordium established by gastrulation movements, and its ongoing elongation through proliferation and growth. In *X. laevis*, the anterior part of the notochord is established by the involution of cells around the dorsal blastopore lip, which establishes the archenteron roof (Keller et al., 1985). Here, the timing of involution relates to the eventual position of internalised cells along the anteroposterior axis – the later the passage through the dorsal blastopore lip, the more posterior the position along the axis (Feroze et al., 2015; Keller, 1975; Keller, 1976). After gastrulation, the notochord is further extended by self-differentiation of the dorsal blastopore lip. Once involution has stopped, the blastopore lip represents a static population of cells, now located at the definitive posterior tip of the embryo. Fate mapping

studies with DiI have revealed this population to give rise to large clones that assemble the posterior half of the notochord and floor plate (Gont et al., 1993), and have raised the possibility that they possess neuromesodermal potential (Davis and Kirschner, 2000). The contribution of the blastopore lip to notochord formation is also shown strikingly in Spemann-Mangold grafts, in which the dorsal lip induces most axial tissues from host cells, but itself constructs the notochord and medial somite compartment (Spemann and Mangold, 1924).

The contribution of proliferative progenitors is much greater in amniotes than in amphibians, in which analogous cell marking approaches have shown cells in the node-streak border of the gastrula to generate the entire post-occipital notochord and floor plate (Krol et al., 2011; Mugele et al., 2018; Psychoyos and Stern, 1996). This has been shown persuasively using the quail-chick chimera system, in which homotopically transplanted node grafts populate the tailbud and lay down both the notochord and floor plate in host embryos (Catala et al., 1996). A subsequent study revealed that homotopic grafts of GFP+ nodes into wild type hosts contribute to either floor plate or notochord depending on the level of Notch signalling, modulated using the γ -secretase inhibitor DAPT (Gray and Dale, 2010). The amniote notochord is also extended through dispersed intercalatory cell division during its morphogenesis (Sausedo and Schoenwolf, 1994). In these cases, the balance between cell rearrangement and progenitor amplification in building the notochord seems to have shifted towards the latter. In contrast, zebrafish, which develop much more rapidly than amniote embryos, exhibit very little proliferation or growth around the chordoneural hinge (Steventon et al., 2016; Sugiyama et al., 2009). Here, extension of the notochord primordium seems to primarily depend on the balance in which progenitor cells in the tailbud are allocated between axial tissues (Row et al., 2016). To a greater extreme, cell division ceases in the ascidian notochord prior to its morphogenesis, which thereon occurs in a population of exactly 40 cells from start to finish (Miyamoto and Crowther, 1985; Munro and Odell, 2002). In this respect, the role of posterior progenitors has diverged extensively in chordate notochord development.

4. 1. 4 Mechanisms of notochord elongation through convergent extension

Having become morphologically resolved from other mesendodermal primordia of the trunk, the notochord rudiment next commences a process of extensive elongation along the anteroposterior axis. A major contributor to this process is convergent extension, in which tissues undergo elongation along one axis through narrowing along the perpendicular axes. Seminal experiments in explants of *X. laevis* dorsal mesoderm led to the characterisation of mediolateral intercalation behaviour (MIB) as an engine for convergent extension (Shih and Keller, 1992a; Shih and Keller, 1992b). In this process, cells adopt a spindle-shape morphology and extend filopodial projections medially and laterally, allowing them to crawl across and between adjacent neighbours and establish bipolar left-right contacts with the boundaries of the notochord field. As a result, cells that are initially adjacent on the mediolateral (ML) axis are forced apart along the anteroposterior (AP) axis, resulting in active tissue-autonomous extension (Glickman et al., 2003; Munro and Odell, 2002; Yamanaka et al., 2007). Polarised intercalation behaviour also drives a stereotypical change in cell topology, towards a single-file column of cells. In turn, the presence of many flattened cells, spread out on their transverse plane and stacked along the anteroposterior axis, is a hallmark of notochord morphology (Stemple, 2005).

Perhaps the simplest programme of mediolateral intercalation behaviour is found in ascidians, in which the process generates a perfect stack of coin-shaped cells, each of which occupies a distinct transverse slice of the tissue along the anteroposterior axis (Miyamoto and Crowther, 1985; Munro and Odell, 2002; Veeman and Smith, 2013). The blocking of intercalation through mosaic fibronectin knockout leads to both a local loss of intercalation and elongation, and loss of the stack-of-coins pattern (Segade et al., 2016). In vertebrates, patterns of intercalation can be more complex. In *xenopus*, cell protrusive activity is initially biased on a mediolateral plane, and reduces notochord width by more than half, but it also increases the number of cell layers on the DV plane (Keller et al., 1989). Once mediolateral intercalation is complete, protrusive activity then spreads to the dorsal and ventral margins of each cell, which reduces the number of layers, and increases the reach of single cells across the notochord cross-section. Cells spread extensively across the notochord diameter, adopting 'pizza slice' morphologies, but do not fully breach the

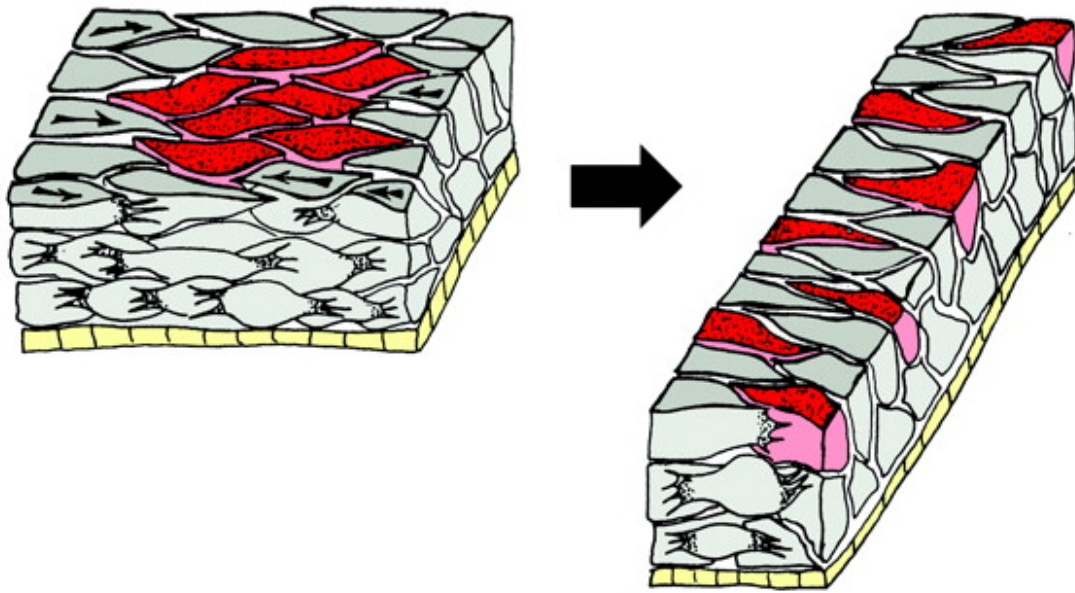


Figure. 4.2. Schematic of convergent extension mediated by mediolateral intercalation behaviour. An initially broad and short field of cells becomes polarised across its mediolateral axis and extends filopodial protrusions left and right. By active crawling on the mediolateral plane, cells exert traction against each other and intercalate. As a result, the tissue narrows and elongates, and each cell occupies a greater proportion of the tissue cross-section. In the process, cells initially adjacent to each other (neighbourhood marked in red) become dispersed across the long axis and interspersed with other cells. Adapted from Keller (2000).

cross-section like in ascidians (Keller et al., 1989; Miyamoto and Crowther, 1985). Interestingly, evidence of intercalation and formation of quasi-stack of coins arrays has been used to identify notochord-like structures outside of the chordates, for example in the axochord of *P. dumerelii* (Lauri et al., 2014).

Polarised intercalation is widely credited for notochord convergent extension, but is not the only mechanism of its kind. In ascidians, mediolateral intercalation is followed by a so-called disk-to-drum transition that drives further convergent extension (Lu et al., 2019; Miyamoto and Crowther, 1985; Sehring et al., 2014). Here, the length of individual cells is increased at the expense of cross-sectional area through formation and contraction of an equatorial actomyosin ring. This can be visualised through the equatorial enrichment of actomyosin related proteins. It can also be functionally blocked using myosin II ATPase or F-actin inhibitors, which results in a significant loss of anteroposterior tissue length and

a maintenance of broad disk-like notochordal cells (Sehring et al., 2014). Currently, it is not clear in the literature whether the disk-to-drum transition acts in addition to cell intercalation in generating length, or instead whether it acts to rectify a loss of cell length imposed by their spreading during intercalation. This will require more detailed morphometric data. Collectively, convergent extension has emerged as a highly conserved morphogenetic process generating notochord length. This is widely underpinned by polarised intercalation behaviour. However, other less conserved processes can also synergise with intercalation to accelerate axial elongation, like the isolated case of the disk-to-drum transition in the ascidian notochord.

4. 1. 5 Mechanisms of notochord elongation through cellular growth

In vertebrate notochords, formation of a quasi-stack-of-coins organisation is followed by formation of a circumferential perinotochordal sheath (Stemple, 2005). This structure has been histologically identified in diverse vertebrates, as well as ascidians and amphioxus (Bancroft and Bellairs, 1976; Bočina and Saraga-Babić, 2006; Jurand, 1974; Trapani et al., 2017). In most cases, the sheath is an acellular compartment, enriched with laminin, collagen and proteoglycans. In zebrafish, however, it also includes a layer of endothelial-like notochord cells segregated through Notch signalling (Yamamoto et al., 2010). As development progresses, the core notochord cells progressively enrich a single large intracellular vacuole through endocytosis, leading to an increase in their volume (*Fig. 4.3a*) (Ellis et al., 2013). At the same time, the internal pressure and flexural stiffness of the notochord increase, thereby increasing its rigidity (Bagnat and Gray, 2020; Bagwell et al., 2020). It has been shown in *X. laevis* that the hydraulic properties of the notochord depend on the presence of the perinotochordal sheath. When the sheath is digested with trypsin and collagenase, the flexural stiffness of the notochord fails to increase and, as a result, it buckles to adopt the topology of a ‘wet noodle’ (Adams et al., 1990; Koehl et al., 2000). Similarly, it has been shown through genetic collapse of notochord vacuoles in zebrafish, using mosaic expression of dominant-negative *Rab32a*, that their formation is required for tissue elongation, acting to enhance the length generated by convergent extension. Here, the pressure generated by vacuole formation is also required to maintain the integrity of the axial midline against the compressive forces of tissue development; when

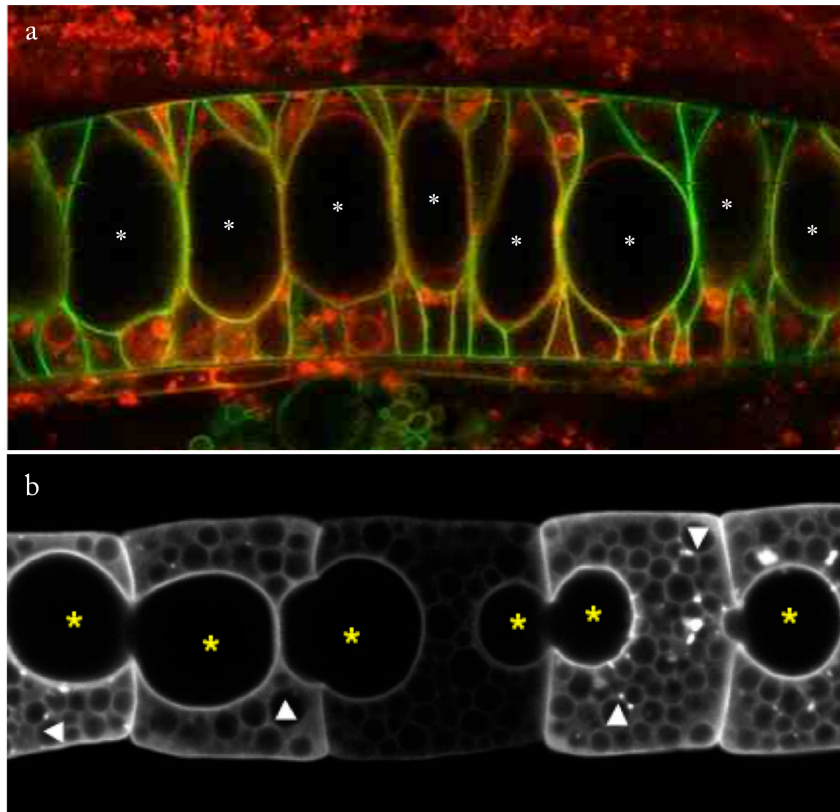


Figure. 4.3. Notochord vacuolation in zebrafish and ascidians. (a) Transgenic GFP-CaaX embryo (membrane-targeted GFP), stained for BODIPY TR methyl ester dye (red), at moment of vacuole inflation. Section through notochord shows presence of large intracellular vacuoles (white asterisk). (b) Section through ascidian notochord at moment of vacuole inflation, with rhodamine phalloidin staining. Vacuoles are intercellular inclusions, initially forming between adjacent notochord cells. Zebrafish section is from Ellis et al (2013). Ascidian section is from Jiang and Smith (2007). Images not to scale.

vacuoles are collapsed, vertebral cartilages buckle inwards and become malformed. In turn, the *spatzle* mutant (named after the kinked pasta form), that fails to form notochord vacuoles, is shortened on the anteroposterior axis, and has a highly kinked and twisted vertebral column (Bagwell et al., 2020).

An interesting variation in principles of vacuolation can be found in ascidians of the genus *Ciona*. Rather than vacuoles, the *Ciona* notochord becomes punctuated with *inter-cellular* inclusions after convergent extension (*Fig. 4.3b*) (Jiang and Smith, 2007; Miyamoto and Crowther, 1985). These inclusions are initially spherical in shape, and are depressed into the anterior and posterior surfaces of notochord cells. However, over time, they expand

towards the notochord circumference and become lenticular in shape, in turn conferring the adjacent cells biconcave morphologies. As they mature, the inclusions rotate to adopt a zig-zag topology along the anteroposterior axis. Eventually, adjacent inclusions fuse, and notochord cells are displaced laterally towards the notochord circumference where they adopt an endothelial-like organisation (Jiang and Smith, 2007). This has been shown to depend on biconcave notochord cells undergoing a mesenchymal-to-epithelial transition and active bidirectional spreading across the anteroposterior axis within the notochord wall (Dong et al., 2009). The notochord therefore develops a luminal structure, composed of a cellular sheath surrounding a fluid-filled lumen. While lumen formation coincides with a 3-fold increase in notochord length post-convergent extension (Jiang and Smith, 2007; Veeman and Smith, 2013), its causality in axial elongation has not been tested. Nonetheless, each inclusion swells to approximately the size of a notochord cell prior to their fusion, and this volumetric change must be accommodated by either one in notochord length or cross-sectional area. Given the ongoing narrowing of the notochord during post-convergent extension elongation, it is plausible that fluid regulation in the ascidian notochord has a similar role to that in the zebrafish and *X. laevis* notochord in contributing to axis extension (Jiang and Smith, 2007; Veeman and Smith, 2013).

4. 1. 6 Knowns and unknowns in amphioxus notochord morphogenesis

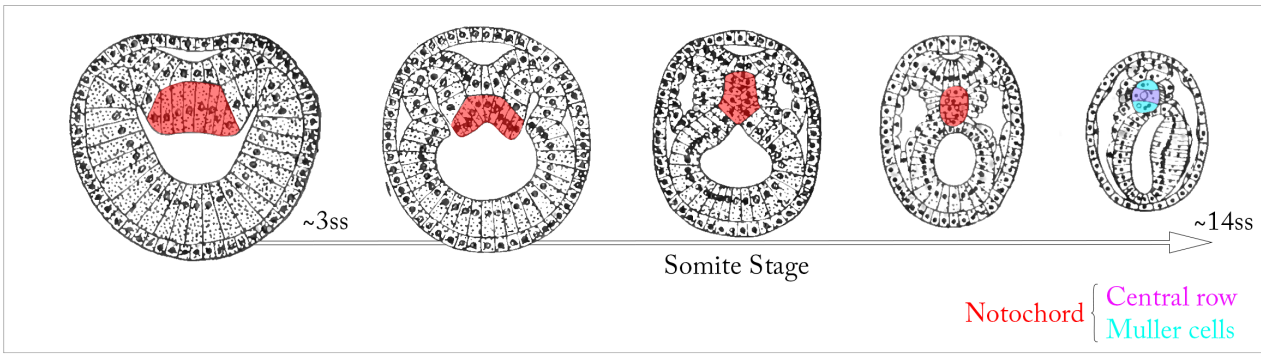
The existing literature on amphioxus notochord development highlights several commonalities with vertebrates and ascidians. Similar to other chordates, the amphioxus notochord derives from a longitudinal evagination of the archenteron roof (*Fig. 4.4a*). This was first identified by light microscopists (Kowalevsky, 1868; Hatschek, 1894; Cerfontaine, 1906), and has since been confirmed by more detailed histological studies (Stach, 1999). During evagination, Conklin (1932) reported a reduction in the number of rows of notochord cells on the mediolateral axis, which accompanies a narrowing and elongation of the overall tissue (*Fig. 4.4b*). Eventually, he described the interdigitation of cells across the midline, thereby resolving a single row of notochord progenitors. This scheme is supported by Hatschek's description (1894) that notochord cells 'grow out over the midline' and 'at last pass over the whole transverse diameter of the notochord', thereby giving rise to 'a many layered dorsal thickening of the archenteron' (*Fig. 4.4a*). Through a poorly-

characterised process, most authors have described the emergence of a trilaminar cell topology in the notochord (*Fig. 4.4a, ~14ss*). This consists of a central row of flattened cells in a ‘stack-of-coins’ topology (*see Fig. 4.4b ~8-9ss*), flanked by two rows of Müller cells lying dorsally and ventrally (Leuckart & Pagenstecher, 1858; Hatschek, 1894; Stach, 1999). The exception is Kowalevsky (1868), who described the fusion of adjacent notochord progenitors to establish a continuous syncytium. All reports since, and the imaging data presented in **Chapter III**, support Hatschek’s statement that ‘Kowalevsky’s account of the histological alterations of the notochord must be regarded as incorrect’.

Having resolved into its trilaminar topology, a host of cellular processes have been attributed to notochord elongation. The most widely supported is formation of intracellular vacuoles in the central notochord layer. Hatschek described the growth of large vacuoles through the coalescence of many smaller vacuoles, and their flattening along the anteroposterior axis, but did not link their emergence to tissue shape change (Hatschek, 1893). In contrast, Conklin associated vacuolation with cell swelling, and implied an increase in tissue rigidity through enrichment of the ‘supporting substance’ (Conklin, 1932). In separate reports, an extracellular matrix sheath has also been described forming around the notochord rudiment, composed of a basal lamina, circumferential collagen fibres, and longitudinal collagen fibres in a concentric organisation (Annona et al., 2015; Bočina and Saraga-Babić, 2006; Flood, 1975). Both Hatschek and Conklin proposed a contribution of cell division and growth to ongoing notochord elongation, although neither is measured or functionally assessed in either account. This has, mistakenly, been interpreted as the sole mechanism of elongation by some authors (Lu et al., 2019). Little attention has been given to changes in notochord shape during elongation, aside from a recent dismissal of convergent extension by Yasuoka (2020). This also seems to rest on a misinterpretation of Hatschek (1893) and Conklin (1932), both of whom report changes in cell topology reminiscent of intercalation in their descriptions. In sum, putative roles for cell growth and cell division have been posed in amphioxus notochord elongation, but without significant descriptive or experimental foundation.

Some descriptions of amphioxus notochord development also expose temporal variation across the anteroposterior axis. This is most extensively discussed by Hatschek,

a. Notochord evagination (~3ss - 14ss) - Hatschek, 1893



b. Notochord intercalation (~2ss - 9ss) - Conklin, 1932

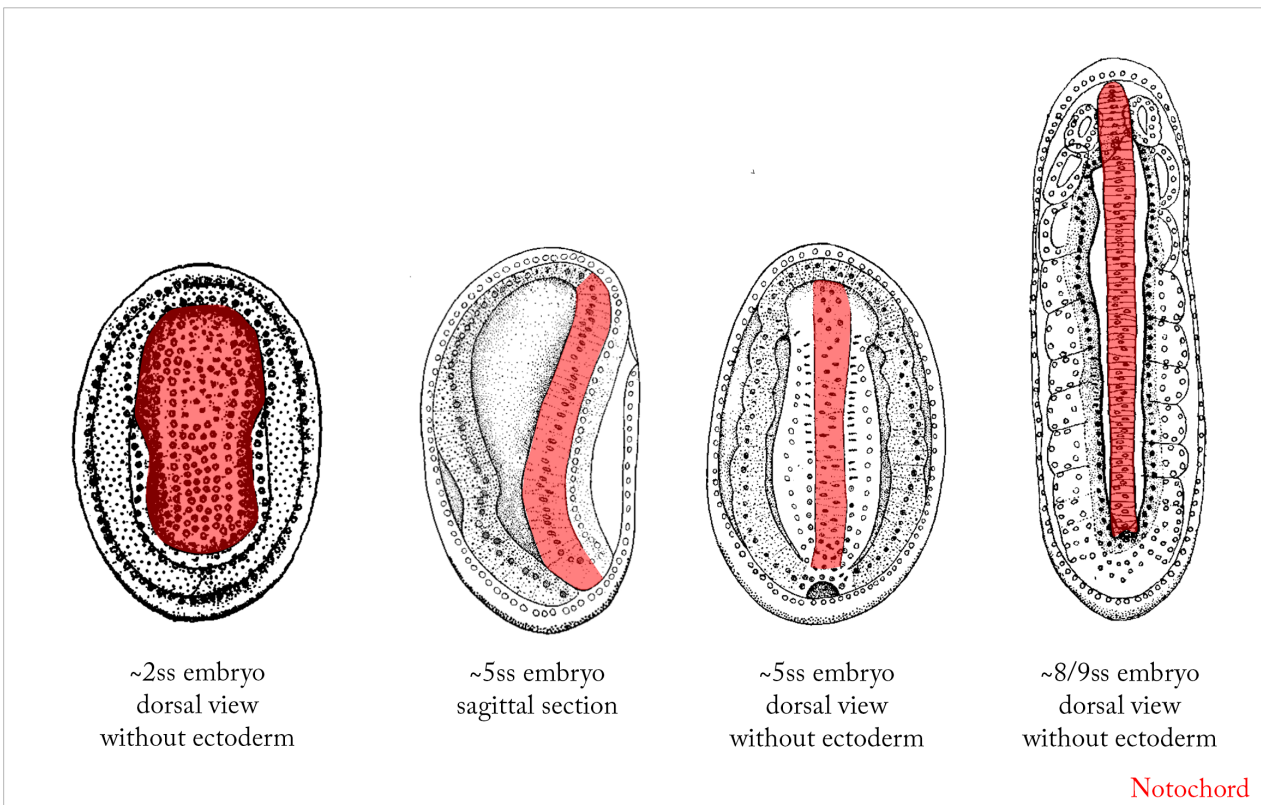


Figure. 4.4. Amphioxus notochord formation according to Hatschek and Conklin. (a) Sketches of amphioxus embryos of successive stages between approximately 3ss and 14ss, shown in transverse section. The notochord rudiment is highlighted in red. Over time, the notochord evaginates from the archenteron roof, and its cells intercalate across the axial midline. Eventually a trilaminar topology is resolved, with a central layer flanked dorsally and ventrally by Müller cells. Sketches are from Hatschek, 1893. (b) Sketches of the amphioxus notochordal plate as it narrows and elongates. An initially broad field of cells narrows to a single-file row in a stack-of-coins organisation. The section shown for the final stage in (b) transects the central layer of notochord cells, the Müller cells are not shown. Sketches are from Conklin, 1932.

who identified an anterior to posterior progression in tissue maturation, ‘very sharply stamped upon the notochord’. This he noted in each of the processes he described, including evagination, formation of a trilaminar cell topology, and the formation of intracellular vacuoles (Hatschek, 1893). Stach (1999) went a step further in also noting an anterior-to-posterior depletion of intracellular yolk granules. Interestingly, Hatschek was the first to note a temporal delay in the formation of the anterior notochord. He observed that this region undergoes a delayed evagination, and then the subsequent maturation steps are exercised ‘from back to front’. More recent studies have highlighted differential gene expression dynamics in the most anterior notochord, which may align with temporal variations in morphogenesis (Albuixech-Crespo et al, 2017). Collectively, the available literature on amphioxus notochord development exposes some similarities with other chordates, but summates as an incomplete and low-resolution description of the process that is inhibitory to robust comparison of cellular dynamics.

4. 1. 7 Specific aims of this chapter

With a strong literature on notochord morphogenesis in vertebrate and ascidian notochord development, and a scarcity of information in amphioxus that is inhibitory to robust comparisons, my aims for this chapter resolved as follows:

- I. To define transitions in cell shape and topology occurring during amphioxus notochord development.
- II. To establish a quantitative framework to holistically map patterns of cell shape changes in a whole developing tissue, and facilitate comparisons of developmental dynamics within and between tissues and species.
- III. To compare the timing and nature of cell shape transitions across the anteroposterior axis of the notochord.
- IV. To predict the relative contributions of specific geometric transitions to global cell morphology using mathematical simulations.

4.2 Collection and visualisation of notochord cell shape data

4.2.1 Cell segmentation approaches

To build a complete picture of the transitions in cell shape and topology underpinning amphioxus notochord development, I first assembled a notochord cell shape database. The first step was image segmentation - the translation of 3D shapes in raw imaging Z-stacks to a form can be computationally processed. For this study, I used rhodamine phalloidin to label the F-actin network, in line with similar investigations in ascidian embryos (Munro and Odell, 2002; Veeman and Smith, 2013). In most amphioxus tissues, staining was weak and diffuse, but it strongly and specifically marked the cortex in notochord cells, thereby delineating cell outlines, as illustrated in **Chapter III** (*Fig. 3.5*). I next trialled a diversity of published computational pipelines for cell segmentation, the extent of which will not be discussed here (for a succinct review see Bodor et al., 2020). A simple approach is image thresholding, in which voxels with values above a user-defined intensity are considered part of, or not part of, a cell (Burger and Burge., 2010). However, when trialled in ImageJ, I found both traditional and adaptive thresholding to be insufficient for segmentation of densely-packed cells (*data not shown*). Another method I tested was machine learning for cell outline detection, for instance using the Ilastik BoundaryCut function (Berg et al., 2019). Despite success with Ilastik for nuclear segmentation (**Chapter V**), it failed to resolve single cells even when trained exhaustively on phalloidin signal (*data not shown*). Of all of the methods tested, LimeSeg was the most promising (Machado et al., 2018). LimeSeg functions by expanding a seed placed in the centre of the cell, whose growth is blocked by surrounding boundary signal. As a result, it comes to fill the contained space. While LimeSeg was promising in capturing the shapes of early notochord progenitors, it failed to capture the detail of more irregular shapes appearing at later developmental stages. This was especially the case when cells were very anisotropic in shape (*data not shown*).

Given the insufficiency of available automated approaches to faithfully segment amphioxus notochord cells stained with rhodamine phalloidin, I ultimately opted for manual approach using the surfaces function in Imaris (Bitplane, 9.2.1). Here, 2D splines

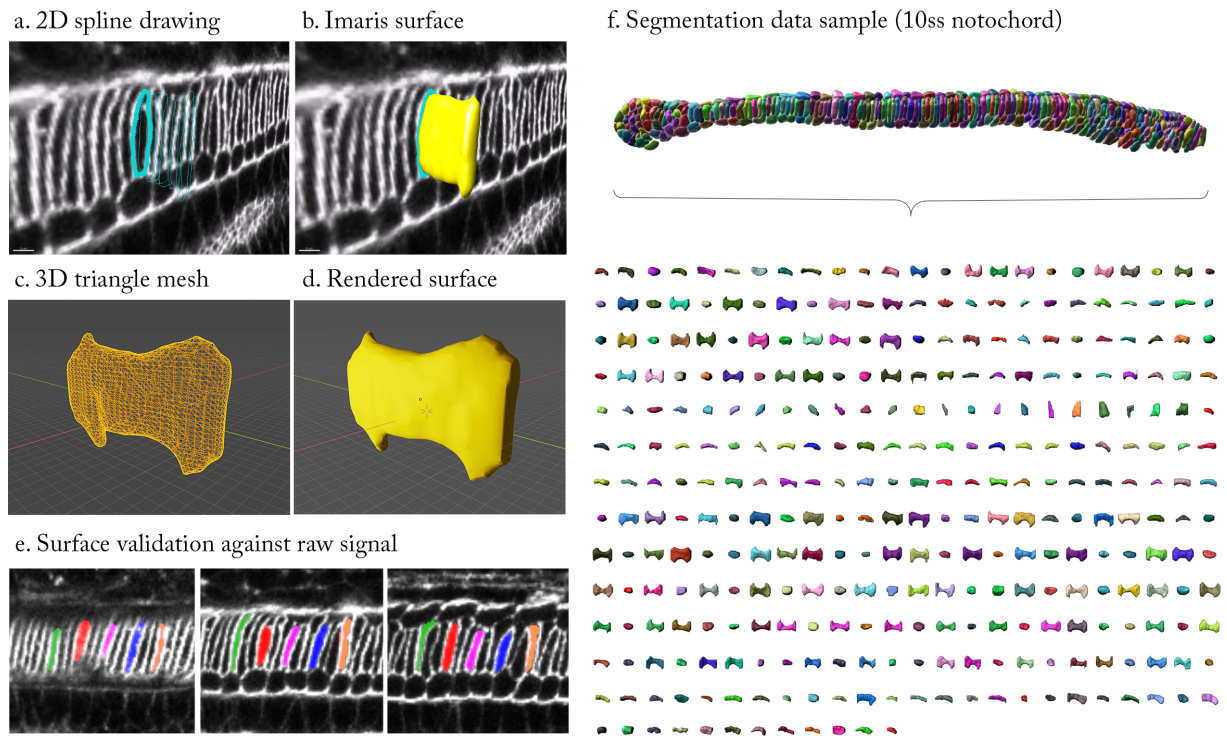


Figure. 4.5. **Manual segmentation of amphioxus notochord cells.** (a) Raw phalloidin staining in the amphioxus notochord, viewed in a single sagittal slice. Cyan lines show a series of 2D contours drawn on successive Z slices. (b) 2D contours in (a) now assembled into a 3D mesh, lying within the surrounding phalloidin signal. (c, d) A single cell isolated from the central part of the notochord, shown either as a triangle mesh (c) (used for shape quantification), or a smoothed rendered surface (d) (used for qualitative analysis). (e) Surfaces were validated by false-colouring the volume and comparing the distribution in parasagittal sections with the raw phalloidin signal. (f) A 10ss notochord with all cells manually segmented and randomly coloured, both intact (top) and collapsed into constituent cells (bottom) each shown in an anterior view. All segmentation was performed in Imaris, and ongoing analysis was performed in Imaris and Blender.

with $0.5\mu\text{m}$ point spacing were drawn around individual cells every 2 slices ($\sim 1.5\mu\text{m}$) on parasagittal planes, and these were subsequently assembled into 3D triangle meshes (*Fig. 4.5a – d*). In each embryo, I validated a sample of the segmented cells by false colouring their contents and studying 2D sections to ensure a faithful fit to the surrounding phalloidin signal (*Fig. 4.5e*). Manual segmentation was performed for groups of approximately 35 neighbouring cells at different positions along the anteroposterior axis at each stage of analysis, such that single-cell morphology could be aligned with multi-cellular topology at

later stages of analysis. *Fig. 4.5f* shows a sample notochord from 10ss, in which all cells across the anteroposterior axis have been manually segmented, and its dispersal into a diversity of single-cell morphologies. In total, 3,796 cells were segmented, from 15 notochords, at five developmental stages between 6ss and 14ss (raw data shown in *Fig. 3.5a*). This dataset represents a comprehensive catalogue of cell shapes populating in the amphioxus notochord, that spans physical space and developmental time.

In order to identify patterns of geometric variation within this large dataset, the next challenge was shape quantification. The first approach I explored for shape quantification was simple linear measurements of cell geometry, based on the dimensions of object-oriented bounding boxes. Bounding boxes were constructed in Imaris based on the length and orientation of the cell's long axis, which is used to register an orthogonal coordinate system (*Fig. 4.6a*). While this object-oriented methodology does not take into account the major orthogonal axes of the embryo (unlike the alternative axis-oriented approach), the resulting bounding boxes typically aligned strongly with the embryonic axes. This meant that, at each stage, the primary axes of the cell could be translated into the AP/ML/DV axes of the embryo at large (*Fig. 4.6b*). Shape changes could now be quantified over time by analysing transitions in length along each of the major embryonic axes. At this stage of optimisation, I focussed specifically on the central, most conserved, layer of notochord cells at the 40-60% level of the anteroposterior axis. In this sample, cell ML length increased to its maximum value between 6ss and 8ss. Meanwhile, cells also underwent increased in DV length over a more extended period between 6ss and 10ss. Together, these transitions capture a progressive spreading of cells across the notochord cross-section. After 10ss, ML length subsequently narrows, while DV length continues to increase at a much lower rate. Coupled to this nature of shape description, morphometric quantities can also be mapped onto groups of segmented cells as a heatmap for visualisation of individual geometric transformations at play during global shape changes (*Fig. 4.6c, d*).

4. 2. 2 Morphospacial embedding of notochord cell shape data

Through the collective analysis of cell length change along the major embryonic axes, we can build a crude mental picture of cell shape change in terms of stepwise

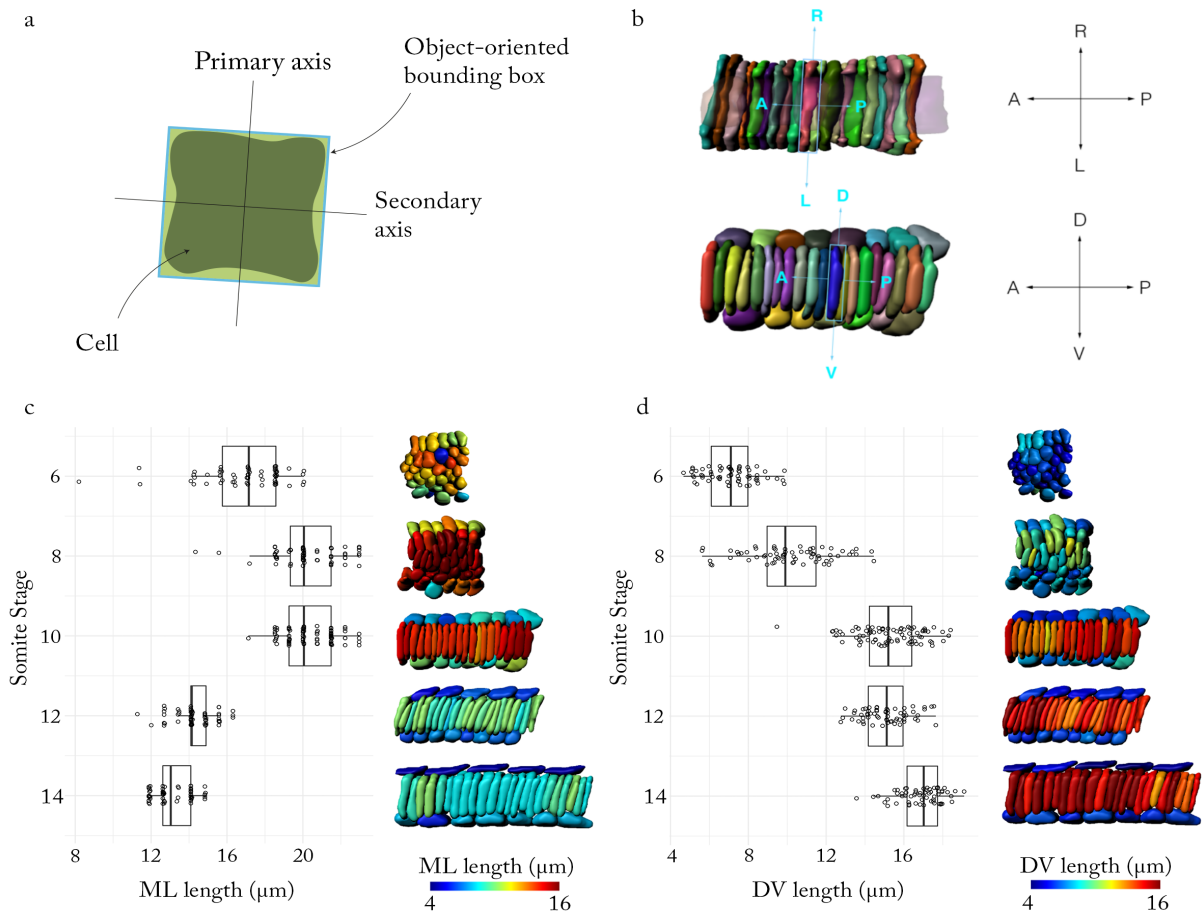


Fig. 4.6. **Simple shape metrics derived from the object-oriented bounding box.** (a) Object-oriented bounding boxes are constructed based on the major axes of the cell. (b) These axes closely aligned with the major orthogonal axes of the embryo, which were used to describe each bounding-box vector. (c) Change in mediolateral cell length over time, shown in a boxplot (left) and heatmap onto groups of sampled cells (right). (d) Change in dorsoventral cell length over time, shown in a boxplot (left) and heatmap onto groups of sampled cells (right). All analysis performed for notochord cells in the 40-60% levels of the anteroposterior axis, in the central layer across the dorsoventral axis. $n = 344$.

transformations applied to a regular cuboid. However, this rationale suffers from a number of major pitfalls, the most significant being a lack of resolution. Cells are not perfect cuboids, and so reducing their shapes to three orthogonal dimensions is highly reductionist of their true shape complexity. In turn, we need to consider other dimensions of cell shape variation, which can be quantified through an expanding list of standard geometric properties. What follows is an integration problem; while we can readily study the dynamics of change in isolated shape variables, it becomes increasingly challenging to draw these

dynamics together into a holistic representation that can be readily communicated, applied for causative explanations of morphogenesis, and compared rigorously between systems. To overcome this problem, I took inspiration from the concept of morphospace, which is a commonplace framework for shape analysis in comparative anatomy (Chartier et al., 2017; Mitteroecker and Huttegger, 2009; Polly and Motz, 2016).

Morphospace can be conceptualised as a theoretical coordinate system, whose axes represent distinct vectors of shape variation used to parameterise the object (Mitteroecker and Huttegger, 2009). Within this framework, the shape of an object is reflected by its 'position' along each axis. A beautiful example is the morphospace for the coiled shell, composed by Raup (1965), in which shells cluster into known phylogenetic categories based on quantitative shape variation, parameterised by that in expansion rate, translation rate and coiling radius. In principle, a morphospace locates all possible variations on a given form (the resolution of which depends on that of the parameterisation), the portion represented by natural variation, and that which has not been, or cannot be, occupied. In morphospace, short distances between specimens reflect morphological similarity, whereas large distances represent disparity. As a result, the construction of morphospaces can be used to cluster forms into distinct groups, as is the case for the coiled shell morphospace (Raup, 1965), and also to expose specific transitions in form over developmental and evolutionary timescales. For example, morphospacial embedding has been elegantly used to show the release of morphological constraint in domesticated dogs, enabling exploration of previously inaccessible regions of morphospace in wild populations (Drake and Klingenberg, 2010). It has also been used to locate an overlap between modern avian skulls and early stages of dinosaur skull development, thereby implicating a role for paedomorphosis in reptilian craniofacial evolution (Bhullar et al., 2012).

With these anatomical studies as inspiration, I sought to use morphospacial embedding to capture and compare patterns of cell shape differentiation during notochord development. Perhaps, I hypothesised, cells from a developing tissue would assemble into streams of shape differentiation when embedded in morphospace, connecting progenitors to different terminal forms. Different cell shapes would be resolved through branching events, and pursue trajectories to unique terminal positions. Others might converge on

similar forms through unique paths. These paths could be continuous or punctuated, reflecting the temporal dynamics of shape change. In a sense, such a representation of morphogenesis would be analogous to a phase portrait in gene regulatory network modelling (e.g. Verd et al., 2018), in which the system converges on one or more ‘attractor’ states given a particular set of starting conditions. In considering morphology, we can then ask, what steers cells to particular attractors? Which paths through morphospace are possible or impossible, and what makes one set of morphological outcomes more likely than another? We can then spatially map this portrait of morphogenesis into the embryo to resolve patterns in processes that might superficially appear chaotic, and locate where and when cells are initiating specific programmes of shape differentiation. With tissue morphogenesis abstracted into morphospace, there is then the potential to ask how processes generating common forms varies between species when overlaid, and therefore infer where evolution has acted on development to generate novelty. With this as a long-term goal, I sought to construct a simple morphospace for amphioxus notochord cells.

In Geometric Morphometrics, ‘shape’ is defined as residual variation in form after the removal of that in position, size and rotation (Klingenberg, 2020).¹ The process of isolating shape variation is termed a ‘Procrustes superimposition’, which is applied after the identification of common landmarks in specimens for comparison. In my first attempt to devise a morphospace for amphioxus notochord cells, I followed the logic of the Procrustes superimposition by defining its axes as the relative lengths of each linear dimension on AP, ML and DV planes. This method captures shape variation when cells are simplified as regular cuboids, as discussed previously, whilst discarding information on position, orientation and true size. Despite the very simple terms of this morphospace, I found cells to disperse in a structured arc-like pattern (*Fig. 4.7a - c*). This arc was composed of groups of cells isolated from adjacent developmental stages, now merging together into a continuous stream across morphospace. According to this sequence, cells first decrease in their AP/DV and AP/ML anisotropy. They then increase their DV/ML anisotropy, and

¹ ‘Geometric Morphometrics’ specifically refers to the discipline of shape comparison using landmark analysis and Procrustes superimposition. In this case, pair-wise ‘Procrustes distances’ are calculated between all objects, based on the residual variation in landmark distribution following Procrustes superimposition. These differences define the topology of objects in morphospace, independent of any user-defined axes. Morphospace is then visualised in low dimensional space by applying principal component analysis to the dataset, which identifies axes of greatest variation between objects that can in turn be used to define a printable xyz coordinate system.

restore their AP/DV and AP/ML anisotropy (*Fig. 4.7a – c*). In other words, they spread on the transverse plane at the expense of their length, and then increase in DV height at the expense of their width. The sequential bursts of ML and DV spreading identified previously can now be illustrated in the form of a heat map along this arc of shape differentiation, revealing them as sequential processes within a complex continuum of shape change along the three defined axes (*Fig. 4.7d, e*). Such ordering of cells through morphospace can be considered a population-scale ‘trajectory’ of shape change – a morphogenetic route from progenitors to differentiated cell types. Here, we can also observe that cells from each developmental stage disperse across the trajectory, and those from successive stages partially overlap. On these terms, we can therefore infer variation in developmental maturity on the scale of individual cells; some cells are precocious in their development and therefore overlap with those from the following stage, while others are atypically slow and therefore overlap with those of the preceding stage.

4. 2. 3 Geometric parameterisation and morphospacial embedding

Having tested the basic principles of morphospacial embedding and trajectory construction, I next sought to increase the resolution of the analysis by including a higher number of geometric parameters. This list came to include; surface area, volume, 3D long axis orientation, transverse cross-sectional area, cell spreading area, smoothness (number of triangles), oriented anisotropy, cuboidness (deviation from a perfect cuboid), sphericity (deviation from a perfect sphere), flatness, and nuclear displacement from the centre of homogenous mass. Note here that size and orientation have now been reintroduced into the analysis. Unlike most geometric morphometric analyses that consider variation between isolated objects that are removed from their native context, for cells in a developing tissue orientation and position are critical elements of morphological variation. In addition, growth is known to be an important process in vertebrate and ascidian notochord development (Ellis et al., 2013; Lu et al., 2019), and so ultimately I decided to include it as part of the shape analysis. The dataset generated here is a high-dimensional description of cell morphology. To identify major axes of variation through it, which could then be employed as dimensions for morphospace construction, I next performed a principal component analysis (PCA). PCA revealed that 86.2% of cell shape variability was explained

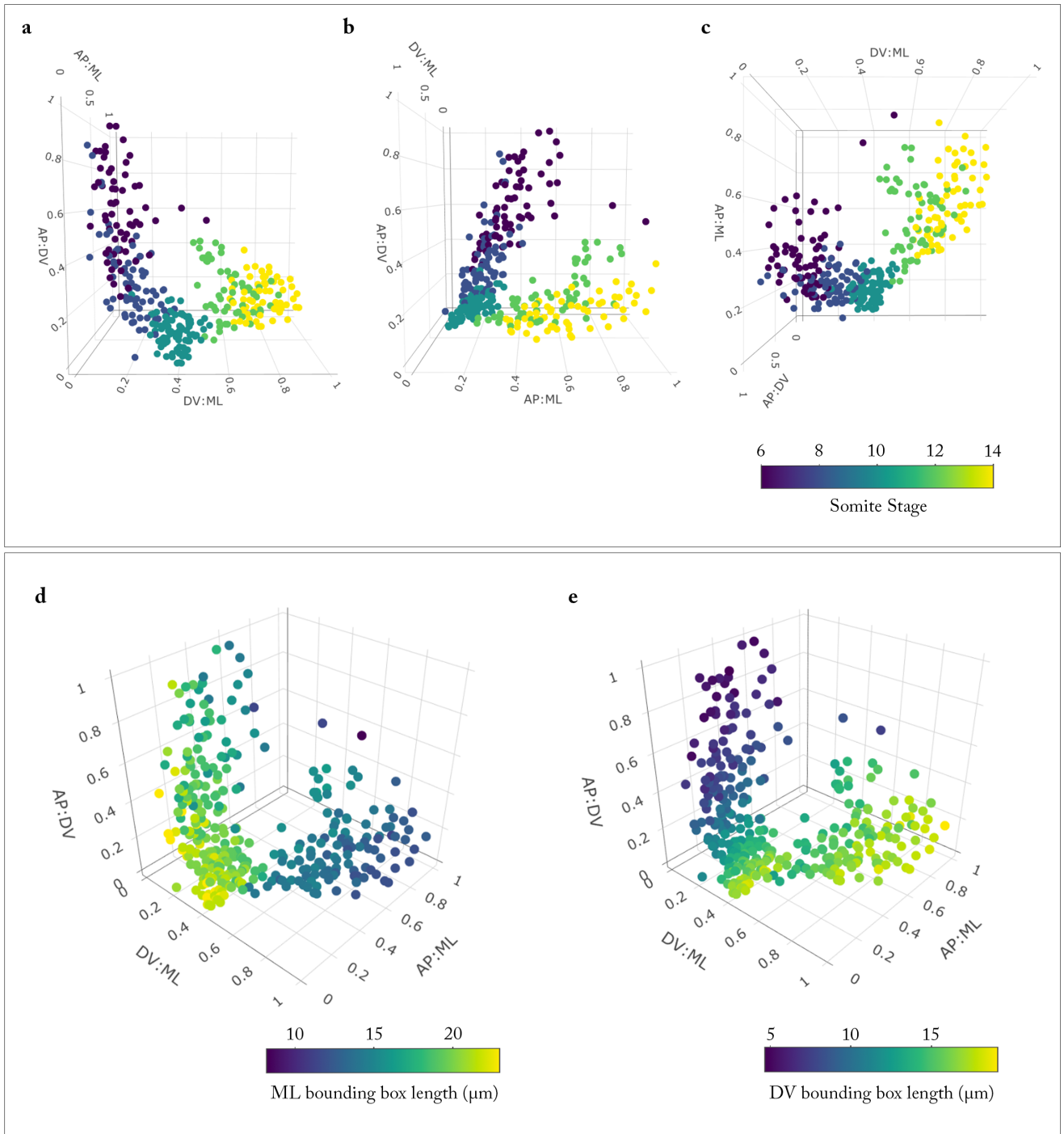


Figure 4.7. A simple morphospace for notochord cell bounding boxes. (a-c) Central layer cells from the 40–60% AP level of the notochord projected into morphospace defined by AP:DV, AP:ML and DV:ML ratios, projected in pseudo-2D in orthogonal views. Colour code reflects somite stage from 6ss to 14ss, spanning notochord elongation. Note that cells from each stage exhibit semi-overlapping regions of morphospace. (d-e) Same projection from (a-c), now colour coded for (d) ML elongation and (e) DV elongation, revealing sequential elongation phases during cell shape differentiation. All plots constructed using *Plotly* in R. $n = 344$.

by 5 eigenvectors, corresponding to distinct aspects of shape variance (*Fig. S1a*); anisotropic elongation along the AP axis (PC1, 36.7% variation; *Fig. S1c*), transverse elongation and orientation (PC2, 20.9% variation; *Fig. S1d*), volume and surface smoothness (PC3, 14.1% variation; *Fig. S1e*), surface convolution (PC4, 9.7% variation; *Fig. S1f*), and nuclear displacement from the centre of homogenous mass (PC5, 4.8% variation; *Fig. S1g*) (*Fig. 4.8a, S1*). These components offered a framework to visualise the topology of geometric variation in a low-dimensional space, analogous to the previous much simpler trajectory analysis.

I next plotted cells against the first three PCs to embed them in a developmental morphospace (*Fig. 4.8b*). In this framework, notochord cells organised in a continuous and highly-structured branching pattern. This consisted of three primary branches that link the seemingly disparate morphologies emerging during morphogenesis (*Fig. 4.8b*). This pattern was highly reproducible across the three embryos analysed per stage, which indicated that most variance in morphospace occupancy were due to temporal variation between stages, rather than stochastic variation between individuals of the same stage (*Fig. S2*). To ask how cells traverse morphospace during their development, I next subdivided the data by developmental stage. At 6ss, all cells occupied the central branch, exhibiting tall DV-elongated morphologies (*Fig. 4.8c, 6ss*). Over time, these morphologies were lost, and cells ‘flowed’ from the central branch into a bifurcation event at the base of the plot, which resolves two distinct streams of morphological differentiation (*Fig. 4.8c, asterix*). Although cells from older specimens populated more distal positions in morphospace with respect to the bifurcation event, a continuum persisted at each stage between immature and differentiated states (*Fig. 4.8c*). In other words, cells do not all undergo the same transitions at the same time, and therefore cells in all maturation states up to the most mature are present somewhere in the notochord at each stage. By categorising cells based on relative DV position, along which distinct cell types are known to emerge, I found the bifurcation event to yield independent trajectories for the central cells and Müller cells (*Fig. 4.8c*). While the Müller cells elongate along the AP axis at the expense of their transverse cross-sectional area (decreasing on PC1), the central cells spread out on a transverse plane at the expense of their length (increasing on PC1). The Müller cell stream was further subdivided for the dorsal and ventral rows, based on distinctive levels of AP anisotropy. Overall, this

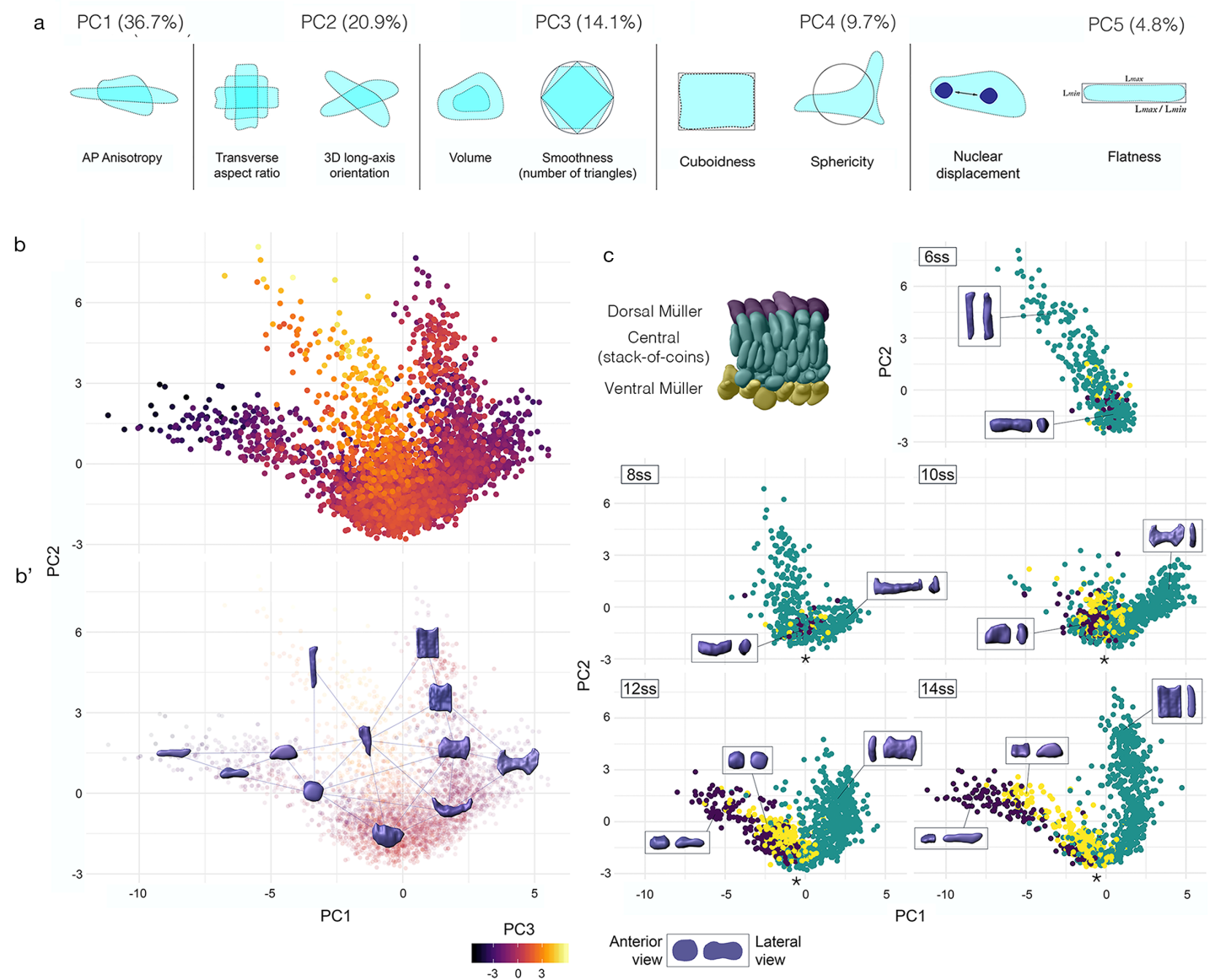


Figure 4.8. A single-cell morphospace captures notochord cell shape diversity. (a) Major geometric correlates of the first five principal components. (b) Notochord cells from all stages and positions projected into morphospace with colour code for PC3. (b') Notochord morphospace illustrated with representative surfaces from segmentation data. (c) Morphospace filtered by developmental stage and colour-coded for position along the DV axis, where Müller and stack-of-coins cell types become resolved. Representative cells for each domain shown in inlays, in anterior (left) and lateral (right) views. 3,796 individually-segmented cells, 5 stages, 3 embryos per stage.

approach flattened notochord morphogenesis into a 2D map of cell state diversity (*Fig. 4.8b*). Therein, there is a progressive exploration of cell shape space, in which a common progenitor is remodelled along diverging shape trajectories to generate a diversity of spatially organised terminal states.

4. 3 Morphospace exploration

4. 3. 1 Single-cell morphometrics highlights two major shape transitions in central notochord cells

From this global view of shape differentiation, I next sought to refine a single shape trajectory for notochord cells by isolating those from a specific position along the anteroposterior axis and mapping their changing distribution in morphospace over time (*Fig. 4.9a*). Collectively, I found central layer cells from the 40-60% level of the anteroposterior axis to disperse in a continuous stream across morphospace. This is illustrated by a partial overlap of the point clouds for cells derived from embryos of successive somite stages, suggesting that cells from each stage are heterogenous in their extent of shape differentiation (*Fig. 4.9a*). I next used the trajectory inference method, Slingshot, to order cells along a pseudotemporal axis (Street et al., 2020).² This identifies one or more principal curves in through dimensionally-reduced data, reflecting putative differentiation trajectories. I applied trajectory inference in a semi-supervised manner, guided by prior information on temporal transitions from somite stages, which I used as a clustering input to construct the minimum spanning tree. The inferred pseudotemporal axis passed through the point clouds for each somite stage in correct temporal sequence, and fit closely to their mean PC coordinates (*Fig. 4.9a*, compare blue and black lines). By plotting the frequency of cells across pseudotime for each somite stage, I found cell shape transitions to be tightly controlled across developmental time, as measured by somite stage (*Fig. 4.9b*). Furthermore, I identified a strong positive correlation between pseudotime and somite stage (Pearson correlation = 0.94), showing that pseudotime is linearly related to developmental time (*Fig. 4.9c*). This validated the inferred pseudotemporal axis as a vector for expressing both the directionality and temporal progression of cell shape changes through morphospace.

Having validated the inferred 40-60% central cell trajectory, I next asked how cell shape varies across it. I examined this both qualitatively, by selecting cells from evenly-

² Advised by Wolfram Pönisch (Department of Physiology, Development and Neuroscience, University of Cambridge)

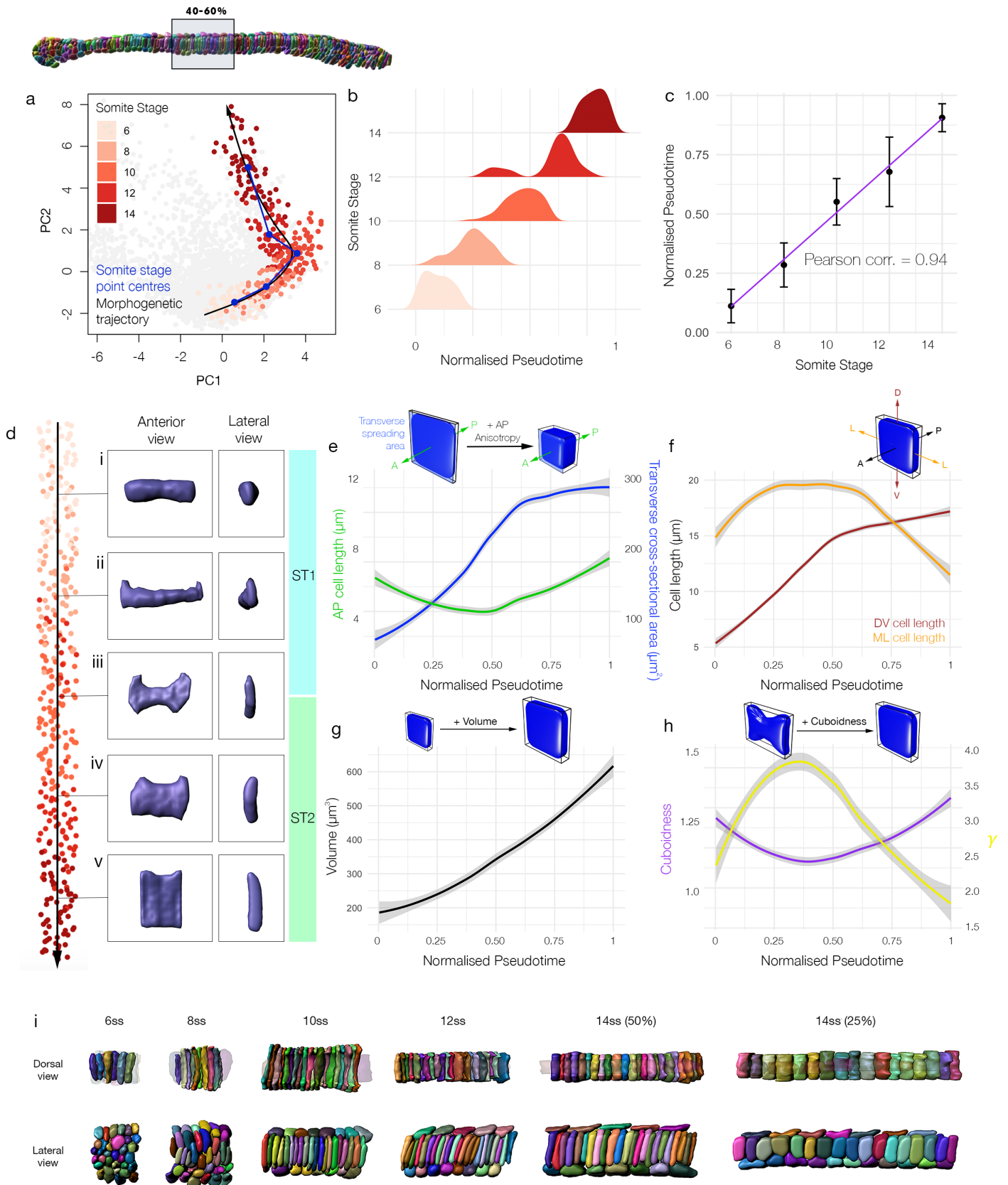


Figure. 4.9. The 40-60% central notochord cell shape trajectory. (a) Notochord cells from the central layer at the 40-60% level of the AP axis projected into morphospace, coloured by somite stage. Blue segmented line connects point cloud centres for each stage, black curve defines the inferred Slingshot trajectory. (b) Density plots showing frequency of cells across pseudotime for each somite stage. (continued overleaf)

spaced intervals across pseudotime, that represent shapes acquired sequentially along the trajectory (*Fig. 4.9d*), and quantitatively, by analysing changes in the major correlates of each principal component (*Fig. 4.9e - h*). Together, the results presented highlight two major shape transitions that occur sequentially in central notochord cells, reflected by two sequential ‘movements’ of different directionality through morphospace:

In the first major shape transition (‘ST1’, 6ss – 10ss), cells transition from a ML-elongated morphology that is rounded in lateral view, to a flattened morphology spread across the transverse plane, with distinct flared margins, similar in shape to a bowtie (*Fig. 4.9di - diii*). In this process, notochord cells decline in AP-oriented anisotropy (anti-correlated with PC1; *Fig. 4.9e, S1b, S3f*), accounted for by an increase in traverse cross-sectional area at the expense of AP length (*Fig. 4.9e*). In parallel, the transverse shape of each cell changes, with an increase in DV:ML ratio (positively correlated with PC2, *Fig. 4.9a, f, S3l*). Cells elongate on both the ML and DV axes during this period, but the earlier plateauing of ML length at 8ss leads to an anisotropic elongation along the DV axis (*Fig. 4.9f*). During the first transition, I also measured an increase in volume (anti-correlated with PC3, *Fig. 4.9g, S1c*), and a decline in cuboidness, which reflects how faithfully the cell fits its object-oriented bounding box (anti-correlated with PC4, *Fig. 4.9h*). This means that the total spreading area of the cell is increased beyond its cross-sectional area through

Figure. 4.9. (*continued*). (c) Mean pseudotime distance for cells of each somite stage, +/- standard deviation. Blue line shows a linear regression, with a Pearson correlation coefficient of 0.94. (d) All 40-60% central layer notochord cells ordered across the inferred trajectory from (a). Segmented cells sampled from each marked position are shown in anterior and lateral view. The two major transitions of cell shape observed are indicated as ST1 and ST2 \pm 1 standard error. (e – h) Changes in specific geometric parameters along the 40-60% central cell trajectory. (e) PC1 is anti-correlated with AP anisotropy, derived from transitions in cell AP length and cross-sectional area. (f) PC2 is positively correlated with DV:ML aspect ratio, influenced by transitions in DV and ML cell length, inferred from bounding box dimensions. (g) PC3 is anti-correlated with cell volume. (h) PC4 is positively correlated with cell surface convolution, quantified here by cuboidness. This affects the discrepancy between cell and bounding box cross-sectional area, which we quantify as γ . (i) Segmented cells from the 40-60% level, shown in dorsal and lateral views across somite stages. In dorsal view, the Müller cells are transparent, enabling visualisation of the central layer. In lateral view, both the central and Müller cells are shown. $n = 344$ cells for 40-60% level central layer cells, $n = 360$ for 25 – 40% cells.

convolution of its surface, which I quantified in a scaling factor, γ (Fig. 4.9b; see Appendix III). When cuboidness reaches its minimum value at 10ss, γ reaches its maximum value (Fig. 4.9b). Collectively, these geometric transitions describe formation of a bowtie morphology at 10ss, which occupies a distinct domain in morphospace that I term the ‘bowtie domain’ (Fig. 4.9a, diii).

During the second major shape transition (‘ST2’, 10ss – 14ss), cells lose their bowtie morphology, and acquire tall cuboidal shapes (Fig. 4.9diii – dvi). Underlying these global changes, AP-oriented anisotropy increases, in this case involving an increase in AP length without further change in cross-sectional area (Fig. 4.9e, S3f). Meanwhile, DV:ML ratio continues to increase due to a further slow increase in DV length, coupled to an almost 2-fold decline of ML length (Fig. 4.9f, S3l). Volume continues to increase during the second major transition (Fig. 4.9g). However, cuboidness and sphericity now increase, thereby reflecting a decline in cell surface convolution (Fig. 4.9b, S3g, h). In turn, γ also declined, corresponding to a lesser spread of the cell beyond its transverse cross-sectional area and loss of the bowtie morphology (Fig. 4.9diii – dvi, 2b). In sum, decomposition of the PCs exposed dynamic profiles of AP anisotropy, DV:ML ratio, volumetric growth and surface convolution as the primary geometric transformations underlying both major shape transitions of the central cell trajectory: First, an expansion of transverse cell spreading area at the expense of AP length, enhanced by surface convolution and emergence of a bowtie morphology. Second, collapse of the bowtie morphology and an increase in AP length associated with ongoing cellular growth.

The sequence of cell shape transitions I identified in central notochord cells define a unique trajectory through morphospace (Fig. 4.9a). I next sought to ask how these behaviours correspond to changes in local multicellular organisation. To address this question, I selected neighbourhoods of 35 adjacent cells at the 40 – 60% level, and aligned changes in their organisation with the transitions in cell shape defined above (Fig. 4.9i). At 6ss, all cells were elongated along their ML axes, with bipolar contacts with both the left and right margins of the chordamesoderm (Fig. 4.9i, Dorsal view, 6ss). Because this stage precedes most of notochord AP elongation (see Chapter III Fig. 3.5a, 3.6c), ML intercalation cannot generate further tissue length. However, I noted an increase in the

number of cell layers on the DV axis between 3ss and 6ss, suggesting that early ML intercalation might drive an early convergent thickening (*Fig. 4.9i Lateral view, Fig. 3.5 compare 3ss and 6ss*). During the first shape transition in central cell progenitors (6ss – 10ss), in which they increase their transverse spread and adopt a bowtie morphology, I actually observed a process of intercalation oriented along the DV axis, that reduces the number of cell layers from 6 to 3 (*Fig. 2i, Lateral view, 6ss – 10ss*). This contrast with the prevailing role for mediolateral intercalation in olfactorian notochord elongation. During this DV intercalation, I found that cell neighbourhoods elongated along their AP axis, despite the AP shortening of individual cells (*Fig. 4.9e, 4.9i*). DV intercalation was then followed by a latter phase of neighbourhood elongation in the absence of further cell rearrangement, coinciding with the second major transition in cell shape, in which cells increased in AP length and volume (*Fig. 4.9e, g, i 10 – 14ss*). This latter elongation phase was most pronounced in the pharyngeal region (*Fig. 4.9i, compare 14ss 40 – 60% and 25 – 40%*). In sum, the sequential shape changes of the central cell trajectory aligned with distinct phases of notochord elongation, mediated first by DV cell intercalation, and second by cell elongation.

4.3.2 Geometric modelling reveals a requirement for growth in coupling convergence and extension

By deconstructing notochord development in morphospace, I found AP anisotropic elongation, DV:ML ratio, growth and surface convolution to be the major geometric transformations underpinning central cell shape differentiation (*Fig. 4.9, 4.10a*). What we observe during development is the summed effect of each of these transformations acting together, which leads to a net output of tissue elongation. This includes change in AP anisotropy, which we know has an adverse effect on cell length, and growth acting together. To understand the interplay between these processes, I next set out to investigate the effect of each transformation on AP length when applied individually either to either single cells or groups of cells undergoing intercalation. To this end, we devised a simplified mathematical framework to model the effect of each transformation on a mean cell from the 6-somite stage notochord at the 40 – 60% level (*Appendix III*).³ This cell is defined by

³ In collaboration with Wolfram Pönisch, who helped to formalise the equations for geometric modelling

its AP length $l_{AP}^{(cell)}$, volume $V^{(cell)}$, and cross-sectional area $A^{(cell)}$. Where s denotes stage, AP length can be calculated as

$$l_{AP}^{(cell)}(s) = \frac{V^{(cell)}(s)}{A^{(cell)}(s)}.$$

We could now measure change in cell length when either volume or cross-sectional area is altered independently, with the other fixed at their 6ss value.

As I found previously, central notochord cells in the 40 - 60% region undergo an early phase of shortening on the AP axis linked to intercalation (6-10 somites), followed by a late phase of elongation in which AP length is restored (10-14 somites) (*Fig. 4.10e, 4.10b black line*). We first tested how cell length would change if governed only by AP anisotropy, in the absence of growth. Here, we allowed cell length to change in accordance with measured changes in cross-sectional area, while maintaining the cell at constant volume (*Fig. 4.10b, blue line*). Under these modelled conditions, cross-sectional area increases at the expense of length, such that cells undergo a 2.16-fold shortening between 6ss and 10ss. Thereafter, instead of restoring length, cells continue to shorten, albeit at a lesser rate, by an additional 1.17-fold change. This suggests that transverse cell spreading has a sustained negative effect on length during intercalation. Without prior knowledge of growth dynamics, we envisaged two scenarios for its effect on shape. First, we considered a scenario in which cells maintain their shape at 6ss, and the growth that we measure (*see Fig. 4.9g*) acts isotropically to expand cell geometry proportionally in all directions. In this scenario, cells underwent a progressive increase in length by a total of 1.37-fold, thereby exceeding the 1.02-fold net length change measured in normal development (*Fig. 4.10b, grey line*). This change was more pronounced in a second scenario of anisotropic growth, in which we prevented radial cell expansion and therefore forced growth to act unidirectionally on AP length. In this case, we measured a 2.59-fold elongation (*Fig. 4.10b, orange line*), again far exceeding the real measured change.

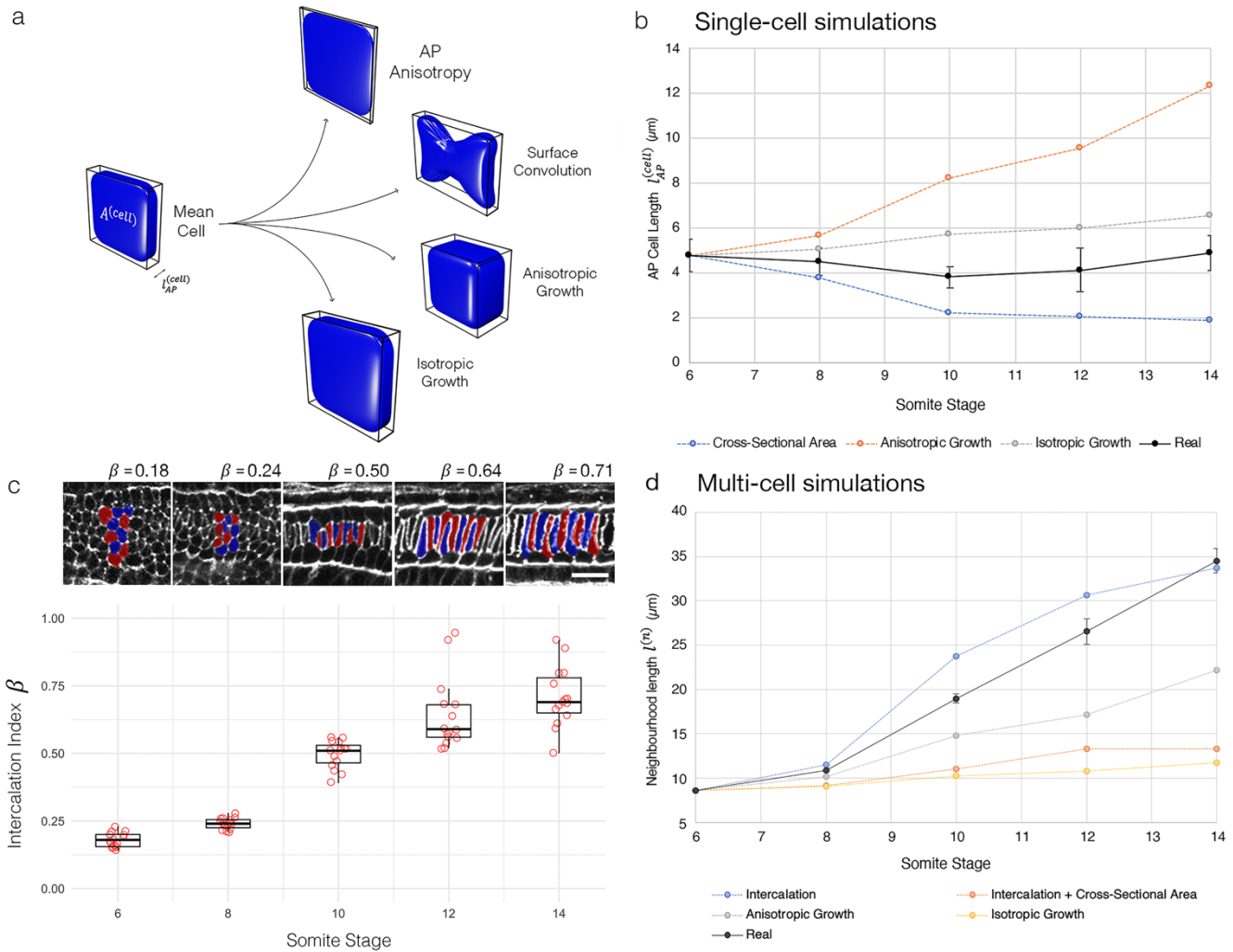


Figure. 4.10. Geometric modelling predicts contributions of shape and size to major transitions of the central cell trajectory (a) Visual renderings of transformations identified in the central cell trajectory. (b) Results of geometric perturbations applied to a mean central cell from the 6-somite stage, over a developmental time course, illustrating predicted change in cell length. Coloured lines represent modelled scenarios, black line represents real measured change ± 1 standard error. (c) Quantification of intercalation index across developmental time, with representative groups of 10 cells per stage. Scale bar shows $20\mu\text{m}$. $n = 15$ neighbourhoods per stage from 3 representative embryos. (d) Predicted change in the length of a neighbourhood of 10 6-somite central cells, integrating changes in both intercalation index and single-cell shape and size. Black line shows real measured length changes, ± 1 standard error.

Collectively, these calculations suggest that transverse cell spreading behaviour and volumetric growth make oppositional contributions to cell AP length, and the real profile of length change is a dynamic balance between the two transformations. We can therefore infer that, up to the 10-somite stage, the rate of transverse cell spreading outweighs that of growth, leading to a net cell shortening during intercalation. When cross-sectional area stabilises at 10ss (*Fig. 4.10e*), growth then dominates to translate a programme of transverse cell spreading into one of elongation.

We next sought to test how this relationship between shape and size in single cells affects the rate of elongation in a group of neighbouring cells undergoing intercalation. We tested this in groups of 10 cells from the 40 - 60% region of the notochord. To investigate the effect of intercalation, we defined an intercalation index, β , which allows calculation of extended AP group length $l^{(n)}$ from cell number n and mean AP cell length $l_{AP}^{(cell)}$ for a given stage (*Fig. 4.10c, Appendix III*);

$$l^{(n)} = n \beta l_{AP}^{(cell)}.$$

For this calculation, we made use of values for $l^{(n)}$ obtained from groups of 10 adjacent cells measured in the embryo at each stage. When $\beta = 1$, group length equates to the summed lengths of all cells, whereas when $\beta < 1$ cells are displaced from the midline and so their individual lengths are not additive in the same plane (*Fig. 4.10c, Appendix III Fig. 2*). We used these metrics to drive intercalation either independently, or in combination with transformations in cell shape and size. First, we tested how intercalation alone contributes to length by applying experimentally obtained intercalation index values (β values, *Fig. 4.10c*) to groups of mean 6ss progenitors. Here, we found that intercalation alone can drive a 3.49-fold AP elongation, occurring at its greatest rate between the 8-somite and 12-somite stages (*Fig. 4.10d, blue line*), falling just short of the length change in real cell neighbourhoods. This is the effect of simply aligning cells into a single-file array, with no accompanied shape change. To then factor in cell shape changes, we applied measured changes in both cross-sectional area (*as for Fig. 4.10b*) and intercalation index, while keeping volume constant (*Fig. 4.10d, orange line*). In this growth-free scenario, intercalation did increase neighbourhood length, despite the shortening of individual cells,

but only to a maximum 1.55-fold extension, measured at the 12ss. This falls significantly short of real measured values, therefore suggesting that the ability of cell intercalation to drive AP tissue elongation is counteracted by cell spreading behaviours that reduce cell length. We therefore hypothesised that growth should account for most of AP elongation. However, acting alone, isometric growth achieved only a 1.76-fold elongation (*Fig. 4.10d, yellow line*), and anisotropic growth only a 2.59-fold elongation (*Fig. 4.10d, grey line*). This means that growth is also insufficient to drive full tissue elongation, therefore exposing a mutual dependency between changes in cell shape, size and topology for full elongation, which synergise to define full axial length. In sum, I propose that growth enables convergent extension in two manners. First, it counteracts loss of cell AP length, which enables intercalation to increase neighbourhood lengths (6ss – 10ss). Second, it further increases cell length after intercalation (10ss - 14ss). In this second phase, the relay of cell growth into tissue length is enhanced by the stack-of-coins topology, which makes cells lengths additive on the anteroposterior plane.

4. 3. 3 Spatial mapping reveals bidirectional gradients of shape maturation

Having previously identified heterogeneity in the extent of shape maturation for cells of the same somite stage (*Fig. 4.8b*), I next sought to test whether this temporal variation is spatially organised. To this end, I isolated all cells in the central notochord layer, this time regardless of position, and used Slingshot to infer a pseudotemporal axis passing through all points. In this case, cells from successive somite stages were strongly overlapping in morphospace, although dispersal across the central cell branch of morphospace increased progressively over time (*Fig. 4.11a*). Here, I therefore used k means clustering to construct the minimal spanning tree, and again prior information on temporal transitions from somite stages to define the trajectory start and end points. The inferred trajectory initiated in the central branch of cells in morphospace, passed through the bifurcation from Müller cells at the base of the plot, and extended through the central cell branch (*Fig. 4.11b*). I next quantified spatial variation in pseudotemporal progression by calculating the mean position in pseudotime for 10 non-overlapping bins of normalised AP notochord length (*Fig. 4.11c*). This was performed for notochords between 8ss and 14ss, when shape heterogeneity becomes explicit across the notochord. Using this method, I

found for each stage that the most advanced cells in pseudotime concentrated in the middle of the notochord, and the state of maturation decreased towards the most anterior and posterior tips (*Fig. 4.11c*). In morphospace, the most advanced cells lie at the leading edge of a shape continuum that extends back to the most immature morphologies towards the posterior tip of the embryo, in which shape maturation correlates strongly with AP position (*Fig. S4 aii – dii*). Cells of the anterior tip also lie proximal to the leading cells in morphospace (*Fig. S4 ai – di*). At 10ss, cells of the 0 – 15% region occupy the same position as 40 – 60% cells at 8ss (*Fig. S4 a, b*), and at 14ss they overlap with 40 – 60% cells at 12ss (*Fig. S4 c, d*). In sum, this analysis reveals temporal variation in cell shape transitions to be spatially organised into bidirectional gradients across the AP axis.

To further illustrate the spatial structure of temporal variation *in situ*, we colour-coded whole notochords by pseudotime (*Fig. 4.11d*). This confirmed the enrichment of leading cells in pseudotime in the middle part of the notochord, and a delay towards the anterior and posterior tips. It additionally revealed a correlation between the extent of shape maturation and changes in multi-cellular topology. Cells in the middle of the notochord were the first to undergo dorsoventral intercalation, as inferred from the local transition from a multi-layered organisation to a trilaminar organisation (*Fig. 4.11d, 10ss*). Unlike the 40-60% level, that undergo DV intercalation between 6ss and 10ss (*Fig. 2j*), cells in the anterior tip remained stratified on the dorsoventral axis until 10ss, and reduced to a single layered organisation by 14ss (*Fig. 4.11d, 10ss – 14ss, Fig. S4e*). This represents a 4-somite delay compared to the trunk region (*Fig. 4.11d, 10ss – 14ss*). We additionally found the posterior notochord to exhibit delayed intercalation. At all stages analysed, progenitors in the most posterior notochord remained stratified on the dorsoventral axis (*Fig. 4.11d, S4e*). Up to 12ss, we also found the persistence of tall columnar cells lacking bipolar left-right contacts at the extreme posterior tip of the notochord (*Fig. 4.11d, S4e*). This is characteristic of the monolayered archenteron roof prior to mediolateral cell intercalation (*Fig. 3.5 a*). Over developmental time, cells organised in both of these topologies were depleted and restricted further towards the posterior tip of the embryo (*Fig. 4.11d, S4e*). This is also reflected in a gradual decline in occupancy of the central branch of the notochord morphospace between 6ss and 10ss (*Fig. 4.8e*). In sum, the middle-to-tips dynamic of cell shape maturation in the notochord spatially and temporally mirrors

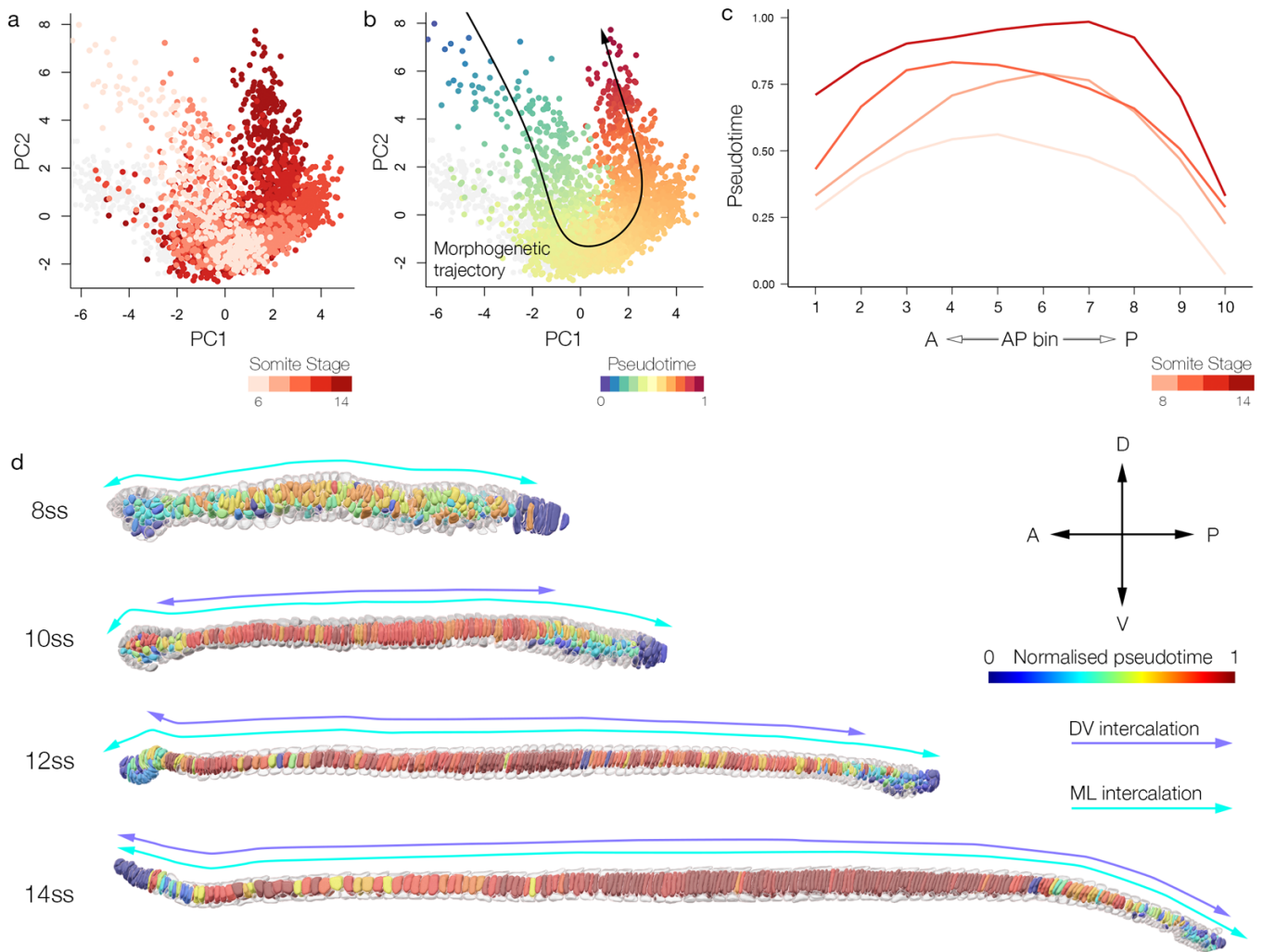


Figure. 4.11. **Temporal variation is spatially organised in bidirectional maturation gradients** (a) All central layer notochord cells, regardless of spatial position on the AP axis, projected into morphospace. Colour-code reflects somite stage. (b) Central notochord cells ordered across an inferred pseudotemporal axis, guided by prior information on temporal transitions (a). (c) Mean pseudotemporal distance for cells in each of 10 evenly-sized bins of the AP axis, in embryos between 8ss and 14ss. 1 is most anterior, 10 is most posterior. (d) Colour-coding of the central notochord layer by pseudotemporal distance, aligned with the progression of ML and DV intercalation events inferred from transitions in cell topology. The progress of ML and DV intercalation is marked by cyan and purple bidirectional arrows.

bidirectional waves of ML and DV intercalation that establish a distinctive stack-of-coins pattern in the central notochord layer.

4. 3. 4 Spatial variants in trajectory structure demonstrate divergent and convergent paths to specific cell morphologies

Having identified spatial variation in developmental timing across the AP axis, we sought to test whether the structure of the central cell trajectory is shared by all cells, regardless of spatial position. We investigated this by constructing region-specific shape trajectories for four candidate regions sampled across the AP axis (*Fig. 4.12a*); anterior (0-15% AP position), pharynx (15-40% AP), trunk (40-60% AP) and posterior (60-100% AP). In each sampled region of the AP axis, we performed trajectory inference as described previously, guided by the temporal information in somite stages. We then analysed variation between regions in trajectory topology and its correlation with developmental time:

In anterior progenitors, the trajectory we inferred involved similar geometric transitions to the trunk (40-60%) level (*compare Fig. 4.12bi and biii, ci and ciii*). This included a transient loss of AP length during intercalation (*Fig. S5a*), and continuous increases in cross-sectional area (*Fig. S5d*), volume (*Fig. S5i*) and DV:ML aspect ratio (*Fig. S5l*). Maturation additionally involved a decline in the coefficient of variation for cuboidness, although the mean values remained constant (*Fig. S5g*), and a progressive decline in sphericity (*Fig. S5h*). In accordance with its temporal delay compared to the pharynx and trunk, the anterior trajectory extended least far into the central cell branch of morphospace (*Fig. 4.12bi, ci*). In addition, and unlike the more posterior regions, there is a poor separation of cells over pseudotime between somite stages, reflecting loose temporal control of shape transitions in this region (*Fig. 4.12di*). Considered together, the anterior region shares common shape transitions to other regions, but is unique in its heterogeneity, with extensive variation in developmental timing between adjacent cells as they progress to their final morphologies.

The shape trajectories of the pharyngeal and trunk levels are similar to one another in that they display the two major transitions observed at the 40 – 60% level, including entry to the ‘bowtie domain’ at the 10-somite stage (*Fig. 4.12bii – iii, cii – iii*). In both cases, and unlike in the anterior notochord (*Fig. 4.12bi*), cell shape changes were tightly

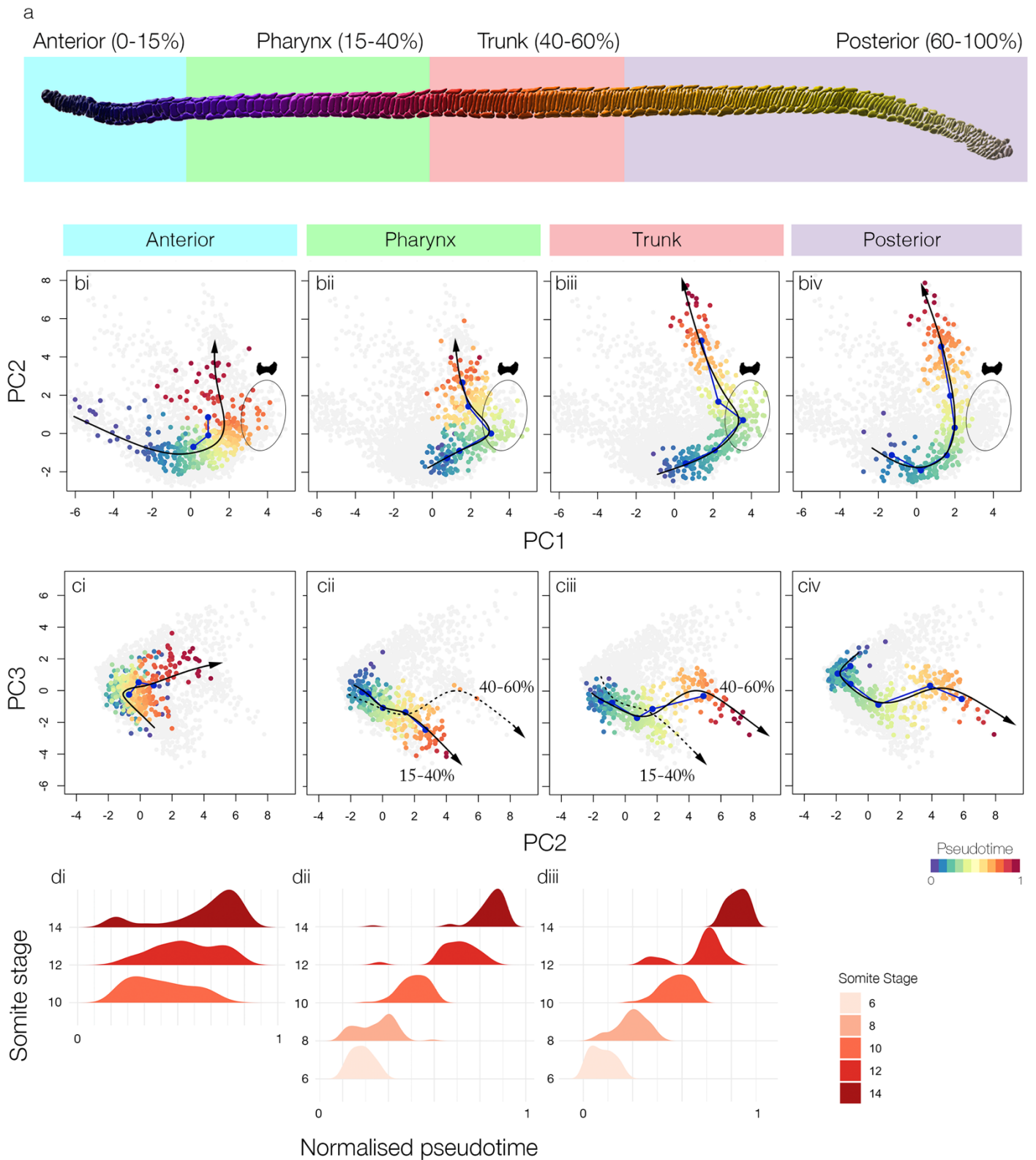


Figure. 4.12. Variation in cell shape trajectory topology and temporal control across the AP axis. (a) A sample 14ss notochord showing sampled regions on the AP axis for trajectory comparison; anterior (0 – 15%), pharynx (15 – 40%), trunk (40 – 60%) and posterior (60 – 100%). (b) Cells from each region defined in (a) now projected in morphospace against PC1 and PC2, with a segmented line connecting point cloud centres for each stage, and an inferred Slingshot trajectory. For the posterior (*continued overleaf*)

controlled in developmental time (*Fig. 4.12dii - iii*). However, the pharyngeal trajectory was contracted on PC2 compared to the trunk trajectory, reflecting a lesser increase in DV:ML ratio, and therefore a stabilisation of a square transverse profile (mean DV:ML ratio of 1.035 at 14ss) rather than further elongating along the DV axis like cells in the trunk region (mean DV:ML ratio of 1.283 at 14ss) (*compare Fig. 4.12bii and biii, Fig. S3l, S6l*). The pharyngeal trajectory also involves greater and more rapid increases in length and volume between the 12- and 14-somite stages (*compare Fig. 4.9e, g with Fig. S6a, i*). Combined, these variations lead to a second bifurcation event in morphospace across PC2 and PC3 between 12ss and 14ss, yielding two unique cell morphologies that are spatially resolved along the AP axis in the pharynx and trunk (*compare Fig. 4.12cii and ciii*).

To predict the trajectory of remaining posterior progenitors (60 – 100% AP position), which continue to differentiate beyond the final timepoint of the analysis here, we used relative AP position to guide trajectory inference. This was justified by the correlation we identified previously between axial position and developmental maturity in this posterior region (*Fig. 4.10, S4*). In this region, cells were similar in initial and final morphologies to the trunk region, but appeared to circumvent the distinctive bowtie morphology, as shown by failure to populate the ‘bowtie domain’ occupied by pharyngeal and trunk cells at 10ss (*compare Fig. 4.12biii and biv*). This implies a shortcut in their trajectories, such that maturation involves a continuous elevation of transverse area (increase in PC1), that is not enhanced by surface convolution. In sum, this analysis reveals discontinuity in shape transitions across the AP axis, in which some trajectories split over time to generate morphological diversity, while others take divergent paths to common morphologies.

Figure 4.12. (*continued*). trajectory, 6 bins of AP length at the 14ss are used instead of somite stage. Colour-code is for pseudotemporal position. (ci -iv) Projections of the same cells as (bi - iv), now against PC2 and PC3. For the 15 – 40% and 40 - 60% levels, both trajectories are highlighted to highlight late shape bifurcation. (di - iv) Density plots showing the frequency of cells across pseudotime for each somite stage in the anterior (di), pharyngeal (dii) and trunk (diii) regions. Anterior, $n = 396$; pharynx, $n = 360$; trunk, $n = 344$; posterior, $n = 408$

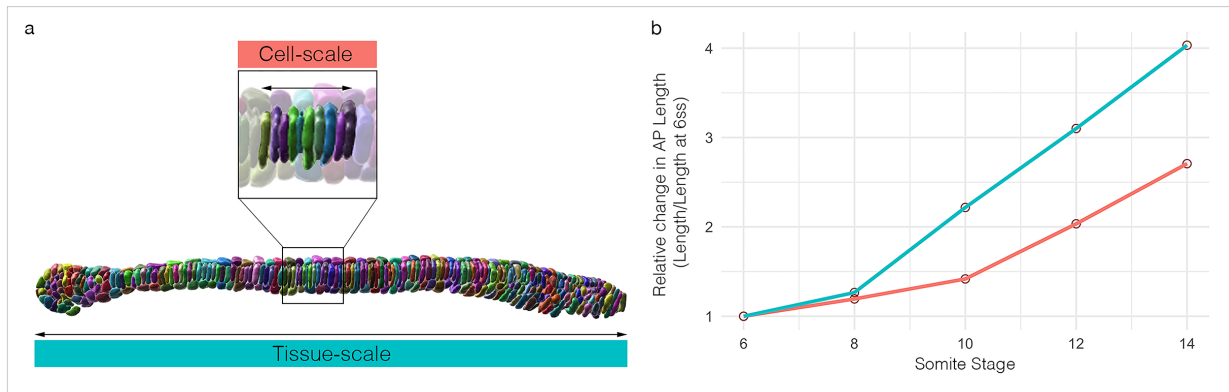


Figure. 4.13. **Tissue-scale morphogenesis is not an extrapolation of local cell behaviours.** (a) 10ss segmented notochord showing cell-scale (top) and tissue-scale (bottom) measurements of AP length. (b) Graph showing relative change in AP length at the cell-scale (neighbourhoods of 10 adjacent cells) and tissue-scale (whole notochords). Points show the mean for 5 neighbourhood measurements per embryo, in 3 embryos per stage, and a total of 33 embryos across the five stages for total length.

4. 3. 5 Can cell shape trajectories explain tissue-scale dynamics?

Morphometric analysis decomposes notochord morphogenesis into a branching series of cell shape trajectories which unravel with complex spatial and temporal dynamics. Our final objective was to test whether the behaviours we identify at this scale are sufficient to account shape change at the tissue-scale. In other words, are local cell shape changes sufficient to account for tissue-scale shape changes? To test this, I compared the dynamics of elongation at the neighbourhood level with that at the tissue level, using direct measurements of total notochord length (*Fig. 4.13a*). Focusing on fold changes in length, I found the amount of whole notochord elongation to exceed that of local cell neighbourhoods, resulting from a specific acceleration between 8ss and 10ss (*Fig. 4.13b*). This finding highlights that processes other than local changes in cell shape and topology are required to generate tissue length, and modulate the elongation curve generated by small cell neighbourhoods. In turn, we cannot explain tissue-scale dynamics by simple extrapolation of local behaviours. Aligning with the results presented in **Chapter III**, this discrepancy in elongation rates likely arises from the contribution of cell division in posterior notochord progenitors, whose division between 6ss and 8ss I showed to be required for full embryo elongation by experimentally blocking it with hydroxyurea

treatment. Collectively, this inter-scale analysis adds another layer of complexity to the process of notochord morphogenesis, in exposing cell division as a regulator of the number of cells entering each cell shape trajectory. Indeed, cell division temporally precedes cell shape transitions and intercalation in the posterior notochord. Considered together, these analyses reveal notochord form to be an emergent property of diverse morphogenetic processes, dispersed over space and developmental time, that ultimately act additively in the regulation of geometry and growth dynamics.

4. 4 Discussion

In this chapter, I have decomposed morphogenesis of the amphioxus notochord by embedding it in a single-cell morphospace. In this environment, morphogenesis is unravelled into a branching portrait of cell shape differentiation, in which cells transit along trajectories specific to cell type to form a stereotypical diversity of morphologies. This analysis identifies novel principles in amphioxus notochord morphogenesis, and offers a quantitative framework for modelling and comparative studies within and between tissues and, potentially, between species. My primary conclusions are as follows:

1. Morphospacial embedding offers a quantitative framework for holistic shape analysis across an entire tissue, whose resolution depends on the quality and throughput of imaging, cell segmentation and shape quantification. In development, cells have a dynamic occupancy of morphospace, and flow through it to different terminal forms. These paths can be conceptualised as trajectories, which can be reconstructed using large numbers of segmented cells in fixed specimens. Quantification of cell shapes in the amphioxus notochord, and the definition of morphospacial trajectories, satisfies both Aim I and Aim II.
2. Cells in the central notochord layer undergo stepwise transitions in shape, correlated with sequential phases of cell intercalation. This includes an early expansion of transverse cell spreading area, through a decrease in AP anisotropy and flaring of lateral margins to generate a 'bowtie' morphology, and a late AP elongation related to ongoing volumetric growth. These descriptions satisfy Aim I.

3. By applying geometric modelling, I show that growth is essential for maintaining an increase in tissue length during cell intercalation. When cells increase their transverse spread and intercalate, growth buffers loss of AP length, such that intercalation generates a length increase on the multi-cellular scale. After intercalation, once the cell cross-sectional area stabilises, growth generates a further length increase in the absence of further changes in cell topology. However, the effect of growth is also amplified by intercalation, which increases the contribution of cell lengths to total tissue length. This exercise satisfies Aim IV.

4. Cell shape trajectories vary across the AP axis in both timing and topology. Developmental timing is graded across the AP axis into bidirectional gradients emanating from the centre of the tissue and propagating towards its tips. This correlates with a corresponding wave of DV cell intercalation. I also identify region-specific variations in shape trajectory topology. This includes variations in temporal control, the bifurcation of trajectories to different terminal forms, and the convergence of cells on common forms through different morphogenetic paths. This satisfies Aim III.

4. 4. 1 What morphometrics can and cannot tell us about development

Morphospacial embedding and trajectory inference offers a high resolution and holistic framework for defining morphogenetic processes. In the case of the amphioxus notochord, this approach reconciles an incredible diversity of cell shapes into a coherent portrait of cell shape diversity, that unfolds over time with complex spatial and temporal dynamics. In this respect, the work presented in this chapter suggests that cell morphology may contain a much richer body of information than is typically assumed, to the point of being predictive of cell identity, spatial position, and developmental time. And, indeed, this is intuitive in so far as cell and tissue morphology must, in principle, be tightly controlled in order for developmental programmes to reproducibly generate traits with the correct geometry, size and cellular architecture. When projected into morphospace, we can consider morphogenesis as a navigational problem, in which cells passage along trajectories of shape change that locally remodel tissues and ultimately build organs. In turn, we can

consider the effect of evolution as an alteration of the topology of these trajectories, as well as the rate and timing at which cells pursue them, and in what numbers. Consider this as analogous to depictions of cell state transitions in scRNA-seq data. From this perspective, morphospacial embedding enables both fine-grade description of morphogenesis, and offers scope for comparative projects through integration of morphological data from multiple tissues or species. In this study, I highlight multiple variations of the central cell trajectory unfolding across the AP axis, by comparing the distribution of cells from each region in a common morphospace. Expanding on this intra-tissue comparison, it may be possible to develop inter-tissue or inter-species comparisons. In doing so, we stand to identify both where evolution has acted on the morphogenetic programme to generate apparent novelty, and to quantitatively define the amount of resting variation in individual systems.

From a navigational perspective, the next set of questions to ask relates to what controls the directionality of cell movement through morphospace. To achieve this, morphometric data needs to be combined with molecular information on cell state, the dynamics of intercellular signalling interactions, and unique properties of the mechanical environment. For example, the temporal dynamics of notochord intercalation might arise downstream of a patterned distribution of Wnt planar cell polarity pathway components (Wallingford et al., 2002; Ybot-Gonzalez et al., 2007). This, and other similar hypothesis, could be tested through a combination of *in situ* hybridisation and pharmacological perturbations. However, with quantitative data at both morphological and molecular scales, we can take a more systems approach to morphogenesis. In this view, form is not a linear readout of molecular patterning information, rather it the product of a dynamic interplay across scales in which the interpretation of patterning information is modulated by changes in cell shape, size and topology. For example, in ascidian embryos the strength of intercellular inductions is influenced by the area of cell-cell contacts (Guignard et al., 2020), and in the zebrafish presomitic mesoderm synchronisation of the somitogenic clock is accelerated by cell mixing (Uriu et al., 2017). In order to infer what drives cells along specific shape trajectories, and how these can be tweaked in evolution, I propose that mathematical modelling is the next hurdle if we are to avoid reductionist explanations. This is to integrate dynamic information on multiple scales, and to infer the interactions responsible for a given set of observed dynamics. These may be intuitive from the starting

conditions, or instead unexpected emergent properties. By combining multi-scale quantifications with modelling and experimental perturbations, we can test what drives cells along specific shape trajectories, and how plastic these are for evolutionary and pathological variation.

4. 4. 2 Implications for notochord development and evolution

A surprising product of geometric modelling in notochord progenitors was the identification of growth as a major contributor to tissue elongation. In the early phase of axial elongation, I found cells to expand their transverse spreading area at the expense of anteroposterior length, and undergo a process of intercalation along the dorsoventral axis. When simulated in the absence of growth, transverse cell spreading almost entirely abrogated the elongating effect of cell intercalation. The local net increase in tissue length was negligible. In turn, we can predict that growth is required in the system to generate axial length. However, the simulation of anisotropic growth acting alone, in the absence of intercalation or spreading behaviour, achieved just over half of the expected length change. We can therefore speculate that the critical role of cell intercalation isn't purely in length generation, rather it is to maximise the relay of length-generating processes in individual cells to total axial length. Indeed, in a single-file row, the lengths of individual cells become additive in their contribution to tissue length. Furthermore, geometry dictates that growth will drive greater and more rapid elongation in narrower shapes than broader shapes when acting unidirectionally. In sum, the geometric modelling presented suggests that convergent extension behaviour in the notochord on a tissue-scale (described in **Chapter III**) emerges from a dynamic interplay between local changes in cell shape, topology and size. During intercalation, growth buffers the loss of cell length due to transverse spreading, thereby allowing intercalation to enforce a net increase in neighbourhood length. Then, after intercalation, growth further increases tissue length once notochord cross-sectional area is stabilised.

Geometric modelling allows us to infer relationships between different transformations in cell morphology and topology in the definition of tissue shape. However, this rests on an abstraction from the biology and series of assumptions and simplifications, and so requires experimental testing. A major assumption is that cell shape

change and growth can be uncoupled, and will proceed with their normal dynamics in isolation. For example, I have assumed that cells will spread to the same true transverse dimensions in the presence and absence of growth. To test the role of growth in amphioxus notochord elongation, embryos could be treated with bafilomycin, which prevents the formation of intracellular vacuoles (Bowman et al., 1988; Ellis et al., 2013). If growth antagonises cell spreading during intercalation, notochord cells in bafilomycin-treated embryos should spread out to their normal dimensions and intercalate, while not generating a significant increase in tissue length. This seems likely given that cells spread and intercalate prior to their most rapid phase of growth. Another possibility, however, is that cellular growth influences the amount of spreading, and so the notochord scales with the reduced volume of its cells. This points towards another important open question of how the directionality of growth is controlled. The role of growth in spreading and intercalation could be tested with bafilomycin. After intercalation, cell length increases without further expansion of transverse area, which may therefore be mechanically restricted. Given the coincident formation of the notochord sheath, the role of the sheath should be tested, for example by digesting it with a collagenase enzyme, or potentially focal laser ablation. If the sheath is required to direct growth along the anteroposterior axis, the notochord should expand isotropically, rather than anisotropically, in its absence. These experiments were not possible during the course of my PhD due to a lack of live embryos after summer 2019, but will be important to test whether the principles identified here *in silico* are biologically meaningful.

In the context of **Chapter III**, a prevailing role for growth in tissue elongation may seem incompatible with a lack of growth in amphioxus axial development at large. However, at the tissue-scale, the notochord does exhibit the greatest relative increase in volume of all axial tissues (see *Fig. 3.8*). The data presented in this chapter indicate that this increase in tissue volume is mediated by growth of individual notochord progenitors in the trunk, rather than simply the addition of tailbud progenitors. In turn, this hints that other tissues must deplete in size, or expand at a rate less than expected for the amount of tissue they receive through differentiation of the unsegmented body. One candidate is the paraxial mesoderm, which appears to compact and reduce in volume between 10ss and 14ss when the notochord is growing at its highest rate (*Fig. 3.8 a*). Another is the ventral endoderm, which expands significantly throughout elongation, but its lumen appears to

decrease in size. With further imaging, volumetric change in the endoderm lumen could be measured directly. The interplay of cell shape and size in the notochord also enriches the discussion initiated in **Chapter III** on comparative growth dynamics. The rapid developmental mode of amphioxus and its lack of net growth align with an external developmental mode, fuelled by a limited supply of intracellular yolk. However, here we also find cell intercalation, and potentially the notochord sheath, amplifying the conversion of cellular growth into tissue length. In this respect, growth is employed sparingly in the developmental programme, but in cellular environments that maximise its morphogenetic output.

An unexpected finding in this study was regional variation in cellular behaviour across the AP axis, within a tissue that appears, at face value, to be morphologically continuous: In the anterior we find a highly variable morphogenesis, perhaps characterised by asynchronous maturation between neighbours; in the pharynx and trunk we find a unique dynamic in which a bowtie morphology disproportionately expands cell spreading area during intercalation; and in the posterior we find a simplified shape trajectory fuelled by cell division. These variations may arise due to a common programme of differentiation occurring under unique mechanical conditions or be the effect of region-specific signalling and genetic regulation. Such correlation is supported by the explicit notochord regionalisation found across vertebrates. In the mouse, live imaging has revealed marked differences in morphogenesis between the anterior head process (AHP), trunk and tail notochord (Yamanaka et al., 2007). Unlike the trunk, AHP progenitors derive from the early- and mid-gastrula organiser without passing through the node (Kinder et al., 2001; Yamanaka et al., 2007), and accordingly are uniquely sensitive to loss of Nodal signalling, but are insensitive to loss of Noto expression (Vincent et al., 2003). In contrast, the tail progenitors are unique in their active migration to move posteriorly to the node late in axis elongation (Yamanaka et al., 2007). Another example of regionalisation is the prechordal plate (PrCP) in all vertebrates, which shares with the AHP its developmental origin from the most anterior axial mesoderm, and forms through anteriorly-directed collective cell migration (Tada and Heisenberg, 2012). Evidence for regionalised behaviour aligns with nested expression of Hox genes in the vertebrate notochord (Prince et al., 1998). Previous work has also identified regionalised gene expression in the amphioxus notochord, and the data presented here adds to this in hinting at readout of these variations as discrete cell

behaviours (Albuixech-Crespo et al., 2017). In terms of evolution, regional variation in development of the amphioxus notochord may suggest that those striking variations in vertebrates – the PrCP, AHP, trunk and tail regions – may have emerged within semi-discrete morphogenetic fields already defined in the first chordates.

The final datapoint I presented in this chapter exposed a discrepancy between the rates of elongation in small cell neighbourhoods and the notochord at large. This discrepancy indicated that some other factors apart from change in cell shape and size must be affecting the rate of tissue elongation. Returning to the results presented in **Chapter III**, this may relate to the number of new cells added to the notochord in the early stages of axial elongation through cell division in posterior progenitors. As shown in *Fig. 3.13*, cell division is required to generate the posterior 20% of notochord length. In this respect, cell division might fuel the notochord shape trajectories with the new cells required for full elongation, and in doing so accelerate the linear rate of elongation measured in small cell neighbourhoods. An interesting complexity is the temporal lag present between cell division in posterior progenitors, which dampens at 9ss (*Fig. 3.11*), and the onset of intercalation and growth in these cells, occurring between 10ss and 14ss. In identifying the determinants of tissue size, geometry and growth dynamics, this analysis therefore reinforces these qualities as emergent properties of cell behaviours acting over extended development timescales. Processes acting early in development, like cell division in this case study, may only have an effect on 3D tissue form at later developmental stages, thereby falling outside the time window selected for experimental study. In this respect, to explain the emergence of form, we must integrate processes occurring on multiple scales of observation, and also over extended developmental time periods.

4. 4. 3 Conclusion

To conclude, the work presented in this chapter offers a novel, quantitative and holistic framework for characterisation of tissue morphogenesis. In this study, I have applied single-cell morphometrics to map out the dynamics of notochord morphogenesis in amphioxus, which has not been previously described in any detail. My findings point towards a remarkably complex morphogenetic scheme in amphioxus, that includes numerous processes also identified in both ascidians and vertebrates. As noted by previous

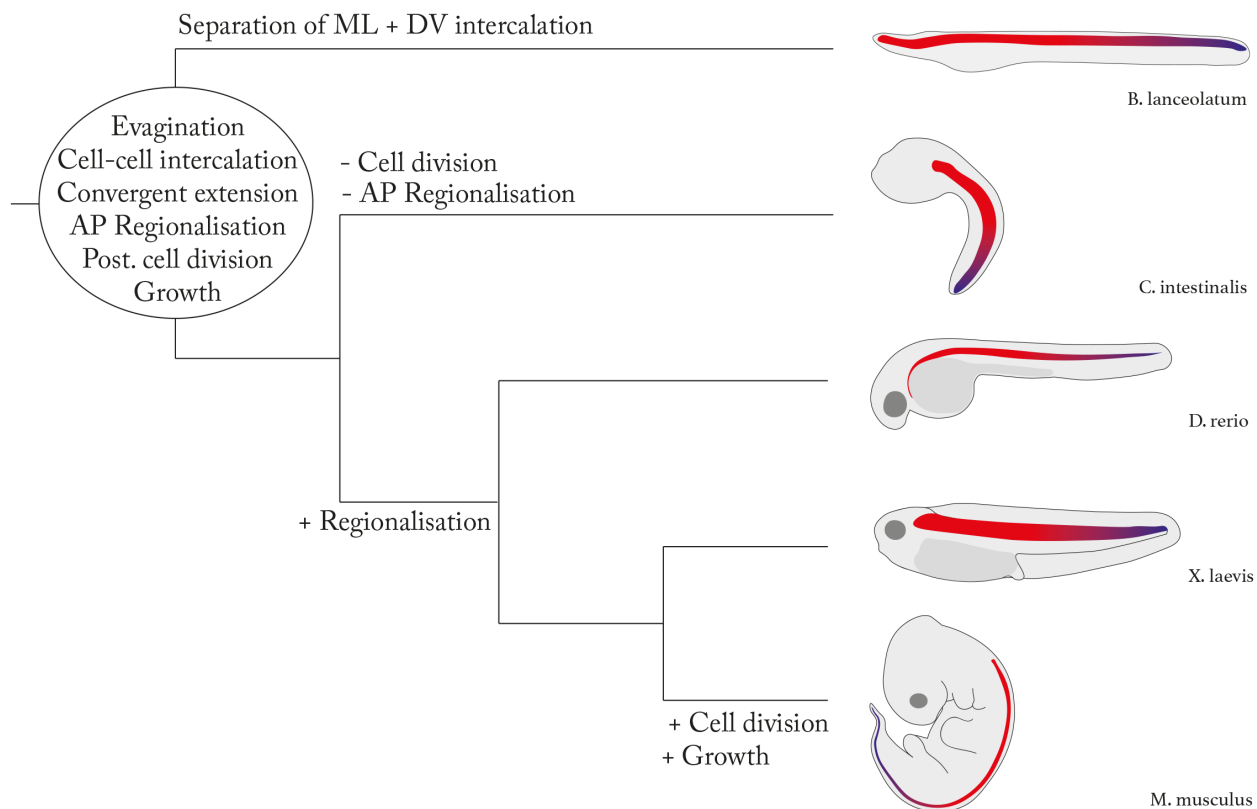


Figure. 4.14. **Proposed schema for evolution of notochord morphogenesis.** Based on observation in both vertebrates and amphioxus, I propose a suite of processes ancestrally linked to notochord formation in chordates, consisting of; evagination of the archenteron roof, cell-cell intercalation leading to formation of a stack-of-coins organisation, convergent extension behaviour, regionalised cell behaviours across the AP axis, posterior cell division and widespread cellular growth linked to axial elongation. From this foundation, processes have been altered in magnitude and timing in extant taxa. In amphioxus, intercalation dynamics are unusual being sequential on ML and DV axes, which is likely a derived condition. In ascidians, cell division during morphogenesis, and AP-regionalised behaviours, appear to have been secondarily lost. In vertebrates, regionalisation is more pronounced, contrasting with the subtle variations present in cephalochordates. The role of posterior cell division is also greatly increased.

authors, this includes evagination from the archenteron roof, and cell intercalation to generate a stack-of-coins topology. I add to this picture in identifying regional variation in developmental timing and patterns of cell shape change across the AP axis, and a role for growth in AP elongation, which here I show to counterbalance the loss of cell length during intercalation. Through parsimony, we can therefore predict that each of these traits are

likely ancestral to the chordates (*Fig. 4.14*). In turn, the apparently novel dynamics present in many extant vertebrates may have arisen through changes in the timing and magnitude of ancestral processes. Meanwhile, their absence in ascidians may reflect a secondary loss. These hypotheses will be further scrutinised by coupling morphometrics with molecular and mechanical information in amphioxus. The notion of a morphogenetic trajectory additionally offers a novel method to conceptualise and depict morphogenesis, that is conducive to rigorous comparative analyses and multi-scale modelling.

Chapter V

Defining axial progenitor cell state diversity with multiplex gene expression analysis

5.1 Introduction

The results presented in this thesis so far have focused on axial morphogenesis - the behaviours of tissues and cells that generate axial tissues and confer them with the correct geometry. This enables form-generating processes to be organised into a phylogenetic framework, and predictions to be made on how evolution has acted on morphogenesis to generate structural novelty and diversity. At the next scale of observation, these morphological phenomena unravel on a mass of cells passaging through fate decisions that confer the embryo with a predictable diversity of cell states and terminal cell types. Cell types are defined both by gene expression signature and dynamic, and behaviours or physical properties that enable them to execute specific functions (Clevers et al., 2017). As such, the innovation of cell types in evolution represents a potential source of morphological novelty (Arendt et al., 2016). In the context of this thesis, it is pertinent to resolve whether variation in strategies of body plan morphogenesis within the chordates has arisen from the emergence of new cell types, or rather changes in the behaviours of conserved cell types. In this chapter, I explore this problem in a case study of neuromesodermal progenitor cells (NMps), which are defined in vertebrates by hallmark embryological and molecular criteria.

5.1.1 Evolution through cell type innovation

An emerging framework for conceptualising morphological and physiological innovation in evolution is the emergence of novel cell 'types'. These have been defined as cells that express a unique combination of transcription factors, whose collective

interactions define a core regulatory complex (CoRC). The CoRC is then readout in a set repertoire of effector genes (encoding receptors, adhesion proteins, intercellular signalling ligands etc), that confer the cell with specific behavioural dynamics (Arendt et al., 2016). This could, for example, be structural, sensory, locomotor, or morphogenetic. Innovation can, in turn, result from the emergence of new cell types. For example, the emergence of ciliary and rhabdomeric photoreceptors has enabled light detection in bilateria (Arendt et al., 2002; Arendt et al., 2004). In vertebrates, emergence of neural crest cells that delaminate from the neural tube and invade into the surrounding embryo has been responsible for a plethora of morphological innovations, including pigment cells, peripheral neurons, glia, and dentary mesenchyme (Green et al., 2015). Innovation can also result from the specification of existing cell types at different times and in different locations. The embryonic skeleton of euechinoid sea urchins is deposited by the precocious specification of skeleton-forming primary mesenchymal cells (PMCs) in embryogenesis, despite their typical emergence during adulthood in the ambulacraria (Ettensohn and Adomako-Ankomah, 2019). Similarly, the novel specification of chondrocytes in the gnathostome neural crest lineage resulted in emergence of the gill arches and craniofacial skeleton as apparent morphological novelties (Chai et al., 2000; Green et al., 2015; Lumsden, 1988; York and McCauley, 2020). The concept of cell type evolution offers an accessible framework to consider the problem of body plan evolution in chordates.

The cell type concept is appealing in resolving the embryo into agents of distinct functionality. But it is important to remember that development is a continuum, in which cells do not necessarily stabilise as discrete ‘types’. This is illustrated in the continuity of gene expression profiles in developmental scRNA-seq datasets (Briggs et al., 2018; Ibarra-Soria et al., 2018; Wagner and Klein, 2020). Rather, cells undergo a series of transitions in gene expression profile en route from pluripotency to one of a number of possible terminal steady states, as depicted famously by the rolling marble in Waddington’s epigenetic landscape (Moris et al., 2016; Waddington, 1942). The state of the cell – the transcriptional output of the gene regulatory network – is actually a dynamic quality, that exhibits variable degrees of stability (Antolović et al., 2019; Mojtahedi et al., 2016; Moris et al., 2016). This has been especially characterised during cell fate decisions, in which the GRN acquires a metastable state between two or more stable attractors (Joo et al., 2018;

Kauffman, 1969). The probability that the GRN will exit the transition state and resolve on either attractor is influenced by intercellular signalling dynamics, which generate an imbalance in transcription factors associated with each outcome (Moris et al., 2016). The trajectory taken by a cell, in terms of sequential transitions in state, can be considered its ‘Waddingtonian’ lineage (Marioni and Arendt, 2017; Steventon and Martinez Arias, 2017). Importantly, this is conceptually distinct from kinship lineage, which refers to relatedness based on descent from common mother cells through subdivision of cytoplasm (Marioni and Arendt, 2017). Embryogenesis can be considered the embedding of the kinship lineage within the Waddingtonian lineage. In other words, the unfolding of cell state diversity in the embryo is coupled to a programme of clonal dynamics that affects their relative abundance, and behaviours that assemble multi-cellular groups into morphological traits. With these concepts in mind, more nodes emerge for evolution to act on; it can, in principle, expand, contract or alter the topology of the Waddingtonian lineage, or generate novelty by tweaking cellular behaviours exhibited by cells in a given state.

5. 1. 2 The neuromesodermal progenitor (NMP)

In the context of chordate body plan innovation, axial progenitors of the tailbud are a potential targets of cell state evolution. The cellular composition of the chordate tailbud has long been a contested issue. Holmdahl proposed that the tailbud is a homogenous blastema, contributing new cells to extend all tissues of the anterior part of the body, which are instead formed through remodelling of the three embryonic germ layers during gastrulation (Holmdahl, 1925, for summary see Davis and Kirschner, 2000). In this model, the tailbud is not germ layer restricted, and can contribute to any axial tissue without germ layer intermediates, though *ad hoc* fate decisions after gastrulation. It also does so without the extensive cell movement observed during gastrulation, instead exhibiting a large amount of proliferation and growth. The unique developmental mode implied by the blastema model is supported by distinct morphogenetic strategies operating in the posterior bodies of some vertebrates. This includes secondary neurulation, in which the neural tube forms through condensation and cavitation of mesenchymal cells, as opposed to epithelial folding (Nikolopoulou et al., 2017). The blastema model contrasts with an opposing view, spearheaded by Vogt (1926), that the tailbud is a mosaic patterned structure, consisting of

cells with predetermined fates (Beck, 2015; Davis and Kirschner, 2000). In this view, tailbud differentiation reflects more a continuation of gastrulation, rather than a novel developmental mode, and posterior body formation is essentially an unravelling of patterns already established within the tailbud. The mosaic model gained support from fate mapping studies identifying a regionalisation of cells with distinct fates within the tailbud (Attardi et al., 2018; Catala et al., 1995; Davis and Kirschner, 2000), and those expressing unique combinations of transcription factors (Beck and Slack, 1998; Gont et al., 1993). Further support has also come from the identification of cell movements typically associated with gastrulation ongoing within the tailbud after blastopore/primitive streak closure, including epithelial-mesenchymal transitions and involution behaviour (Goto et al., 2017; Taniguchi et al., 2017). The reality actually appears to fall between these two extreme models, in which cells of regionalised fate exhibit broad germ layer competence and position-dependent plasticity.

The last 10 years has seen an explosion of interest in an enigmatic population of axial progenitor cells termed neuromesodermal progenitors (NMps). NMps were first definitively identified in a landmark study of 2009, in which Tzouanacou and colleagues performed retrospective clonal analysis in the mouse, by expressing a *LacZ* construct under a ubiquitously-expressed *Rosa26* promoter (Tzouanacou et al., 2009). In this system, an internal duplication enforces a frame-shift in the *LacZ* gene, thereby encoding a non-function β -galactosidase enzyme. However, this is corrected at low frequency through spontaneous recombination, which recovers β -galactosidase activity in single cells and their derivative clones (Bonnerot and Nicholas, 1993). In the Tzouanacou et al (2009) study, the authors found that numerous clones backdated to E8.5 extended into single axial tissues, but also located a small number appearing to contribute to both the dorsolateral neural tube *and* the paraxial mesoderm. While this study remains the gold standard in terms of single cell labelling, other embryological studies have expanded our understanding of NMP dynamics. Also in the mouse embryo, Cambray and Wilson demonstrated the presence of two regions of the E8.5 gastrula with long-term contributions to neural and mesodermal tissues; the node-streak border and the caudo-lateral epiblast (Cambray and Wilson, 2002; Cambray and Wilson, 2007). As previously shown in avians using the quail-chick chimera system, the node-streak border contributes cells to the post-occipital notochord and floor

plate (Catala et al., 1995). However, like the NMps identified by Tzouanacou et al (2009), cells of the caudo-lateral epiblast contribute to the dorsolateral neural tube and paraxial mesoderm over large axial lengths, and continue to do so through multiple rounds of serial transplantation (Cambray and Wilson, 2002; Cambray and Wilson, 2007). The fate mapping presented by Cambray and Wilson has been reinforced by a less invasive method, DiO labelling (Mugele et al., 2018), and by genetic lineage tracing (Albors et al., 2018). Collectively, these studies point toward the presence of NMps in amniotes that make large contributions to the post-occipital body axis and may exhibit the stem cell quality of self-renewal.

Cells with NM properties have also been identified beyond the amniotes. In zebrafish, Martin and Kimelman (2012) demonstrated that progenitors of the tailbud mesenchyme are competent to commit to either neural or mesodermal fates, depending on the level of Wnt signalling (Martin and Kimelman, 2012). Single cells expressing a heat-shock inducible dominant-negative TCF construct were shown to generate either neurons or muscle fibres when grafted into wild-type tailbuds. However, when exposed to heat shock, cells were forced to neural fates. This study offers conclusive evidence that the zebrafish tailbud harbours cells with NM competence – the *potential* to generate either neural or mesodermal cells. However, lineage tracing in the zebrafish tailbud using a photoactivatable dye to mark the putative NM domain identified no cells that contribute to both lineages during axial elongation *in vivo* (Attardi et al., 2018). In this respect, zebrafish NMps are bipotent, but not bifated. Instead, live imaging highlighted a much earlier segregation of neural and mesodermal precursors during gastrulation, and the presence of a small quiescent population that retains NM potential until the end of tail formation (Attardi et al., 2018). At the termination of axial elongation, cells in this quiescent population finally contribute either to the posterior neural tube or paraxial mesoderm. This unifatedness may be due to the low level of cell division in the zebrafish tailbud compared to amniotes, which is inhibitory to formation of large clones (Attardi et al., 2018; Steventon and Martinez Arias, 2017). Given its traction for imaging and genetic perturbation, the zebrafish is the only anamniote to offer conclusive insight into NMP dynamics. However, fate mapping in *Xenopus* has also identified small patches of cells that contribute to multiple tissues (Davis and Kirschner, 2000). At present, whether single cells

are bifated in amphibians is unresolved. In the context of studies in amniotes, it appears that cells in an NM transition state - suspended between neural and mesodermal GRNs - are conserved in vertebrates, but the state is coupled to highly divergent clonal and behavioural dynamics (Steventon and Martinez Arias, 2017).

As described, NMps are defined first and foremost by hallmark embryological criteria – position, plasticity and fate. Since their identification, however, NMp properties have been correlated with a gene expression signature, including coexpression of the neural marker, *Sox2*, and the mesodermal marker, *Brachyury*. This has been shown convincingly in the chick (Olivera-Martinez et al., 2012) and in zebrafish (Martin and Kimelman, 2012), where expression of *Sox2* and *Brachyury* overlaps at a medium intensity in the posterior neural plate and chordoneural hinge. While the presence of RNA for both markers has not been demonstrated unambiguously in the mouse (Mugele et al., 2018; Wymeersch et al., 2016), immunohistochemistry is persuasive in showing double-positivity for both transcription factor proteins (Garriock et al., 2015; Henrique et al., 2015). The discrepancy here may result from the more protracted development of murine embryos compared to avians and zebrafish. Expanding on these correlations, studies *in vitro* have sought to define a gene regulatory network that balances neural and mesodermal contributions of NMps, and have highlighted other candidate markers of the population, and potential heterogeneities (Edri et al., 2018; Gouti et al., 2017; Tsakiridis et al., 2014; Turner et al., 2014). However, the extent to which *in vitro*-derived NMps resemble those emerging *in vivo* is a source of contention (Edri et al., 2019). *Sox2*⁺/*Brachyury*⁺ cells have also been highlighted in numerous scRNA-seq datasets, but their relation to NMp dynamics in the embryo remains unclear (Briggs et al., 2018; Ibarra-Soria et al., 2018; Wagner et al., 2018). *In vivo*, the *Sox2*⁺ *Brachyury*⁺ expression signature of NMps has been well validated in zebrafish, where NM differentiation involves resolution of coexpression to that of a single marker (Martin and Kimelman, 2012). Recently, evidence has also been presented that NMps cannot enter the mesoderm without turning off *Sox2* expression, thereby hinting at a functional significance of the *Sox2/Brachyury* cassette (Kinney et al., 2020). Most functional studies of the mouse NMp GRN have been performed *in vitro*, and have identified a mutual antagonism between *Sox2* and *Brachyury* that enforces germ layer commitment (Koch et al., 2017).

As a result of these studies, coexpression of *Sox2* and *Brachyury* has been widely adopted as an indelible marker of NMps. However, the strength of this correlation has certainly been exaggerated by the choice of *Sox2* and *Brachyury* as a definition for ‘NMps’ differentiated *in vitro* from embryonic stem cells; while the cells obtained *in vitro* may exhibit this gene expression signature, it does not invariably mean they correspond to cells with NM dynamics emerging in real embryos. A study from Mugele et al (2018) offers a cautionary tale with regard to the *Sox2/Brachyury* signature. In this study, the authors inducibly labelled cells expressing either *Sox2* or *Brachyury* at E8.5 using the mTmG reporter system (Muzumdar et al., 2007). When *Brachyury*⁺ cells were labelled, the clones generated both posterior mesoderm and posterior neural tissue, thereby showing that a proportion of the labelled cells have neuromesodermal fate. Meanwhile, *Sox2*⁺ cells labelled at the same timepoint only populated the posterior spinal cord and failed to generate mesoderm. The fidelity of cell marking in this approach is certainly limited by the sensitivity of the reporter system and the dose of tamoxifen used for induction at E8.5. As noted previously, mouse NMps are also positive for both *Sox2* and *Brachyury* protein, and so this study does not dispel the proposed functionality of each transcription factor in the NMp GRN (Garriock et al., 2015; Henrique et al., 2015). Nonetheless, the study warns that simple *in situ* hybridisation is not necessarily sufficient to delineate the NMp domain, and should, where possible, be coupled to cell marking approaches to test fate and competence. Indeed, true NMps are ultimately defined by their unique clonal dynamics.

The *ad hoc* fate decision between neural and mesodermal lineages occurring post-gastrulation in NMps is instructed by local molecular and mechanical cues, as shown by the ability of NMps to contribute to different lineages when grafted to novel regions of the epiblast (Wymeersch et al., 2016). The best-characterised of these signals is Wnt (*wingless-int1*). Wnt signalling plays a highly conserved role in bilaterian axial elongation (Martin and Kimelman, 2009), and drives the posterior expression of *Brachyury* in mouse (Yamaguchi et al., 1999), zebrafish (Martin and Kimelman, 2008) and hemichordate embryos (Fritzenwanker et al., 2019). Wnt also appears to bias tailbud progenitors to mesodermal fates at the expense of neural tissue, given the dramatic expansion, or ectopic formation, of neural tissue when Wnt is inhibited (Martin and Kimelman, 2012; Yamaguchi et al., 1999; Yoshikawa et al., 1997). While Wnt signalling favours mesodermal

differentiation, neurons can still form when Wnt signalling is constitutively activated (Garriock et al., 2015), and prospective mesodermal cells can switch to neural identities and form ectopic neural tubes if the mesodermal GRN is destabilised, for example with loss of *Tbx6* expression (Takemoto et al., 2011). FGF also plays important roles in NMP maintenance (Cunningham et al., 2015), and mesodermal differentiation through activation of *Brachyury* (Isaacs et al., 1994). It comes as no surprise that Wnt and FGF have been shown to interact in a positive feedback loop in the tailbud, that both maintains the NMP niche and promotes paraxial mesoderm formation (Aulehla et al., 2003; Goto et al., 2017; Henrique et al., 2015). Both exogenous FGF2 and Wnt activation, with the GSK-3 inhibitor Chiron, are common place in *in vitro* NMP differentiation protocols from embryonic stem cells (Gouti et al., 2014; Henrique et al., 2015; Tsakiridis et al., 2014; Turner et al., 2014). The studies described suggest that the balance of neural and mesodermal fates in NMPs may emerge from the magnitude and timing of FGF and Wnt signalling.

Notch signalling, on the other hand, appears to regulate the induction and maintenance of neural progenitors from NMPs. In the chick embryo, Gray and Dale (2010) showed that heterotopic grafts of GFP+ nodes into wild type hosts generate both notochord and floor plate. However, pre-incubation of grafted nodes in the Notch inhibitor, DAPT, biased their contribution to notochord identity. This suggests that Notch plays a role in the commitment of bicompetent cells to neural identity. Similarly, in zebrafish and *Xenopus*, inhibition of Notch signalling appears to expand the notochord at the expense of floor plate and hypochord (Appel et al., 1999; Peyrot et al., 2011). However, in this case, Notch primarily seems to promote floor plate expansion by increasing cell division in posterior neural progenitors, as opposed to altering progenitor allocation (Latimer and Appel, 2006; Row et al., 2016). This, in turn, is consistent with the role of Notch signalling in maintaining cell division in the posterior spinal cord stem zone in chick, which is activated downstream of FGF signalling (Akai et al., 2005). It also aligns with studies in lamprey, showing a requirement for Notch signalling in the maintenance of floor plate proliferation, and the subsequent emergence of motor neurons (Lara-Ramirez et al., 2018). In its myriad of developmental functions, Notch is also a conserved master regulator of the vertebrate somitogenic clock, which partitions the paraxial mesoderm into a metamer pattern of

somites (Liao and Oates, 2017). In zebrafish, Notch synchronises cyclic gene expression in adjacent cells of the presomitic mesoderm, which manifests periodic propagating waves of cyclic gene expression from posterior to anterior, eventually stabilising at prospective intersomitic boundaries (Liao et al., 2016; Özbudak and Lewis, 2008). In this respect, Notch signalling plays a diversity of roles in axial progenitor differentiation and downstream behaviour.

5. 1. 3 Specific aims of this chapter

The cell state composition of the amphioxus tailbud has not been characterised in any detail. In **Chapter III**, I described the progressive assembly of the amphioxus tailbud through, first, the internalisation of the dorsal blastopore lip to define the chordoneural hinge and, second, definition of the posterior wall through neural tube closure. In addition, I demonstrated the presence of proliferative cells in the chordoneural hinge that contribute to elongation of the posterior notochord and floor plate, but not to the paraxial mesoderm or dorsolateral neural tube, during axial elongation. Within this topology, *in situ* hybridisation has exposed a patchwork distribution of gene expression domains, including Wnt pathway genes (Beaster-Jones et al., 2008; Schubert et al., 2001; Somorjai et al., 2018), Notch pathway genes (Rasmussen et al., 2007; Holland et al., 2001; Belgacem et al., 2003) regionalised mesodermal markers (Aldea et al., 2015; Belgacem et al., 2011; Holland et al., 1995) and parahox genes (Ferrier et al., 2001; Zhong et al., 2020). However, no specific progenitor cell states have been defined, nor correlated with specific fates, behaviours or clonal dynamics. With this context, I sought to scrutinise the cell state composition of the amphioxus tailbud, with a specific focus on the presence and dynamics of cells in a neuromesodermal state. To this end, my aims resolved as follows:

- I. To perform multiplex *in situ* hybridisation for tissue-specific markers of the posterior body within the intact morphology of the embryo and identify putative domains of coexpression.
- II. To quantify gene expression levels in single cells, then quantitatively categorise and spatially map resolved cell states within the morphology of the embryo.

- III. To locate putative NMps in the amphioxus gastrula and early neurula using the *Sox2+/*Brachyury+** coexpression signature.
- IV. To define the fate of putative NMps using focal Dil labelling.
- V. To test the germ layer competence of putative NMps with pharmacological signalling perturbations.

5.2 Quantitative and multiplex imaging of amphioxus gene expression

5.2.1 Optimisation of hybridisation chain reaction (HCR) for amphioxus embryos

Colorimetric *in situ* hybridisation (ISH) is a powerful strategy for analysing the spatial patterns of gene expression during embryonic development and has been applied successfully in diverse animal phyla. This includes the amphioxus, in which it has been used to define tissue diversity and predict signalling interactions during axis extension (eg. Bertrand et al., 2011; Yu et al., 2007). However, colorimetric ISH is limited in its potential for multiplex imaging and quantitative expression analysis, both of which are required for the identification of cell types and states, which are defined by coexpression of multiple transcription factors (Arendt et al., 2016). For multiplex and quantitative imaging of gene expression, we therefore turned to an alternative approach, hybridisation chain reaction (HCR), for gene expression profiling in amphioxus embryos (Andrews et al., 2020a).¹ This method is formulated on the design of DNA probe pairs that bind in tandem to mRNA molecules of interest, and together form a platform for the focal amplification of kinetically-trapped hairpins, conjugated to fluorescent Alexa fluor moieties. The result is formation of a fluorescent polymer anchored to the target mRNA, whose net fluorescence intensity is proportional to the local concentration of RNA (Choi et al., 2018; Trivedi et al., 2018). The specificity of adapter sequences, and commercial availability of DNA hairpins conjugated to different fluorophores (Molecular Instruments), allows multiplexing of probes to target up to five different mRNA species, in the same specimen, in a single reaction (Choi et al., 2018). The HCR method is therefore multiplex, sensitive and quantitative.

High quality HCR imaging in amphioxus required extensive optimisation of the standard method. Ultimately, we identified an effective staining strategy by combining the published HCR zebrafish protocol with the traditional amphioxus *in situ* hybridisation

¹ In collaboration with Lara Busby (Department of Genetics, University of Cambridge), Giacomo Gattoni and Michael Schwimmer (Department of Zoology, University of Cambridge)

protocol (Holland & Holland, 1993), and in house permeabilisation approaches normally applied for immunohistochemistry. An essential addition was inclusion of a bleaching step, in 3% hydrogen peroxide and 3% formamide, which reduces the intensity of endogenous autofluorescence by virtue of an extensive GFP repertoire in amphioxus (Bomati et al., 2009). Autofluorescence is especially problematic in the 488 channel. A bleaching step was critical in establishing the high signal:noise ratio required for quantitative HCR imaging (Trivedi et al., 2018). We also found that a much higher probe concentration was required to generate strong and specific signal in amphioxus compared to zebrafish, such that our final method included 40nM probe, 10-times the concentration applied in the zebrafish protocol (Choi et al., 2014) (*Fig. 5.1*). At this concentration, we deemed the probes to be in excess, given that higher concentrations no longer rendered significant signal improvement. Finally, we found that an incubation in proteinase K, which is standard in amphioxus ISH protocols to improve antibody penetrance into the tissue, made no significant improvement to HCR staining in amphioxus (*Fig. 5.1*). Removal of a proteinase K digestion allowed for better maintenance of tissue integrity, and therefore analysis of patterns of gene expression within a robust morphological context. With these modifications, and imaging specimens using confocal microscopy at 30X optical magnification, I achieved strong HCR staining at single-cell resolution across all stages of amphioxus axial development.

5. 3. 2 Multiplex HCR imaging of posterior axial markers

To capture amphioxus axial progenitor diversity, I focussed my analysis on a small battery of genes that define major subcompartments of the chordate posterior body, and have been used for progenitor definition in vertebrates (Martin and Kimelman, 2012; Olivera-Martinez et al., 2012; Wymeersch et al., 2016). *SoxB1* family genes are strongly expressed in neural tissue. In amphioxus, *Soxb1a* and *Soxb1b* are redundantly expressed in the early neural plate from late gastrulation into early segmentation, at which point their expression falls and is replaced by *Soxb1c* (Holland et al., 2000; Meulemans and Bronner-Fraser, 2007). *Brachyury1/2* is a conserved marker of nascent mesoderm across bilateria and is required for formation and elongation of posterior mesoderm (Martin and Kimelman, 2010; Technau, 2001; Wilson et al., 1995). The *Brachyury1/2* locus in amphioxus has experienced a tandem duplication, such that the complete pattern is represented by both

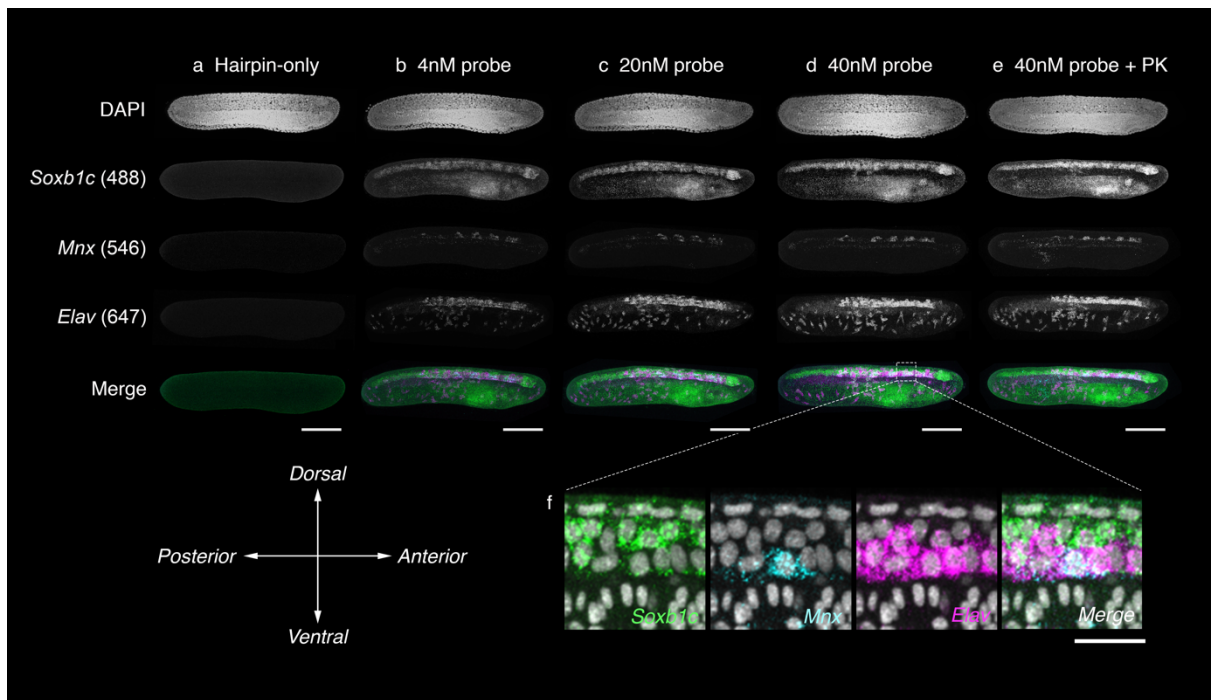


Figure 5.1. **Triple HCR in whole-mount embryos of *B. lanceolatum*.** HCR staining was performed on whole amphioxus embryos reared to 24 hpf at 21°C with varying concentrations of probe, and in the presence and absence of proteinase K digestion. For this combination, 20-pair probe sets were designed against *Soxb1c* for broad labelling of the neural tube, *Mnx* for labelling of motor neuron progenitors, and *Elav* for postmitotic neurons. Exposure to hairpins in the absence of probes generates channel-specific background fluorescence profiles (a). This is conspicuous in all channels, but most severe following excitation at a 488 nm wavelength. A 4nM probe concentration, as suggested for use on zebrafish embryos, generates specific signal but with a poor signal:noise ratio, even after extensive washing (b). In the 488 channel, signal can be difficult to distinguish from background. Signal:noise is greatly improved with expose to 20nM (c) and 40nM (d) probe concentrations for common incubation times. At 40nM, signal can readily be resolved from background. Proteinase K (PK) treatment is common in amphioxus ISH protocols to enhance embryo permeability. However, treatment with PK did not enhance HCR signal beyond that achieved with only permeabilization in TritonX-100 and DMSO (e). (f) Magnified view of parasagittal section through anterior neural tube of embryo in (d), revealing regional differences in expression profiles for each gene, and a single triple-positive cell. Scale bars measure 100µm (a–e) and 20µm (f).

Brachyury1 and *Brachyury2* (Holland et al., 1995; Zhang et al., 1997). *Tbx6/16* family genes are strongly expressed in presomitic mesoderm and are widely required for its differentiation (Belgacem et al., 2011; Bouldin et al., 2015; Griffin and Kimelman, 2002;

Griffin et al., 1998). *Noto*, the notochord homeobox, is typically expressed in nascent axial mesoderm and is required for notochord formation, mediated by cell-autonomous repression of paraxial identity (Amacher and Kimmel, 1998; Halpern et al., 1995; Melby et al., 1997). The expression profiles I captured for these genes with HCR complemented and expanded the current published data, and are described in detail below:

Brachyury1/2. While *Brachyury* has duplicated in amphioxus, I found the two transcripts, *Brachyury1* and *Brachyury2*, to be insufficiently different for the design of distinct HCR probe sets. As a result, and following previous authors (Holland et al., 1995; Terazawa and Satoh, 1997), the probes designed captured the complete expression pattern represented by both mRNA species. In the cup-shaped gastrula, *Brachyury1/2* is expressed circumferentially around the blastopore lip (Fig. 5.2ai). Here, expression appears in both the inner and outer lips, but extends furthest anteriorly on the inner side, within the early archenteron (Fig. 5.2ai, bottom). This is to the greatest extent in the lateral lips. As the blastopore closes, *Brachyury1/2* expression shifts towards the dorsal side of the archenteron, in which it spreads almost to the anterior tip of the archenteron (Fig. 5.2bi). This is strongest in the prospective paraxial mesoderm, and weakest in the chordamesoderm at the midline (Fig. 5.2bi, top). The shift in *Brachyury1/2* expression towards the dorsal side of the embryo in this time period mirrors the previous identification of involution and convergence during blastopore closure (Chapter III). In the paraxial mesoderm of embryos at 10hpf, expression in the anterior part of the embryo exhibits a clear pattern of 2-3 transverse stripes, that are separated by unlabelled cells (Fig. 5.2bi, magenta brackets). Even at this early stage, the emergence of segmental patterns is asymmetrical across the left-right axis (Fig. 5.2bi). On the ventral side of the embryo, expression of *Brachyury1/2* remains closely restricted to the inner blastopore lip, extending only 1/4th the anteroposterior length observed on the dorsal side (Fig. 5.2bi, bottom). After blastopore narrowing, expression of *Brachyury1/2* loses its circumferential expression in the outer blastopore lip and is absent from the majority of the surface ectoderm (Fig. 5.2bi). This is with the exception of the posterior half of the neural plate, in which *Brachyury1/2* expression persists at a low level (Fig 5.2bi, red arrow).

At 14hpf, expression of *Brachyury1/2* declines in the anterior paraxial mesoderm to match the low intensity observed in the chordamesoderm at the midline (*Fig. 5.2ci, top*). Now, the strongest expression is in the posterior half of the PSM, which is highlighted in the HCR staining as a distinct arc of tissue, with two arms extending anteriorly, and bilaterally, from the narrowed blastopore (*Fig. 5.2ci, top*). These bands of expression overlap with the presomitic mesoderm as defined by morphological criteria in **Chapter III**. In most 14hpf embryos, single additional transverse stripes of *Brachyury1/2* expression are observed at the anterior tips of each band of presomitic mesoderm, separated by a stripe of unlabelled cells of equal length (*Fig. 5.2ci, top*). This was previously noted by Zhang and Holland (1997). Ventrally, expression of *Brachyury1/2* remains strong in the internalised ventral blastopore lip (*Fig. 5.2ci, bottom*). Importantly, at 14hpf the region of low *Brachyury1/2* expression in the posterior half of the neural plate appears to have split into two domains of medium expression that are separated across the anteroposterior axis (*Fig. 5.2ci, bottom*). Splitting of the posterior neural *Brachyury1/2* domain may result from loss of expression in intervening cells, although cell movement cannot be excluded. The more anterior expression domain is now disconnected from other *Brachyury1/2*-expressing tissues, while the posterior domain occupies the dorsal side of the chordoneural hinge and is therefore continuous with the posterior mesoderm on its ventral side.

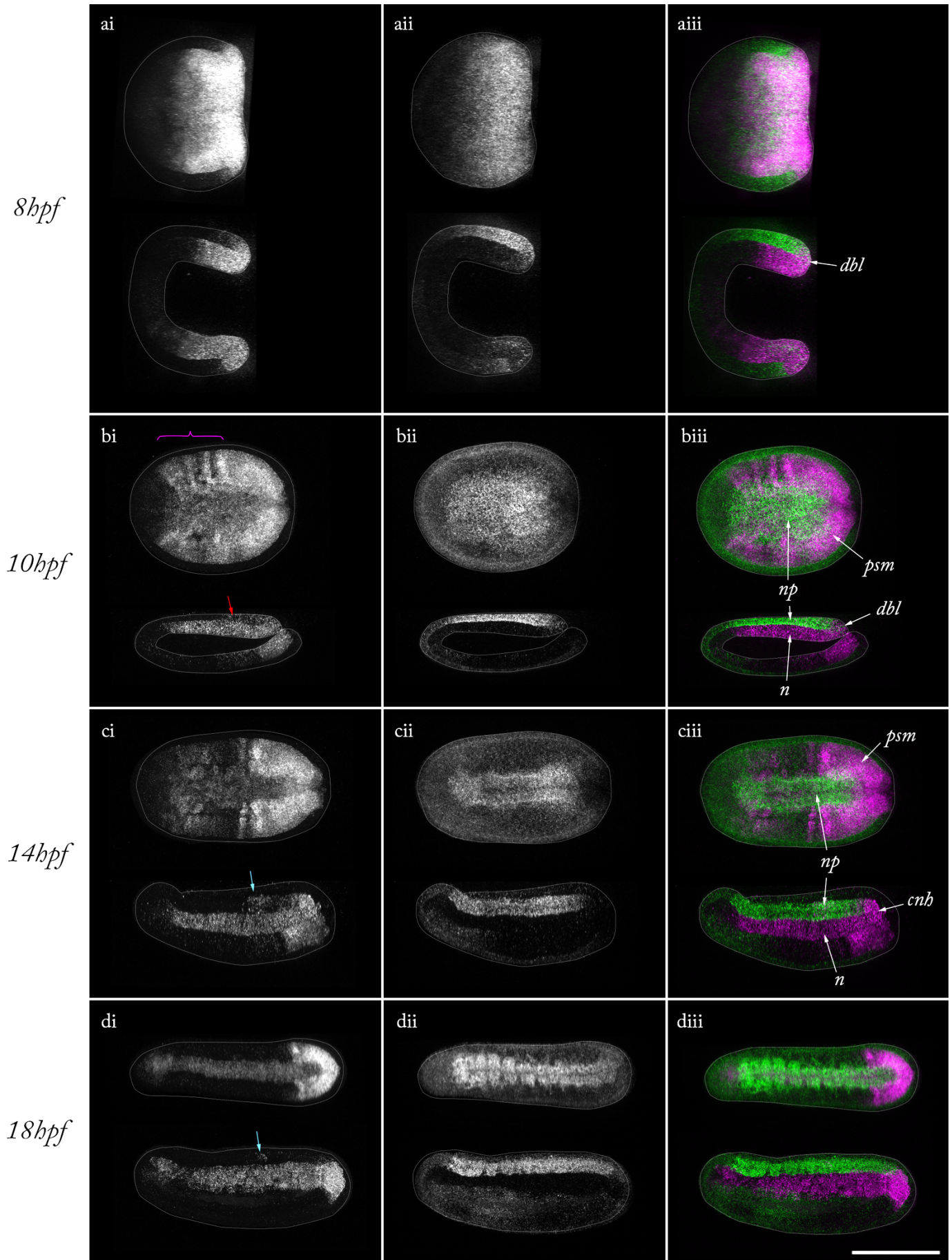
At 18hpf, epidermal sealing of the embryo is complete, and the neural plate has been internalised. The embryo has also commenced elongation along its anteroposterior axis (**Chapter III**). At this stage, expression of *Brachyury1/2* is lost from the anterior of the

Figure. 5.2. Expression patterns of *Brachyury1/2* and *Soxb1a/c* using multiplex HCR (overleaf). (a – d) HCR staining for *Brachyury1/2* and *Soxb1a/c* at the cup-shaped gastrula (ai – iii), narrowed-blastopore (bi – iii), 2ss (ci – iii) and 6ss (di – iii). Columns show *Brachyury1/2* expression (xi), *Soxb1a/c* expression (xii) and a merge (xiii). In each panel, the stained embryo is shown in Z-projection from a dorsal view (top) and small Z-projection through the axial midline in lateral view (bottom). (bi) Red arrow indicates expression of *Brachyury1/2* in the posterior neural plate. (ci, di) Cyan arrows indicate anterior expression domain of *Brachyury1/2* in the posterior neural plate. (a – d iii) In the merge panels, arrows also indicate landmarks discussed in **Chapter III**. dbl, dorsal blastopore lip; psm, presomitic mesoderm; np, neural plate; cnh, chordoneural hinge; n, notochord/chordamesoderm. Scale bar shows 100µm.

Brachyury1/2

Soxb1a/c

Brachyury1/2 + Soxb1a/c



paraxial mesoderm, overlapping with the segmented portion of the body axis (*Fig 5.2di, top*). However, it persists strongly in the posterior unsegmented body, again marking the two bilateral bands of presomitic mesoderm, and an additional anterior transverse stripe separated by a region of unlabelled tissue (*Fig 5.2di, top*). Meanwhile, *Brachyury1/2* expression persists at a medium level in the chordamesoderm at the midline of the archenteron (*Fig 5.2di, bottom*). Over the next 8 hours, these cells will intercalate along the dorsoventral axis to define the distinctive trilaminar cell topology of the notochord (**Chapter IV**). At 18hpf, the posterior domain of *Brachyury1/2* expression in the neural plate is lost, leaving expression only active on the ventral side of the chordoneural hinge. Nonetheless, expression persists in the more anterior domain, which persists as a small cluster of *Brachyury1/2+* cells punctuating the centre of the neural plate.

Soxb1a/c. *Soxb1a* and *Soxb1c* can be stained for individually using distinct HCR probe sets (Meulemans and Bronner-Fraser, 2007). However, for this study, I stained for both transcripts simultaneously, given that they complement to define a pan-neural expression pattern reminiscent of vertebrate *Sox2*. In the cup-shaped gastrula, expression of *Soxb1a/c* appears at a low level throughout the surface ectoderm, but most strongly on the dorsal side, in the prospective neural plate (*Fig 5.2aii*). At this stage, the neural plate is wide on the mediolateral plane, and short on the anteroposterior plane (*Fig 5.2aii*). In the dorsal blastopore lip, expression is strongest in the outer aspect, but also extends around the blastopore rim and into the inner aspect at a lower intensity (*Fig 5.2aii*). As a result, expression of *Brachyury1/2* and *Soxb1a/c* is overlapping in the posterior half of the neural plate and the dorsal blastopore lip during gastrulation (*Fig 5.2aiii*). A very similar distribution of *Soxb1a/c* can also be observed after blastopore narrowing, at 10hpf (*Fig 5.2bii*). Expression remains strong in the neural plate, which has now narrowed and elongated along the anteroposterior axis, and also spreads laterally into the epidermal ectoderm at a much lower intensity (*Fig 5.2bii*). Once more, expression of *Soxb1a/c* extends from the posterior neural plate around the blastopore rim and into the posterior tip of the chordamesoderm, where it overlaps with *Brachyury1/2* (*Fig 5.2bii, biii*).

Once the inner blastopore lip has been internalised, expression of *Soxb1a/c* declines in the chordoneural hinge (*Fig 5.2cii*). As such, at 14hpf, expression strongly marks the

neural plate, which is now covered on its dorsal side by a layer of epidermal ectoderm (*Fig 5.2cii*). This expression domain seems to overlap with the central cluster of *Brachyury1/2+* cells (*Fig 5.2ciii*). The other structure marked by *Soxb1a/c* expression at this stage is the anterior ventral endoderm, which exhibits a low level of *de novo* expression (*Fig 5.2cii, bottom*). Finally, at 18hpf, we can observe a very similar pattern of expression to 14ss. *Soxb1a/c* continues to mark the entirety of the neural plate, plus the epidermal ectoderm at a very low-level intensity (*Fig 5.2dii*). It has also expanded in the anterior ventral endoderm, although expression maintains its highest intensity in the anterior half of the tissue, that will later give rise to the pharyngeal arches (*Fig 5.2dii*). An interesting transition evident at 18hpf is that from a homogenous distribution of *Soxb1a/c* across the neural plate, to an apparently segmental pattern across the anteroposterior axis (*compare Fig 5.2cii and dii*). This is conspicuous in the anterior half of the tissue but collapses into a homogenous pattern more posteriorly. A segmental pattern in the anterior neural plate is highly reminiscent of the vertebrate hindbrain, marked by a segmental pattern of rhombomeres (Graham et al., 2014). And, indeed, a putative homology has been cast between these two structures (Jackman et al., 2000). Further investigation is required to discern whether the segmental pattern of *Soxb1a/c* in amphioxus is the result of variation in expression intensity between adjacent cells, or instead due to changes in cell spacing and boundary conditions.

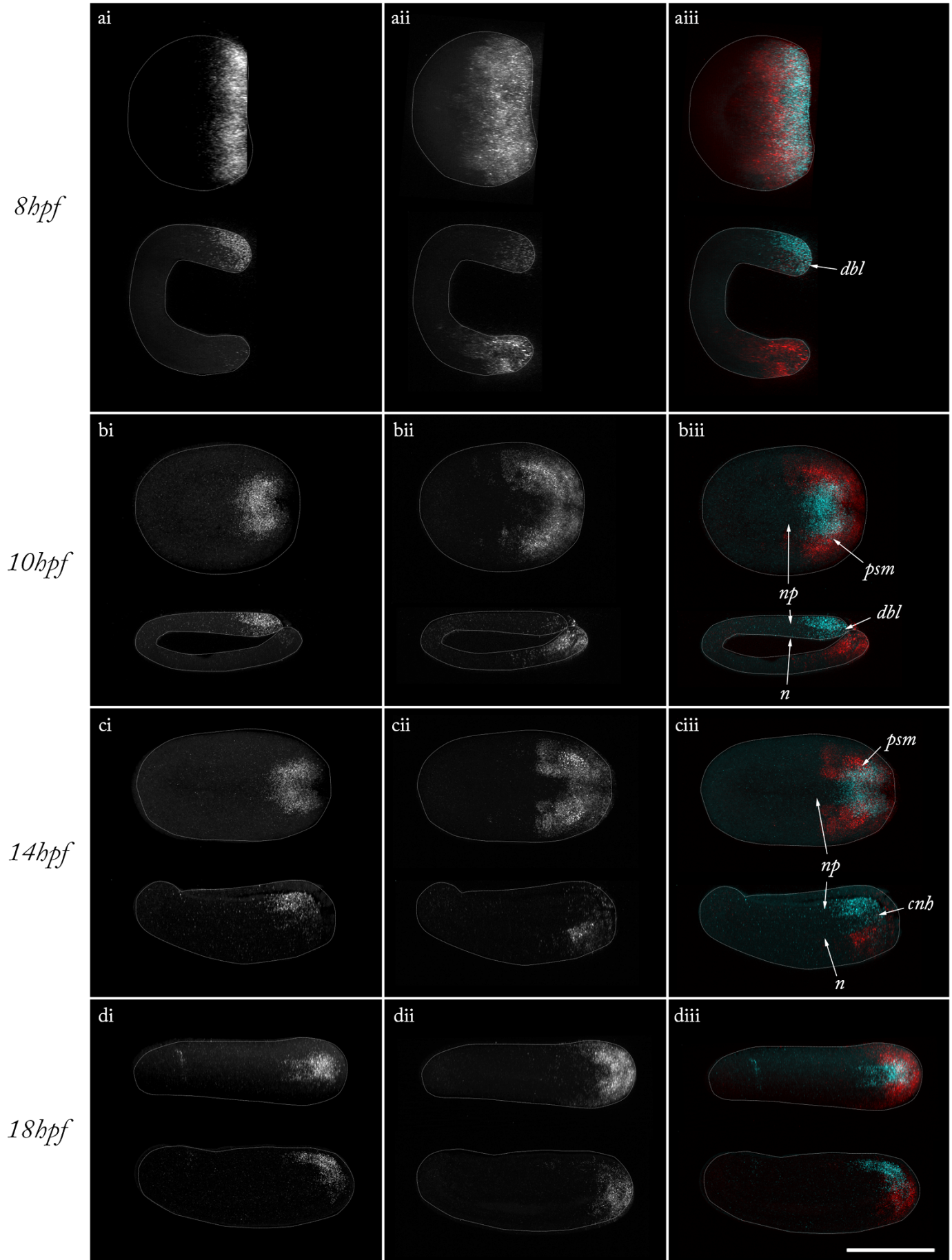
Noto. To my knowledge, expression of *Noto* has not been described previously in amphioxus. In the cup-shaped gastrula, *Noto* is expressed exclusively in the dorsal blastopore lip, with expression strongest into the ectoderm on the dorsal side, and weaker in the chordamesoderm on the ventral side (*Fig. 5.3ai*). *Noto* expression spreads across approximately 1/3rd of the neural tube length, as delineated by *Soxb1a/c* expression

Figure. 5.3 Expression patterns of *Noto* and *Tbx6/16* using multiplex HCR (overleaf). (a – d) HCR staining for *Noto* and *Tbx6/16* at the cup-shaped gastrula (ai – iii), narrowed-blastopore (bi – iii), 2ss (ci – iii) and 6ss (di – iii). Columns show *Noto* expression (xi), *Tbx6/16* expression (xii) and a merge (xiii). In each panel, the stained embryo is shown in Z-projection from a dorsal view (top) and small Z-projection through the axial midline in lateral view (bottom). (a – d iii) In the merge panels, arrows also indicate landmarks discussed in **Chapter III**. dbl, dorsal blastopore lip; psm, presomitic mesoderm; np, neural plate; cnh, chordoneural hinge; n, notochord/chordamesoderm. Scale bar shows 100µm.

Noto

Tbx6/16

Noto + *Tbx6/16*



(Fig. 5.3ai, compare with Fig 5.2aii). In this domain, the *Noto* pattern overlaps with that of both *Soxb1a/c* and *Brachyury1/2* (Fig. 5.3aiii). At 10hpf, after blastopore narrowing, *Noto* continues to exhibit a very similar expression pattern, with weak staining in the inner dorsal blastopore lip, and strong staining in the posterior neural plate, where it occupies a roughly circular domain when viewed dorsally (Fig. 5.3bi). At 14hpf, after epidermal sealing, the pattern of *Noto* expression is again largely unchanged, although the area it covers in the posterior neural plate appears to be slightly reduced (Fig. 5.3ci). Finally, at 18hpf, the area of expression is further reduced, while remaining at the most posterior tip of the neural plate (Fig. 5.3di). At this stage, the expression domain also appears to have elongated slightly along the anteroposterior axis, thereby losing its circular shape (compare Fig. 5.3ci and di). Now, in sagittal section, *Noto* expression can be located spreading from the posterior neural plate into the neurenteric canal, eventually dissipating upon entry to the posterior archenteron (Fig. 5.3di). In addition to its posterior expression at 18hpf, *Noto* also becomes expressed in 2-3 cells in the anterior tip of the neural plate, which manifest as a small transverse stripe (Fig. 5.3di, top).

Tbx6/16. In the cup-shaped gastrula, *Tbx6/16* is most strongly expressed in the inner lateral and ventral blastopore lips, thereby partially overlapping with the *Brachyury1/2* expression domain, and complementary to the *Noto* domain (Fig. 5.3aii, compare with Fig. 5.2aiii). However, expression can also be identified at a low level extending into the inner dorsal blastopore lip, where it therefore overlaps with both *Noto* and *Soxb1a/c* (Fig. 5.3aii). After blastopore narrowing, *Tbx6/16* follows the transition described for *Brachyury1/2* in shifting towards the dorsal side of the archenteron, where it becomes enriched in the presomitic mesoderm (Fig. 5.3bii). Unlike *Brachyury1/2*, *Tbx6/16* is restricted to the presomitic mesoderm throughout axial development, with no anterior expression in the paraxial mesoderm, and no expression in the chordamesoderm (Fig. 5.3bii). It does, however, exhibit weak transverse stripes anterior to the presomitic mesoderm at 10hpf, in a manner analogous to *Brachyury1/2* (Fig. 5.3bii). As development progresses, *Tbx6/16* expression restricts posteriorly with the shortening length of the presomitic mesoderm (Chapter III). All the while, it remains continuous between the two bands of presomitic

mesoderm across the ventral side of the embryo in the posterior archenteron (Fig. 5.3bii, cii). This is also matched by *Brachyury1/2* (Fig. 5.2bi, ci). Meanwhile, the expression pattern is discontinuous at the chordoneural hinge, which is occupied by the *Noto* expression domain (Fig. 5.3biii, ciii). In this respect, *Tbx6/16* and *Noto* expression remain largely mutually exclusive throughout early axial development (Fig. 5.3aiii - diii). Finally, at 18hpf, *Tbx6/16* expression has further restricted towards the posterior pole of the embryo, where its expression complements *Noto* on the ventral side of the neurenteric canal (Fig. 5.3dii, diii). At this stage, an additional expression domain can also be clearly identified in the posterior ectoderm, overlaying the neurenteric canal (Fig. 5.3dii, diii).

In the patterns described, *Brachyury1/2*, *Soxb1a/c*, *Noto* and *Tbx6/16* occupy a patchwork distribution of gene expression domains across the amphioxus posterior body. Considered in only binary on/off states, this summates to 15 potential expression states in individual cells, and the number increases *ad infinitum* if gene expression magnitude is also considered. In this respect, a rich body of information on cell state diversity lies within the HCR data collected, but this cannot be accessed through the qualitative description of single gene expression domains offered thus far. Having acquired these data, a method to integrate HCR data to resolve coherent quantitative definitions of cell states, at the single-cell scale, therefore crystallised as the next major hurdle. This would require local signal quantification, cell state clustering, and spatial mapping of topological domains – a major computational challenge.

5.3 Methods for cell type classification *in situ*

Any method for cell state definition from these data must overcome a number of important challenges; nuclear and/or cell segmentation, local quantification of gene expression intensity, discretisation of cell states within continuous gene expression domains, and faithful spatial mapping of cell states into the morphological structure of the embryo. The method that I will outline – ASCRIBE (Amphioxus Single-cell state Resolution with Integration Between Embryos) – passed through a series of iterations before reaching its final version, each of which had different pitfalls and successes that motivated further optimisation, and collectively highlight important thought processes in

quantitative gene expression analysis. For this reason, here I will describe development of ASCRIBE in its entirety.

5. 3. 1 Nuclear spheroids (Imaris)

The first approach I implemented equated the nucleus of each cell to a spheroid - a perfect sphere of fixed diameter, laid over the centre of homogenous mass for each DAPI-stained nucleus. This was achieved in Imaris (Bitplane, 9. 2. 1) using the *Spots* function, which I applied to the DAPI channel with a predicted nuclear diameter of $3.5\mu\text{m}$ (Fig. 5.4a - c). I found that underestimation of nuclear diameter was essential to resolve touching nuclei, which would otherwise be considered a single entity. Here, centre of mass detection was performed across the whole embryo (Fig. 5.4a - c), but validated in 2D sections by masking the centre of each putative spheroid (Fig. 5.4d). I next quantified the mean signal intensity for all HCR channels across all voxels contained within each spheroid. I chose the mean value as a way to determine the total amount of mRNA in the nucleus. Cytoplasmic signal was not considered using this approach, which would demand faithful segmentation of all cells in the embryo, and so was not possible with resources currently available in amphioxus. Instead, I considered nuclear signal the most important to sample, as a means to identify cells actively expressing each gene at the moment of analysis. It should be noted, however, that mRNA present in the cytoplasm, synthesised prior to fixation, will also influence the level of protein. Ultimately, immunohistochemistry against transcription factor proteins will be required to precisely determine GRN topology.

Removing them from their spatial context, I next dispersed all spheroids in a 3D coexpression scatter plot (Fig. 5.4e, f). The axes of the 3D scatter plot were normalised fluorescence intensities for *Brachyury1/2*, *Soxb1a/c* and *Tbx6/16* HCR signal, while the colour-code represented *Noto* signal intensity (Fig. 5.4e, f). In this expression space, the points dispersed into groups based on combinatorial expression of each candidate gene (Fig. 5.4f). For many cells, expression of the candidate markers was mutually exclusive, and so spheroids adhered tightly to the x, y and z axes of the scatter plot (Fig. 5.4f). In contrast, others exhibited coexpression of two or more candidate genes (Fig. 5.4f). To delineate

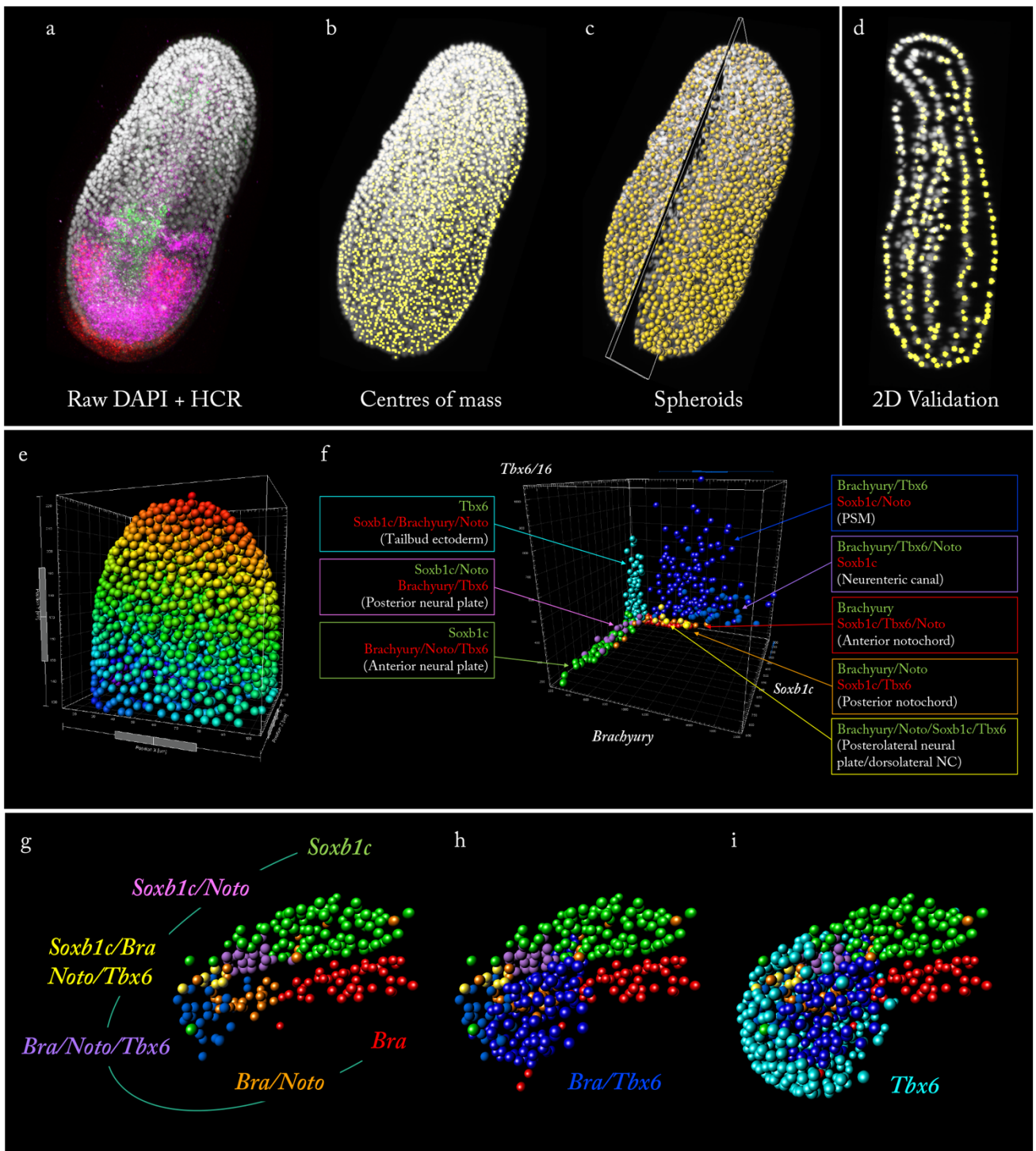


Figure. 5.4. Cell state classification using nuclear spheroids. (a – d) Nuclear spot detection and validation. (a) 3D projection of DAPI-stained nuclei and raw HCR signal for *Soxb1a/c*, *Brachyury1/2*, *Tbx6/16* and *Noto*. (b) Centres of mass detected in the DAPI channel using a 3.5 μ m prediction of nuclear diameter. (c) Nuclear spheroids overlaid onto the DAPI channel. (d) 2D sagittal section from plane marked in (c), showing DAPI staining and spheroids. (e) Spheroids from posterior half of embryo shown in (a – d), projected against AP, DV and ML coordinates. (f) Spheroids from posterior half of embryo shown in (a – d), projected against HCR signal intensities in 3D scatter plot. Colour-code corresponds to states defined using binary on/off thresholds. (g – i) Projection of states defined in (f) in AP/DV/ML coordinate system,

boundaries between each state represented in expression space, I applied a binary on/off threshold for expression of each gene, based on a manual measurements of channel-specific background intensity. With this logic, I circumscribed all possible combinations of expressed genes, from expression only of one single gene to simultaneous expression of all genes, and conferred each state represented in the embryo with a unique colour-code (Fig. 5.4f).

Once classified, cell states identified with the thresholding approach were then projected into the xyz coordinate system of the embryo to elucidate relative position and topological relationships, thereby offering a quantitative projection of the diversity and relative abundance of cell states. This is nicely demonstrated in the regionalisation of cell states from neural to mesodermal identity around the chordoneural hinge at 3ss (Fig. 5.4g - i). In the neural plate, cells exclusively expressed *Soxb1c*. Moving more posteriorly, cells coexpressed *Soxb1c* with *Noto*, and, in the chordoneural hinge, they also expressed the mesodermal markers *Brachyury1/2* and *Tbx6/16* (Fig. 5.4g). Moving forward from the chordoneural hinge into the axial mesoderm, expression of *Soxb1c* and *Noto* is lost, ultimately leaving cells only positive for *Brachyury1/2* (Fig. 5.4g). On the mediolateral plane, the mesoderm is also regionalised into *Brachyury+* *Tbx6/16-* cells at the midline, flanked by *Brachyury+* *Tbx6/16+* cells in the paraxial mesoderm (Fig. 5.4g, h). Finally, the early tailbud is ensheathed in a layer of *Tbx6/16+* ectoderm (Fig. 5.4i). The spheroid method is a relatively user-friendly approach for sampling cell states in HCR data, but it suffers from some important pitfalls. Namely, spheroids fail to capture the non-spherical detail of nuclei, which can result in both under-sampling of nuclear HCR signal and, when nuclear shape is particularly anisometric, inappropriate sampling of surrounding cytoplasmic signal (see Fig. 5.4d). The success of nuclear sampling is also tissue-specific, which risks a bias in the representation of cell states in datasets extracted from the embryo. Thus, although the spheroid approach was useful for an initial screening of cell state diversity, accurate nuclear segmentation was required for finer-grade cell state definition.

5. 3. 2 Nuclear segmentation (Imaris)

To address the poor capture of nuclear shape in the spheroid method, I sought to holistically segment nuclei, and began by using the Imaris automated surfaces function. This function applies an intensity threshold to the DAPI channel to construct a deformable surface around all objects, and then subdivides this surface between nuclei according to the distribution of nuclear spheroids (*Fig 5.5a, b*). I found this method to be very effective for the blastopore lip of the cup-shaped gastrula, in which nuclei are both large and loosely packed. After segmentation, I validated its resolution of distinct nuclei by random false colouring of each object, which revealed a mosaic pattern of colours across the blastopore (*Fig 5.5c*). From this foundation, I quantified the mean intensity of each HCR channel in all nuclei (*Fig 5.5d*), and defined cell states with on/off threshold as per the spheroid method. In this case, I trialled the use of a ven diagram to illustrate cell state diversity, showing all possible combinations of genes included in the HCR data, and those actually represented in the embryo (*Fig 5.5e*). To enhance the interactivity of these data, I also false-coloured the DAPI channel according to cell state (*Fig 5.5e, f*). By this method, their diversity and topology can be explored in 3D projections and slices of the embryo, as demonstrated by the landscaping of cell states around the dorsal blastopore lip (*Fig 5.5f*). This mirrors the distribution described around the chordoneural hinge using the spheroid approach. In addition, cell types could be validated by isolating nuclear HCR signal, and manually confirming the presence of punctae for specific mRNA species (*Fig 5.5g*).

This approach was very promising in permitting quantitative resolution of cell states with full sampling of nuclear HCR signal, and the exploration of cell state diversity within the interactive 3D interface offered by Imaris. However, I encountered a major obstacle in the failure of the Imaris surfaces function to faithfully segment nuclei after gastrulation. This was most likely due to ongoing rounds of volumetrically-reductive cell division which, as I discussed in **Chapter III**, act to focally increase nuclear density and reduce cell size. In turn, when applied in stages after gastrulation, many nuclei were fused in the segmentation map, which generated numerous false-positives in the later steps of cell state definition. Although under-segmented objects can be removed by applying a volume-filter to the data, this led to removal of large groups of cells, resulting in a poor sampling of nuclei in the

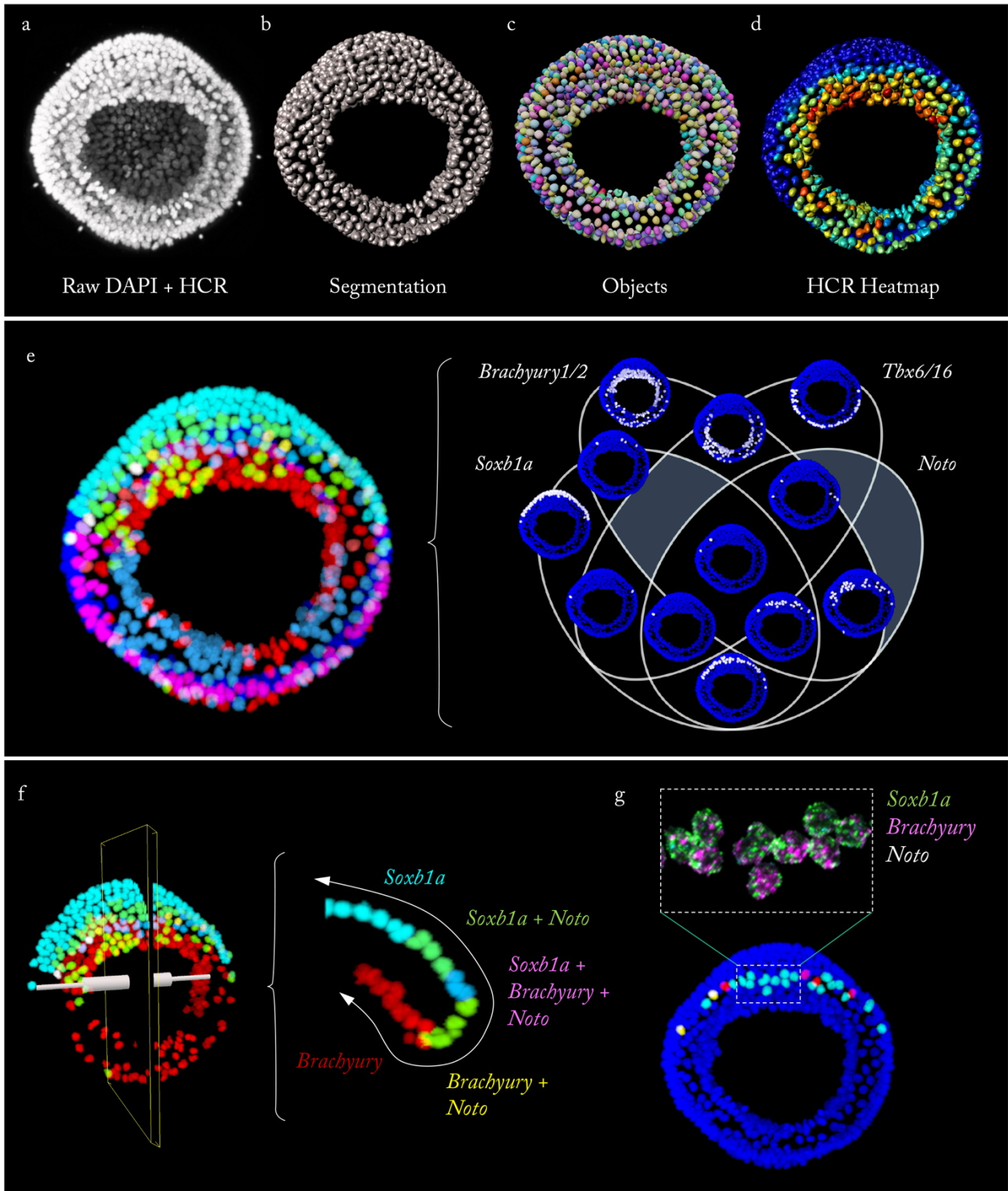


Figure. 5.5. Cell state classification in the cup-shaped gastrula using Imaris surfaces. (a – d) Nuclear segmentation workflow. An automated surfaces function is applied to the raw DAPI channel (a, b), and partitioned between nuclei located using the spots function (c). (d) HCR signal is quantified within each segmented nucleus. (e) Binary definition of on/off thresholds locates cells in each of 15 potential expression states, colour-coded in a single embryo (left), and dispersed in a ven diagram (right). (f) Cell states mapped into spatial context by false-colouring DAPI channel, revealing regionalisation around dorsal blastopore lip. (g) Masking of HCR signal within the *Soxb1a/c+ Brachyury1/2+ Noto+* state classification.

posterior body. For this reason, I needed to seek a more sensitive method for nuclear segmentation.

5.3.3 Nuclear boosting (Ilastik/Imaris)

I next performed a screen of available open-source nuclear segmentation approaches. The method that I found most fruitful was the machine learning platform, Ilastik (Berg et al., 2019). Here, manual labelling of signal and background iteratively trains an object classifier, that translates the raw DAPI channel into a pixel prediction map, defining which pixels are, and are not, part of the object group (*Fig 5.6a, b*). Pixels deemed part of the object group are then clustered into distinct objects in a process of hysteresis thresholding (*Fig 5.6c*). Here, a high threshold is applied to identify the centre of each object, whilst sacrificing peripheral details of nuclear shape. Next, these objects are dilated according to a secondary low threshold to capture the shape of the entire nucleus, in the process retaining a memory of object identity established by the first threshold. As such, if adjacent nuclei come into contact during the dilation step, they are not merged into a single object. The default pixel-classification workflow in Ilastik was suitable for early embryos but, like Imaris, was unable to cleanly segment those from later stages when nuclei are more densely-packed. However, I achieved high quality segmentation using an auto-context pipeline, in which two rounds of pixel classification are performed. After the first round, the pixel classification map is added to the raw data as a new input layer, thereby boosting the signal-to-background ratio. This enabled the second round of training to achieve high quality segmentation for multiple developmental stages, even in small and densely packed nuclei (*Fig 5.6d*). After segmentation I found that I could threshold out over-segmented and fused (under-segmented) nuclei based on object volume, thereby depleting false-negatives and -positives in the dataset (*Fig 5.6e, f*). In all, the auto-context method successfully segmented 95.12% of all nuclei for stages between cup-shaped gastrula and 6ss.

To maintain the interactivity of cell type analysis, I first used Ilastik segmentation to expand the stages fit for analysis with the Imaris method. This evolved into what I termed the 'boost method'. The Ilastik pixel-prediction map alone could not be interpreted by the Imaris surfaces function because it lacked the spatial variation in signal

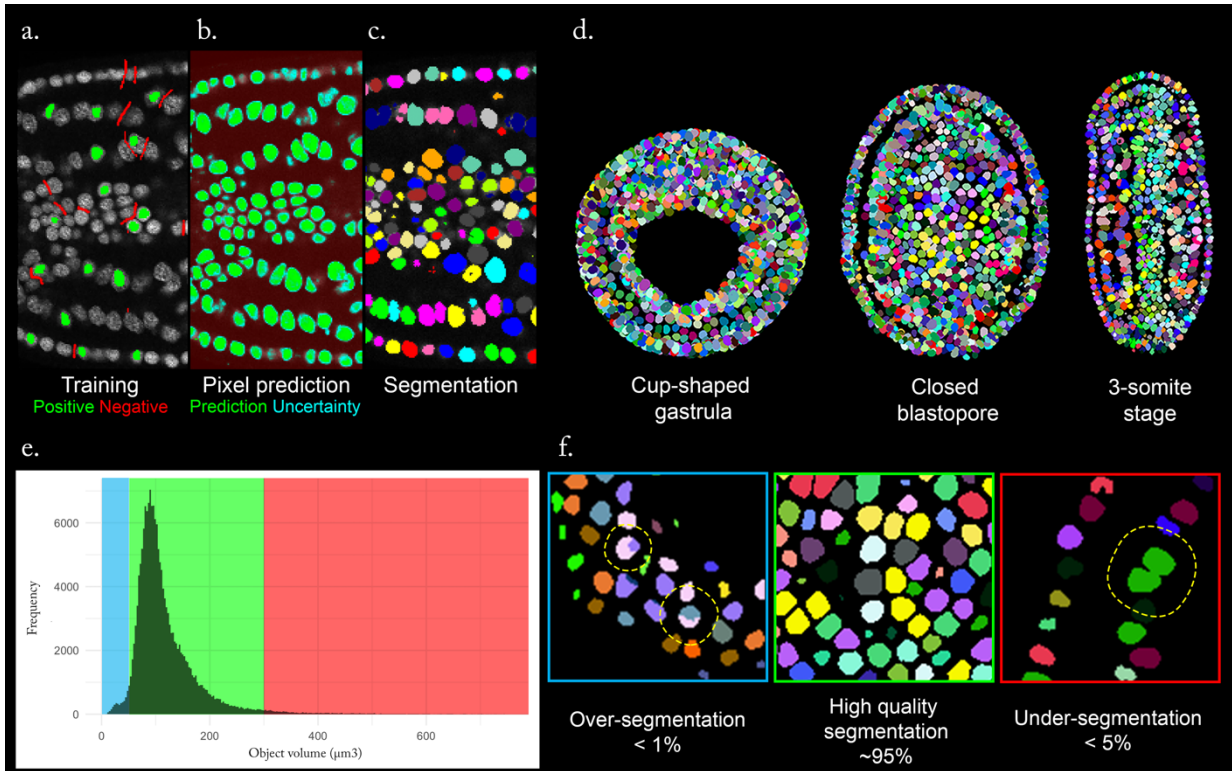


Figure 5.6. Pipeline for nuclear segmentation with Ilastik. (a) A small sample of the DAPI channel is imported to Ilastik for classifier training, based on allocation of positive (green) and negative (red) labelling of the raw data. (b) The training output is a pixel prediction map, reflecting the likelihood that individual pixels are part of the objects of interest. (c) Pixels are grouped into objects using hysteresis thresholding, with an initial threshold of 0.85 and a secondary threshold of 0.6. (d) Samples of the three developmental stages analysed so far, generated as max projections through the whole embryo for the cup-shaped gastrula, or just the coronal midline for subsequent stages. (e) Histogram of nuclear volumes, showing a sharp peak for correctly segmented nuclei, and the surrounding distribution of outliers. (f) Samples of correctly and incorrectly segmented nuclei with estimated abundance.

intensity required to split touching objects. I therefore used the Ilastik segmentation map to aid the identification of objects within the DAPI channel given as input to Imaris, analogous to the logic of the Ilastik auto-context method. Here, I segmented the entire embryo in Ilastik, and used a mask of the segmentation map to enhance the signal-to-background ratio of the DAPI channel. To achieve this, I binarised the Ilastik segmentation map and converted it to 8-bit, thereby enforcing a maximum pixel intensity of 255. I then added this to the DAPI channel, thereby ‘boosting’ the positive signal against

noise and background, without enforcing a binary distinction. In Imaris, this permitted effective nuclear segmentation across all stages, and therefore interactive definition of cell types. Stages in this workflow are illustrated in *Fig 5.7a*. Proof-of-concept analysis revealed interesting changes in cell type abundance between the cup-shape gastrula and 6-somite stage (*Fig 5.7b*). Namely, it seemed that there was a progressive depletion of coexpressing cell states, possibly reflecting commitment to specific tissue fates in the wake of gastrulation. A major problem with this method, however, was the extremely low throughput and user-bias. In all, cell type classification of a single embryo took 2-3 hours, in addition to the time required for segmentation in Ilastik and nuclear boosting. This proved inhibitory to collection of enough data for a statistically meaningful analysis. In addition, I found that manual definition of on/off thresholds in each embryo introduced bias between specimens, and identification of blanket thresholds to be apply across all specimens was challenging given that imaging data for each specimen was analysed sequentially rather than in parallel.

5.3.4 ASCRIBE I: Dispersal of nuclei in gene expression space

My response to these limitations was to develop a bespoke cell-typing pipeline external to Imaris, that permitted rapid and parallel analysis of multiple specimens, identify flexible non-binary gene expression thresholds, and ensure efficient mapping of cell states into mean embryo morphology. The product is ASCRIBE (Amphioxus Segmentation and Cell-state Resolution with Integration Between Embryos), which, unlike the previous iterations, can be executed entirely with free and open-source software. This makes the approach much more accessible and appealing in non-model systems. First, auto-context Ilastik segmentation is performed for all specimens, requiring a training set to be developed manually for each developmental stage and then applied in a batch processing step across the entire dataset. This training sample consists of approximately $\frac{1}{4}$ the Z-stack for a single specimen, that is representative of the total heterogeneity in nuclear shape and granularity. On average, the training requires ~30 minutes of active manual training per stage. The resulting segmentation maps are imported into ImageJ, and overlaid onto the raw data for each embryo. Next, the 3D ROI manager plugin (Ollion et al., 2013) is used to calculate the mean signal intensity for each HCR channel in all segmented nuclei. In this case, I

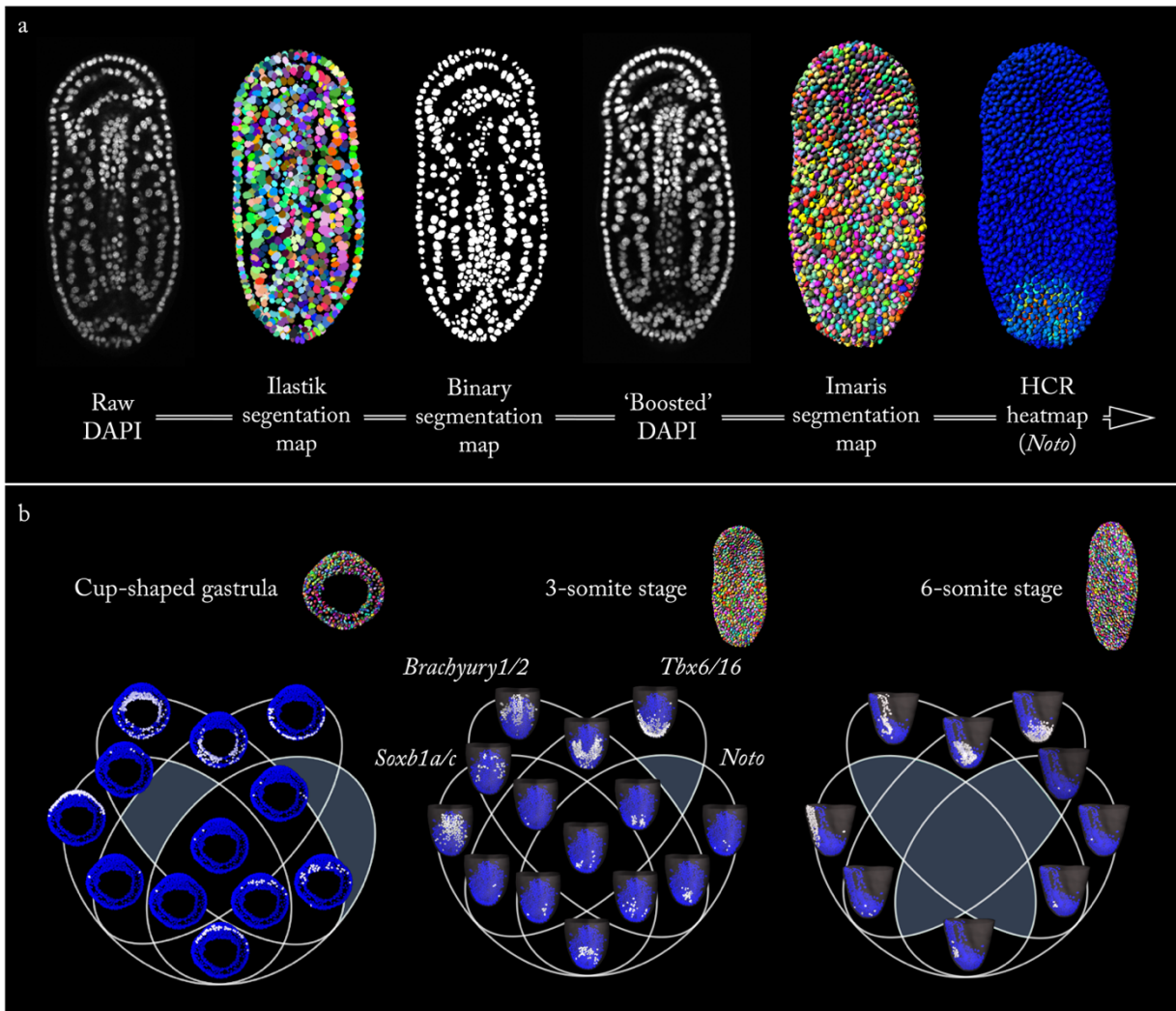


Figure. 5.7. Cell state classification using a nuclear boosting workflow. (a) Pipeline for enhanced nuclear segmentation in Imaris using nuclear boosting. The raw DAPI channel is imported to Ilastik for nuclear segmentation in an auto-context pipeline. The output is binarised in ImageJ and added to the raw DAPI channel to 'boost' positive signal and enhance the signal:background ratio. The Imaris surfaces function is used to segment the boosted DAPI signal. (b) Cell state classification in stages following gastrulation; the cup-shaped gastrula (posterior view), 3-somite stage (dorsal view) and 6-somite stage (lateral view). Shaded panels show states not represented by any nuclei in the embryo.

wrote a simple macro to rapidly collect intensity values for all nuclei in all embryos, and then code the resulting .csv files by stage and embryo identity. The remainder of the analysis is performed simultaneously across all embryos in the dataset using a code written in R script.

In the design of this method, I wanted to avoid the reductionist view and user bias of gene expression states dependent on calculation of on/off thresholds. Indeed, cell states depend not only on which genes are expressed, but their relative intensities. I therefore removed the on/off thresholding step applied in previous iterations of this method. In ASCRIBE, I first performed a routine signal normalisation between a measured channel-specific background value and the 95th percentile, thereby removing saturated pixels that carry no quantitative information; these must, nonetheless, be present in small numbers during imaging to ensure the dispersal of intensity values across the full extent of the greyscale. The data collected here can be considered to occupy a four-dimensional gene expression space. To explore this space, I took inspiration from Trivedi et al (2018) and sampled gene expression in pairwise coexpression scatter plots, in which cells occupy a series of semi-continuous domains (*Fig 5.8a*). Cells in each of these domains can be isolated in a unique data frame for further analysis using a polygonal selection tool (*Fig 5.8b*). Unlike in the previous approaches, the thresholds applied to isolate cell states in ASCRIBE are defined for all embryos simultaneously.

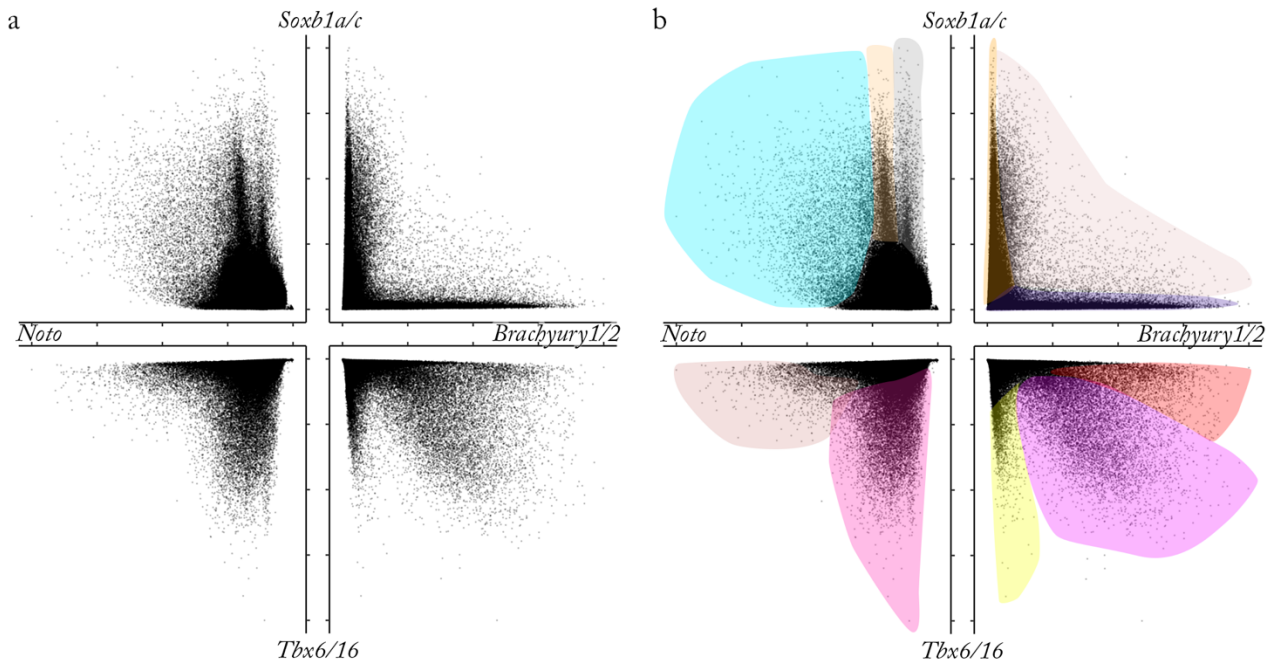
5.3.5 ASCRIBE II: Spatial mapping of putative cell states

The next challenge is to map groups of cells resolved in gene expression space back into their spatial context in the embryo. Unlike the previous methods discussed, this approach considers nuclei from numerous embryos and is removed from the graphical user interface of Imaris, so returning from gene expression space to morphological space is not trivial. Given the population scale of the expression analysis, I decided that the most informative method would be to construct ‘average’ embryos containing information from all specimens in the analysis (*Fig 5.8c*). To illustrate mean embryo shape, the nuclei of all embryos from a specific stage were superimposed by removing variation in size. This is achieved by normalising the length of each axis, and then scaling this length to the mean. If not achieved during imaging, rotational variation also needs to be removed for effective superimposition. Where necessary, I rotated the points for individual specimens in R using the ‘spdep’ package (Bivand and Wong, 2018), to avoid changes in pixel intensity prior to signal quantification due to interpolation performed in most rotation functions in ImageJ. Next, a density map was plotted across all superimposed nuclei, thereby exposing the mean

shape in any given view (*Fig 5.8c*). Cell states sampled from the gene expression matrices are then projected over the density plot using normalised xyz positions (*Fig 5.8c*). Three-dimensional information is offered by ordering and colour-coding cells by z position, and exploring each average embryo in multiple views. It is important to note that the patterns resolved through spatial mapping are made up of cells from all embryos, which means that any given cell state will be over-represented compared to their abundance in individual specimens. However, for poorly represented cell states, this is powerful in translating scattered cells into coherent domains. This can inform of the *possible* distribution of cells, regardless of true abundance.

Many cell states separated in the coexpression plots correspond to known tissue compartments, while others define previously unidentified cell states (*Fig 5.8c*). Presomitic mesoderm (PSM), as defined in **Chapter III**, is here composed of cells coexpressing *Brachyury1/2* and *Tbx6/16*, with weak expression of *Noto*. These cells are initially circumblastoporal, and later populate both bands of PSM and the neurenteric canal. A neighbouring cell state in the *Brachyury1/2* vs *Tbx6/16* scatter plot exhibits stronger *Brachyury1/2* expression and weaker *Tbx6/16*, and maps into early anterior somites and the chordamesoderm. Conversely, a posterior ectodermal stripe, that comes to occupy the posterior pole of the embryo, is defined by stronger *Tbx6/16* expression and weaker *Brachyury1/2*. The neural plate is marked by expression of *Soxb1a/c*, but is regionalised along the anteroposterior axis by coexpression of *Noto*, as also noted in the raw data. Cells in the most posterior neural plate coexpress both markers, while *Noto* is weak or absent in

Figure. 5.8. Sampling of cell states separated in expression space reveals known and unknown populations (overleaf). (a) Nuclei from all three stages analysed dispersed in four pair-wise coexpression scatter plots based on mean fluorescence intensity within the segmented nucleus. Data normalised between measured channel-specific background intensities and the 95th percentile. Values of 0 not shown. (b) Domains of expression space sampled for spatial distribution using a polygonal manual selection tool, with colour corresponding to mapping in (c). (c) Distribution of sampled cells in average embryos for each developmental stages, all projected in dorsal view. Heat map reflects Z-position, with warmest colours dorsally and coldest ventrally. Dataset consists of 134,812 nuclei from 32 specimens imaged at 30X optical magnification.



more anterior neural cells. The posterior neural plate is also home to a pair of bilateral domains coexpressing both *Noto* and *Tbx6/16*. In sum, the cell states sampled in expression space map onto coherent spatial domains in the embryo, illustrated on a population-scale as average embryos. ASCIBE therefore enables rapid quantification of cell state diversity across multiple embryos from *in situ* imaging data, and interactive information flow from morphological space to gene expression space (and back) for single-cell state classification *in situ*.

5.4 Location, fate and potency of neuromesodermal cell states

Having established ASCRIBE as a reliable approach to define and spatially map cell states *in situ*, I sought to apply it to test for the presence of neuromesodermal progenitors (NMps) in the amphioxus embryo. Here, I combined ASCRIBE with pharmacological perturbation and cell marking to define the presence and dynamics of NMps in amphioxus development per their molecular and embryological definition in vertebrate systems; a) Coexpression of neural and mesodermal genes after gastrulation, b) neuromesodermal fate, referring to their contribution to both lineages in normal development, and c) neuromesodermal competence, referring to their ability to generate neural or mesodermal derivatives.

5.4.1 Isolation of neuromesodermal cells with gene expression thresholding

I first screened for NM cells in stages spanning the termination of amphioxus gastrulation (following criteria detailed in **Chapter III**) by filtering nuclei positive in expression for both *Soxb1a/c* and *Brachyury1/2*. If germ layer segregation is truly restricted to gastrulation, respective genetic markers should exhibit entirely mutually exclusive expression patterns. When dispersed in a *Soxb1a/c* x *Brachyury1/2* coexpression scatter plot, nuclei exhibited a continuous distribution, from those uniquely expressing one marker, to those combinatorially expressing both markers (*Fig 5.8a, 5.9ai – ci*). Within this, expression of each marker was largely anti-correlated, such that the strongest expression of one gene invariably correlated with weakest expression of the other - no cells were present that expressed both *Brachyury1/2* and *Soxb1a/c* at their highest intensity values. However,

between these states were cells expressing both *Soxb1a/c* and *Brachyury1/2* at a similar medium intensity (5.9ai – ci). Given the continuous distribution of nuclei across the coexpression scatter plot, we can infer that the NM state is not discrete. In other words, there is no distinct cluster of *Soxb1a/c*+ *Brachyury1/2*+ cells. Instead, cells possess NM quality to different extents, from those expressing both genes at similar intensity, to those predominantly expressing one marker. This finding aligned with expectation from studies in vertebrate systems, in that the NMP is part of a developmental continuum, in which NMP progeny will differentiate towards states in which either *Soxb1a/c* or *Brachyury1/2* expression dominates and the other is lost; at late developmental stages, we should expect a perfectly anti-correlated distribution in expression space.

In order to locate NM cells in the embryo, I elevated minimum threshold values for normalised expression intensities of *Soxb1a/c* and *Brachyury1/2* (Fig 5.9a – c). In a continuum of gene expression intensities, any binary threshold defined is inherently arbitrary. In turn, such a threshold can be tuned to extract greater or lesser fractions of cells from the total population. When I applied only low thresholds for *Soxb1a/c* and *Brachyury1/2*, I isolated a large proportion of cells in the embryo (Fig 5.9ai, aii). This covered the blastopore of the cup-shaped gastrula, and, later, the posterior half of the neural plate, also spreading into patches of surface ectoderm, ventral endoderm and paraxial mesoderm (Fig 5.9aii). There seemed to be very poor tissue specificity to this cellular fraction. When the thresholds were elevated to isolate cells expressing medium to high levels of *Soxb1a/c* and *Brachyury1/2*, I enriched those more specifically restricted to the posterior neural plate after gastrulation, while removing the majority of cells in the ectoderm, endoderm and paraxial mesoderm (Fig 5.9bi, bii). Finally, when I elevated the thresholds further, the density of cells in each of these regions further declined such that they no longer occupied coherent domains (Fig 5.9ci, cii). For the purposes of this investigation, I continued analysis using the medium thresholds identified for *Soxb1a/c* and *Brachyury1/2*, which isolated coherent domains in the embryo, enriched with cells exhibiting an NM expression signature.

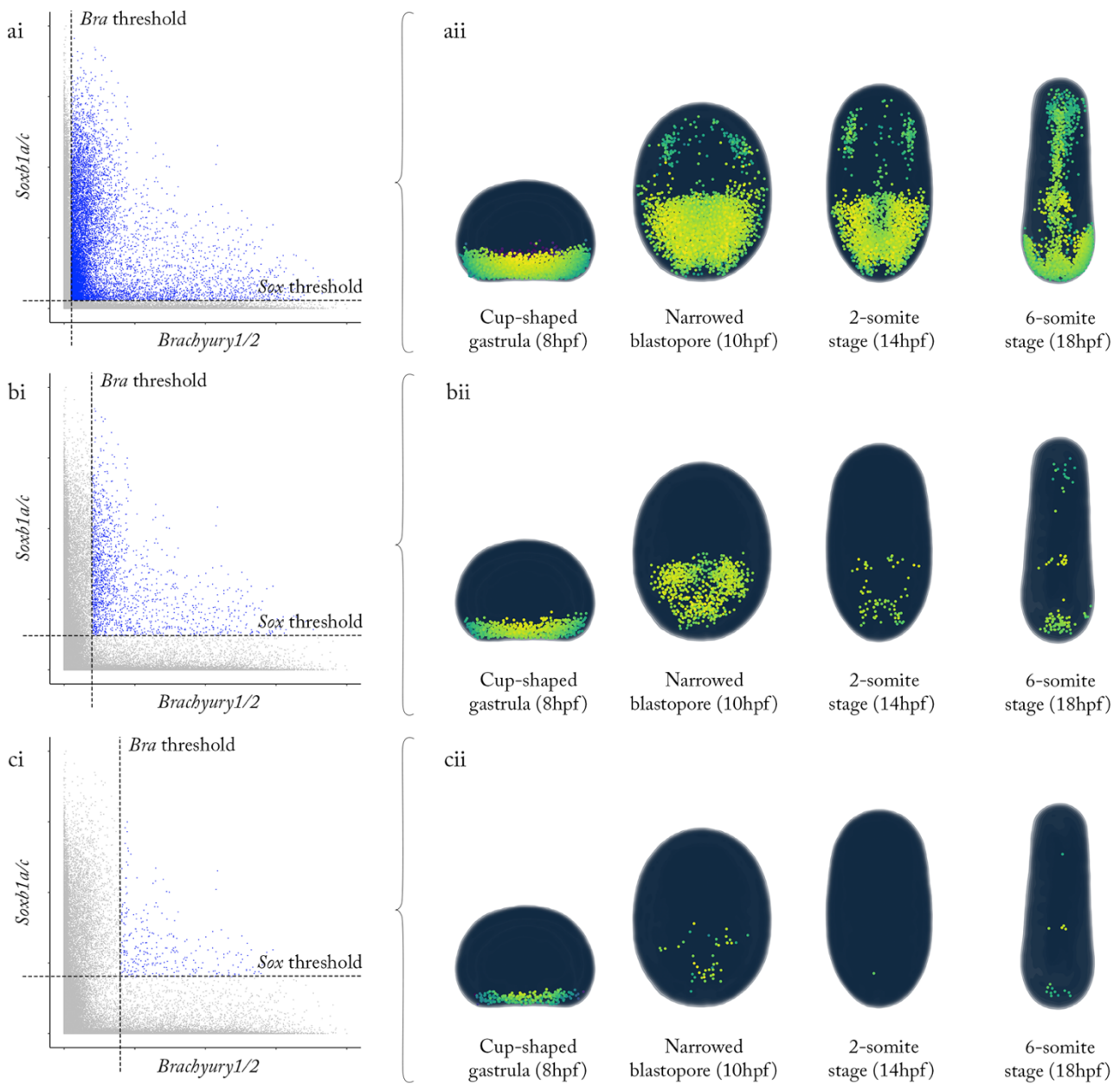


Figure 5.9. Definition of gene expression intensity thresholds to isolate *Soxb1a/c*⁺ *Brachyury1/2*⁺ cells. Three proposed thresholds applied to normalised expression intensities of *Soxb1a/c* and *Brachyury1/2*, with spatial mapping of NM population at successive developmental stages; a low threshold (0.05) (a), medium threshold (0.1) (b) and high threshold (0.2) (c). The low threshold (a) extracts cells with poor tissue specificity. The medium threshold (b) extracts those in coherent domains. The high threshold (c) extracts those in the same domains, but at lower density.

5. 4. 2 Spatial mapping of neuromesodermal cells

Next, I performed a closer analysis of the changing distribution of NM cells isolated with medium threshold values for *Soxb1a/c* and *Brachyury1/2*. Spatial mapping on a population scale, into average embryos, revealed a series of major transitions in NM topology over developmental time. Here, it is important to reiterate that the average embryos contain *all* cells, in this case derived from 8 different embryos for a given stage, and so patterns reflect changes in the position and size of domains occupied by NM cells, and relative changes in density, but *not* changes in true number. NM cells were initially located in the dorsal blastopore lip of the cup-shaped gastrula, with a density depleting from dorsal to ventral (*Fig 5.10a*). Only very occasionally were NM cells detected in the ventral blastopore lip. After blastopore narrowing, at 10hpf, NM cells were enriched in the posterior half of the neural plate (*Fig 5.10b*). Superficially, this appeared to consist of three clusters of cells; a bilateral pair of clusters anteriorly, on the left and right sides of the embryo, lying in front of another posterior cluster in a midline position (*Fig 5.10b*). In the next eight hours, the density of NM cells in each of these domains declined, to leave one small population associated with the chordoneural hinge, and another more anteriorly in the centre of the neural plate (*Fig 5.10c, c*). These two groups of cells were non-overlapping, separated by a region devoid of NM cells (*Fig 5.10c, d*). Between 2ss and 6ss, another sparse population also emerged at the anterior tip of the embryo, which was non-overlapping with the posterior domains (*Fig 5.10d*).

I next spatially mapped NM cells into single embryos from each developmental stage to resolve the specific tissues containing NM cells, and to validate NM through qualitative analysis of intranuclear HCR signal. In *Fig. 5.10e - h*, a representative embryo from each stage is shown in orthogonal views, with cells classified as NM in gene expression space highlighted in white. At each stage, the HCR signal within each NM nucleus is isolated, showing the presence of puncta for both *Soxb1a/c* and *Brachyury1/2* mRNA, and a more restricted distribution of *Noto* and *Tbx6/16* (*Fig. 5.10e - h, inlays*). This validates classification of the cells isolated in gene expression space as being in a NM state. The inhomogeneous distribution of *Noto* and *Tbx6/16* expression across the NM population also hints at further heterogeneity. This is most conspicuous at 10hpf and 14hpf, in the

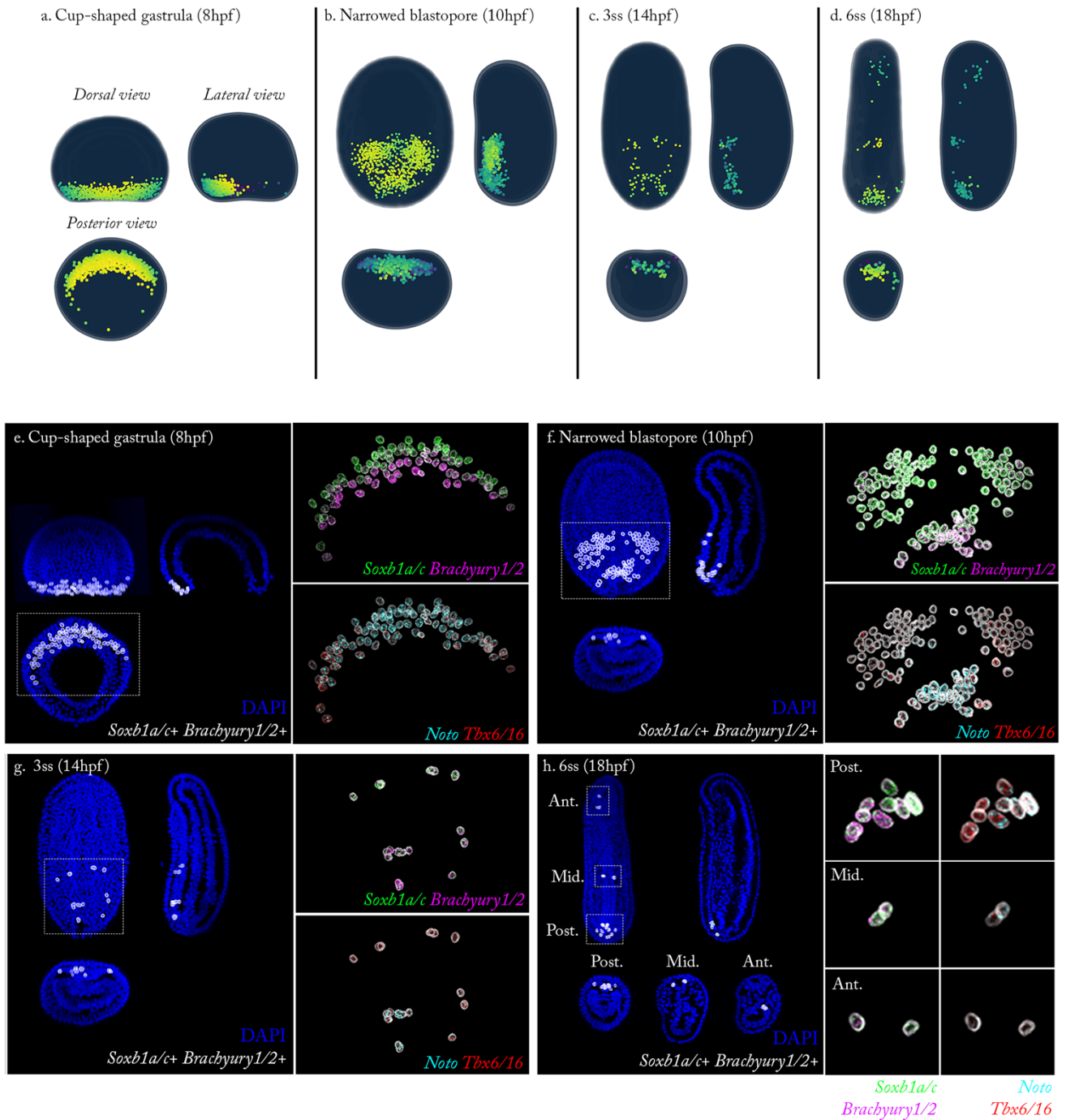


Figure 5.10 Spatial mapping of neuromesodermal cells. (a – d) Spatial mapping of NM cells isolated using medium threshold intensities in average embryos, between cup-shaped gastrula and 6ss. In each panel, a – d, average embryos are shown in dorsal view, lateral view and posterior view as annotated in panel (a). (e – h) Spatial mapping of NM cells into single embryos using *MorphoLibJ* to mask ASCRIBE-filtered NM nuclei in ImageJ. In main panel of (e – f), single embryos are shown in dorsal, lateral and posterior views as annotated in (a). NM nuclei are false-coloured in white over blue DAPI staining. Inlays show NM cells in dorsal view, with HCR signal for *Soxb1a/c* and *Brachyury1/2*, and *Noto* and *Tbx6/16* separately. In panel (h), separate inlays are provided for the posterior, middle and anterior NM groups emerging along the anteroposterior axis, in this case shown in lateral view.

expression of *Noto* and *Tbx6/16* only in posterior NM cells, while the more anterior clusters are exclusively positive for *Soxb1a/c* and *Brachyury1/2* (Fig. 5.10f - g). Spatial mapping of NM cells into individual embryos confirmed their early concentration in the posterior neural plate rather than adjacent epidermal ectoderm or mesoderm (Fig. 5.10e, f). However, in sagittal sections of the 10hpf embryo, NM cells can be identified extending from the posterior neural plate into the chordoneural hinge, thereby coming to lie posterior to axial mesodermal precursors (Fig. 5.10f). Analysis of single embryos also revealed that the 3 spatial clusters present in the posterior neural plate at 10hpf are matched by the pattern in individual embryos, rather than emerging as a batch effect (Fig. 5.10f). At 18hpf, sagittal and transverse sections confirmed the sustained presence of NM cells at the posterior tip of the neural plate, and an additional smaller domain in the centre of the neural plate (Fig. 5.10h). In the embryos studied in this dataset, the latter population contained 1-3 nuclei, which are biased towards the lateral margins of the neural plate. Finally, transverse sections through the anterior body showed the third late-emerging population to reside in the anterior endoderm (Fig. 5.10h). The most parsimonious interpretation is that this latter population emerges *de novo* at the onset of *Soxb1a/c* expression in the endoderm, where *Brachyury1/2* is already expressed (see Fig 5.2).

5. 4. 3 Temporal transitions in neuromesodermal cell number and diversity

Having verified the presence of NM cells in the amphioxus embryo, and mapped their changing spatial distribution in the early stages of axial development, I next sought to define how NM number and diversity changes over time. To this end, I first explored the distribution of *Soxb1a/c*+ *Brachyury1/2*+ cells across all pairwise coexpression scatter plots. In doing so, I found that NM cells classified by this method disperse into domains associated with both posterior neural (*Soxb1a/c*+ *Noto*+) and presomitic mesodermal identity (*Brachyury1/2*+ *Tbx6/16*+) (Fig 5.11a). Within the *Soxb1a/c* x *Noto* scatter plot, NM cells separated into two groups: one group exhibited mid-to-high expression of *Soxb1a/c* and low expression of *Noto* (Fig 5.11a, red group), while the other group exhibited mid-to-high expression of *Noto* with a medium level of *Soxb1a/c* (Fig 5.11a, cyan group). Following this observation, I introduced a new classifier for each group, and examined their respective distributions across the other scatter plots. The low-*Noto* NM population

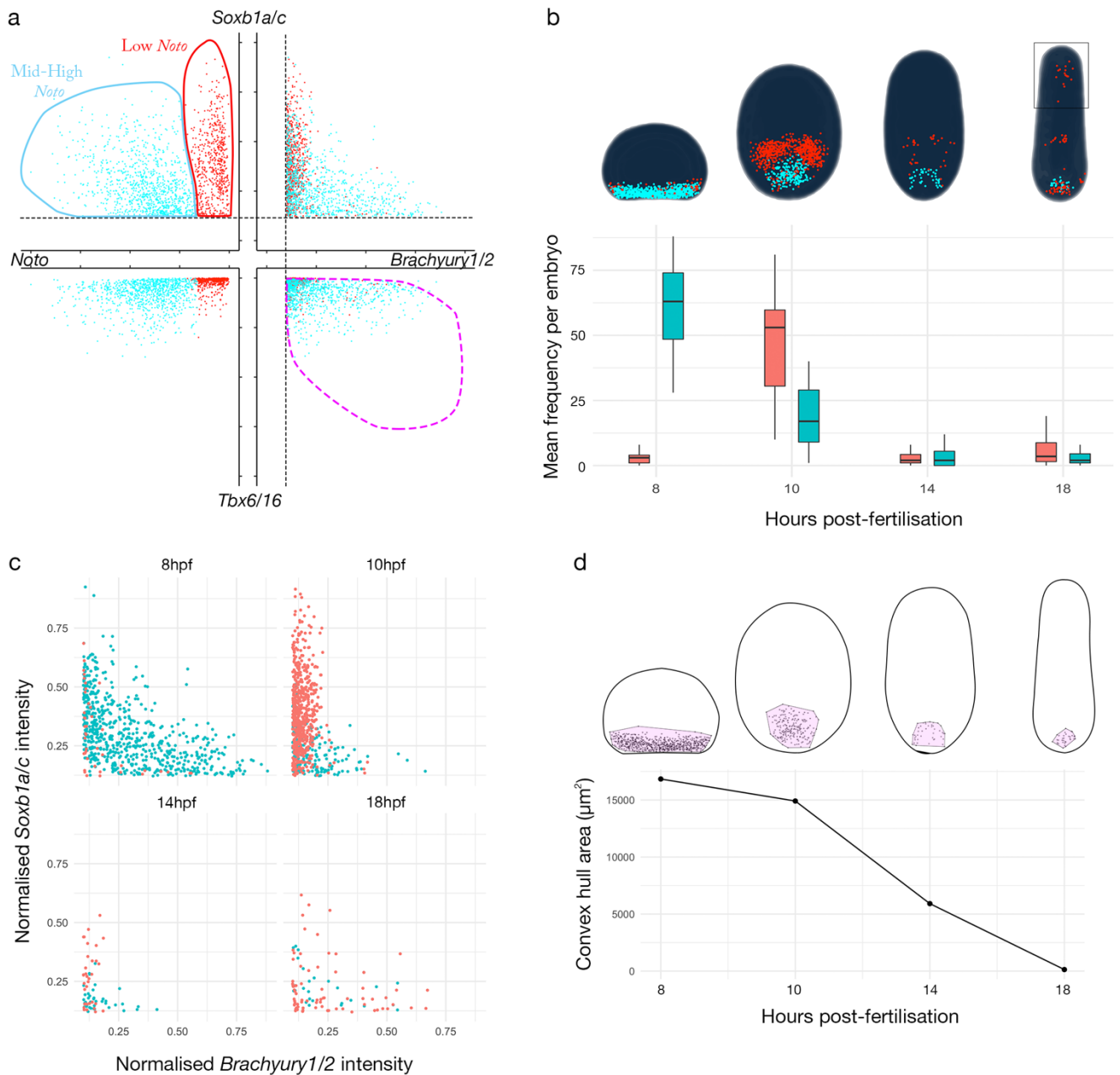


Figure 5.11. **Dynamics of NM depletion after amphioxus gastrulation.** (a) 4 pairwise coexpression scatter plots, showing the dispersal of NM cells isolated using medium thresholds for *Soxb1a/c* and *Brachyury1/2*. These thresholds are marked with dashed lines, and the isolated subset is shown in the top-right panel. NM cells separate into two groups in the *Noto* x *Soxb1a/c* scatter plot (top-left). Cells are colour-coded based on this grouping, Low-*Noto* NM cells disperse poorly into mesodermal domains, as defined in Fig 5.8, but high-*Noto* cells disperse extensively. This includes into the PSM domain, highlighted with a dashed magenta line in the bottom-left plot. (b) Boxplots showing changes in the mean frequency of each type of NM cell over time. Average embryos above show changes in the distribution of each group in the embryo over time. (c) Changes in the relative intensity of *Soxb1a/c* and *Brachyury1/2* expression in NM cells over time, carrying the classification defined in (a). (d) Changes in the convex area of the NM domain, defined by the limits of dispersal in average embryos.

dispersed poorly across gene expression space, and failed to enter territories classified as mesodermal (Fig 5.11a). In the *Soxb1a/c* x *Brachyury1/2* scatter plot, the low-*Noto* group aligned strongly with the y axis, reflecting only very low expression of *Brachyury1/2* with medium to high expression of *Soxb1a/c* (Fig 5.11a). Meanwhile, the high-*Noto* NM population spread extensively into mesodermal domains, including the *Brachyury1/2*+ *Tbx6/16*+ presomitic mesoderm, and represented the majority of nuclei with either correlated *Soxb1a/c* and *Brachyury1/2* or *Brachyury1/2*-dominant expression states in the *Soxb1a/c* x *Brachyury1/2* scatter plot (Fig 5.11a).

Having resolved high-*Noto* and low-*Noto* NM subtypes in gene expression space, I next mapped changes in their distribution and number over developmental time. In the cup-shaped gastrula, almost all NM cells were in a high-*Noto* state, aside from a small number of low-*Noto* NM cells that appeared at the lateral margins of the NM domain (Fig 5.11b, c, 8hpf). After blastopore narrowing, NM cells disperse across the posterior half of the neural plate (Fig 5.11b, c, 10hpf). At this stage, while those in the posterior domain, extending anteriorly from the chordoneural hinge, maintain a high-*Noto* state, those in the more anterior domains fall into a low-*Noto* state (Fig 5.11b, c, 10hpf). Now, very few cells exhibit correlated levels of *Soxb1a/c* and *Brachyury1/2* (Fig 5.11c, 10hpf). Thereafter, both populations declined in cell number, whilst retaining a segregated distribution across the anteroposterior axis of the neural plate (Fig 5.11b, 10hpf–18hpf). In the process, the high-*Noto* domain also declines in its area of coverage in the neural plate, to become more tightly restricted around the chordoneural hinge (Fig 5.11d). At 6ss, the posterior NM domain also appears to shift towards differentiation, with a local increase in the number of low-*Noto* NM cells, at the expense of the high-*Noto* state (Fig 5.11b, c, 18hpf). Now, the majority of cells in the neural plate are negative for expression of mesodermal markers. The single exception to normal differentiation is the small cluster of NM cells in the middle of the neural plate, which maintains a neuromesodermal signature late into axial development (Fig 5.11b, 18hpf, and data not shown).

5. 4. 4 Neuromesodermal cells in the late blastopore lip are neurally fated

The presence of cells that maintain a neuromesodermal gene expression state after gastrulation raises the important question of whether these cells can generate both neural and mesodermal derivatives. As described in **Chapter III**, the majority of the amphioxus epiblast and hypoblast become discontinuous after 12hpf, which physically prevents further internalisation of cells to expand the archenteron after gastrulation. However, the neural plate retains continuity with the mesoderm via the margins of the neurenteric canal. This therefore offers a putative interface for the delivery of NM cells residing in the posterior neural plate to both neural and mesodermal lineages. To test if such a transfer occurs *in vivo*, I DiI labelled cells in the posterior neural plate of embryos at 10hpf, before it is submerged beneath the surface ectoderm, using the same method for DiI crystal preparation as described in **Chapter III**. At this stage, however, embryos have hatched from the chorion and swim freely by virtue of motile cilia in the surface ectoderm. In this experiment, I therefore used an eyelash wand to manually immobilise individual embryos against the bottom of a glass plate, while labelling cells with a DiI-coated needle mounted in a micromanipulator. This method was very challenging and low throughput, not helped by the poor survival of labelled specimens and their propensity to extrude DiI labelled cells (*data not shown*). However, I did manage to label a broad field of cells in the posterior neural plate in a small number of specimens, which I then raised to 14ss (*Fig 5.12*), which offer interesting preliminary data on amphioxus NM cell fate.

In this experiment, I found that DiI-labelled cells contributed exclusively to the posterior neural tube and the chordoneural hinge (*Fig. 5.12a - c*). In the latter, they came to lie posterior to the notochord progenitors, but did not appear to intermix with them (*Fig. 5.12d*). No labelled cells were identified in the posterior somites, ventral endoderm or epidermis (*Fig. 5.12a - d*). This distribution suggests that no further flow of cells occurs between the neural plate and archenteron after 10hpf, and therefore that NM cells are exclusively of neural fate in amphioxus. The number of successfully labelled embryos in this experiment was very small, and so further labelling is required to test the reproducibility of the preliminary findings. Unfortunately, this was not viable within the duration of my PhD, given the unavailability of live embryos for *in vivo* experiments in the summer of 2020.

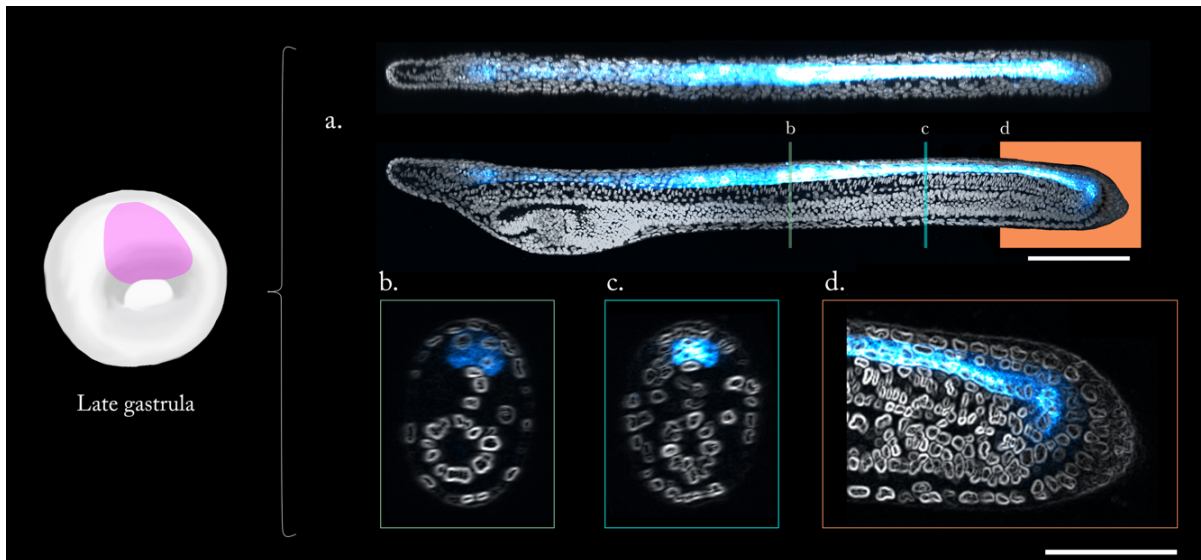


Figure 5.12. **The posterior neural plate is neurally fated.** Dechorionated gastrulas at 10hpf were broadly labelled with DiI in the posterior neural plate and left to develop to 34hpf in petri dishes coated with 0.5% agarose. (a) Cells labelled in the posterior neural plate at 10hpf give rise exclusively to neural tissue in the 34hpf larva. A representative specimen is shown in dorsal (top) and lateral projections (bottom). (b, c) Transverse sections from regions marked in a (bottom), showing specific neural enrichment of DiI, and depletion of DiI intensity from posterior to anterior. (d) 5 μ m sagittal projection through axial midline from region marked in a (bottom) Scale bar shows 100 μ m. $n = 4$ successful posterior neural labels.

Nonetheless, the experiment highlights a potentially interesting case of neuromesodermal gene expression not overlapping with neuromesodermal fate.

5. 4. 5 Neuromesodermal cells require pro-neural signalling for germ layer commitment

The preliminary DiI labelling experiment described hinted at amphioxus NM cells only giving rise to neural progeny. However, this test of *fate* does not necessarily reflect *competence* – what the cell *can* generate, given a different set of environmental conditions. Next, I therefore sought to ask whether, and if so how, the dynamics of NM cell depletion are governed by intercellular signalling cues. Notch and Wnt signalling appear to be conserved regulators of axial progenitor dynamics in vertebrates, which promote differentiation and maintenance of neural and mesodermal fates respectively (Goto et al., 2017; Gray and Dale, 2010; Martin and Kimelman, 2012; Row et al., 2016). In amphioxus,

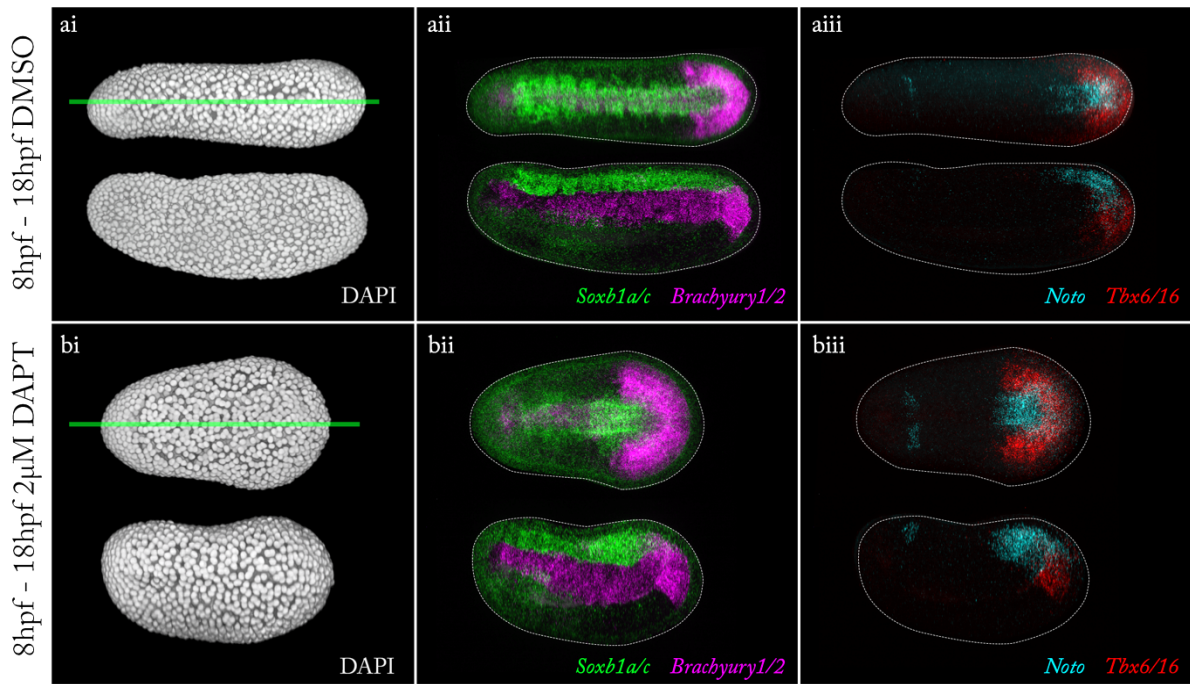


Figure. 5.13. Morphology and axial marker gene expression in DAPT-treated embryos. (ai – aiii) Embryos treated with 1:1000 DMSO between 8hpf and 18hpf. In each panel, the embryo is shown in a dorsal (top) and lateral (bottom) view. (ai) Embryo morphology shown using a 3D rendering of the DAPI channel. (aii, aiii) Expression of axial markers *Soxb1a/c* and *Brachyury1/2* (ii) and *Noto* and *Tbx6/16* (iii) in dorsal view of 3D projection (top) and sagittal section through the axial midline (bottom). (bi – biii) Embryos treated with 20µM DAPT between 8hpf and 10hpf, presented as per panels in (a). Embryos are representative of $n = 10$.

Notch signalling pathway components have already been shown to be expressed in the neural plate and paraxial mesoderm during axial development (Holland et al., 2001; Minguillón et al., 2003; Rasmussen et al., 2007). In the cup-shaped gastrula, *Notch* is expressed circumblastoporally. Meanwhile, *Delta* is most strongly expressed in the lateral blastopore lips, with weaker expression also in the dorsal lip (Fig. S2a). After gastrulation, both *Notch* and *Delta* are expressed in the presomitic mesoderm, *Notch* broadly and *Delta* in a strong anterior stripe (Fig. S2b). *Delta* is also expressed strongly in the anterior neural plate in a punctate distribution, but only very weakly in the posterior neural plate where I also located NM cells. It therefore appears that signalling through the Notch pathway is associated with neural differentiation in amphioxus, like in vertebrates. To ask whether the neural differentiation of NM cells is under the control of Notch signalling, I sought to

perturb signalling *in vivo* with a pharmacological approach. In this experiment, I exposed embryos at 8hpf, when NM cells are in greatest abundance, to 20 μ M DAPT, which inhibits the γ -secretase enzyme required for release of the Notch intracellular domain into the cytoplasm after ligand-receptor binding (Myers et al., 2014). I then fixed embryos at 18hpf, after NM cells have nearly depleted in normal developmental conditions (Fig 5.13).

In the DAPT phenotype, I found that embryos were shorter than untreated siblings, and exhibited a distinct pear-shaped morphology due to swelling at their posterior end (compare Fig 5.14ai and bi). Expression of *Delta* also lost its punctate expression in the neural plate, and coherent stripe in the anterior presomitic mesoderm, collapsing into a weak and diffuse pattern (Fig S2c). This confirmed successful perturbation of Notch signalling with DAPT. By performing HCRs for axial markers, I found that the presomitic mesoderm, which is marked strongly by *Brachyury1/2* and *Tbx6/16* expression, was greatly enlarged (Fig 5.13). This can, in part, be attributed to failure of normal somitogenesis (data not shown). In parallel, the area of the neural plate, defined by the distribution of *Soxb1a/c* expression, was reduced (Fig 5.13). This appeared to result from loss of *Soxb1a/c* expression in the anterior part of the neural plate, where it now appeared patchy, and at a weak intensity similar to the surrounding surface ectoderm (Fig. 5.13bii). From superficial observation, it therefore appeared that Notch inhibition had resulted in expansion of the presomitic mesoderm, and a diminishing of the neural plate. It was not feasible without further live embryos and optimisation of the DiI labelling protocol to fate map the NM domain in DAPT-treated embryos, which would inform if this phenotype was affected by a change in the allocation of NM progeny between neural and mesodermal lineages. I could, however, examine the effect of perturbed Notch signalling on the maintenance of NM cells in the neural plate in the wake of gastrulation by, once again, applying the ASCRIBE protocol.

To define the distribution of NM cells in the DAPT condition, I segmented all nuclei in the embryo using Ilastik, and dispersed them in pairwise coexpression matrices as previous (Fig. S1).² I then isolated *Soxb1a/c+* *Brachyury1/2+* nuclei using the same medium

² Sophie Kraunsoe (now Cambridge Stem Cell Institute), an undergraduate project student in the lab, performed a trial analysis on DAPT-treated embryos using the ASCRIBE method

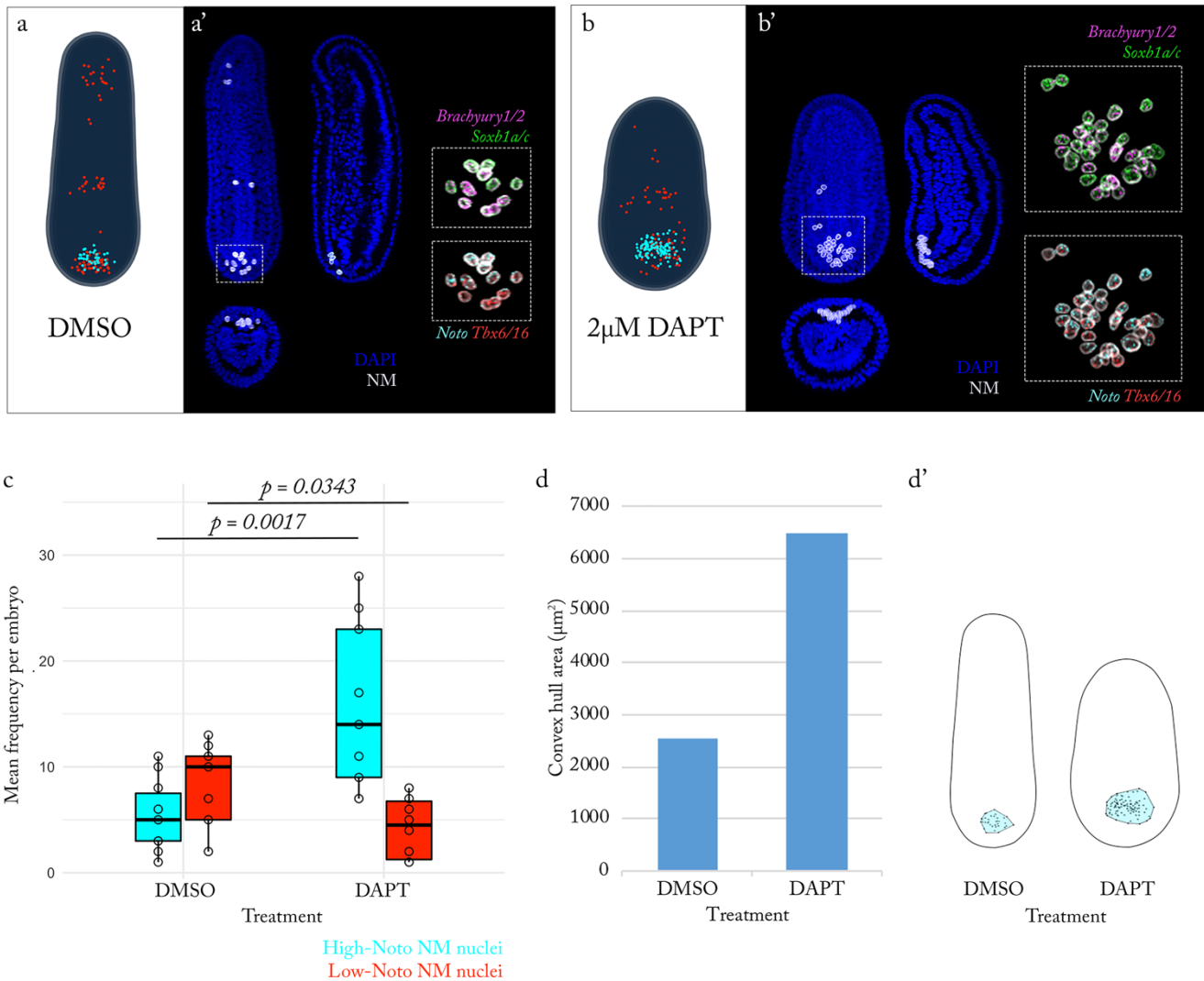


Figure. 5.14. Altered dynamics of NM depletion in DAPT-treated embryos. (a, b) Embryos treated between 8hpf and 18hpf with 1:1000 DMSO (a, a') or 20 μM DAPT (b, b'). (a, b) Average embryos in dorsal view, showing distribution of low-*Noto* and high-*Noto* NM cells. (a', b') Spatial mapping of NM cells into individual embryos from each dataset, shown (as in Fig. 5.10) dorsal and lateral views, and transverse sections through the posterior domain. Insets show punctae of *Soxb1a/c*, *Brachyury1/2*, *Noto* and *Tbx6/16* HCR staining within nuclei of the posterior NM domain. (c) Boxplot showing mean frequencies of low-*Noto* and high-*Noto* NM cells in DMSO or DAPT-treated embryos. (d) Convex hull area for the high-*Noto* MN domain, derived from average embryos for the DMSO and DAPT conditions (representing $n = 8$). (d') Illustration of convex hull area for the DMSO and DAPT conditions, and quantification shown in (d). $n = 8$ embryos per condition in quantitative analysis. $n = 33,105$ DMSO nuclei; $n = 32,546$ DAPT nuclei.

thresholds on normalised HCR signal intensities as applied for the time-course analysis. This was possible given imaging of the DAPT experiment in the same session, and with

identical laser powers, to the time series experiment. In the DAPT phenotype, like in the DMSO treatment and wild type analysis, NM cells were found in the neural plate, in the same three spatial clusters identified in untreated embryos; a circular posterior domain extending anteriorly from the chordoneural hinge, a smaller domain approximately half way across the anteroposterior axis, and a sparse distribution within the anterior endoderm (*Fig 5.14a, b*). Within this broad pattern, however, there were marked differences in NM cell abundance. While the high-*Noto* NM population increased in number by nearly 3-fold, the number of low-*Noto* NM cells almost halved (*Fig 5.14, c*). This reflects a net increase in total NM cell number, and retention of mesodermal marker expression compared to untreated embryos. In turn, the posterior domain occupied by high-*Noto* NM cells was expanded in convex area by 2.54-fold, thereby occupying a larger total proportion of the neural plate than in untreated embryos (*Fig 5.14, d*). Collectively, these observations hint at a prolonged maintenance of NM cells in the posterior neural plate of the DAPT treated embryos, and failure of neural differentiate at its normal rate. This may suggest that neural fate is not specified in NM cells during gastrulation, and the instead require pro-neural signalling after gastrulation to down-regulate expression of mesodermal genes, exit the NM state, and commit to neural identity.

5.5 Discussion

In this chapter, I have presented methods for *in situ* definition of cell states in the amphioxus embryo, which I have applied to define the presence and dynamics of cells in a neuromesodermal cell state within the posterior neural plate of the early neurula. My primary experimental conclusions are as follows:

- Hybridisation chain reaction (HCR) facilitates high-resolution multiplex imaging of gene expression in the amphioxus embryo by combining the published zebrafish protocol with a classical amphioxus *in situ* hybridisation protocol (*Fig. 5.1*). With this method, I showed that tissue-specific markers of the neural plate, axial and paraxial mesoderm occupy largely mutually exclusive, but semi-overlapping, domains in the posterior end of the amphioxus embryo in the wake of gastrulation

(Fig. 5.2, 5.3). This includes a conspicuous domain positive for both *Soxb1a/c* and *Brachyury1/2* in the posterior neural plate (Fig. 5.2). This satisfies Aim I.

- A range of methods are possible for cell state classification from HCR data, offering variable resolution and throughput (Fig 5.4 – 5.8). Here, I established ASCRIBE as an efficient method to quantify local nuclear HCR signal intensities across multiple embryos, and disperse them in a gene expression space. Cells disperse in gene expression space into semi-discrete populations, that map into spatially coherent domains in the embryo (Fig. 5.8). This satisfies Aim II.
- By defining minimal threshold intensities for *Soxb1a/c* and *Brachyury1/2*, I located a population of cells in a neuromesodermal state in the posterior neural plate immediately after gastrulation. This population progressively depletes in both cell number and spatial area of potential occupancy prior to axial elongation, and progressively down-regulates expression of markers associated with mesodermal differentiation. This satisfies Aim III.
- Using DiI labelling, I offered preliminary evidence that the posterior neural plate specifically gives rise to the posterior spinal cord, and cells of the chordoneural hinge lying posterior to notochord progenitors. Further methodological optimisation and experimental repeats are required to further define the fates of NM cells. This work partially satisfies Aim IV.
- Inhibition of Notch signalling led to an increase in the number of NM cells and their area of potential occupancy in the posterior neural plate, and an increase in expression of the paraxial and axial mesodermal markers *Tbx6/16* and *Noto*. This suggests that NM cells are not committed to neural identity, and exit the NM state under the influence of intercellular signalling. Although the NM state can be maintained experimentally, its ability to generate mesoderm remains unclear. This will require perturbation of other signalling pathways, and potentially grafting and *in vitro* cell culture for full assessment. This partially satisfies Aim V.

5. 5. 1 Strategies for cell state definition: current options and future prospects

As presented in this chapter, HCR and local nuclear quantification offers an accessible method for cell state definition in a diversity of systems - the limits to its application are technical optimisation of HCR imaging, and high-resolution nuclear imaging. As a candidate approach, it is ideal for comparative studies in enabling a screen for cell states with known markers. On the other hand, this renders it limited for non-bias cell state characterisation. One method to overcome this limitation is an increase in gene number. Where wet lab approaches are constrained, this could be achieved computationally by superimposing embryos stained for different combinations of genes. Here, 'pseudo'-cells could be defined by binning the embryonic axes into compartments with the mean dimensions of real nuclei. If pseudo-cells exhibit coexpression of a given set of transcription factors, this could be tested directly through novel combinations of HCR probes. In a sense, this computational method offers a predictive framework to expand the existing ASCRIBE approach. An alternative is to perform iterative rounds of HCR imaging on the same embryos, and then determine combinatorial expression in individual nuclei by superimposing the same embryo stained for different genes (Lignell et al., 2017). This offers new computational hurdles, and is also limited by damage to embryo morphology and RNA quality in each round of imaging. The most promising method may instead be to increase the information density of HCR staining with barcoding. In this case, multiple probe sets would be designed for each gene, then each transcript would be identified by a combination of fluorophores, with four hairpin species permitting identification of fifteen transcripts. If spectral unmixing is possible to resolve similar emission spectra, the number of fluorophores could also be increased, thereby permitting a greater number of total encoded transcripts.

In situ hybridisation approaches are favourable given that embryo morphology is left intact, enabling cell state to be considered alongside topology, shape and bounding conditions. However, for denser cell state characterisation, embryos can be dissociated for single-cell RNA sequencing (scRNA-seq). In this case, the number of transcripts considered is increased an order of magnitude, to thousands of mRNA molecules and their relative abundance. This methodology has allowed holistic definition of cell state diversity

in entire embryos in a diversity of organisms, including mouse (Ibarra-Soria et al., 2018), amphibians (Briggs et al., 2018), zebrafish (Wagner et al., 2018) and nematostella (Sebé-Pedrós et al., 2018). The emerging challenge is then to map cell states back into the morphology of the embryo, so they can be aligned with experimental studies of behaviour and clonal dynamics. For scRNA-seq data, this is generally dependent on a high-resolution atlas of embryonic gene expression, in which cell location is predicted based on a correspondence of marker gene expression in single cells and discrete spatial locations (Achim et al., 2015; Satija et al., 2015). In deterministic systems, where nuclear number and position exhibits limited variation, single-cell gene expression profiles can be mapped to single nuclei with a limited degree of error, and has been aligned beautifully with cell morphology analysis (Vergara et al., 2017; Vergara et al., 2020). However, in larger mosaic systems, this level of resolution is currently not possible, or inhibited by interspecies variation. Hybrid solutions are also available, that enable local RNA sequencing within the spatial context of the embryo, each varying in sequencing depth and throughput. This includes slide-seq, in which RNA is collected on nodes in a dense array across a tissue plane and then sequenced, therefore preserving reasonable spatial information (Rodrigues et al., 2019). Another option is seq-FISH, in which unique barcodes are assembled on different mRNA species through sequential rounds of *in situ* hybridisation, similar to the simpler HCR barcoding approach described above (Eng et al., 2019; Lubeck et al., 2014). Embedding scRNA-seq data in an atlas of 387 genes constructed using seq-FISH recently generated a high-resolution 3D map of cell state diversity in mouse embryos (Lohoff et al., 2020). Considered together, scRNA-seq technology is expanding for detailed cell state characterisation, and is progressively overcoming hurdles of spatial resolution and accessibility.

5. 5. 2 Maintenance of the NM transition state is a conserved motif in chordate development

By employing a quantitative approach, I identified an enrichment of cells expressing both *Soxb1a/c* and *Brachyury1/2* at medium intensity in the amphioxus late dorsal blastopore lip and, later, the posterior neural plate. This overlaps with the prevailing definition of NMps from studies in vertebrates in terms of both gene expression signature and position (Henrique et al., 2015). In this respect, maintenance of a neuromesodermal

cell state post-gastrulation emerges as a conserved motif in chordate development. Despite extensive variation in the shape, size and developmental dynamics of different chordate embryos during, and in the wake of, gastrulation, the Waddingtonian landscape of germ layer resolution appears to be common, and to unfold in similar spatiotemporal sequence. Here, a small subset of cells remains trapped in the neuromesodermal transition state after gastrulation, and undergoes a late allocation to the elongating body axis. Variation between chordate species is instead conspicuous in the clonal dynamics and behaviours of cells when trapped in the NM state. In amphioxus, the number and area of potential occupancy of NM cells depletes almost entirely prior to axial elongation. And, despite the distribution of NM cells throughout the early posterior neural plate, proliferation in the chordoneural hinge only contributes to elongation of the prospective floor plate (**Chapter III**). Therefore, although it has not been directly measured here, it seems that cells in the NM population are largely quiescent during axial elongation. This bears strong similarity to the zebrafish, where NMps persist into axial elongation, but remain quiescent and eventually exit the NM transition state to form the tip of the tail (Attardi et al., 2018). In contrast, the NM state in amniotes is associated with extensive self-renewal (Cambray and Wilson, 2002). Diversity of cell behaviour in the tailbud between chordates can therefore be attributed not to the emergence of novel cell states, but to tweaks in the dynamic behaviours of cells in a conserved NM transition state.

While this helps to explain how morphogenetic processes have diverged in the chordates, and the potential role of the NMp in that process, it does not account for the emergence of NMps in the first chordates. One possibility is that the apparent maintenance of the NM state at the posterior tip of the embryo is an accident, potentially a by-product of the anterior-to-posterior directionality of axial differentiation. During gastrulation, a large proportion of cells in the embryo are *Soxb1a/c*⁺ *Brachyury1/2*⁺, when the mesendoderm is specified and segregated into the embryo through invagination and involution. As cells exit the NM transition state, they will resolve to expression of either *Soxb1a/c* or *Brachyury1/2*, and it may be that cells of the posterior tip of the embryo, which are the last to differentiate, are the last to exit the transition state. However, this is challenged by the prolonged maintenance of the NM state in the posterior neural plate when Notch signalling is perturbed. This instead hints that the posterior NM pool is

uniquely trapped in the NM state until this is destabilised by signalling. We now need to ask what properties are possessed by cells in the NM state that are subsequently lost. One possibility is that, despite their apparently neural fate in normal conditions, NM cells are also competent to generate mesoderm under the right conditions. In this scenario, the posterior neural plate would be of fixed size, but flexible in its contributions to the body axis, thereby offered a level of robustness to stochastic variations in cell number or elongation rates in the axial mesoderm and neural tube. If this balance is variable during normal development, then it should be susceptible to experimental perturbation. Having focussed on Notch signalling in this chapter, the Wnt and FGF pathways are strong candidates for regulating NMp allocation.

A curious further possibility is that amphioxus NM cells do possess neuromesodermal competence, but mesodermal fates are inhibited *in vivo* due to morphological constraint. Unlike vertebrate tailbuds, which have a conspicuous mesenchymal component, the amphioxus is a predominantly epithelial structure. It may therefore be the case that the cell movements that allow mixing of cells between compartments, and behaviours that typically mediate NMp addition to the mesoderm, are impaired. Indeed, in zebrafish, NMps extend the presomitic mesoderm by delaminating from the posterior neural plate into the tailbud mesenchyme, in which there is extensive cell mixing (Goto et al., 2017). In amphioxus, we might hypothesise that the entire posterior neural plate would have to fold and invert in order to contribute to the presomitic mesoderm. These exact movements have been described in axolotl, although the mechanical conditions required to enable such a radical change in tissue topology are not necessarily shared by amphioxus (Taniguchi et al., 2017). If signalling perturbations failed to generate mesodermal fate in amphioxus NM cells, an unrestricted test of NM competence would be to remove them from their native context in the posterior neural plate and establish an *in vitro* culture, inspired by established conditions for NMp differentiation from embryonic stem cells (Edri et al., 2018; Gouti et al., 2014; Tsakiridis et al., 2014). In this environment, both molecular and mechanical conditions could be altered to test if mesodermal differentiation is possible. For amphioxus NM cells to possess NM competence, but mesodermal differentiation to not be possible *in vivo*, would introduce a twist into the evolutionary story. As suggested previously, maintenance of the NM state

after gastrulation could be an accidental by-product of a rapid developmental mode and an anterior-to-posterior differentiation gradient. In contrast, bicompetent NMps may have contributed to both neural and mesodermal lineages in the ancestral chordate, but become locked into neural fates in amphioxus due to secondary changes in tailbud morphology, leaving bicompetent NMps a non-functional vestigial trait. Indeed, amphioxus is important for inferring ancestral traits, but is not itself an ancestor.

This study offers data to support a role for Notch signalling in NM cell commitment to neural identity, and their exit from the progenitor domain located at the posterior tip of the neural plate. Such a dynamic in amphioxus mirrors those in vertebrates, where Notch also makes pro-neural contributions. While some studies have supported a role for Notch signalling in the allocation of axial progenitors to the neural tube (Gray and Dale, 2010; Peyrot et al., 2011), in zebrafish it primarily supports to proliferation of posterior floor plate progenitors (Appel et al., 1999; Latimer and Appel, 2006). Given the very small amount of proliferation in the amphioxus posterior neural plate after gastrulation, and the response to DAPT being an *increase* in NM cell number rather than a decrease, a similar role in proliferative control in amphioxus might seem unlikely. However, it is interesting that the pulse-chase experiments discussed in **Chapter III** show a specific contribution of proliferative cells in the posterior neural plate to the floor plate, with no conspicuous labelling of the dorsolateral neural tube. As a result, further work should aim to discern any change in the amount of proliferation downstream of Notch signalling, and the extent to which this contributes to the change in NM cell number; the phenotype observed here is not purely due to changes in Notch activity in NM cells. On this note, the phenotype features many qualities associated with defective axial elongation and somitogenesis, unrelated to NM cell dynamics. We cannot exclude the possibility that axial elongation itself affects axial progenitor cell behaviour, and indeed this has been described in amniotes (Xiong et al., 2020). As a starting point, the effect of DAPT treatment could be studied when combined with hydroxyurea treatment, which would uncouple the effects of Notch on cell fate determination and proliferation. Ultimately, testing the cell-autonomous function of Notch signalling (or that of any other pathway) would require specific desensitisation of the NM population to Notch receptor activation, which may be possible through grafting of DAPT-treated cells into untreated hosts (akin

to Gray and Dale, 2010), or those in which Notch pathway components are genetically inactivated (akin to Martin and Kimelman, 2012).

5. 5. 3 Conclusion

To conclude this section, the work presented in this chapter offers an accessible methodology for the *in situ* definition of cell types in non-model systems, with suggestions for methodological development to permit analysis of larger gene sets. Applied here, I offer the first evidence for maintenance of cells trapped in a neuromesodermal state after gastrulation in the amphioxus embryo, which make a delayed commitment to neural identity, in part under the influence of Notch signalling within the neural plate. From these data, I propose that neuromesodermal cells may have emerged in evolution serendipitously, simply by virtue of the anterior-to-posterior directionality of axial development, combined with rapid developmental modes. In the absence of clonal dynamics typified by amniote NMps, the presence of progenitors with neuromesodermal competence in the tailbud may have been favourable in development by enabling an adaptability to stochastic variations in axial tissue sizes and elongation rates, thereby accounting for their persistence in evolution. The functional significance of the NM state in the first chordates will clarify through further comparative studies in other cephalochordate and anamniote vertebrate taxa, and the optimisation of parallel embryological approaches to test fate and competence. Combined with studies in vertebrate systems, this work suggests that maintenance of the NM transition state is a conserved motif in the chordate Waddingtonian lineage. In turn, diversity in developmental growth dynamics has emerged through tweaks in the clonal dynamics and behaviours of cells in the NM transition state, likely through changes in the pattern and interpretation of intercellular signalling dynamics.

Chapter VI

On the evolution of morphogenesis

6.1 How to build a chordate

The primary aim of this thesis was to reconstruct processes underpinning body plan morphogenesis in the first chordates by performing a multi-scale decomposition of amphioxus (*B. lanceolatum*) axial development. In response, each chapter is a case study, in which morphogenesis is defined on a unique scale of observation, from tissue-scale growth dynamics (**Chapter III**), to cell behaviour (**Chapter IV**), and cell state diversity and dynamics (**Chapter V**). These case studies both identify putative ancestral properties of the chordate morphogenetic programme, and offer a suite of quantitative tools for the study of morphogenesis that are specifically optimised for research in non-model organisms, where experimental traction is limited. In this section, I will reiterate how my findings in each chapter shine new light on the morphogenetic programme operating in the first chordates, and, in doing so, hypothesise how this has been subsequently tweaked to generate species-specific variations in embryonic growth dynamics. This leads me to a more theoretical consideration of morphogenetic plasticity and constraint, and, ultimately, a reframing of the aims of research in Evo-Devo moving forward.

First and foremost, this thesis offers novel insight into morphogenetic processes operating in the amphioxus embryo and, by inference, the ancestral chordate condition. In **Chapter III**, I show that elongation of the amphioxus embryo primarily depends on the conserved gastrulation movements of invagination, involution and convergent extension. Here, convergent extension is the length generating process, but the preceding phase of involution acts to expand the size of the cellular substrate available for elongation, at the expense of prospective ectoderm. Length is generated through the action of convergent extension across the anteroposterior extent of the body axis, rather than the restriction of

length-generating processes to the tailbud (Bénazéraf, 2019; Steventon et al., 2016). Moreover, convergent extension occurs in all axial tissues, even though quantitative measurements of cell neighbourhood topology indicate differential underlying cell behaviours. In line with these findings, morphometric measurements identify a lack of net growth during elongation, which supports the predominance of tissue rearrangement in generating axial length. As highlighted in **Chapter IV**, this does not mean that growth is entirely absent from the developmental programme. Rather, I show that it is deployed in very specific contexts, and, where this occurs, its effect is amplified by other cell behaviours to drive radical morphological change. In the case study of notochord elongation, geometric modelling suggests that cellular growth and intercalation synergise to enforce a rapid increase in tissue length. Given these findings, and the similar minor role for tissue growth in the axial development of externally-developing anamniotes (Steventon et al., 2016), I propose that rearrangement-based morphogenetic strategies are likely ancestral in chordate embryogenesis, thereby rendering posterior growth a secondarily derived process in some vertebrate systems (Bénazéraf and Pourquié, 2013; Bénazéraf et al., 2017).

An important contribution of my work to the field, however, is evidence that the apparently novel posterior growth dynamic observed in amniotes is not without precedent. I show in **Chapter III** that amphioxus embryos also possess proliferative axial progenitor cells, that emerge in the late blastopore lip and are transmitted to the tailbud. There, their proliferation is required for full elongation of the body axis. Unlike amniotes, however, cell division is not linked to volumetric growth. Rather, it is a volumetrically-reductive process, in which cell division leads to focal increases in cell number, and decreases in cell size. I provide evidence that volumetrically-reductive division acts to scale cell size to the total cellular material available for morphogenesis. In half embryos, generated through blastomere-splitting at the 2-cell stage, where the total cellular mass of the embryo is depleted but cell size is unaffected, notochord progenitors assemble into a notochord that is too large for the number of cells available to build it. This means that the notochord fails to elongate fully, and is pathologically short and wide. The extent to which such a scaling is important in vertebrates remains to be resolved, although the pattern of cleavage divisions, and their effect on cell size, has been shown to be critical for defining the tapered contour of the ascidian notochord (Winkley et al., 2019). Given the shared role for axial

progenitors in elongation of amphioxus and vertebrate embryos, the morphogenetic programmes seem to vary primarily in the timing and magnitude of cell division and growth acting in a conserved axial progenitor cell. In amphioxus, the volumetrically-reductive mode of embryonic cell divisions is protracted into axial development, and a linkage with cellular growth only emerges in earnest in metamorphic development. In mouse, however, the shift is earlier, at the mid-blastula transition, in which the cell cycle gap phases are elongated, thereby coupling cell division to an increase in tissue volume. In sum, we can speculate that the seemingly discrete morphogenetic programmes operating in amniotes and amphioxus in fact exist on a continuum, separated by quantitative variation in common morphogenetic parameters.

A similar case applies for neuromesodermal progenitors (NMps), which I explore in **Chapter V**. In amphioxus, I show that cells in an NM transition state persist in the posterior neural plate after gastrulation, and seem to require pro-neural signalling after gastrulation for germ layer commitment. However, cells in this NM state do not generate the large neuromesodermal clones observed in vertebrates (Tzouanacou et al., 2009), and instead deplete progressively, and specifically give rise to the neural plate. In this respect, cells with large neuromesodermal clones are indeed a vertebrate novelty, but again not without precedent; the data presented in **Chapter V**, suggests that NMps with long-term contributions to the body axis and neuromesodermal fates may have emerged through quantitative changes in the clonal dynamics of cells in a highly conserved NM transition state. In other words, the Waddingtonian lineage appears to be conserved between vertebrates and amphioxus, but the kinship lineage embedded within it is plastic. A more unexpected case study for innovation through changes in the magnitude of morphogenetic processes arose in **Chapter IV**. Here, I found that the amphioxus notochord exhibits a subtle anteroposterior regionalisation, manifest in the expression of differential cell behaviours (formalised as morphogenetic trajectories), and their regulation in developmental time, across the anteroposterior axis. More investigation is required to characterise the regulation of these behaviours, and to what extent the notochord is patterned into different spatial domains. However, we can hypothesise that the subtle regionalisation in amphioxus may precede the stark regionalisation of the mammalian notochord (Yamanaka et al., 2007). In each of these case studies, macroscopic novelty

contrasts with continuity in underlying morphogenetic processes. As a result, these are not discrete evolutionary transitions, as might be apparent in ‘novelties’ at the macroscopic scale, rather they depend on tweaks in the timing and magnitude of a core set of morphogenetic processes already operating in the first chordates.

The study of morphogenesis in a phylogenetic framework enables us to both identify iterative transitions over evolutionary time, and, more broadly, to identify the free parameters available for evolution to tweak – along which axes of variation is morphogenesis *evolvable*? Although other strategies may be possible in theory – from the perspective of an engineer designing a new embryo – natural diversity tells us what options are viable in real developmental systems. Importantly, the availability of free parameters for evolutionary variation will depend on both the geometric transformation at play, in dictating the task cells need to perform physically, and also whether variation can be tolerated by the system at large. A rich literature already exists on the role of pleiotropy in molecular constraint, showing that the ability of a signalling input to change function in one context may be limited by its function in another. For example, the role of *Tbx5* in vertebrate limb development is constrained by its parallel role in cardiac hypertrophy (Garrity et al., 2002). The number of cervical vertebrae is also constrained by the pleiotropic function of *Hox* genes in stem cell regulation (Galis, 1999). However, pleiotropy can also operate on a morphogenetic scale. In **Chapter III**, I show experimentally that large variations in axial length can be tolerated in amphioxus, because elongation is not required for normal somite patterning. In contrast, a pleiotropic functionality for notochord elongation in somite patterning would potentially constrain midline progenitor dynamics as a free parameter for evolutionary change. Furthermore, in half embryos, I show that a stable body plan can form even with radical perturbations of axial tissue geometry. In exhibiting such robustness to perturbation, and an apparent lack of pleiotropic interactions between tissue-specific morphogenetic programmes, the amphioxus morphogenetic programme exhibits hallmarks of evolvability, with numerous unconstrained nodes for evolution to act upon.

The timing and magnitude of specific morphogenetic processes is also limited by developmental context, which dictates the viable parameter space. For example, the pace

and growth-dependence of chordate development appears to correlate strongly with internal vs external developmental modes and the size of the nutritional supply (O'Farrell, 2015; Steventon et al., 2016). As described previously, externally-developing anamniotes assemble their body axes primarily through gastrulation movements, including convergent extension, that generate conserved tissues through tissue rearrangement (Gomez et al., 2008; Steventon et al., 2016). This carries the lowest nutritional demand, and enables rapid development where predation is a major threat to viability. In turn, broods are large, often on the scale of thousands or more, and synchronised between individuals (O'Farrell, 2015). In internally developing amniotes, with large nutritional supplies, we tend to observe more protracted developmental processes, and a greater dependence on growth. In these cases, a larger proportion of organismal growth is contained within the window of embryonic development, occurring prior to birth or hatching, thereby contrasting with growth occurring concomitantly with active feeding during the larval phase of most anamniotes. The role for mechanical conditions in steering morphogenesis is also increasingly apparent. For example, synthetic embryos derived from mouse (gastruloids) and zebrafish (pescoids) embryonic cells removed from their native conditions exhibit striking morphological similarity (Anlas and Trivedi, 2020; Trivedi et al., 2019; Van Den Brink et al., 2014). This implicates the mechanical environment of the mouse uterine wall, and the surface of the spherical zebrafish yolk, as instructive in constraining morphogenetic parameter space. Thus, while the availability of free parameters is dictated by sources of molecular and mechanical constraint, their range of action is also limited by environmental context.

With these influences in mind, the presence of quantitative nodes of variation in the morphogenetic programme enables it to act as an adaptive system, when considered over evolutionary time, in that it consists of a common network of interconnected processes that stabilise a conserved set of patterns under a diversity of constraining conditions (Bentley et al., 2014; Edelman et al., 2010; Gell-Mann, 2005). This conserved set of patterns is manifest at the end of gastrulation, when the tailbud has formed, at the phylotypic stage (Duboule, 1994; Slack et al., 1993). In a simplified fashion, these principles are depicted in *Fig 6. 1*, in which evolution is personified as an engineer tasked with building a chordate. Said engineer is in command of a panel of dials, representing nodes of quantitative variation in a set of free morphogenetic parameters – in this case, axial

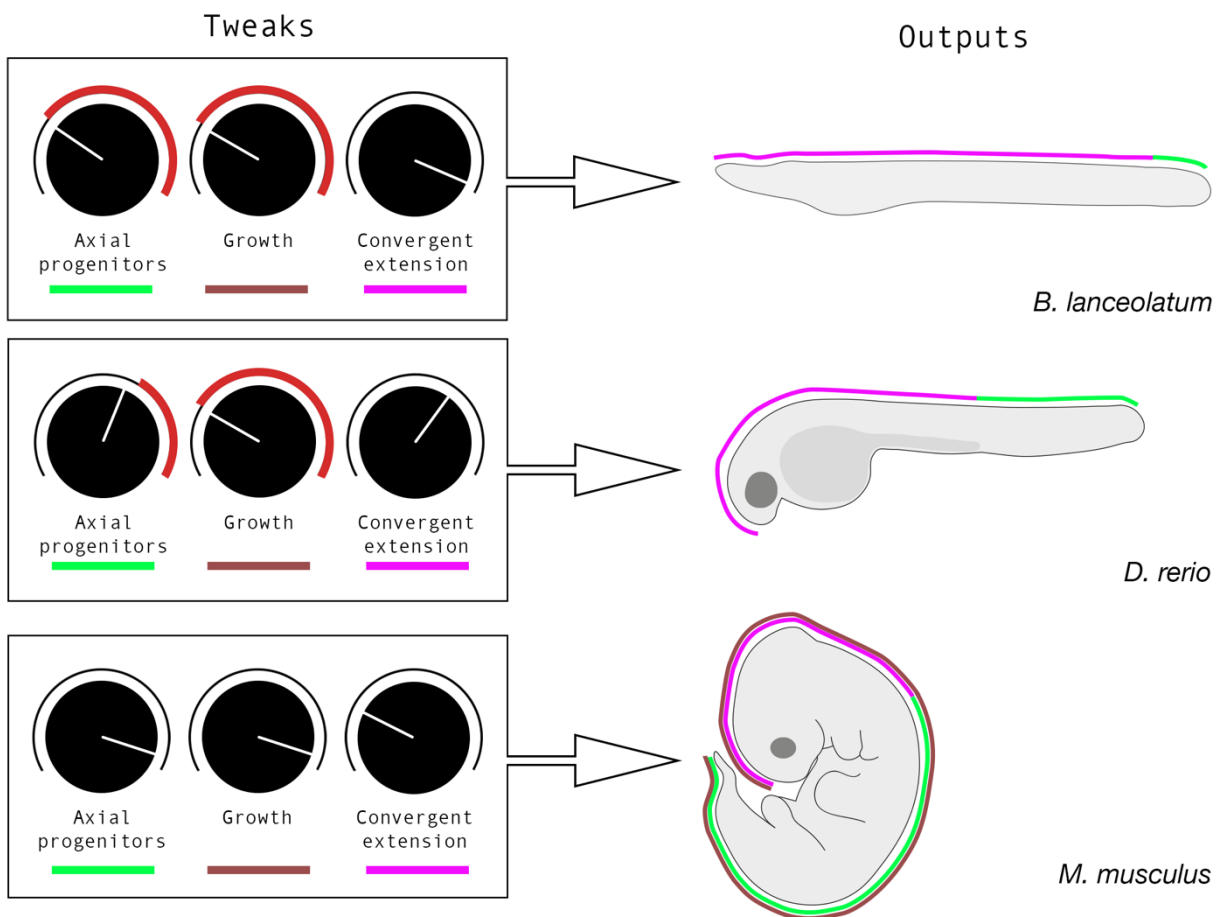


Figure. 6.1. Evolution through tinkering of morphogenetic parameter space. Here evolution is personified as an engineer tasked with building a chordate in diverse conditions by altering a conserved set of morphogenetic parameters – illustrated here as a series of dials for axial progenitor clone sizes, volumetric growth and convergent extension. In each dial, the thin black lines shows the region of free parameter space that the engineer can explore, thereby generating organisms with differing growth dynamics, and exhibiting different geometric variations. The dark red line marks inaccessible parameter space, restricted due to an environmental constraint. In the corresponding embryos, shown on the right, the relative contributions of each process are also shown in coloured lines across the anteroposterior axis. In each case, form is conserved, but developmental dynamics are variable.

progenitor clone sizes, volumetric growth, and convergent extension. The engineer can tune these parameters to generate embryos of different scales and geometries, and that exhibit different growth dynamics. However, the limits of the dials can be restricted by constraining conditions within the brief. This means that, depending on the conditions,

the parameter space the engineer can actively explore is limited, despite the much wider range of possibilities they might be able to dream up. In the first example, the engineer faces a limitation on time and space so, with these lacking, increases convergent extension to build the body quickly and efficiently. The product is an amphioxus. In the second, the engineer is offered a small yolk supply, and so has a greater range of options for cell division. In this case, they tune down convergent extension, and increase the contribution of axial progenitors. The product is a zebrafish. In the final example, the engineer is given full control, with the promise of time and resources, and in this case makes a mouse. In each case, a common set of patterns emerges from a differing balance of conserved processes, tuned within limits dictated by context.

With the action of evolution considered from this perspective, chordate developmental diversity is not irreconcilable, as it might appear at face value. Rather, placing it in a phylogenetic context exposes it as symptomatic of a morphogenetic programme that acquires robustness by virtue of being adaptive. This adaptability, through plasticity in the timing and magnitude of ancient processes enables the mapping of a conserved set of morphological traits that define the body plan – manifest at the phylotypic stage of development – onto a diversity of cellular substrates, in a diversity of constraining conditions. This confers the bottom half of the chordate developmental hourglass its flared base and tapered contour, leading from apparent diversity to unity (Duboule, 1994). The ideas raised in this thesis are congruent with those of Francois Jacob who, prior to the formulation of Evo-Devo as a coherent research programme, proposed that evolution innovates through tinkering (Jacob, 1977). With the application of quantitative approaches across scales in chordate morphogenesis, this hypothesis is increasingly supported by data. In the paradigm of chordate morphogenesis, what may appear novel is instead exposed as a temporal and topological reorganisation of ancient parts and processes.

6.2 Future directions

In the above discussion, I posit that evolution stabilises the chordate body plan in different developmental contexts by tuning a variable selection of free morphogenetic parameters. This is a working hypothesis based on comparative morphogenesis, but is only

the beginning of a research programme in the evolution of morphogenesis. On one level, ongoing work needs to add resolution to the transitions that have occurred in chordate evolution by acquiring a detailed picture of morphogenesis in diverse taxa. On another, it needs to abstract from the specific problem of chordate evolution to dissect the nature morphogenetic plasticity and evolvability. In this respect, I propose that further studies must continue in three primary directions.

A non-anthropocentric diversity of research organisms needs to be embraced in biological research (as argued at length by Sánchez Alvarado, 2017). At present, morphogenetic studies are limited to a small number of organisms for which experimental approaches have been optimised, which together represent a poor sampling of total diversity within each animal phylum. In chordates, this includes zebrafish, chick and quail, mouse, frog, axolotl and ascidian embryos. While a much more extensive list of non-model organisms is actively studied in Evo-Devo research, including amphioxus, lamprey (Lara-ramirez et al., 2018; Shimeld and Donoghue, 2012), hagfish (Fujimoto et al., 2013; Pascual-Anaya et al., 2018), dogfish (Sauka-Spengler et al., 2003) and skate embryos (Gillis and Hall, 2016; Gillis et al., 2017), such studies are largely restricted to *in situ* hybridisation and classical embryological techniques. For the study of morphogenesis, the work presented in this thesis highlights that these non-model system are not necessarily inaccessible for studying cell and tissue behaviour, and a huge amount of information is available by combining simple fluorescent imaging with advanced imaging analysis - live imaging and transgenesis are not required in the first instance. As microscopy, tissue clearing strategies and automated image segmentation continue to advance, we will be able to readily collect quantitative data on tissue and cell shape in diverse non-model systems. When quantified, morphogenetic processes can then be rigorously compared, and their axes of variation correlated with factors like phylogeny and developmental context. The approach of morphospacial embedding, presented in **Chapter IV**, is ideal for high-throughput shape comparison. Combined, these approaches will offer a high-resolution picture of the extent to which morphogenetic processes are shared throughout the phylum, and to what extent they exhibit plasticity, or are constrained. This will take advantage of computational and statistical methods already optimised for anatomical shape comparison. The extent to which these studies are possible depends on less gene-centric approaches to

evolution being embraced, the fostering of positive interdisciplinary collaborations within the Evo-Devo community, and greater financial investment in Evo-Devo.

For the study of form, descriptions of morphological and molecular transitions must be substantiated with experimental embryology where possible. This is to identify causative interactions between processes in the emergence of form and, in turn, how this is influenced by variation in underlying molecular, cellular and mechanical parameters. While enthusiasm for experimental embryology has paled with the emergence of single-cell genomics, it remains irreplaceable in the research programme of Developmental Biology, and Evo-Devo, given that cell behaviour during development is not a deterministic readout of gene expression. A beautiful demonstration of this principle is a recent study in ascidian embryos, which shows that softening of the cell membrane during mitosis enables orientation of the mitotic spindle according to the directionality of tension across the surrounding tissue (Godard et al., 2020). Here, division orientation is not genetically programmed, rather cell-autonomous changes in mechanical properties coupled to cell cycle progression sensitises the cell to external cues. A similar case study in the zebrafish heart demonstrates that cells of the prospective inner contractile layer delaminate from the outer layer not through molecular induction, rather as a response to an increase in cell packing density, arising from division within the epithelial plane. In fact, this symmetry breaking cue lies upstream of Notch-dependent fate specification (Priya et al., 2020). In these examples, form is exposed as the product of dynamic interactions between cells, not simply a linear readout of genetic information. On this scale of analysis, experiments are of course limited to a smaller range of model systems than for descriptive studies. However, these can be used to guide simpler screening experiments in non-model system, as a means to test for evolutionary conservation and variation (eg. Gillis and Hall, 2016; Lara-Ramirez et al., 2018). In sum, rigorous studies in Evo-Devo are dependent on rigorous Developmental Biology, as a means identify how form is stabilised in development, and how this can be perturbed in experimentation and evolution.

This thesis has focussed on the collection of morphological data. However, the emergence of form is ultimately a systems problem, in which traits emerge through dynamic interactions between processes operating on molecular, mechanical and morphological

scales. If we are to understand how developmental systems stabilise specific traits, and to identify sources of plasticity and constraint, we therefore need to develop models of morphogenesis that integrate multi-scale information, inclusive of intercellular signalling dynamics, cell shape, size, topology and bounding conditions. Importantly, this depends on morphogenesis becoming a quantitative discipline. Computational modelling is a means to integrate dynamic information on multiple scales, and simulate the origins of specific dynamics and emergent principles. If we can recapitulate development *in silico*, we can then ask how tweaks in gene expression propagate into changes in 3D tissue form and function, what morphological outcomes are possible, how form is constrained, and how it is plastic. I suggest that in these studies, morphogenetic systems can be visualised in a similar framework to dynamical gene regulatory networks, that resolve on one of a number of possible ‘attractor states’ based on a given set of initial conditions, in this case representing the forms resolved in different species (inspired by Verd et al., 2018; Yin et al., 2014). This abstracts from superficial differences in form that may detract from mechanistic similarity. Currently, 3D modelling of morphogenesis is challenging in chordate development, given its complexity. However, modelling has been applied very successfully in other simpler systems, which offer proof-of-concept case studies. This includes plants, in which shape emerges through differential growth in the absence of cell movement. For example, an exemplar study from Kierzkowski et al (2019) combined live imaging, morphometrics and modelling to predict, and experimentally recapitulate, the emergence of simple or dissected leaf shapes based on differential expression of the homeobox genes *Shootmeristemless* and *Reduced Complexity*. Similarly, in vascular morphogenesis, modelling the interplay between intercellular signalling and cell shape changes has identified a role for filopodia in generating switch-like behaviour in blood vessel branching (Zakirov et al., 2020). Multi-scale modelling will be key to defining how morphogenetic systems stabilise form, and identifying how this can be perturbed to generate novelty.

6.3 Conclusion

The work presented in this thesis contributes to the field of Evo-Devo on conceptual and technical scales. Despite its well-established phylogenetic position as the sister group to all other chordates, amphioxus morphogenesis has remained unexamined

with modern imaging and analytical tools. Here, I have optimised experimental and analytical approaches to study amphioxus morphogenesis on three scales of observation. In doing so, I offer novel insight into embryonic growth dynamics, cell behaviour and cell state diversity in the ancestral chordate condition. In addition, I demonstrate the importance of quantitative approaches for rigorous descriptions of morphogenetic processes. This also makes morphology accessible as a quantitative variable to combine with molecular information for a systems-view of morphogenesis, and paves the way for rigorous inter-species comparisons of developmental dynamics. In highlighting the deep conservation of morphogenetic processes responsible for axial development in chordates, I argue that evolution extracts a common set of biological patterns from diverse cellular substrates, and in diverse contexts, through quantitative tuning of morphogenetic parameters. In turn, the apparent paradox of morphological conservation with morphogenetic diversity emerges as a symptom of robustness through evolvability. This motivates a research programme in Evo-Devo that seeks to define the parameter space for evolutionary variation, and on what terms (and within what limits) tweaks can be made within morphogenetic systems.

Bibliography

- Abzhanov, A. (2013). Von Baer's law for the ages: Lost and found principles of developmental evolution. *Trends Genet.* 29, 712–722
- Achim, K., Pettit, J.-B., Saraiva, L. R., Gavriouchkina, D., Larsson, T., Arendt, D. and Marioni, J. C. (2015). High-throughput spatial mapping of single-cell RNA-seq data to tissue of origin. *Nat. Biotechnol.* 33, 503–509
- Adams, D. S., Keller, R. and Koehl, M. A. R. (1990). The mechanics of notochord elongation, straightening and stiffening in the embryo of *Xenopus laevis*. *Development* 110, 115–130
- Akai, J., Halley, P. A. and Storey, K. G. (2005). FGF-dependent Notch signaling maintains the spinal cord stem zone. *Genes Dev.* 19, 2877–2887
- Albors, A. R., Halley, P. A. and Storey, K. G. (2018). Lineage tracing of axial progenitors using Nkx1-2CreER^{T2} mice defines their trunk and tail contributions. *Development.* 145, dev164319
- Albuxech-Crespo, B., López-Blanch, L., Burguera, D., Maeso, I., Sánchez-Arrones, L., Moreno-Bravo, J. A., Somorjai, I., Pascual-Anaya, J., Puellas, E., Bovolenta, P., et al. (2017). Molecular regionalization of the developing amphioxus neural tube challenges major partitions of the vertebrate brain. *PLoS Biol.* 15 e2001573
- Aldea, D., Leon, A., Bertrand, S. and Escriva, H. (2015). Expression of Fox genes in the cephalochordate *Branchiostoma lanceolatum*. *Front. Ecol. Evol.* 3, 1–12
- Amorim, J. P., Gali-Macedo, A., Marcelino, H., Bordeira-Cariço, R., Naranjo, S., Rivero-Gil, S., Teixeira, J., Galhardo, M., Marques, J. and Bessa, J. (2020). A Conserved Notochord Enhancer Controls Pancreas Development in Vertebrates. *Cell Rep.* 32, 107862
- Andrews, T. G. R., Gattoni, G., Busby, L., Schwimmer, M. A., and Benito-Gutierrez, E. (2020a). Hybridization Chain Reaction for Quantitative and Multiplex Imaging of Gene Expression in Amphioxus Embryos and Adult Tissues. In: Nielsen B., Jones J. (eds) *In Situ Hybridization Protocols. Methods in Molecular Biology*, vol 2148. Humana, New York, NY
- Andrews, T. G. R., Pönisch, W., Paluch, E., Steventon, B. and Benito-Gutierrez, E. (2020b). Single-cell morphometrics reveals ancestral principles of notochord development. *Biorxiv*
- Anlas, K. and Trivedi, V. (2020). Studying evolution of the primary body axis in vivo and in vitro. *Rxiv*.
- Annona, G., Holland, N. D. and D'Aniello, S. (2015). Evolution of the notochord. *Evodevo* 6, 1–13.
- Anthwal, N., Fenelon, J., Johnston, S. D., Renfree, M. B. and Tucker, A. S. (2020). Transient role of the middle ear as a lower jaw support across mammals. *eLife* 9, e57860
- Antolović, V., Lenn, T., Miermont, A. and Chubb, J. R. (2019). Transition state dynamics during a stochastic fate choice. *Dev.* 146, dev173740
- Appel, B., Fritz, A., Westerfield, M., Grunwald, D. J., Eisen, J. S. and Riley, B. B. (1999). Delta-mediated specification of midline cell fates in zebrafish embryos. *Curr. Biol.* 9, 247–256
- Arendt, D., Tessmar, K., Medeiros de Campos-Baptista, M. I., Dorresteijn, A. and Wittbrodt, J. (2002). Development of pigment-cup eyes in the polychaete *Platynereis dumerilii* and evolutionary conservation of larval eyes in bilateria. *Development* 129, 1143–1154
- Arendt, D., Tessmar-Raible, K., Snyman, H., Dorresteijn, A. W. and Wittbrodt, J. (2004). Ciliary photoreceptors with a vertebrate-type opsin in an invertebrate brain. *Science* 306, 869–871
- Arendt, D., Musser, J. M., Baker, C. V. H., Bergman, A., Cepko, C., Erwin, D. H., Pavlicev, M., Schlosser, G., Widder, S., Laubichler, M. D., et al. (2016). The origin and evolution of cell types. *Nat. Rev. Genet.* 17, 744–757

- Arthur, W. (2004). *Biased Embryos and Evolution*. Cambridge: Cambridge University Press.
- Attardi, A., Fulton, T., Florescu, M., Shah, G., Muresan, L., Huisken, J., Oudenaarden, A. van, Steventon, B., Lenz, M. O., Lancaster, C., et al. (2018). Neuromesodermal progenitors are a conserved source of spinal cord with divergent growth dynamics. *Development* 145, dev166728
- Aulehla, A., Wehrle, C., Brand-Saberi, B., Kemler, R., Gossler, A., Kanzler, B. and Herrmann, B. G. (2003). Wnt3a plays a major role in the segmentation clock controlling somitogenesis. *Dev. Cell* 4, 395–406
- Auman, T., Vreede, B. M. I., Weiss, A., Hester, S. D., Williams, T. A., Nagy, L. M. and Chipman, A. D. (2017). Dynamics of growth zone patterning in the milkweed bug *Oncopeltus fasciatus*. *Development* dev.142091
- Averof, M. and Patel, N. H. (1997). Crustacean appendage evolution associated with changes in Hox gene expression. *Nature* 388, 682–686
- Bagnat, M. and Gray, R. S. (2020). Development of a straight vertebrate body axis. *Development* 147, dev175794
- Bagwell, J., Norman, J., Ellis, K., Peskin, B., Hwang, J., Ge, X., Nguyen, S., McMenamin, S. K., Stainier, D. Y. R. and Bagnat, M. (2020). Notochord vacuoles absorb compressive bone growth during zebrafish spine formation. *eLife* 9, e51221
- Baker, N. E. (1987). Molecular cloning of sequences from wingless, a segment polarity gene in *Drosophila*: The spatial distribution of a transcript in embryos. *EMBO J.* 6, 1765–1773
- Balmer, S., Nowotschin, S. and Hadjantonakis, A. K. (2016). Notochord morphogenesis in mice: Current understanding and open questions. *Dev. Dyn.* 245, 547–557
- Bancroft, M. and Bellairs, R. (1976). The development of the notochord in the chick embryo, studied by scanning and transmission electron microscopy. *J. Embryol. Exp. Morphol.* 35, 383–401
- Bardot, E. S. and Hadjantonakis, A. (2020). Mouse gastrulation: coordination of tissue patterning, specification and diversification of cell fate. *Mech Dev* 163, 103617
- Beaster-Jones, L., Kaltenbach, S. L., Koop, D., Yuan, S., Chastain, R. and Holland, L. Z. (2008). Expression of somite segmentation genes in amphioxus: A clock without a wavefront? *Dev. Genes Evol.* 218, 599–611
- Beck, C. W. (2015). Development of the vertebrate tailbud. *Wiley Interdiscip. Rev. Dev. Biol.* 4, 33–44
- Beck, C. W. and Slack, J. M. W. (1998). Analysis of the developing xenopus tail bud reveals separate phases of gene expression during determination and outgrowth. *Mech. Dev.* 72, 41–52
- Behrndt, M., Salbreux, G., Campinho, P., Hauschild, R., Oswald, F., Roensch, J., Grill, S. W. and Heisenberg, C. (2012). Forces Driving Epithelial Spreading in Zebrafish Gastrulation. *Sci. Rep.* 338, 257–260
- Belgacem, M. R., Escande, M. L., Escriva, H. and Bertrand, S. (2011). Amphioxus Tbx6/16 and Tbx20 embryonic expression patterns reveal ancestral functions in chordates. *Gene Expr. Patterns* 11, 239–243
- Bénazéraf, B. (2019). Dynamics and mechanisms of posterior axis elongation in the vertebrate embryo. *Cell. Mol. Life Sci.* 76, 89–98
- Bénazéraf, B. and Pourquié, O. (2013). Formation and segmentation of the vertebrate body axis. *Annu. Rev. Cell Dev. Biol.* 29
- Bénazéraf, B., Francois, P., Baker, R. E., Denans, N., Little, C. D. and Pourquié, O. (2010). A random cell motility gradient downstream of FGF controls elongation of an amniote embryo. *Nature* 466, 248–252
- Bénazéraf, B., Beaupeux, M., Tchernookov, M., Wallingford, A., Salisbury, T., Shirtz, A., Shirtz, A., Huss, D.,

- Pourquié, O., François, P., et al. (2017). Multiscale quantification of tissue behavior during amniote embryo axis elongation. *Development* 144, 4462–4472
- Bensch, R., Song, S., Ronneberger, O. and Driever, W. (2013). Non-directional radial intercalation dominates deep cell behaviour during zebrafish epiboly. *Biol. Open* 2, 845–854
- Bentley, K., Philippides, A. and Ravasz Regan, E. (2014). Do endothelial cells dream of eclectic shape? *Dev. Cell* 29, 146–158
- Berg, S., Kutra, D., Kroeger, T., Strachle, C. N., Kausler, B. X., Haubold, C., Schiegg, M., Ales, J., Beier, T., Rudy, M., et al. (2019). Ilastik: Interactive Machine Learning for (Bio)Image Analysis. *Nat. Methods* 16, 1226–1232
- Bertrand, S. and Escriva, H. (2011). Evolutionary crossroads in developmental biology: amphioxus. *Development* 138, 4819–4830
- Bertrand, S., Camasses, A., Somorjai, I., Belgacem, M. R., Chabrol, O., Escande, M.-L., Pontarotti, P. and Escriva, H. (2011). Amphioxus FGF signaling predicts the acquisition of vertebrate morphological traits. *Proc. Natl. Acad. Sci. U. S. A.* 108, 9160–5
- Bhullar, B. A. S., Marugán-Lobón, J., Racimo, F., Bever, G. S., Rowe, T. B., Norell, M. A. and Abzhanov, A. (2012). Birds have paedomorphic dinosaur skulls. *Nature* 487, 223–226.
- Bijtel, J. H. (1958). The growth of the tail in urodele larvae. *Experientia* 12, 259.
- Bininda-Emonds, O. R. P., Jeffery, J. E. and Richardson, M. K. (2003). Inverting the hourglass: Quantitative evidence against the phylotypic stage in vertebrate development. *Proc. R. Soc. B Biol. Sci.* 270, 341–346
- Bivand, R. S. and Wong, D. W. S. (2018). Comparing implementations of global and local indicators of spatial association. *Test* 27, 716–748
- Blom, J. and Lilja, C. (2005). A comparative study of embryonic development of some bird species with different patterns of postnatal growth. *Zoology* 108, 81–95
- Bo"ina, I. and Saraga-Babi!, M. (2006). The notochordal sheath in amphioxus - An ultrastructural and histochemical study. *Coll. Antropol.* 30, 361–367
- Bodor, D. L., Pönisch, W., Endres, R. G. and Paluch, E. K. (2020). Of Cell Shapes and Motion: The Physical Basis of Animal Cell Migration. *Dev. Cell* 52, 550–562
- Bomati, E. K., Manning, G. and Deheyn, D. D. (2009). Amphioxus encodes the largest known family of green fluorescent proteins, which have diversified into distinct functional classes. *BMC Evol. Biol.* 9:77
- Bowman, E. J., Siebers, A. and Altendorf, K. (1988). Bafilomycins; A class of inhibitors of membrane ATPases from microorganisms, animal cells, and plant cells. *Proc. Natl. Acad. Sci. U. S. A.* 85, 7972–7976
- Briggs, J. A., Weinreb, C., Wagner, D. E., Megason, S., Peshkin, L., Kirschner, M. W. and Klein, A. M. (2018). The dynamics of gene expression in vertebrate embryogenesis. *Science* 5780, 1–17
- Brun, R. B. and Garson, J. A. (1984) Notochord Formation in the Mexican Salamander (*Ambystoma mexicanum*) is Different From Notochord Formation in *Xenopus laevis*. *J. Exp. Zoo* 240, 235–240
- Cambray, N. and Wilson, V. (2002). Axial progenitors with extensive potency are localised to the mouse chordoneural hinge. *Development* 129, 4855–66
- Cambray, N. and Wilson, V. (2007). Two distinct sources for a population of maturing axial progenitors. *Development* 134, 2829–40
- Campàs, O. (2016). A toolbox to explore the mechanics of living embryonic tissues. *Semin. Cell Dev. Biol.* 55, 119–130

- Carroll, S. B. (2008). Evo-Devo and an Expanding Evolutionary Synthesis: A Genetic Theory of Morphological Evolution. *Cell* 134, 25–36
- Catala, M., Teillet, M. A. and Le Douarin, N. M. (1995). Organization and development of the tail bud analyzed with the quail-chick chimaera system. *Mech. Dev.* 51, 51–65
- Catala, M., Teillet, M. A., De Robertis, E. M. and Le Douarin, N. M. (1996). A spinal cord fate map in the avian embryo: While regressing, Hensen's node lays down the notochord and floor plate thus joining the spinal cord lateral walls. *Development* 122, 2599–2610
- Cerfontaine, P. (1906). Recherches sur le développement de l'amphioxus. *Arch. Biol. Liège.* 22, 229–418
- Chai, Y., Jiang, X., Ito, Y., Bringas, P., Han, J., Rowitch, D. H., Soriano, P., McMahon, A. P. and Sucov, H. M. (2000). Fate of the mammalian cranial neural crest during tooth and mandibular morphogenesis. *Development* 127, 1671–1679
- Chartier, M., Jabbour, F., Gerber, S. and Mitteroecker, P. (2017). The floral morphospace – a modern comparative approach to study angiosperm evolution. *New Phytol.* 204, 841–853
- Chen, J.-Y. (2009). The sudden appearance of diverse animal body plans during the Cambrian explosion. *Int. J. Dev. Biol.* 53: 733–751
- Choi, K. S., Cohn, M. J. and Harfe, B. D. (2008). Identification of nucleus pulposus precursor cells and notochordal remnants in the mouse: Implications for disk degeneration and chordoma formation. *Dev. Dyn.* 237, 3953–3958
- Choi, H. M. T., Beck, V. A. and Pierce, N. A. (2014). Next-generation in situ hybridization chain reaction: Higher gain, lower cost, greater durability. *ACS Nano* 8, 4284–4294
- Choi, H. M. T., Schwarzkopf, M., Fornace, M. E., Acharya, A., Artavanis, G., Stegmaier, J., Cunha, A. and Pierce, N. A. (2018). Third-generation in situ hybridization chain reaction: Multiplexed, quantitative, sensitive, versatile, robust. *Development* 145, dev165753
- Choudhary, D., Mossa, A., Jadhav, M. and Cecconi, C. (2019). Bio-molecular applications of recent developments in optical tweezers. *Biomolecules* 9, 1–19.
- Clark, E. and Akam, M. (2016). Odd-paired controls frequency doubling in *Drosophila* segmentation by altering the pair-rule gene regulatory network. *eLife* 5, e18215
- Clevers, H., Rafelski, S., Elowitz, M., Klein, A., Shendure, J., Trapnell, C., Lein, E., Lundberg, E., Uhlen, M., Martinez-Arias, A., et al. (2017). What Is Your Conceptual Definition of “Cell Type” in the Context of a Mature Organism? *Cell Syst.* 4, 255–259
- Cole, N. J. and Currie, P. D. (2007). Insights from sharks: Evolutionary and developmental models of fin development. *Dev. Dyn.* 236, 2421–2431
- Compagnon, J., Barone, V., Rajshekar, S., Kottmeier, R., Pranjić-Ferscha, K., Behndt, M. and Heisenberg, C. P. (2014). The notochord breaks bilateral symmetry by controlling cell shapes in the Zebrafish laterality organ. *Dev. Cell* 31, 774–783
- Conklin, E. G. (1932). The embryology of amphioxus. *J. Morphol.* 54, 69–151
- Conklin, E. G. (1933). The development of isolated and partially separated blastomeres of Amphioxus. *J. Exp. Zool.* 64, 303, 375
- Costa, G. (1834). Cenni zoologici ossia descrizione sommaria della specie nuove di animali scoperti in diverse contrade del regno nell'anno 1834. *Azzolino*, Naples.

- Cretokos, C. J., Wang, Y., Green, E. D., Martin, J. F., Rasweiler IV, J. J. and Behringer, R. R. (2008). Regulatory divergence modifies limb length between mammals. *Genes Dev.* 22, 141–151
- Croce, J. C. and McClay, D. R. (2008). Evolution of the Wnt Pathways. *Methods Mol. Biol.* 469, 417–429
- Cunningham, T. J., Brade, T., Sandell, L. L., Lewandoski, M., Trainor, P. A., Colas, A., Mercola, M. and Duester, G. (2015). Retinoic acid activity in undifferentiated neural progenitors is sufficient to fulfill its role in restricting Fgf8 expression for somitogenesis. *PLoS One* 10, 0137894
- Danos, M. C. and Yost, H. J. (1995). Linkage of cardiac left-right asymmetry and dorsal-anterior development in *Xenopus*. *Development* 121, 1467–1474
- Davis, R. L., and Kirschner, M. W. (2000). The fate of cells in the tailbud of *Xenopus laevis*. *Development* 127, 255–267
- Dawkins, R. (1976). *The Selfish Gene*. Oxford ; New York :Oxford University Press.
- De Bree, K., De Bakker, B. S. and Oostra RJ (2018). The development of the human notochord. *PLoS One* 13, e0205752
- Delos Santos, N., Azmat, S., Cuenca, Y., Drenth, J., Lauper, J. and Tseng, A. S. (2016). Effects of the biocide methylisothiazolinone on *Xenopus laevis* wound healing and tail regeneration. *Aquat. Toxicol.* 181, 37–45
- Delsuc, F., Brinkmann, H., Chourrout, D. and Philippe, H. (2006). Tunicates and not cephalochordates are the closest living relatives of vertebrates. *Nature* 439, 965–968
- Dietrich, A. C., Lombardo, V. A. and Abdelilah-Seyfried, S. (2014). Blood Flow and Bmp Signaling Control Endocardial Chamber Morphogenesis. *Dev. Cell* 30, 367–377
- Dong, B., Horie, T., Denker, E., Kusakabe, T., Tsuda, M., Smith, W. C. and Jiang, D. (2009). Tube formation by complex cellular processes in *Ciona intestinalis* notochord. *Dev. Biol.* 330, 237–249
- Drake, A. G. and Klingenberg, C. P. (2010). Large-scale diversification of skull shape in domestic dogs: Disparity and modularity. *Am. Nat.* 175, 289–301
- Drost, H. G., Janitza, P., Grosse, I. and Quint, M. (2017). Cross-kingdom comparison of the developmental hourglass. *Curr. Opin. Genet. Dev.* 45, 69–75
- Duboule, D. (1994). Temporal colinearity and the phylotypic progression: A basis for the stability of a vertebrate Bauplan and the evolution of morphologies through heterochrony. *Development* 120, 135–142
- Duboule, D. (2007). The rise and fall of Hox gene clusters. *Development* 134, 2549–2560
- Duboule, D. (2010). The evo-devo comet. *EMBO Rep.* 11, 489
- Echelard, Y., Epstein, D. J., St-Jacques, B., Shen, L., Mohler, J., McMahon, J. A. and McMahon, A. P. (1993). Sonic hedgehog, a member of a family of putative signaling molecules, is implicated in the regulation of CNS polarity. *Cell* 75, 1417–1430
- Edelman, L. B., Chandrasekaran, S. and Price, N. D. (2010). Systems biology of embryogenesis. *Reprod. Fertil. Dev.* 22, 98–105
- Edri, S., Hayward, P., Jawaid, W. and Arias, A. M. (2019). Neuro-mesodermal progenitors (NMPPs): A comparative study between pluripotent stem cells and embryo-derived populations. *Dev.* 146, dev180190
- Edri, S., Hayward, P., Baillie-Johnson, P., Steventon, B. J. and Arias, A. M. (2019). An epiblast stem cell-derived multipotent progenitor population for axial extension. *Development* 146, dev168187
- Ellis, K., Bagwell, J. and Bagnat, M. (2013). Notochord vacuoles are lysosome-related organelles that function in axis and spine morphogenesis. *J. Cell Biol.* 200, 667–679

- Eng, C. H. L., Lawson, M., Zhu, Q., Dries, R., Koulena, N., Takei, Y., Yun, J., Cronin, C., Karp, C., Yuan, G. C., et al. (2019). Transcriptome-scale super-resolved imaging in tissues by RNA seqFISH+. *Nature* 568, 235–239
- Ettensohn, C. A. and Adomako-Ankomah, A. (2019). The evolution of a new cell type was associated with competition for a signaling ligand. *PLoS Biol.* 17, e3000460
- Fabrezi, M., Quinzio, S. I., Goldberg, J., Cruz, J. C., Pereyra, M. C. and Wassersug, R. J. (2016). Developmental changes and novelties in ceratophryid frogs. *Evodevo* 7:5
- Ferrier, D. E., Minguillón, C., Cebrián, C. and Garcia-Fernández, J. (2001). Amphioxus *Evx* genes: implications for the evolution of the Midbrain-Hindbrain Boundary and the chordate tailbud. *Dev. Biol.* 237, 270–281
- Feroze, R., Shawky, J. H., von Dassow, M. and Davidson, L. A. (2015). Mechanics of Blastopore Closure during Amphibian Gastrulation. *Dev. Biol.* 398, 57–67
- Flood, R. (1975). Fine structure of the notochord of amphioxus. *Symp. zool. Soc. L.* 36, 81–104
- Fouquet, B., Weinstein, B. M., Serluca, F. C. and Fishman, M. C. (1997). Vessel patterning in the embryo of the zebrafish: Guidance by notochord. *Dev. Biol.* 183, 37–48
- Fritzenwanker, J. H., Uhlinger, K. R., Gerhart, J., Silva, E. and Lowe, C. J. (2019). Untangling posterior growth and segmentation by analyzing mechanisms of axis elongation in hemichordates. *Proc. Natl. Acad. Sci. U. S. A.* 116, 8403–8408
- Fujimoto, S., Oisi, Y., Kuraku, S., Ota, K. G. and Kuratani, S. (2013). Non-parsimonious evolution of hagfish *Dlx* genes. *BMC Evol. Biol.* 13, 15–17
- Fulton, T., Trivedi, V., Attardi, A., Anlas, K., Dingare, C., Arias, A. M. and Steventon, B. (2020). Axis Specification in Zebrafish Is Robust to Cell Mixing and Reveals a Regulation of Pattern Formation by Morphogenesis. *Curr. Biol.* 30, 2984–2994
- Galant, R. and Carroll, S. B. (2002). Evolution of a transcriptional repression domain in an insect Hox protein. *Nature* 415, 910–913
- Galis, F. (1999). Why do almost all mammals have seven cervical vertebrae? Developmental constraints, Hox genes, and cancer. *J. Exp. Zool.* 285, 19–26
- Garriock, R. J., Chalamalasetty, R. B., Kennedy, M. W., Canizales, L. C., Lewandoski, M. and Yamaguchi, T. P. (2015). Lineage tracing of neuromesodermal progenitors reveals novel wnt-dependent roles in trunk progenitor cell maintenance and differentiation. *Development* 142, 1628–1638
- Garrity, D. M., Childs, S. and Fishman, M. C. (2002). The heartstrings mutation in zebrafish causes heart/fin *Tbx5* deficiency syndrome. *Development* 129, 4635–4645
- Gazave, E., Lapébie, P., Richards, G. S., Brunet, F., Ereskovsky, A. V., Degnan, B. M., Borchiellini, C., Vervoort, M. and Renard, E. (2009). Origin and evolution of the Notch signalling pathway: An overview from eukaryotic genomes. *BMC Evol. Biol.* 9, 1–27
- Gell-Mann, M. (2005). Complex adaptive systems. *Collect. Dyn. Nonlinear Disord. Syst.* XIX, 359–369
- Gerhart, J. (2001). Evolution of the organizer and the chordate body plan. *Int. J. Dev. Biol.* 45, 133–153
- Gillis, J. A. and Hall, B. K. (2016). A shared role for sonic hedgehog signalling in patterning chondrichthyan gill arch appendages and tetrapod limbs. *Development.* 143, 1313–1317
- Gillis, J. A., Alsema, E. C. and Criswell, K. E. (2017). Trunk neural crest origin of dermal denticles in a cartilaginous fish. *Proc. Natl. Acad. Sci.* 114, 201713827

- Gilmour, D., Rembold, M. and Leptin, M. (2017). From morphogen to morphogenesis and back. *Nature* 541, 311–320
- Glickman, N. S., Kimmel, C. B., Jones, M. A. and Adams, R. J. (2003). Shaping the zebrafish notochord. *Development* 130, 873–87
- Godard, B. G., Munro, E., Chenevert, J., Mcdougall, A., Munro, E. and Chenevert, J. (2020). Article Apical Relaxation during Mitotic Rounding Promotes Article Apical Relaxation during Mitotic Rounding Promotes Tension-Oriented Cell Division. *Dev Cell* 55, 1–12
- Gomez, C., Ozbudak, E. M., Wunderlich, J., Baumann, D., Lewis, J. and Pourquie, O. (2008). Control of segment number in vertebrate embryos. *Nature* 454, 335–339
- Gont, L. K., Steinbeisser, H., Blumberg, B. and De Robertis, E. M. (1993). Tail formation as a continuation of gastrulation: The multiple cell populations of the *Xenopus* tailbud derive from the late blastopore lip. *Development* 119, 991–1004
- Gonzalez, P., Uhlinger, K. R. and Lowe, C. J. (2017). The Adult Body Plan of Indirect Developing Hemichordates Develops by Adding a Hox-Patterned Trunk to an Anterior Larval Territory. *Curr. Biol.* 27, 87–95
- Goto, H., Kimmey, S. C., Row, R. H., Matus, D. Q. and Martin, B. L. (2017). FGF and canonical Wnt signaling cooperate to induce paraxial mesoderm from tailbud neuromesodermal progenitors through regulation of a two-step EMT. *Development* 144, 1412–1424
- Gouti, M., Tsakiridis, A., Wymeersch, F. J., Huang, Y., Kleinjung, J., Wilson, V. and Briscoe, J. (2014). In vitro generation of neuromesodermal progenitors reveals distinct roles for wnt signalling in the specification of spinal cord and paraxial mesoderm identity. *PLoS Biol.* 12, 885–890
- Gouti, M., Delile, J., Stamataki, D., Wymeersch, F. J., Huang, Y., Kleinjung, J., Wilson, V. and Briscoe, J. (2017). A Gene Regulatory Network Balances Neural and Mesoderm Specification during Vertebrate Trunk Development. *Dev. Cell* 41, 243–261
- Graham, A. and Richardson, J. (2012). Developmental and evolutionary origins of the pharyngeal apparatus. *EvoDevo* 3:24
- Graham, A., Papalopulu, N. and Krumlauf, R. (1989). The murine and *Drosophila* homeobox gene complexes have common features of organization and expression. *Cell* 57, 367–378
- Graham, A., Butts, T., Lumsden, A. and Kiecker, C. (2014). What can vertebrates tell us about segmentation? *EvoDevo* 5:24
- Gray, S. D. and Dale, J. K. (2010). Notch signalling regulates the contribution of progenitor cells from the chick Hensen's node to the floor plate and notochord. *Development* 137, 561–8
- Green, S. A., Simoes-Costa, M. and Bronner, M. E. (2015). Evolution of vertebrates as viewed from the crest. *Nature* 520, 474–482
- Guignard, L., Fiúza, U. M., Leggio, B., Laussu, J., Faure, E., Michelin, G., Biasuz, K., Hufnagel, L., Malandain, G., Godin, C., et al. (2020). Contact area-dependent cell communication and the morphological invariance of ascidian embryogenesis. *Science* 369, eaar5663
- Haeckel, E. (1866). *Generelle morphologie der organismen. Allgemeine grundzüge der organischen formen-wissenschaft, mechanisch begründet durch die von Charles Darwin reformirte descendenztheorie.* Berlin: Reimer
- Haeckel, E. (1874). *Anthropogenie oder Entwicklungsgeschichte des Menschen. Gemeinverständliche wissenschaftliche Vorträge über die Grundzüge der menschlichen Keimes- und Stammes- Geschichte.* Leipzig: Engelmann.
- Hall, B. K. (2012). Evolutionary Developmental Biology (Evo-Devo): Past, Present, and Future. *Evol. Educ. Outreach* 5,

- Hardin, J. and Keller, R.** (1988). The behaviour and function of bottle cells during gastrulation of *Xenopus laevis*. *Development* 103, 211–230
- Harrington, M. J., Hong, E. and Brewster, R.** (2009). Comparative analysis of neurulation: First impressions do not count. *Mol. Reprod. Dev.* 76, 954–965
- Hasley, A., Chavez, S., Danilchik, M., Wühr, M. and Pelegri, F.** (2017). Vertebrate embryonic cleavage pattern determination. *Adv. Exp. Med. Biol.* 953, 117–171
- Hatschek, B.** (1893). The amphioxus and its development. Swan Sonnenschein & Co, London.
- Hausmann, G., Von Mering, C. and Basler, K.** (2009). The Hedgehog signaling pathway: Where did it come from? *PLoS Biol.* 7, e1000146
- Henrique, D., Abranches, E., Verrier, L. and Storey, K. G.** (2015). Neuromesodermal progenitors and the making of the spinal cord. *Development* 142, 2864–2875
- Hirsinger, E., Carvalho, J. E., Chevalier, C., Lutfalla, G., Nicolas, J.-F., Peyri eras, N. and Schubert, M.** (2015). Expression of Fluorescent Proteins in *Branchiostoma lanceolatum* by mRNA Injection into Unfertilized Oocytes. *J. Vis. Exp.* 95, e52042
- Holland, N. D. and Holland, L. Z.** (1993) Embryos and larvae of invertebrate deuterostomes, in: *Essential Developmental Biology: A Practical Approach* (Stem, C. D. and Holland, P. W. H., eds.), Oxford: IRL Press at Oxford University Press, pp. 21–32
- Holland, N. D. and Holland, L. Z.** (2006). Stage- and tissue- specific patterns of cell division in embryonic and larval tissues of amphioxus during normal development. *Evol. Dev.* 8, 142–149
- Holland, P. W. H., Koschorz, B., Holland, L. Z. and Herrmann, B. G.** (1995). Conservation of Brachyury (T) genes in amphioxus and vertebrates: Developmental and evolutionary implications. *Development* 121, 4283–4291
- Holland, L. Z., Schubert, M., Holland, N. D. and Neuman, T.** (2000). Evolutionary conservation of the presumptive neural plate markers *AmphiSox1/2/3* and *AmphiNeurogenin* in the invertebrate chordate amphioxus. *Dev. Biol.* 226, 18–33
- Holland, L. Z., Rached, L. a, Tamme, R., Holland, N. D., Kortschak, D., Inoko, H., Shiina, T., Burgtorf, C. and Lardelli, M.** (2001). Characterization and developmental expression of the amphioxus homolog of Notch (*AmphiNotch*): evolutionary conservation of multiple expression domains in amphioxus and vertebrates. *Dev. Biol.* 232, 493–507
- Holland, L. Z., Holland, N. D. and Gilland, E.** (2008). Amphioxus and the evolution of head segmentation. *Integr. Comp. Biol.* 48, 630–646
- Hopwood, N.** (2015a). The cult of amphioxus in German Darwinism; or, Our gelatinous ancestors in Naples’ blue and balmy bay. *Hist. Philos. Life Sci.* 36, 371–393
- Hopwood, N.** (2015b). *Haeckel’s Embryos: Images, Evolution and Fraud*. Chicago: *University of Chicago Press*.
- Huebner, R. J. and Wallingford, J. B.** (2018). Coming to Consensus: A Unifying Model Emerges for Convergent Extension. *Dev. Cell* 46, 389–396
- Huycke, T. R., Miller, B. M., Gill, H. K., Nerurkar, N. L., Sprinzak, D., Mahadevan, L. and Tabin, C. J.** (2019). Genetic and Mechanical Regulation of Intestinal Smooth Muscle Development. *Cell* 179, 90–105
- Huxley, J.** (1942). *Evolution: The Modern Synthesis*. London: *George Allen and Unwin Ltd.*

- Ibarra-Soria, X., Jawaid, W., Pijuan-Sala, B., Ladopoulos, V., Scialdone, A., Jörg, D. J., Tyser, R. C. V., Calero-Nieto, F. J., Mulas, C., Nichols, J., et al. (2018). Defining murine organogenesis at single-cell resolution reveals a role for the leukotriene pathway in regulating blood progenitor formation. *Nat. Cell Biol.* doi.org/10.1038/s41556-017-0013-z
- Imura, T., Yang, X., Weijer, C. J. and Pourquié, O. (2007). Dual mode of paraxial mesoderm formation during chick gastrulation. *Proc. Natl. Acad. Sci. U. S. A.* 104, 2744–9
- Irie, N. and Kuratani, S. (2011). Comparative transcriptome analysis reveals vertebrate phylotypic period during organogenesis. *Nat. Comms.* 2:248
- Irie, N. and Kuratani, S. (2014). The developmental hourglass model: A predictor of the basic body plan? *Development* 141, 4649–4655
- Jackman, W. R., Langeland, J. A. and Kimmel, C. B. (2000). Islet Reveals Segmentation in the Amphioxus Hindbrain Homolog. *Dev. Biol.* 220, 16–26
- Jacob, F. (1977). Evolution and Tinkering. *Science* 196, 1161–1166
- Jacobson, A. G. (1981). Morphogenesis of the neural plate and tube. In *Morphogenesis and Pattern Formation* (eds. T. G. Connelly, L. Brinkley, and B. Carlson). New York: Raven Press, pp. 223–263
- Jain, A., Ulman, V., Mukherjee, A., Prakash, M., Cuenca, M. B., Pimpale, L. G., Münster, S., Haase, R., Pan, K. A., Jug, F., et al. (2020). Regionalized tissue fluidization is required for epithelial gap closure during insect gastrulation. *Nat. Comms.* 11:5604
- Jiang, D. and Smith, W. C. (2007). Ascidian notochord morphogenesis. *Dev. Dyn.* 236, 1748–1757
- Joo, J. Il, Zhou, J. X., Huang, S. and Cho, K. H. (2018). Determining Relative Dynamic Stability of Cell States Using Boolean Network Model. *Sci. Rep.* 8:12077 |
- Jurand, A. (1974). Some aspects of the development of the notochord in mouse embryos. *J. Embryol. Exp. Morphol.* 32, 1–33
- Kanki, J. P. and Ho, R. K. (1997). The development of the posterior body in zebrafish. *Development* 124, 881–893
- Kauffman, S. A. (1969). Metabolic stability and epigenesis in randomly constructed genetic nets. *J. Theor. Biol.* 22, 437–467
- Keller, R. E. (1975). Vital dye mapping of the gastrula and neurula of *Xenopus laevis*. I. Prospective Areas and Morphogenetic Movements of the Superficial Layer. *Dev. Biol.* 42, 222–241
- Keller, R. E. (1976). Vital dye mapping of the gastrula and neurula of *Xenopus laevis*. II. Prospective areas and morphogenetic movements of the deep layer. *Dev. Biol.* 51, 118–137
- Keller, R. E., Danilchik, M., Gimlich, R. and Shih, J. (1985). The function and mechanism of convergent extension during gastrulation of *Xenopus laevis*. *J. Embryol. Exp. Morphol.* 89, 185–209
- Keller, R., Cooper, M. S., Danilchik, M., Tibbetts, P. and Wilson, P. A. (1989). Cell intercalation during notochord development in *Xenopus laevis*. *J. Exp. Zool.* 251, 134–154
- Kierzkowski, D., Runions, A., Vuolo, F., Strauss, S., Lymbouridou, R., Routier-Kierzkowska, A. L., Wilson-Sánchez, D., Jenke, H., Galinha, C., Mosca, G., et al. (2019). A Growth-Based Framework for Leaf Shape Development and Diversity. *Cell* 177, 1405–1418
- Kim, S. K., Hebrok, M. and Melton, D. A. (1997). Notochord to endoderm signaling is required for pancreas development. *Development* 124, 4243–4252

- Kimmel, C. B., Ballard, W. W., Kimmel, S. R., Ullmann, B. and Schilling, T. F. (1995). Stages of embryonic development of the zebrafish. *Dev. Dyn.* 203, 253–310
- Kinney, B. A., Row, R. H., Tseng, Y. J., Weidmann, M. D., Knaut, H. and Martin, B. L. (2020). Sox2 and canonical Wnt signaling interact to activate a developmental checkpoint coordinating morphogenesis with mesodermal fate acquisition. *Biorxiv*
- Klaatsch H. (1897). Bemerkungen über die Gastrula des amphioxus. *Morph. Jahrb.* 25, 224–43
- Klingenberg, C. P. (2020). How Exactly Did the Nose Get That Long? A Critical Rethinking of the Pinocchio Effect and How Shape Changes Relate to Landmarks. *Evol. Biol.* 10.1007
- Knezevic, V., De Santo, R. and Mackem, S. (1998). Continuing organizer function during chick tail development. *Development* 125, 1791–1801
- Koç, A., Wheeler, L. J., Mathews, C. K. and Merrill, G. F. (2004). Hydroxyurea Arrests DNA Replication by a Mechanism that Preserves Basal dNTP Pools. *J. Biol. Chem.* 279, 223–230
- Koch, F., Scholze, M., Wittler, L., Schifferl, D., Sudheer, S., Grote, P., Timmermann, B., Macura, K. and Herrmann, B. G. (2017). Antagonistic Activities of Sox2 and Brachyury Control the Fate Choice of Neuro-Mesodermal Progenitors. *Dev. Cell* 42, 514–526
- Koehl, M. A. R., Quillin, K. J. and Pell, C. A. (2000). Mechanical design of fiber-wound hydraulic skeletons: The stiffening and straightening of embryonic notochords. *Am. Zool.* 40, 28–41
- Kowalevsky, A. (1867). Entwicklungsgeschichte des Amphioxus lanceolatus. *Mém. Acad. Imp. Sci. St-Petersb.* (Ser. VIII) 11: 1-17
- Kmeta-Stankic, V., Sabillo, A. and Domingo, C. R. (2010). Temporal and spatial patterning of axial myotome fibers in *Xenopus laevis*. *Dev. Dyn.* 239, 1162–1177
- Krol, A. J., Roellig, D., Dequéant, M. L., Tassy, O., Glynn, E., Hattem, G., Mushegian, A., Oates, A. C. and Pourquié, O. (2011). Evolutionary plasticity of segmentation clock networks. *Development* 138, 2783–2792
- Krumlauf, R., Holland, P. W. H., McVey, J. H. and Hogan, B. L. M. (1987). Developmental and spatial patterns of expression of the mouse homeobox gene, *Hox2.1*. *Development* 99, 603–617
- Lacalli, T. (2018). Amphioxus, motion detection, and the evolutionary origin of the vertebrate retinotectal map. *Evodevo* 9, 4–8
- Lankester, E. R. (1889). Memoirs: Contributions to the Knowledge of Amphioxus lanceolatus, Yarrell. *J. Cell. Sci.* s2-29: 365–408
- Lara-Ramirez, R., Pérez-González, C., Anselmi, C. and Patthey, C. (2019). A Notch-regulated proliferative stem cell zone in the developing spinal cord is an ancestral vertebrate trait. *Development* 146, dev166595
- Latimer, A. J. and Appel, B. (2006). Notch signaling regulates midline cell specification and proliferation in zebrafish. *Dev. Biol.* 298, 392–402
- Lauri, A., Brunet, T., Handberg-Thorsager, M., Fischer, A. H. L., Simakov, O., Steinmetz, P. R. H., Tomer, R., Keller, P. J. and Arendt, D. (2014). Development of the Annelid Axochord: Insights into notochord evolution. *Science* 345, 1365–1368
- Lawton, A. K., Nandi, A., Stulberg, M. J., Dray, N., Sneddon, M. W., Pontius, W., Emonet, T. and Holley, S. A. (2013). Regulated tissue fluidity steers zebrafish body elongation. *Development* 140, 573–582.
- Le Petillon, Y., Luxardi, G., Scerbo, P., Cibois, M., Leon, A., Subirana, L., Irimia, M., Kodjabachian, L., Escriva, H. and Bertrand, S. (2017). Nodal–Activin pathway is a conserved neural induction signal in chordates. *Nat. Ecol.*

- Legland, D., Arganda-Carreras, I. and Andrey, P. (2016). MorphoLibJ: Integrated library and plugins for mathematical morphology with ImageJ. *Bioinformatics* 32, 3532–3534
- Lemaire, P. (2011). Evolutionary crossroads in developmental biology: the tunicates. *Development* 138, 2143–2152
- Lenne, P. F., Munro, E., Heemskerk, I., Warmflash, A., Bocanegra-Moreno, L., Kishi, K., Kicheva, A., Long, Y., Fruleux, A., Boudaoud, A. et al. (2020). Roadmap on multiscale coupling of biochemical and mechanical signals during development. *Phys. Bio.* 10.1088
- Levin, M. (2012). Molecular bioelectricity in developmental biology: New tools and recent discoveries. *BioEssays* 34, 205–217
- Lewis, E. B. (1978). A gene complex controlling segmentation in *Drosophila*. *Nature* 276, 565–570
- Liao, B. K. and Oates, A. C. (2017). Delta-Notch signalling in segmentation. *Arthropod Struct. Dev.* 46, 429–447
- Liao, B.-K., Jörg, D. J. and Oates, A. C. (2016). Faster embryonic segmentation through elevated Delta-Notch signalling. *Nat. Comms.* 7, 11861
- Lignell, A., Kerosuo, L., Streichan, S. J., Cai, L. and Bronner, M. E. (2017). Identification of a neural crest stem cell niche by Spatial Genomic Analysis. *Nat. Comms.* 8, 10.1038
- Linsenmayer, T. F., Gibney, E. and Schmid, T. M. (1986). Segmental appearance of type X collagen in the developing avian notochord. *Dev. Biol.* 113, 467–473
- Löfberg, J. (1974). Apical surface topography of invaginating and noninvaginating cells. A scanning-transmission study of amphibian neurulae. *Dev. Biol.* 36, 311–329
- Lohoff, T., Ghazanfar, S., Missarova, A., Koulena, N., Pierson, N., Griffiths, J. A., Bardot, E. S., Eng, C. H. L., Tyser, R. C. V., Argelaguet, R., et al. (2020). Highly multiplexed spatially resolved gene expression profiling of mouse organogenesis. *Biorxiv*.
- Louis, A., Roest Crolius, H. R. and Robinson-Rechavi, M. (2012). How much does the amphioxus genome represent the ancestor of chordates? *Brief. Funct. Genomics* 11, 89–95
- Lowe, C. J., Wu, M., Salic, A., Evans, L., Lander, E., Stange-Thomann, N., Gruber, C. E., Gerhart, J. and Kirschner, M. (2003). Anteroposterior patterning in hemichordates and the origins of the chordate nervous system. *Cell* 113, 853–865
- Lowe, C. J., Clarke, N., Medeiros, D. M., Rokhsar, D. S., and Gerhart, J. (2015). The deuterostome context of chordate origins. *Nature*. 520, 456–465
- Lowery, L. A. and Sive, H. (2004). Strategies of vertebrate neurulation and a re-evaluation of teleost neural tube formation. *Mech. Dev.* 121, 1189–1197
- Lu, Q., Bhattachan, P. and Dong, B. (2019). Ascidian notochord elongation. *Dev. Biol.* 448, 147–153.
- Lubeck, E., Coskun, E. L., Zhiyentayev, T., Ahmad, M. and Cai, L. (2014). Single cell in situ RNA profiling by sequential hybridisation. *Nat. Methods* 11, 360–361
- Lukinavičius, G., Blaukopf, C., Pershagen, E., Schena, A., Reymond, L., Derivery, E., Gonzalez-Gaitan, M., D'Este, E., Hell, S. W., Gerlich, D. W., et al. (2015). SiR-Hoechst is a far-red DNA stain for live-cell nanoscopy. *Nat. Comms.* 6, ncomms9497
- Lumsden, A. G. S. (1988). Spatial organization of the epithelium and the role of neural crest cells in the initiation of the mammalian tooth germ. *Development* 103, 155–169

- MacBride, E. W. (1898). The early development of amphioxus. *Quart. J. Microsc. Sci.* 40, 589–612
- Machado, S., Mercier, V. and Chiaruttini, N. (2018). LimeSeg: A coarsed-grained lipid membrane simulation for 3D image segmentation. *Biorxiv*
- Maisey, J. G. (1986). Heads and Tails: a Chordate Phylogeny. *Cladistics* 2, 201–256
- Marioni, J. C. and Arendt, D. (2017). How Single-Cell Genomics Is Changing Evolutionary and Developmental Biology. *Annu. Rev. Cell Dev. Biol.* 33, 537–553
- Marlétaz, F., Firbas, P. N., Maeso, I., Tena, J. J., Bogdanovic, O., Perry, M., Wyatt, C. D. R., de la Calle-Mustienes, E., Bertrand, S., Burguera, D., et al. (2018). Amphioxus functional genomics and the origins of vertebrate gene regulation. *Nature* 564, 64–70
- Martin, B. L. and Kimelman, D. (2008). Regulation of Canonical Wnt Signaling by Brachyury Is Essential for Posterior Mesoderm Formation. *Dev. Cell* 15, 121–133
- Martin, B. L. and Kimelman, D. (2009). Wnt Signaling and the Evolution of Embryonic Posterior Development. *Curr. Biol.* 19, 215–219
- Martin, B. L. and Kimelman, D. (2012). Canonical Wnt Signaling Dynamically Controls Multiple Stem Cell Fate Decisions during Vertebrate Body Formation. *Dev. Cell* 22, 223–232
- Martinez Arias, A. and Steventon, B. (2018). On the nature and function of organizers. *Development* 145, dev159525
- Martínez Vergara, H., Bertucci, P. Y., Hantz, P., Tosches, M. A., Achim, K., Vopalensky, P. and Arendt, D. (2017). Whole-organism cellular gene-expression atlas reveals conserved cell types in the ventral nerve cord of *Platynereis dumerilii*. *Proc Natl Acad Sci USA* 114, 5878–5885
- McGrew, M. J., Sherman, A., Lillico, S. G., Ellard, F. M., Radcliffe, P. A., Gilhooley, H. J., Mitrophanous, K. A., Cambray, N., Wilson, V. and Sang, H. (2008). Localised axial progenitor cell populations in the avian tail bud are not committed to a posterior Hox identity. *Development* 135, 2289–99
- Meulemans, D. and Bronner-Fraser, M. (2007). The amphioxus SoxB family: Implications for the evolution of vertebrate placodes. *Int. J. Biol. Sci.* 3, 356–364
- Minguillón, C., Jiménez-Delgado, S., Panopoulou, G. and Garcia-Fernández, J. (2003). The amphioxus Hairy family: differential fate after duplication. *Development* 130, 5903–5914
- Mitteroecker, P. and Huttegger, S. M. (2009). The Concept of Morphospaces in Evolutionary and Developmental Biology: Mathematics and Metaphors. *Biol. Theory* 4, 54–67
- Miyamoto, D. M. and Crowther, R. J. (1985). Formation of the notochord in living ascidian embryos. *J. Embryol. Exp. Morphol.* 86, 1–17
- Mojtahedi, M., Skupin, A., Zhou, J., Castaño, I. G., Leong-Quong, R. Y. Y., Chang, H., Trachana, K., Giuliani, A. and Huang, S. (2016). Cell Fate Decision as High-Dimensional Critical State Transition. *PLoS Biol.* 14, 1–28
- Mongera, A., Rowghanian, P., Gustafson, H. J., Shelton, E., Kealhofer, D. A., Cam, E. K., Serwane, F., Lucio, A. A., Giammona, J. and Campàs, O. (2018). A fluid-to-solid jamming transition underlies vertebrate body axis elongation. *Nature* 561, 401–405
- Mookerjee, S. (1953). An experimental study of the development of the notochordal sheath. *Embryol. Exp. Morphol.* 1, 411–416
- Morgan, T. H. and Hazen, A. P. (1900). The gastrulation of amphioxus. *J. Morphol.* 16, 569–600

- Morgan, T. H. (1896). The number of cells in Larvae from isolated Blastomeres of Amphioxus. *Arch. für Entwicklungsmechanik der Org.* 3, 269–294
- Moris, N., Pina, C. and Arias, A. M. (2016). Transition states and cell fate decisions in epigenetic landscapes. *Nat. Rev. Genet.* 17, 693–703
- Morita, H., Grigolon, S., Bock, M., Krens, S. F. G., Salbreux, G. and Heisenberg, C. P. (2017). The Physical Basis of Coordinated Tissue Spreading in Zebrafish Gastrulation. *Dev. Cell* 40, 354–366
- Mugele, D., Moulding, D., Savery, D., Mole, M., Greene, N., Martinez-Barbera, J. P. and Copp, A. (2018). Genetic approaches in mice demonstrate that neuro-mesodermal progenitors express T/Brachyury but not Sox2. *Biorxiv*
- Müller, G. B. (2007). Evo-devo: extending the evolutionary synthesis. *Nat. Rev. Genet.* 73, 314–315
- Müller, G. B. (2017). Why an extended evolutionary synthesis is necessary. *Interface Focus* 7, 20170015
- Munro, E. M. and Odell, G. M. (2002). Polarized basolateral cell motility underlies invagination and convergent extension of the ascidian notochord. *Development* 129, 13–24
- Munsterberg, A. E. and Lassar, A. B. (1995). Combinatorial signals from the neural tube, floor plate and notochord induce myogenic bHLH gene expression in the somite. *Development* 121, 651–660
- Muzumdar, M. D., Tasic, B., Miyamichi, K., Li, L. and Luo, L. (2007). A Global Double-Fluorescent Cre Reporter Mouse. *Genesis* 45, 76–82
- Myers, C. T., Appleby, S. C. and Krieg, P. A. (2014). Use of small molecule inhibitors of the Wnt and Notch signaling pathways during *Xenopus* development. *Methods* 66, 380–389
- Nerurkar, N. L., Mahadevan, L. and Tabin, C. J. (2017). BMP signaling controls buckling forces to modulate looping morphogenesis of the gut. *Proc. Natl. Acad. Sci. U. S. A.* 114, 2277–2282
- Newgreen, D. F., Scheel, M. and Kastner, V. (1986). Morphogenesis of sclerotome and neural crest in avian embryos - In vivo and in vitro studies on the role of notochordal extracellular material. *Cell Tissue Res.* 244, 299–313
- Nieuwkoop, P. D. (1946). Experimental investigations on the origin and determination of the germ cells, and on the development of the lateral plates and germ ridges in urodeles. *Arch. Neerl. Zool.* 8, 1–205
- Nikolopoulou, E., Galea, G. L., Rolo, A., Greene, N. D. E. and Copp, A. J. (2017). Neural tube closure: Cellular, molecular and biomechanical mechanisms. *Dev.* 144, 552–566
- Novoselov, V. V. (1995). Notochord formation in amphibians: Two directions and two ways. *J. Exp. Zool.* 271, 296–306
- Nowotschin, S. and Hadjantonakis, A. K. (2009). Use of KikGR a photoconvertible green-to-red fluorescent protein for cell labeling and lineage analysis in ES cells and mouse embryos. *BMC Dev. Biol.* 9:49
- Nüsslein-Volhard, C. and Wieschaus, E. (1980). Mutations affecting segment number and polarity in *Drosophila*. *Nature* 287, 795–801
- O'Farrell, P. H. (2015). Growing an embryo from a single cell: A hurdle in animal life. *Cold Spring Harb. Perspect. Biol.* 7, a019042
- Oginuma, M., Moncuquet, P., Xiong, F., Karoly, E., Chal, J., Guevorkian, K. and Pourquié, O. (2017). A Gradient of Glycolytic Activity Coordinates FGF and Wnt Signaling during Elongation of the Body Axis in Amniote Embryos. *Dev. Cell* 40, 342–353
- Olivera-Martinez, I., Harada, H., Halley, P. A. and Storey, K. G. (2012). Loss of FGF-Dependent Mesoderm Identity and Rise of Endogenous Retinoid Signalling Determine Cessation of Body Axis Elongation. *PLoS Biol.* 10, e1001415

- Ollion, J., Cochenne, J., Loll, F., Escudé, C. and Boudier, T. (2013). TANGO: A generic tool for high-throughput 3D image analysis for studying nuclear organization. *Bioinformatics* 29, 1840–1841
- Özbudak, E. M. and Lewis, J. (2008). Notch signalling synchronizes the zebrafish segmentation clock but is not needed to create somite boundaries. *PLoS Genet.* 4, e15
- Pallas, P. A. (1774). *Spicilegia zoologica, quibus novae imprimis et obscurae animalium species iconibus, descriptionibus atque commentariis illustrantur cura. Berolini*
- Pascual-Anaya, J., Adachi, N., Álvarez, S., Kuratani, S., D'Aniello, S. and Garcia-Fernández, J. (2012). Broken colinearity of the amphioxus Hox cluster. *Evodevo* 3:28
- Pascual-Anaya, J., Sato, I., Sugahara, F., Higuchi, S., Paps, J., Ren, Y., Takagi, W., Ruiz-Villalba, A., Ota, K. G., Wang, W., et al. (2018). Hagfish and lamprey Hox genes reveal conservation of temporal colinearity in vertebrates. *Nat. Ecol. Evol.* 2, 859–866
- Petridou, N. I., Grigolon, S., Salbreux, G., Hannezo, E. and Heisenberg, C. P. (2019). Fluidization-mediated tissue spreading by mitotic cell rounding and non-canonical Wnt signalling. *Nat. Cell Biol.* 21, 169–178
- Peyrot, S. M., Wallingford, J. B. and Harland, R. M. (2011). A revised model of *Xenopus* dorsal midline development: Differential and separable requirements for Notch and Shh signaling. *Dev. Biol.* 352, 254–266
- Placzek, M. and Briscoe, J. (2018). Sonic hedgehog in vertebrate neural tube development. *Int. J. Dev. Biol.* 62, 221–230
- Placzek, M., Tessier-Lavigne, M., Yamada, T., Jessell, T. and Dodd, J. (1990). Mesodermal control of neural cell identity: Floor plate induction by the notochord. *Science* 250, 985–988
- Polly, P. D. and Motz, G. J. (2016). Patterns and Processes in Morphospace: Geometric Morphometrics of Three-Dimensional Objects. *Paleontol. Soc. Pap.* 22, 71–99
- Pourquié, O., Coltey, M., Teillet, M. A., Ordahl, C. and Le Douarin, N. M. (1993). Control of dorsoventral patterning of somitic derivatives by notochord and floor plate. *Proc. Natl. Acad. Sci. U. S. A.* 90, 5242–5246
- Priya, R., Allanki, S., Gentile, A. and Mansingh, S. (2020). Tension heterogeneity directs form and fate to pattern the myocardial wall. *Nature*
- Psychoyos, D. and Stern, C. D. (1996). Fates and migratory routes of primitive streak cells in the chick embryo. *Development* 122, 1523–34
- Rasmussen, S. L. K., Holland, L. Z., Schubert, M., Beaster-Jones, L. and Holland, N. D. (2007). Amphioxus Amphidelta: Evolution of Delta Protein Structure, Segmentation, and Neurogenesis. *Genesis* 45, 76–82
- Raup, D. M. and Michelson, A. (1965). Theoretical morphology of the coiled shell. *Science* 147, 1294–1295
- Renn, J., Büttner, A., To, T. T., Chan, S. J. H. and Winkler, C. (2013). A col10a1: NIGFP transgenic line displays putative osteoblast precursors at the medaka notochordal sheath prior to mineralization. *Dev. Biol.* 381, 134–143
- Richardson, M. K., Hanken, J., Gooneratne, M. L., Pieau, C., Raynaud, A., Selwood, L. and Wright, G. M. (1997). There is no highly conserved embryonic stage in the vertebrates: Implications for current theories of evolution and development. *Anat. Embryol.* 196, 91–106
- Rickert, C., Kunz, T., Harris, K-L., Whittington, P., Technau, G. (2013). Labeling of Single Cells in the Central Nervous System of *Drosophila melanogaster*. *J. Vis. Exp.* 73, e50150
- Rijsewijk, F., Schuermann, M., Wagenaar, E., Parren, P., Weigel, D. and Nusse, R. (1987). The *Drosophila* homology of the mouse mammary oncogene int-1 is identical to the segment polarity gene wingless. *Cell* 50, 649–657
- Rodrigues, S. G., Stickels, R. R., Goeva, A., Martin, C. A., Murray, E., Vanderburg, C. R., Welch, J., Chen, L. M.,

- Chen, F. and Macosko, E. Z. (2019). Slide-seq: A Scalable Technology for Measuring Genome-Wide Expression at High Spatial Resolution. *Biorxiv*
- Ronshaugen, M., McGinnis, N. and McGinnis, W. (2002). Hox protein mutation and macroevolution of the insect body plan. *Nature* 415, 914–917
- Row, R. H., Tsotras, S. R., Goto, H. and Martin, B. L. (2016). The zebrafish tailbud contains two independent populations of midline progenitor cells that maintain long-term germ layer plasticity and differentiate in response to local signaling cues. *Development* 143, 244–254.
- Rozbicki, E., Chuai, M., Karjalainen, A. I., Song, F., Sang, H. M., Martin, R., Knölker, H. J., Macdonald, M. P. and Weijer, C. J. (2015). Myosin-II-mediated cell shape changes and cell intercalation contribute to primitive streak formation. *Nat. Cell Biol.* 17, 397–408
- Sánchez Alvarado, A. (2017). To solve old problems, study new research organisms. *Dev. Biol.* 433, 111–114
- Sander, K. (1983). The evolution of patterning mechanisms: gleanings from insect embryogenesis and spermatogenesis. In *Development and Evolution* (eds. B. C. Goodwin, N. Holder and C. C. Wylie), pp. 124–137
- Sanders, E. J., Khare, M. K., Ooi, V. C. and Bellairs, R. (1986). An experimental and morphological analysis of the tail bud mesenchyme of the chick embryo. *Anat. Embryol.* 174, 179–185
- Satija, R., Farrell, J. A., Gennert, D., Schier, A. F. and Regev, A. (2015). Spatial reconstruction of single-cell gene expression data. *Nat. Biotechnol.* 33, 495–502
- Sauka-Spengler, T., Baratte, B., Lepage, M. and Mazan, S. (2003). Characterization of Brachyury genes in the dogfish *S. canicula* and the lamprey *L. fluviatilis*. Insights into gastrulation in a chondrichthyan. *Dev. Biol.* 263, 296–307
- Sausedo, R. A. and Schoenwolf, G. C. (1994). Quantitative analyses of cell behaviors underlying notochord formation and extension in mouse embryos. *Anat. Rec.* 239, 103–112
- Savin, T., Kurpios, N. A., Shyer, A. E., Florescu, P., Liang, H., Mahadevan, L. and Tabin, C. J. (2011). On the growth and form of the gut. *Nature* 476, 57–63
- Scarpa, E., Finet, C., Blanchard, G. B. and Sanson, B. (2018). Actomyosin-Driven Tension at Compartmental Boundaries Orients Cell Division Independently of Cell Geometry In Vivo. *Dev. Cell* 47, 727–740
- Schaeffer, B. (1987). Deuterostome Monophyly and Phylogeny. *Evol. Biol.* 21, 179–235.
- Schubert, M., Holland, L. Z., Stokes, M. D. and Holland, N. D. (2001). Three amphioxus Wnt genes (AmphiWnt3, AmphiWnt5, and AmphiWnt6) associated with the tail bud: the evolution of somitogenesis in chordates. *Dev. Biol.* 240, 262–273
- Sebé-Pedrós, A., Saudemont, B., Chomsky, E., Plessier, F., Mailhé, M. P., Renno, J., Loe-Mie, Y., Lifshitz, A., Mukamel, Z., Schmutz, S., et al. (2018). Cnidarian Cell Type Diversity and Regulation Revealed by Whole-Organism Single-Cell RNA-Seq. *Cell* 173, 1520–1534
- Segade, F., Cota, C., Famiglietti, A., Cha, A. and Davidson, B. (2016). Fibronectin contributes to notochord intercalation in the invertebrate chordate, *Ciona intestinalis*. *Evodevo* 7, 16
- Sehring, I. M., Dong, B., Denker, E., Bhattachan, P., Deng, W., Mathiesen, B. T. and Jiang, D. (2014). An Equatorial Contractile Mechanism Drives Cell Elongation but not Cell Division. *PLoS Biol.* 12, e1001781
- Sen, O., Saurin, A. T. and Higgins, J. M. G. (2018). The live cell DNA stain SiR-Hoechst induces DNA damage responses and impairs cell cycle progression. *Sci. Rep.* 8:7898 |
- Serwane, F., Mongera, A., Rowghanian, P., David, A., Lucio, A. A., Hockenbery, Z. M. and Campàs, O. (2017). In vivo quantification of spatially-varying mechanical properties in developing tissues. *Nat. Methods* 14, 181–186

- Shape, J. (2017). Computer modeling in developmental biology: growing today, essential tomorrow. *Development*, 144, 4214–4225
- Shih, J. and Keller, R. (1992a). Patterns of cell motility in the organizer and dorsal mesoderm of *Xenopus laevis*. *Development* 116, 915–930
- Shih, J. and Keller, R. (1992b). Cell motility driving mediolateral intercalation in explants of *Xenopus laevis*. *Development* 116, 901–914
- Shimeld, S. M. and Donoghue, P. C. J. (2012). Evolutionary crossroads in developmental biology: cyclostomes (lamprey and hagfish). *Development* 139, 2091–2099
- Shindo, A. (2018). Models of convergent extension during morphogenesis. *Wiley Interdiscip. Rev. Dev. Biol.* 7:e293
- Signor, S. A. and Nuzhdin, S. V. (2018). The Evolution of Gene Expression in cis and trans. *Trends Genet.* 34, 532–544
- Singh, A. and Xu, Y. J. (2016). The cell killing mechanisms of hydroxyurea. *Genes*. 7, 99
- Slack, J. M., Holland, P. W. and Graham, C. F. (1993). The zootype and the phylotypic stage. *Nature* 361, 490–492
- Smith, S. J., Rebeiz, M. and Davidson, L. (2018). From pattern to process: studies at the interface of gene regulatory networks, morphogenesis, and evolution. *Curr. Opin. Genet. Dev.* 51, 103–110
- Solnica-Krezel, L. (2005). Conserved patterns of cell movements during vertebrate gastrulation. *Curr. Biol.* 15, 213–228.
- Somorjai, I. M. L., Martí-Solans, J., Diaz-Gracia, M., Nishida, H., Imai, K. S., Escrivà, H., Cañestro, C. and Albalat, R. (2018). Wnt evolution and function shuffling in liberal and conservative chordate genomes. *Genome Biol.* 19, 1–17
- Soukup, V., Yong, L. W., Lu, T. M., Huang, S. W., Kozmik, Z. and Yu, J. K. (2015). The Nodal signaling pathway controls left-right asymmetric development in amphioxus. *Evodevo* 6, 5
- Spemann, H. and Mangold, H. (1924). Über Induktion von Embryonalanlagen durch Implantation artfremder Organisatoren. *Arch. für Mikroskopische Anat. und Entwicklungsmechanik* 100, 599–638
- Stach, T. (1999). The ontogeny of the notochord of *Branchiostoma lanceolatum*. *Acta Zoologica* 80, 25–33
- Steel, M. and Penny, D. (2000). Parsimony, Likelihood, and the Role of Models in Molecular Phylogenetics. *Mol. Biol. Evol.* 17, 839–850
- Stemple, D. L. (2005). Structure and function of the notochord: An essential organ for chordate development. *Development* 132, 2503–2512
- Stern, C. D. and Arthur, K. (2019). The ‘Omics Revolution’: How an Obsession with Compiling Lists Is Threatening the Ancient Art of Experimental Design. *Bioessays* 41, 1900168
- Steventon, B. and Martinez Arias, A. (2017). Evo-engineering and the cellular and molecular origins of the vertebrate spinal cord. *Dev. Biol.* 432, 3–13
- Steventon, B., Duarte, F., Lagadec, R., Mazan, S., Nicolas, J.-F. and Hirsinger, E. (2016). Species-specific contribution of volumetric growth and tissue convergence to posterior body elongation in vertebrates. *Development* 1732–1741
- Sugiyama, M., Sakaue-Sawano, A., Iimura, T., Fukami, K., Kitaguchi, T., Kawakami, K., Okamoto, H., Higashijima, S. and Miyawaki, A. (2009). Illuminating cell-cycle progression in the developing zebrafish embryo. *PNAS* 106, 20812–20817
- Sulik, K., Dehart, D. B., Inagaki, T., Carson, J. L., Vrablic, T., Gesteland, K. and Schoenwolf, G. C. (1994). Morphogenesis of the murine node and notochordal plate. *Dev. Dyn.* 201, 260–278

- Szabó, A., Cobo, I., Omara, S., McLachlan, S., Keller, R. and Mayor, R. (2016). The Molecular Basis of Radial Intercalation during Tissue Spreading in Early Development. *Dev. Cell* 37, 213–225
- Tam, P. P. L. and Beddington, R. S. P. (1987). The formation of mesodermal tissues in the mouse embryo during gastrulation and early organogenesis. *Development* 99, 109–126
- Tam, P. P. L. and Behringer, R. R. (1997). Mouse gastrulation: The formation of a mammalian body plan. *Mech. Dev.* 68, 3–25
- Taniguchi, Y., Kurth, T., Weiche, S., Reichelt, S., Tazaki, A., Perike, S., Kappert, V. and Epperlein, H. H. (2017). The posterior neural plate in axolotl gives rise to neural tube or turns anteriorly to form somites of the tail and posterior trunk. *Dev. Biol.* 422, 155–170
- Tenin, G., Wright, D., Ferjentsik, Z., Bone, R., McGrew, M. J. and Maroto, M. (2010). The chick somitogenesis oscillator is arrested before all paraxial mesoderm is segmented into somites. *BMC Dev. Biol.* 10, 13–20
- Terazawa, K. and Satoh, N. (1997). Formation of the chordamesoderm in the amphioxus embryo: Analysis with Brachyury and fork head/HNF-3 genes. *Dev. Genes Evol.* 207, 1–11
- Thewissen, J. G. M. (2018). Highlights of cetacean embryology. *Aquat. Mamm.* 44, 591–602
- Trapani, V., Bonaldo, P. and Corallo, D. (2017). Role of the ECM in notochord formation, function and disease. *J. Cell Sci.* 130, 3203–3211
- Trivedi, V., Choi, H. M. T., Fraser, S. E. and Pierce, N. A. (2018). Multidimensional quantitative analysis of mRNA expression within intact vertebrate embryos. *Development* 145, 1–8
- Tsakiridis, A., Huang, Y., Blin, G., Skylaki, S., Wymeersch, F., Osomo, R., Economou, C., Karagianni, E., Zhao, S., Lowell, S., et al. (2014). Distinct Wnt-driven primitive streak-like populations reflect in vivo lineage precursors. *Development* 141, 1209–1221
- Tucker, A. S. and Slack, J. M. W. (1995). The *Xenopus laevis* tail-forming region. *Dev. Biol.* 262, 249–262
- Turner, D. A., Hayward, P. C., Baillie-Johnson, P., Rue, P., Broome, R., Faunes, F. and Martinez Arias, A. (2014). Wnt/ -catenin and FGF signalling direct the specification and maintenance of a neuromesodermal axial progenitor in ensembles of mouse embryonic stem cells. *Development* 141, 4243–4253
- Tzouanacou, E., Wegener, A., Wymeersch, F. J., Wilson, V. and Nicolas, J. F. (2009). Redefining the Progression of Lineage Segregations during Mammalian Embryogenesis by Clonal Analysis. *Dev. Cell* 17, 365–376
- Uchida, Y., Uesaka, M., Yamamoto, T., Takeda, H. and Irie, N. (2018). Embryonic lethality is not sufficient to explain hourglass-like conservation of vertebrate embryos. *Evodevo* 9, 7
- Uriu, K., Bhavna, R., Oates, A. C. and Morelli, L. G. (2017). A framework for quantification and physical modeling of cell mixing applied to oscillator synchronization in vertebrate somitogenesis. *Biol. Open.* 6, 1235–1244
- Van Den Brink, S. C., Baillie-Johnson, P., Balayo, T., Hadjantonakis, A. K., Nowotschin, S., Turner, D. A. and Arias, A. M. (2014). Symmetry breaking, germ layer specification and axial organisation in aggregates of mouse embryonic stem cells. *Development* 141, 4231–4242
- Veeman, M. T. and Smith, W. C. (2013). Whole-organ cell shape analysis reveals the developmental basis of ascidian notochord taper. *Dev. Biol.* 373, 281–289
- Verd, B., Clark, E., Wotton, K. R., Janssens, H., Jiménez-Guri, E., Crombach, A. and Jaeger, J. (2018). A damped oscillator imposes temporal order on posterior gap gene expression in *Drosophila*. *PLoS Biol.* 16, 1–24
- Vergara, H., Pape, C., Meechan, K., Zinchenko, V., Genoud, C., Wanner, A., Titze, B., Templin, R., Bertucci, P., Simakov, O., et al. (2020). Whole-body integration of gene expression and single-cell morphology. *Biorxiv*

- Voiculescu, O., Bertocchini, F., Wolpert, L., Keller, R. E. and Stern, C. D. (2007). The amniote primitive streak is defined by epithelial cell intercalation before gastrulation. *Nature* 449, 1049–1052
- Voiculescu, O., Bodenstern, L., Jun, I. L. and Stern, C. D. (2014). Local cell interactions and self-amplifying individual cell ingression drive amniote gastrulation. *eLife* 3, e01817
- von Baer, K.E. (1828) Über Entwicklungsgeschichte der Thiere: Beobachtung und Reflektion. *Bornträger*
- Wada, H., Garcia-Fernández, J. and Holland, P. W. H. (1999). Colinear and segmental expression of amphioxus Hox genes. *Dev. Biol.* 213, 131–141
- Waddington, C. H. (1942). Canalization of Development and the Inheritance of Acquired Characters. *Nature* 150, 563–565
- Waddington, C. H. (1952). Modes of Gastrulation in Vertebrates. *J. Cell Sci.* s3-93, 221–229
- Wagner, D. E. and Klein, A. M. (2020). Lineage tracing meets single-cell omics: opportunities and challenges. *Nat. Rev. Genet.*
- Wagner, D. E., Weinreb, C., Collins, Z. M., Briggs, J. A., Megason, S. G. and Klein, A. M. (2018). Single-cell mapping of gene expression landscapes and lineage in the zebrafish embryo. *Science*, 4362, aar4362
- Wallingford, J. B., Fraser, S. E. and Harland, R. M. (2002). Convergent extension: The molecular control of polarized cell movement during embryonic development. *Dev. Cell* 2, 695–706
- Wanninger, A. (2015). Morphology is dead - long live morphology! Integrating MorphoEvoDevo into molecular EvoDevo and phylogenomics. *Front. Ecol. Evol.* 3:54
- Ward, L., Pang, A. S. W., Evans, S. E. and Stern, C. D. (2018). The role of the notochord in amniote vertebral column segmentation. *Dev. Biol.* 439, 3–18
- Warga, R. M. and Kimmel, C. B. (1990). Cell movements during epiboly and gastrulation in zebrafish. *Development* 108, 569–580
- Warmflash, A., Sorre, B., Etoc, F., Siggia, E. D. and Brivanlou, A. H. (2014). A method to recapitulate early embryonic spatial patterning in human embryonic stem cells. *Nat. Methods* 11, 847–854
- Wicht, H. and Lacalli, T. (2005). The nervous system of amphioxus: structure, development, and evolutionary significance. *Canadian Journal of Zoology* 83, 122–150
- Willmore, K. E. (2012a). An Introduction to Evolutionary Developmental Biology. *Evol. Educ. Outreach* 5, 181–183
- Willmore, K. E. (2012b). The Body Plan Concept and Its Centrality in Evo-Devo. *Evol. Educ. Outreach* 5, 219–230
- Wilson, E. B. (1893). Amphioxus and the Mosaic Theory of Development. *J. Morph.* 8, 579–639
- Winchell, C. J., Sullivan, J., Cameron, C. B., Swalla, B. J. and Mallatt, J. (2002). Evaluating hypotheses of deuterostome phylogeny and chordate evolution with new LSU and SSU ribosomal DNA data. *Mol. Biol. Evol.* 19, 762–776
- Winkley, K., Ward, S., Reeves, W. and Veeman, M. (2019). Iterative and Complex Asymmetric Divisions Control Cell Volume Differences in *Ciona* Notochord Tapering. *Curr. Biol.* 29, 3466–3477
- Wopat, S., Bagwell, J., Sumigray, K. D., Dickson, A. L., Huitema, L. F. A., Poss, K. D., Schulte-Merker, S. and Bagnat, M. (2018). Spine Patterning Is Guided by Segmentation of the Notochord Sheath. *Cell Rep.* 22, 2026–2038
- Wymeersch, F. J., Huang, Y., Blin, G., Cambray, N., Wilkie, R., Wong, F. C. K. and Wilson, V. (2016). Position-dependent plasticity of distinct progenitor types in the primitive streak. *eLife* 5, e10042

- Xiong, F., Ma, W., Bénazéraf, B., Mahadevan, L. and Pourquié, O. (2020). Mechanical Coupling Coordinates the Co-elongation of Axial and Paraxial Tissues in Avian Embryos. *Dev. Cell* 5, 1–13
- Yamada, T., Pfaff, S. L., Edlund, T. and Jessell, T. M. (1993). Control of cell pattern in the neural tube: Motor neuron induction by diffusible factors from notochord and floor plate. *Cell* 73, 673–686
- Yamaguchi, T. P., Takada, S., Yoshikawa, Y., Wu, N. and McMahon, A. P. (1999). T (Brachyury) is a direct target of Wnt3a during paraxial mesoderm specification. *Genes Dev.* 13, 3185–3190
- Yamamoto, A., Amacher, S. L., Kim, S.-H., Geisler, D., Kimmel, C. B. and De Robertis, E. M. (1998). Zebrafish paraxial protocadherin is a downstream target of spadetail involved in morphogenesis of gastrula mesoderm. *Development* 125, 3389–97
- Yamamoto, M., Morita, R., Mizoguchi, T., Matsuo, H., Isoda, M., Ishitani, T., Chitnis, A. B., Matsumoto, K., Crump, J. G., Hozumi, K., et al. (2010). Mib-Jag1-Notch signalling regulates patterning and structural roles of the notochord by controlling cell-fate decisions. *Development* 137, 2527–2537
- Yamanaka, Y., Tamplin, O. J., Beckers, A., Gossler, A. and Rossant, J. (2007). Live Imaging and Genetic Analysis of Mouse Notochord Formation Reveals Regional Morphogenetic Mechanisms. *Dev. Cell* 13, 884–896
- Yarrell, W. (1836). A history of British fishes (Edition 1), Volume 2. *Van Voorst*, London.
- Yasuoka, Y. (2020). Morphogenetic mechanisms forming the notochord rod: The turgor pressure-sheath strength model. *Dev. Growth Differ.* 62, 379–390
- Ybot-Gonzalez, P., Savery, D., Gerrelli, D., Signore, M., Mitchell, C. E., Faux, C. H., Greene, N. D. E. and Copp, A. J. (2007). Convergent extension, planar-cell-polarity signaling and initiation of mouse neural tube closure. *Development* 134, 789–799
- Yin, Z., Sailem, H., Sero, J., Ardy, R., Wong, S. T. C. and Bakal, C. (2014). How cells explore shape space: A quantitative statistical perspective of cellular morphogenesis. *BioEssays* 36, 1195–1203
- York, J. R. and McCauley, D. W. (2020). The origin and evolution of vertebrate neural crest cells. *Open Biol.* 10, 190285
- Yoshikawa, Y., Fujimori, T., McMahon, A. P. and Takada, S. (1997). Evidence that absence of Wnt-3a signaling promotes neuralization instead of paraxial mesoderm development in the mouse. *Dev. Biol.* 183, 234–242
- Yu, J.-K., Satou, Y., Holland, N. D., Shin-I, T., Kohara, Y., Satoh, N., Bronner-Fraser, M. and Holland, L. Z. (2007). Axial patterning in cephalochordates and the evolution of the organizer. *Nature* 445, 613–617
- Zakirov, B., Charalambous, G., Aspalter, I. M., Van-Vuuren, K., Mead, T., Harrington, K., Thuret, R., Regan, R., Herbert, S. P. and Bentley, K. (2020). Active Perception during Angiogenesis: Filopodia speed up Notch selection of tip cells in silico and in vivo. *Biorxiv*
- Zhang, S., Holland, N. D. and Holland, L. Z. (1997). Topographic changes in nascent and early mesoderm in amphioxus embryos studied by DiI labeling and by in situ hybridization for a Brachyury gene. *Dev. Genes Evol.* 206, 532–535
- Zhong, Y., Herrera-Úbeda, C., Herrera-Úbeda, C., Garcia-Fernández, J., Li, G. and Holland, P. W. H. (2020). Mutation of amphioxus Pdx and Cdx demonstrates conserved roles for ParaHox genes in gut, anus and tail patterning. *BMC Biol.* 18, 1–15

Appendix I
Supplementary figures relevant to Chapter III

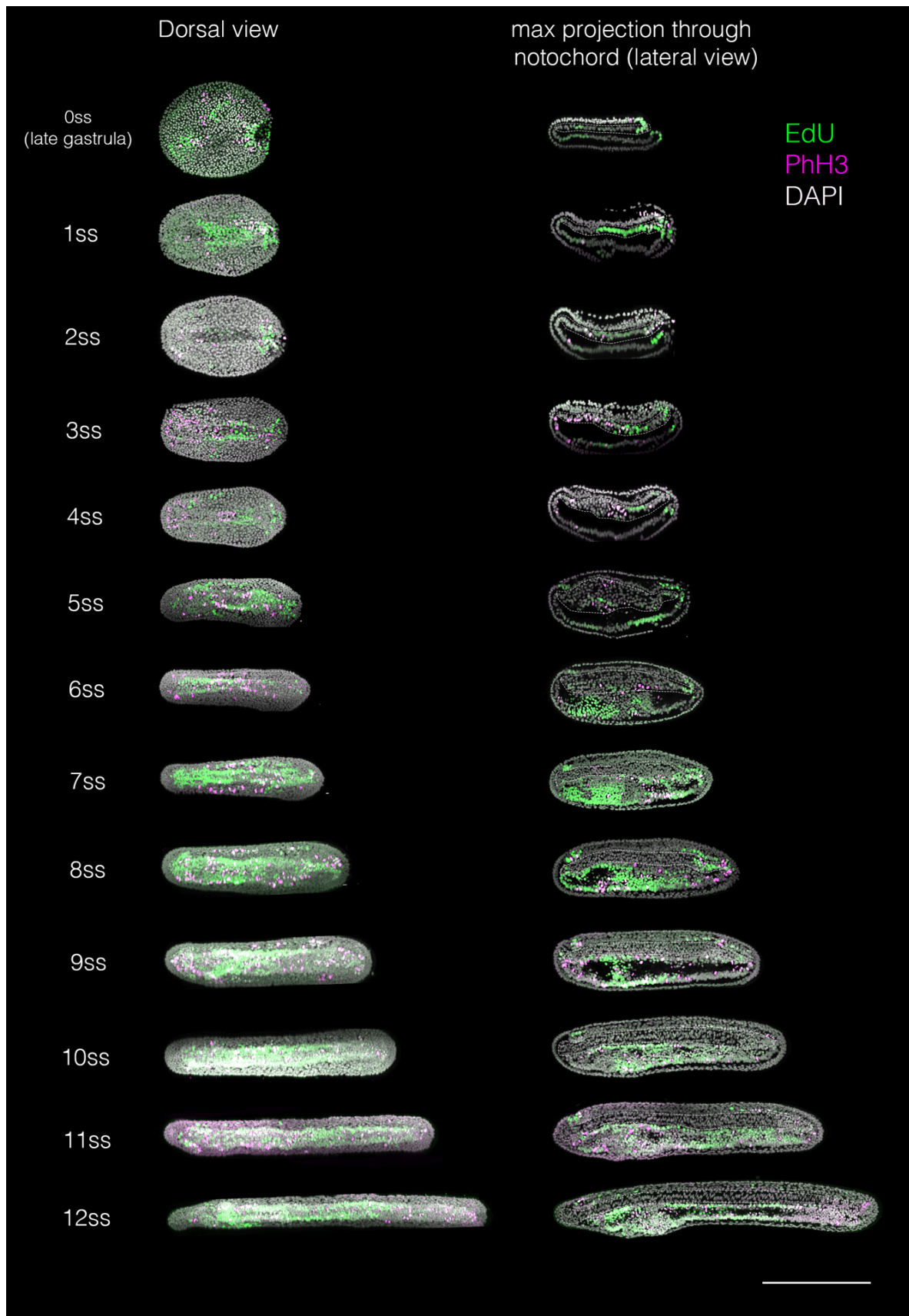


Figure S1. Labelling of proliferative cells between gastrulation and 14ss. Embryos at successive somite stages were incubated in 20µM EdU for 2 hours prior to fixation (green), and additionally immunostained for PhH3 after fixation (magenta). For each stage, embryos are in maximal projection in a dorsal view (left) and in midline sagittal section (right). Scale bar shows 200µm.

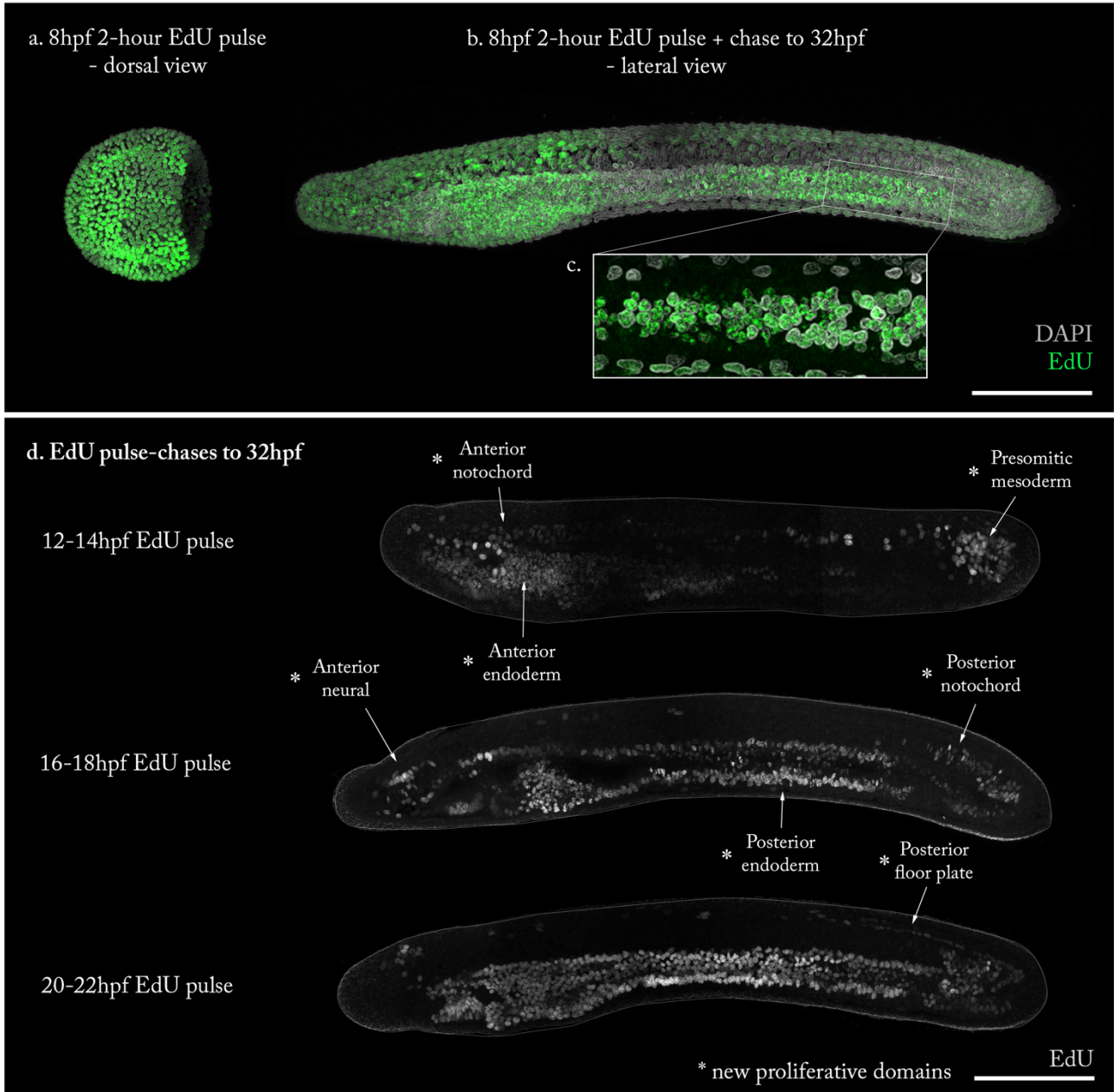


Figure S2. Validation of EdU pulse-chase strategy. (Top panel) An EdU dilution test. EdU+ nuclei in the gastrula (a) can still be identified at the end of axial development (b, c). Instead of fading, EdU signal appears to become speckled and inhomogeneous within labelled nuclei that have undergone multiple rounds of division (c). (Bottom panel, d) An EdU depletion test. Comparison of 3 EdU pulse-chase experiments representing successively later pulses across axial development, with embryos shown in sagittal sections. Later EdU pulses mark novel domains that are not marked in earlier pulses. These domains are labelled with an asterisk. If EdU were not sufficiently depleted, labelling would continue after the pulse, and so no new domains would be observed. Scale bar shows 100 μ m.

Appendix II
Supplementary figures relevant to Chapter IV

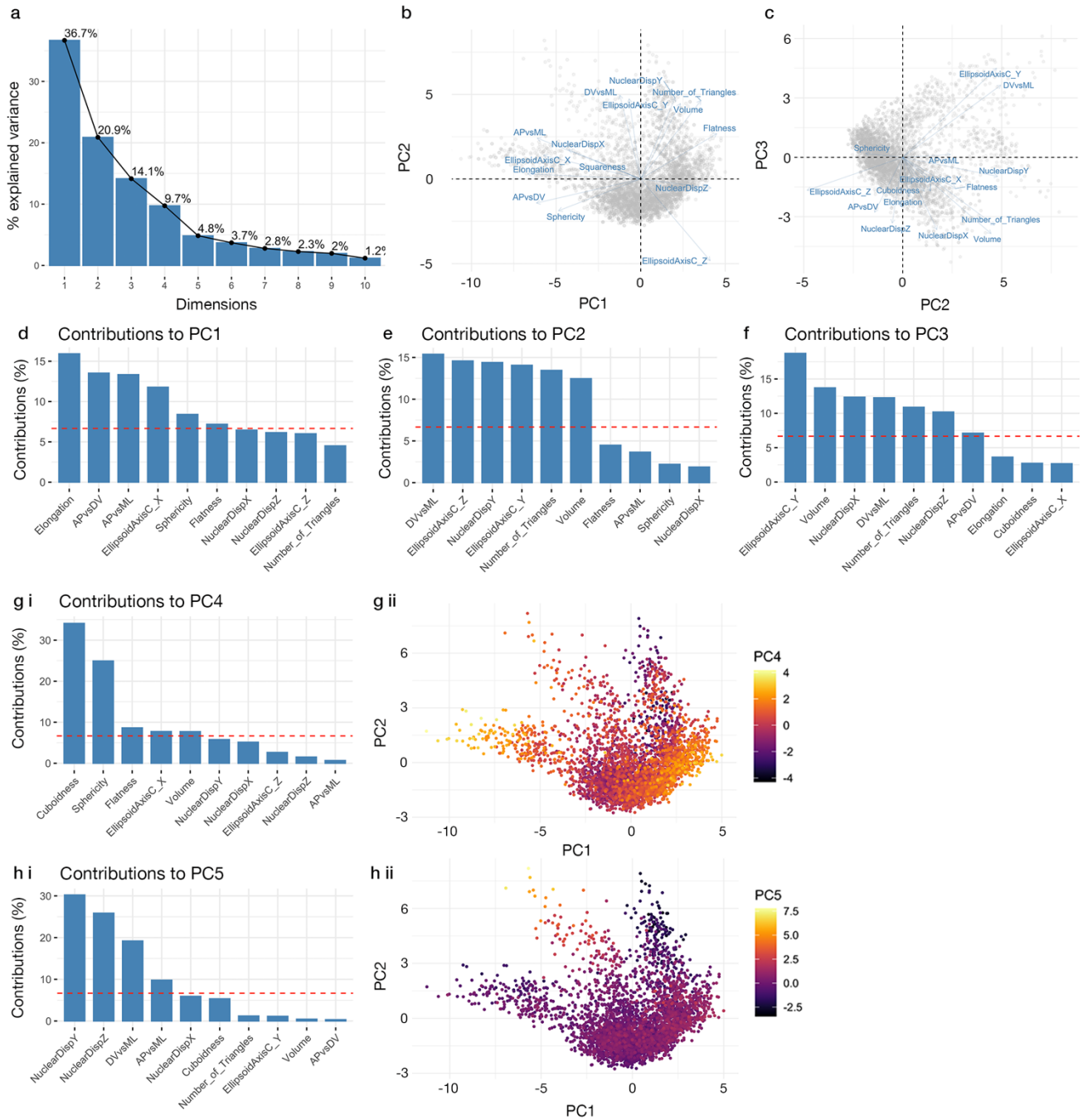


Figure S1. **Principal component analysis.** (a) Scree plot showing contribution of eigenvectors to total dataset variation. First 5 eigenvectors account for 86.2% total variation. (b, c) Compass plot showing direction of correlation between individual shape variables against PC1 and PC2 (b) and PC2 and PC3 (c). (d-h) Major correlates of PCs. f ii and g ii show all plots plotted against PC1 and PC2, colour-coded for PC4 (f ii) and PC5 (g ii).

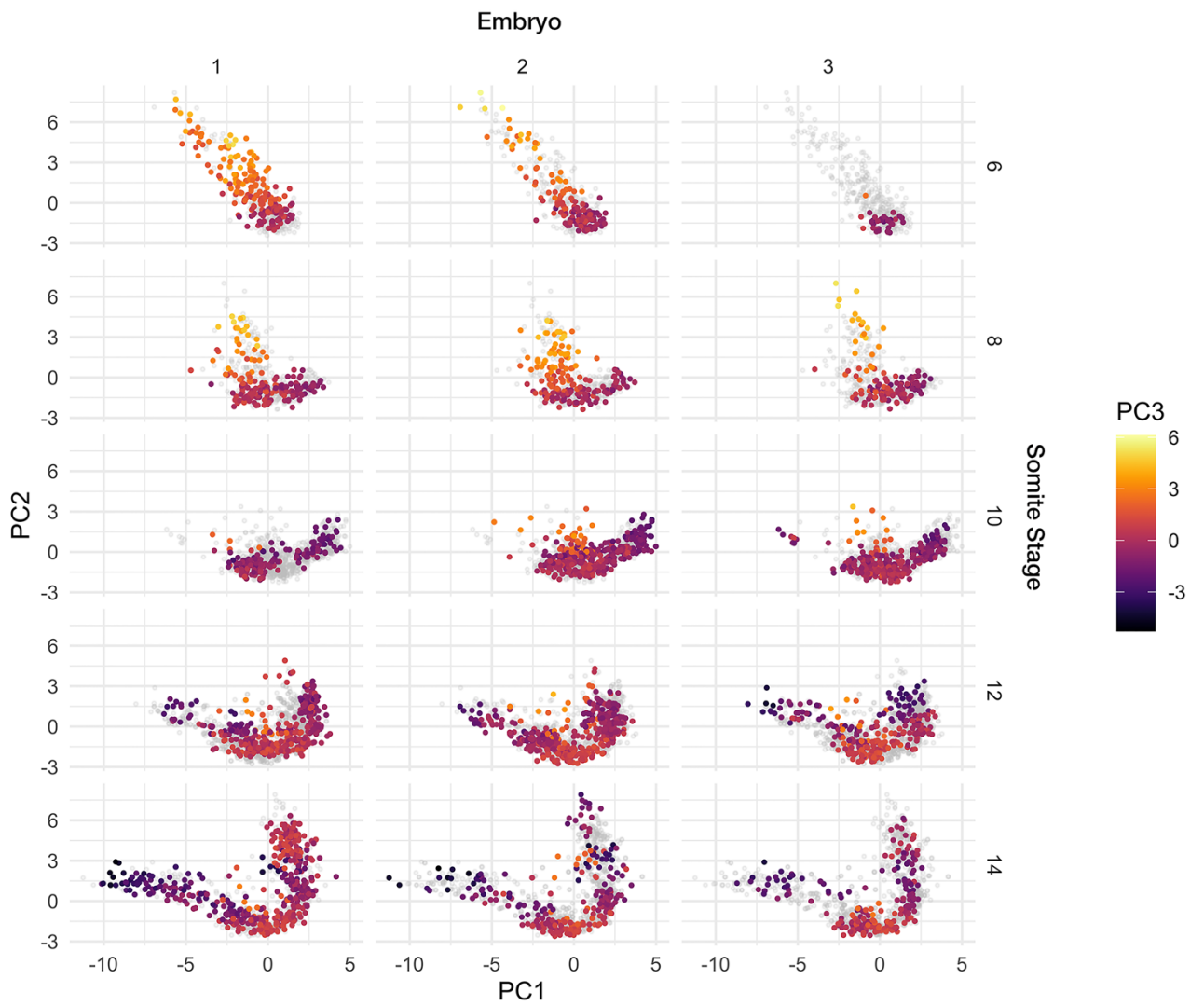


Figure S2. **Cell shape diversity is reproducible between different embryos.** Graphs show total morphospace filtered by somite stage and embryo. Grey points show all cells for the specified developmental stage. Colour-code illustrates distribution on PC3.

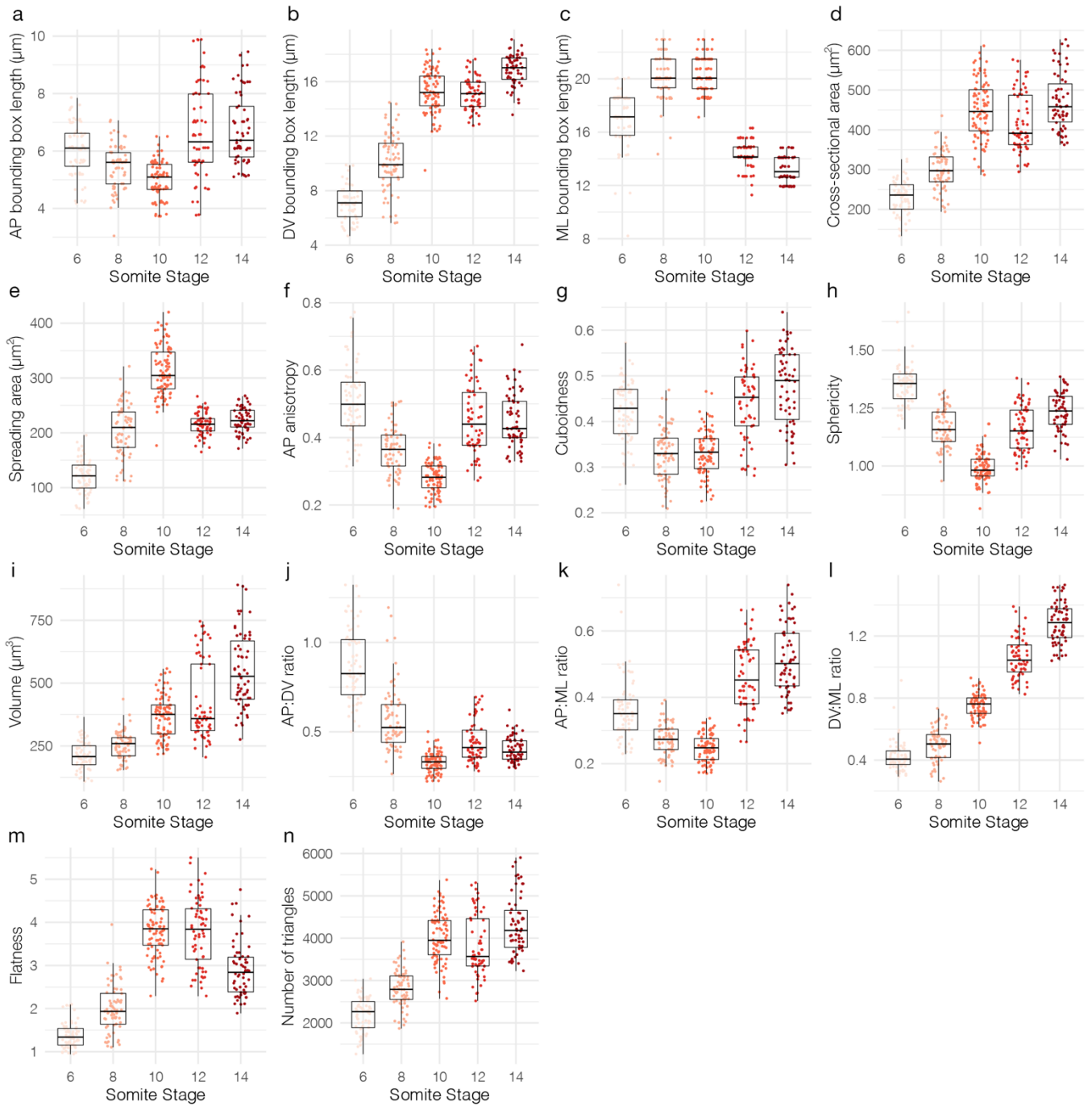


Figure S3. **Further geometric changes in cells from the 40 - 60% level of the notochord.** $n = 344$.

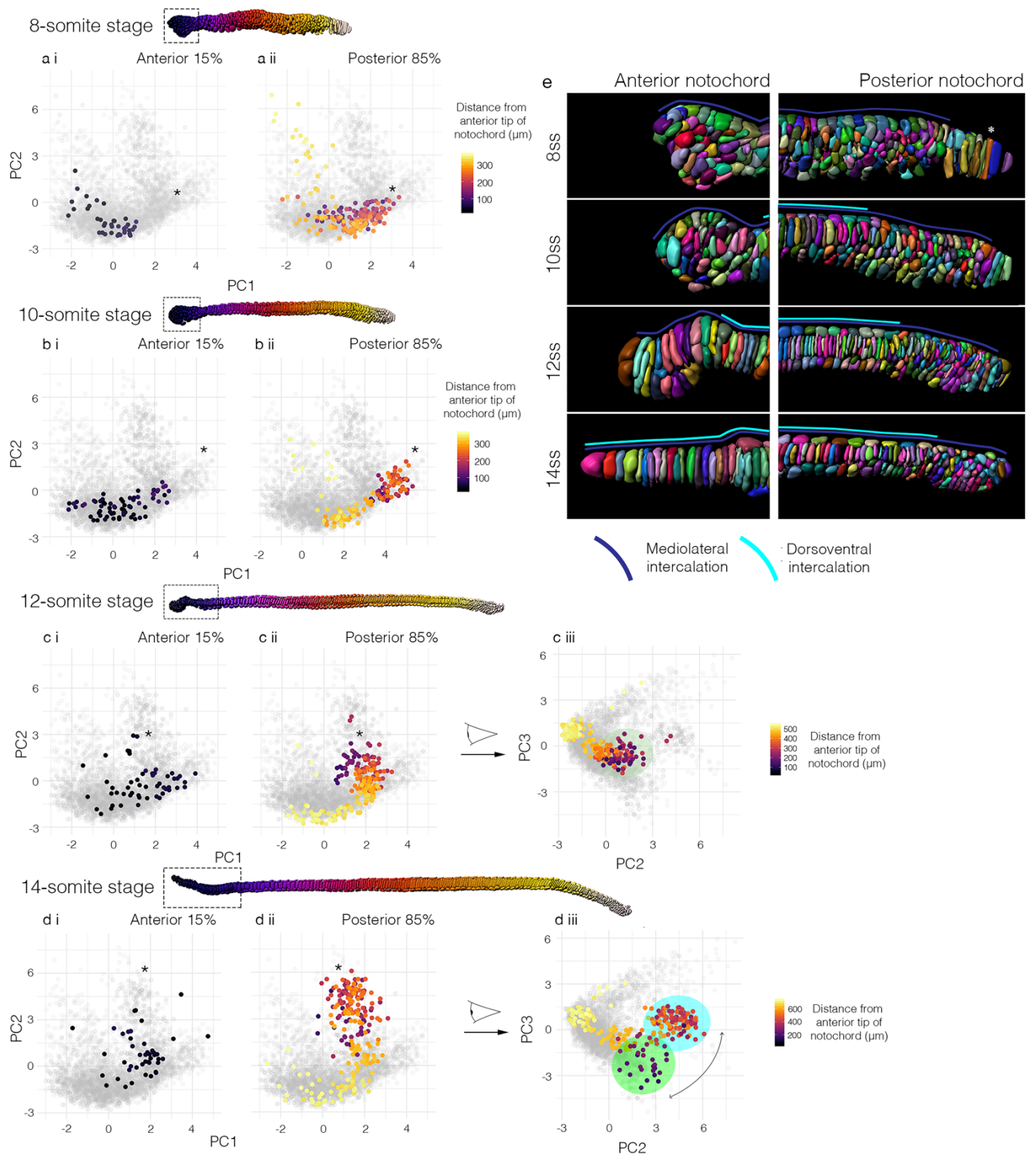


Figure S4. Morphospacial mapping of whole notochords reveals spatial variation in developmental timing.

(a-d) Central layer progenitors from whole notochords at the 8- (a), 10- (b), 12- (c) and 14- (d) somite stages mapped into morphospace. Cells in the anterior 0.15 of axial length (boxes shown in each notochord) are mapped into a single graph (left, panel i), and the rest in a separate graph (right, panel ii). Colour-code reflects distance from the anterior tip of the notochord. c iii and d iii show the same cells dispersed on PC2 and PC3, revealing spatial separation of cells in either side of the bifurcation event in the stack-of-coins trajectory – cells in the pharyngeal region are qualitatively different to those in the more posterior trunk. (e) View of segmented anterior (left) and posterior (right) tips of the notochord at the 8-14 somite stages, showing temporal delays in mediolateral and dorsoventral intercalation relative to the central progenitors.

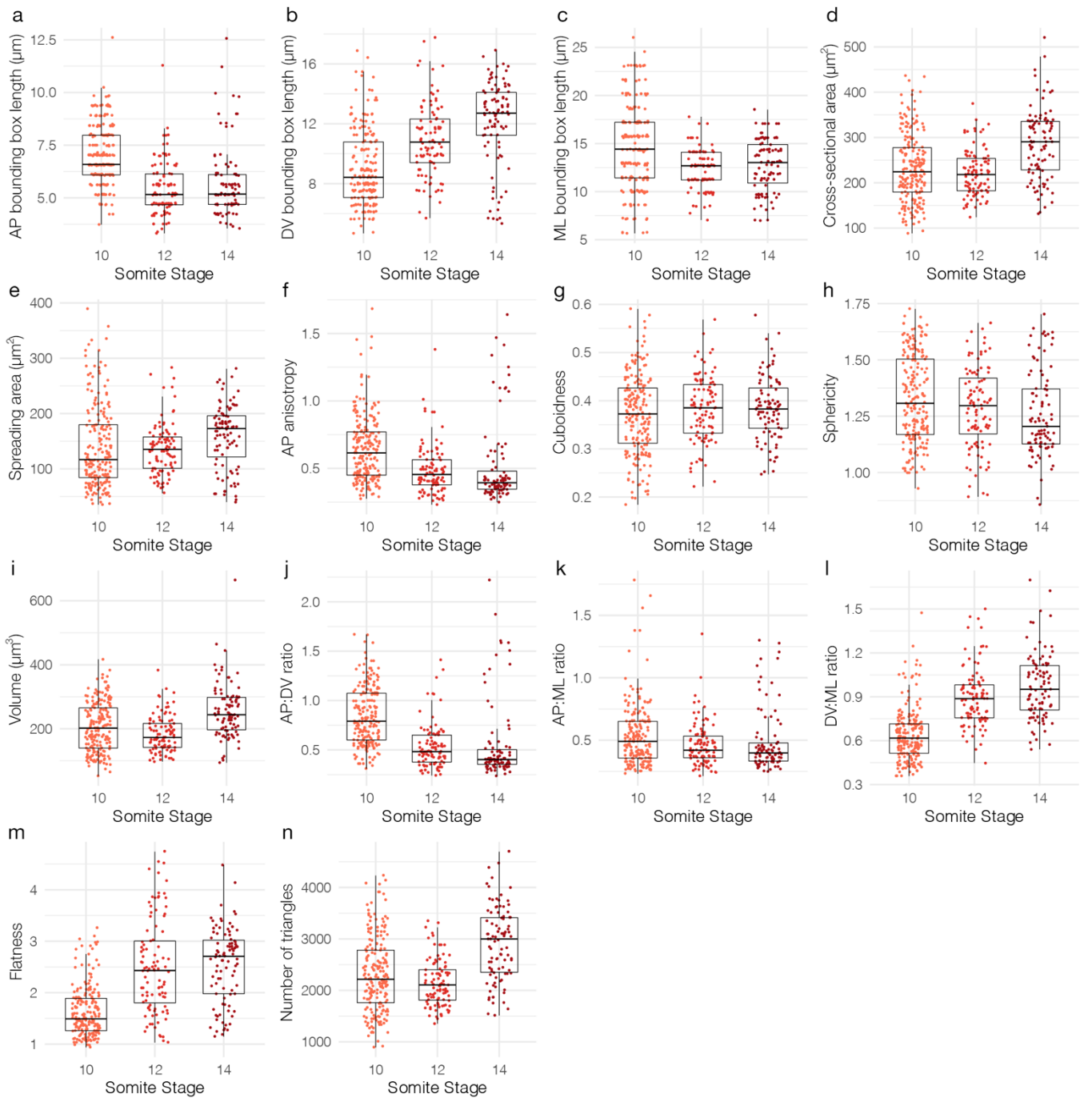


Figure S5. **Geometric changes in cells from the 0 - 15% level of the notochord.** $n = 396$.

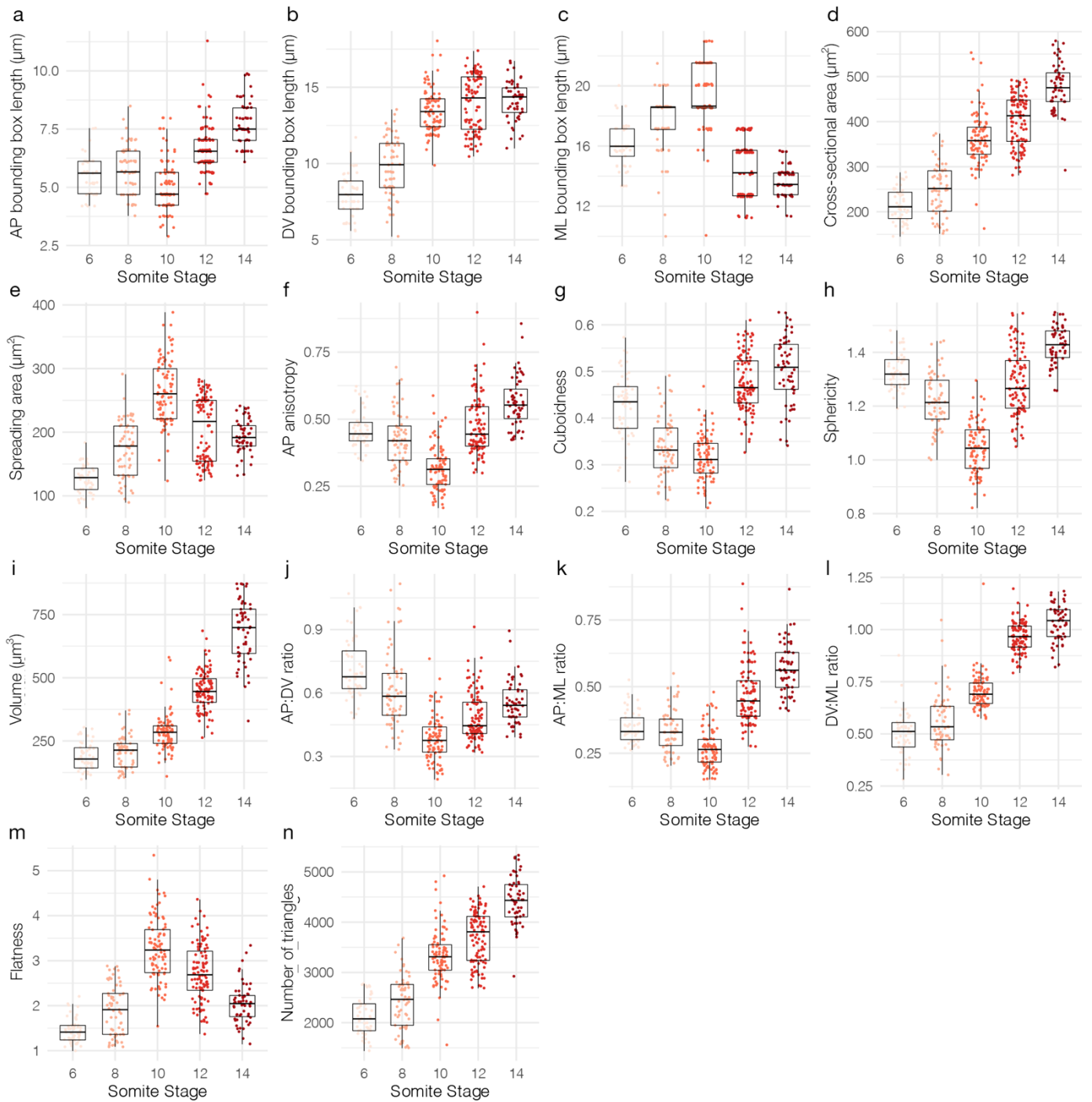


Figure S6. **Geometric changes in cells from the 15 - 40% level of the notochord.** $n = 360$.

Appendix III:
Mathematical modelling of notochord cell shape transitions

Geometric perturbation of a single cell

The aim of the *in silico* geometric perturbations is to identify how different geometric transformations change cell and tissue length. We first need to define a set of measures that allow for a simplified characterisation of the cell shapes and shape changes. To this aim, we first create the object-oriented bounding box of the cell corresponding to the three-dimensional cell shape and find that the box aligns to the anterior-posterior axis (AP-axis), the dorsal-ventral axis (DV-axis) and the medial-lateral axis (ML-axis) of the embryo (see Fig. 1a). The bounding box has the volume $V^{(bb)}$ and is defined by three lengths, $l_{AP}^{(bb)}$, $l_{DV}^{(bb)}$ and $l_{ML}^{(bb)}$ (see Fig. 1b). We assume that the cells can be approximated as a two-dimensional shape that is oriented along the $DV - ML$ plane and then projected along the AP axis for a length $l_{AP}^{(cell)}$ (see Fig. 1b and 1c). We find that bounding box length $l_{AP}^{(bb)}$ is a good approximation for cell length $l_{AP}^{(cell)}$, but convolution of the membrane on the transverse $DV - ML$ plane generates a discrepancy between cell spreading area, defined by the bounding box $A^{(bb)}$, and real cell area $A^{(cell)}$. In this case, we can assume

$$l_{AP}^{(cell)} \approx l_{AP}^{(bb)}.$$

We then define the spreading area

$$A^{(bb)} = l_{DV}^{(bb)} \cdot l_{ML}^{(bb)},$$

which corresponds to the transverse area (the area in the $DV - ML$ plane) of the bounding box and the transverse area of the cell,

$$A^{(cell)} = \frac{V^{(cell)}}{l_{AP}^{(cell)}},$$

where $V^{(cell)}$ is the cell volume. We also define the ratio

$$\gamma = \frac{A^{(cell)}}{A^{(bb)}},$$

which is a measure of how convoluted the transverse cell shape is in the $DV - ML$ plane. For a small γ , the cell is characterised by one more several long and thin elongations, for $\gamma = 1$ it fills the complete rectangle (see Fig. 1c).

We now start with a cell at somite stage $s \in \{6,8,10,12,14\}$ which has the volume $V^{(cell)}(s)$, the anterior-posterior length $l_{AP}^{(cell)}(s)$ and the ratio $\gamma(s)$. In this case, the spreading area is given by

$$A^{(bb)}(s) = \frac{A^{(cell)}(s)}{\gamma(s)} = \frac{V^{(cell)}(s)}{l_{AP}^{(cell)}(s) \gamma(s)}.$$

Alternatively, to calculate change in length $L_{AP}^{(cell)}$, we start with a cell of volume $V^{(cell)}(s)$, area $A^{(cell)}$ and ratio $\gamma(s)$. The length $L_{AP}^{(cell)}$ is now given by

$$L_{AP}^{(cell)}(s) = \frac{V^{(cell)}(s_0)}{A^{(cell)}(s)}.$$

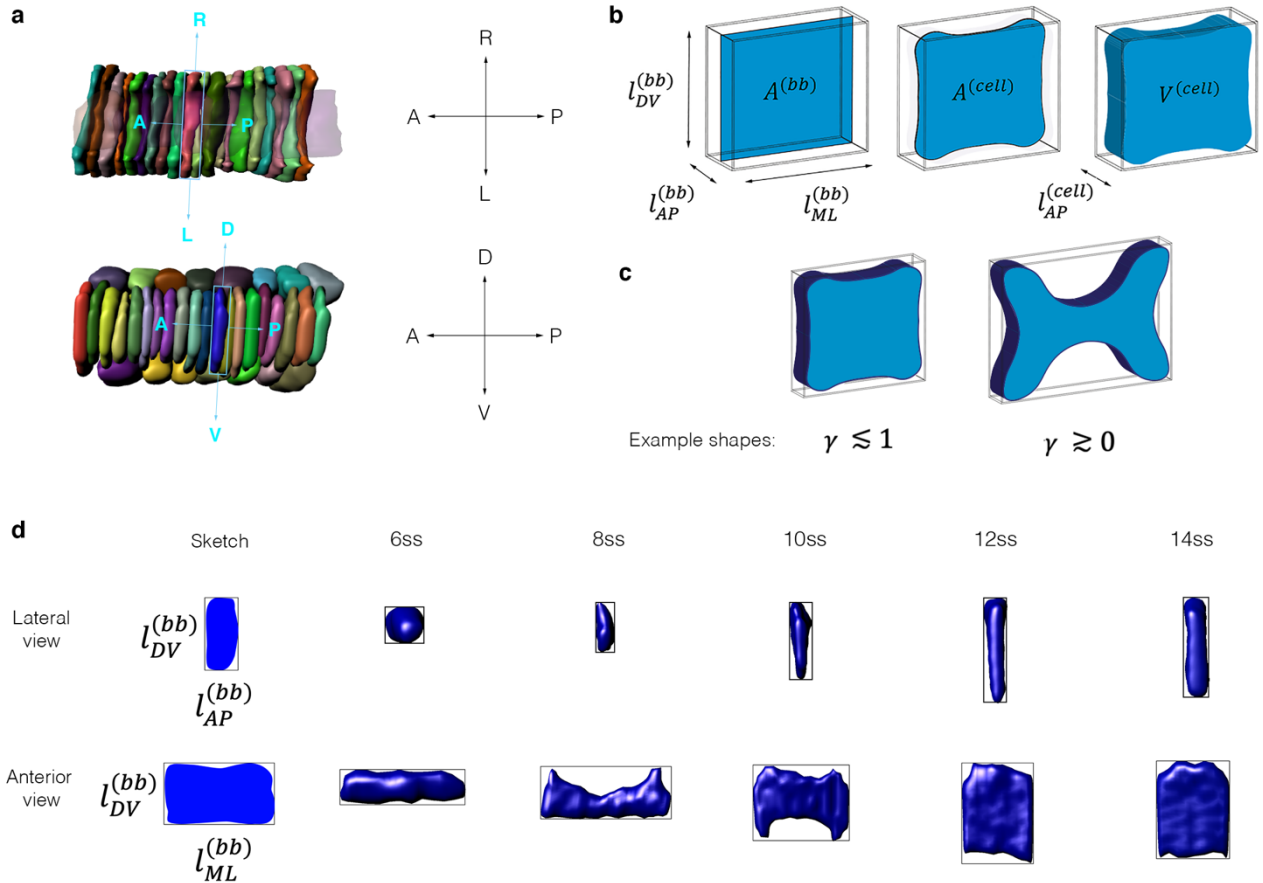
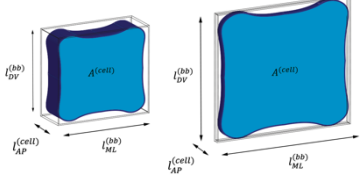
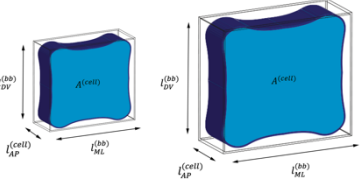
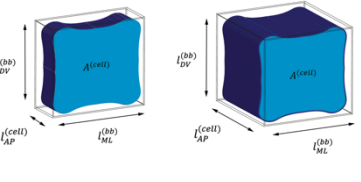
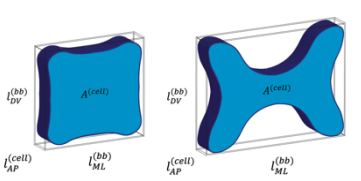


Figure A1. Cell shape metrics used for geometric perturbations. (a) Object-oriented bounding boxes are calculated for each cell, and their axes are aligned to the AP, DV and ML axes of the embryo. (b) Schematised cells within object-oriented bounding boxes, showing the measurements of length, area and volume acquired. (c) Cells define the dimensions of their bounding boxes through variable degrees of surface convolution, which we quantify as γ . (d) Sample cells for each stage of development in lateral (top row) and anterior (bottom row) view within object-oriented bounding boxes.

We can now study different types of geometric transformations and check how they affect these quantities:

Transformation	<i>AP</i> cell length $l_{AP}^{(cell)}(s)$	Sketch
Change only in transverse cross sectional area $A^{(cell)}(s)$	$\frac{V^{(cell)}(s_0)}{A^{(cell)}(s)}$	
Isotropic growth $V^{(cell)}(s)$	$l_{AP}^{(cell)}(s_0) \sqrt[3]{\frac{V^{(cell)}(s)}{V^{(cell)}(s_0)}}$	
Anisotropic growth only along <i>AP</i> axis $l_{AP}^{(cell)}(s)$	$\frac{V^{(cell)}(s)}{A^{(cell)}(s_0)}$	
Convolution in the transverse plane	$l_{AP}^{(cell)}(s_0)$	

where s_0 defines the initial state of the cell at stage s_0 . We find that the cell length along the *AP* axis only change when the cell is elongated in this direction, grows anisotropically in this direction or isotropically in all directions. A convolution that does not affect the transverse area $A^{(cell)}(s)$ will also not affect the elongation.

Effects of geometric perturbation on groups of cells

To compute how these geometric transformations affects the length of a group of cells, we define a measure of cell intercalation at each stage. To this aim, we assume that the length contribution of a group of n cells (where we assume that n is large) in the AP direction is given by $l^{(n)}$ and the equation

$$l^{(n)}(s) = n \beta(s) l_{AP}(s),$$

with the intercalation correction $\beta(s)$. For $\beta = 1$, the cells are stacked on the AP axis, for small $\beta \gtrsim 0$, many layers of cells are present on the DV and ML planes (see Fig. 2).

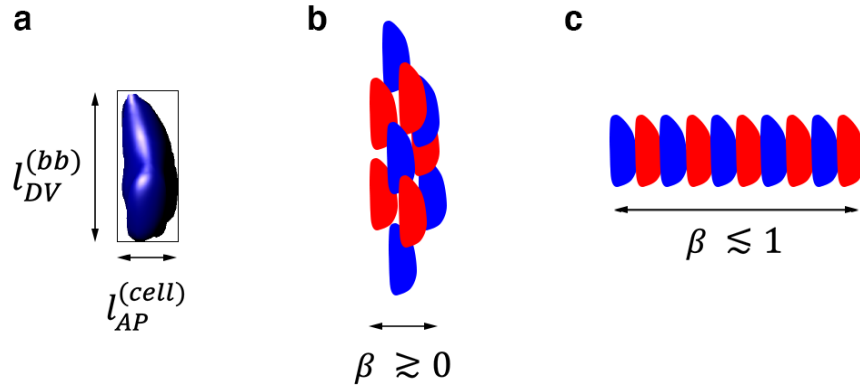
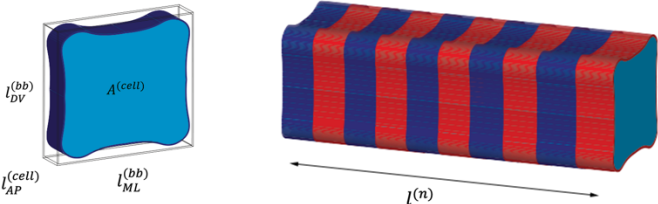
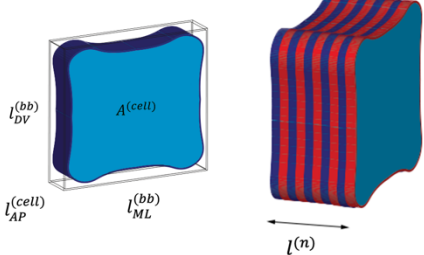
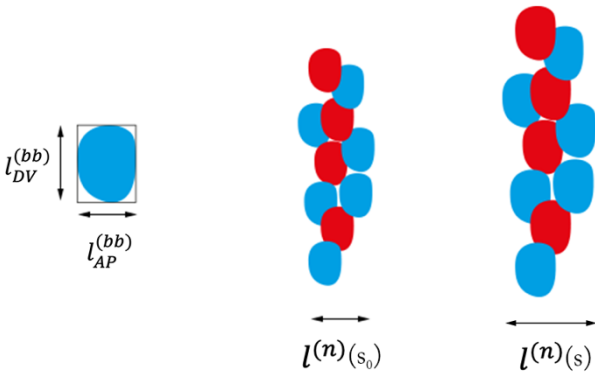
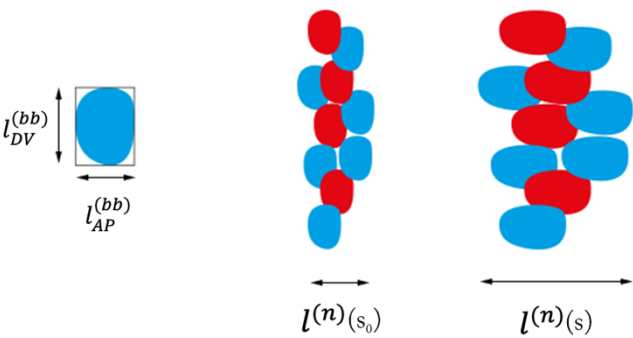


Figure A2. Calculation of intercalation correction β in a neighbourhood of 10 cells. (a) Sample cell from 8ss in lateral view showing the direction of AP length $l_{AP}^{(cell)}$, approximated by $l_{AP}^{(bb)}$. (b, c) Schematic of a neighbourhood of 10 cells in lateral view, showing two extremes of β , approaching 0 in (b) and approaching 1 in (c).

We now start with a group of n cells, each of volume $V^{(cell)}(s)$, area $A^{(cell)}(s)$ and ratio $\gamma(s)$, and an intercalation of $\beta(s)$, and calculate neighbourhood length as

$$l^{(n)}(s) = n \beta(s) \frac{V^{(cell)}(s)}{A^{(cell)}(s)}.$$

We can study the effect of each geometric transformation, with and without intercalation, on neighbourhood length $l^{(n)}(s)$:

Transformation	AP neighbourhood length $l^{(n)}(s)$	Sketch
Intercalation only $\beta(s)$	$n \beta(s) \frac{V^{(cell)}(s_0)}{A^{(cell)}(s_0)}$	
Intercalation $\beta(s)$ with transverse cross-sectional area $A^{(cell)}(s)$	$n \beta(s) \frac{V^{(cell)}(s_0)}{A^{(cell)}(s)}$	
Isotropic growth $V^{(cell)}(s)$ without intercalation	$n \beta(s_0) l_{AP}^{(cell)}(s_0) \sqrt[3]{\frac{V^{(cell)}(s)}{V^{(cell)}(s_0)}}$	
Anisotropic growth $V^{(cell)}(s)$ only along AP axis $l_{AP}^{(cell)}(s)$, without intercalation	$n \beta(s_0) \frac{V_{cell}(s)}{A^{(cell)}(s_0)}$	

Appendix IV
Supplementary figures relevant to Chapter V

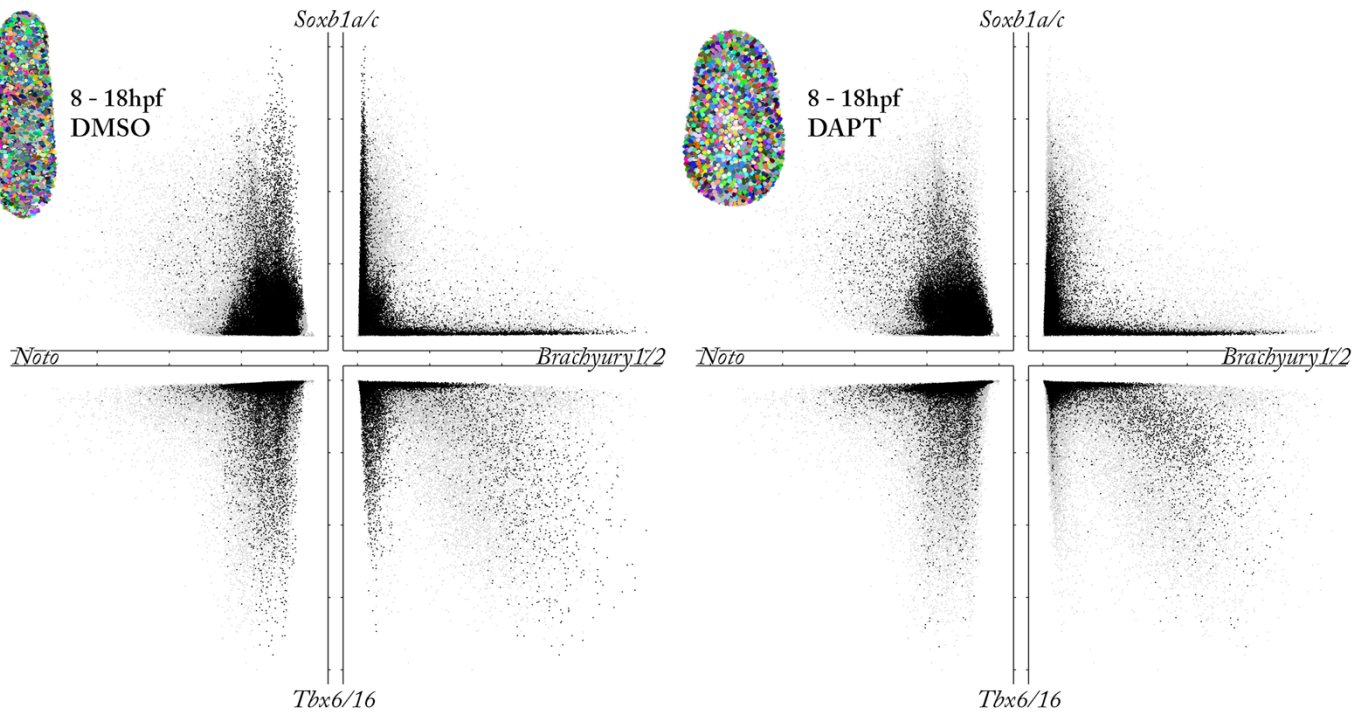


Figure. S1. **Dispersal of nuclei from DMSO- and DAPT-treated embryos in gene expression space.** Nuclei from embryos treated with either DMSO (left) or 20 μ M DAPT (right) between 8hpf and 18hpf dispersed in pairwise coexpression plots for *Soxb1a/c*, *Brachyury1/2*, *Tbx6/16* and *Noto*, with normalised axes ranging from 0 to 1. Black dots mark cells from the stated condition, grey background dots show the full dataset, including all stages between cup-shaped gastrula and 18hpf. Inlays show Ilastik segmentation for each condition, with the embryo in a dorsal view. $n = 33,105$ DMSO nuclei; $n = 32,546$ DAPT nuclei, derived from $n = 8$ embryos per condition.

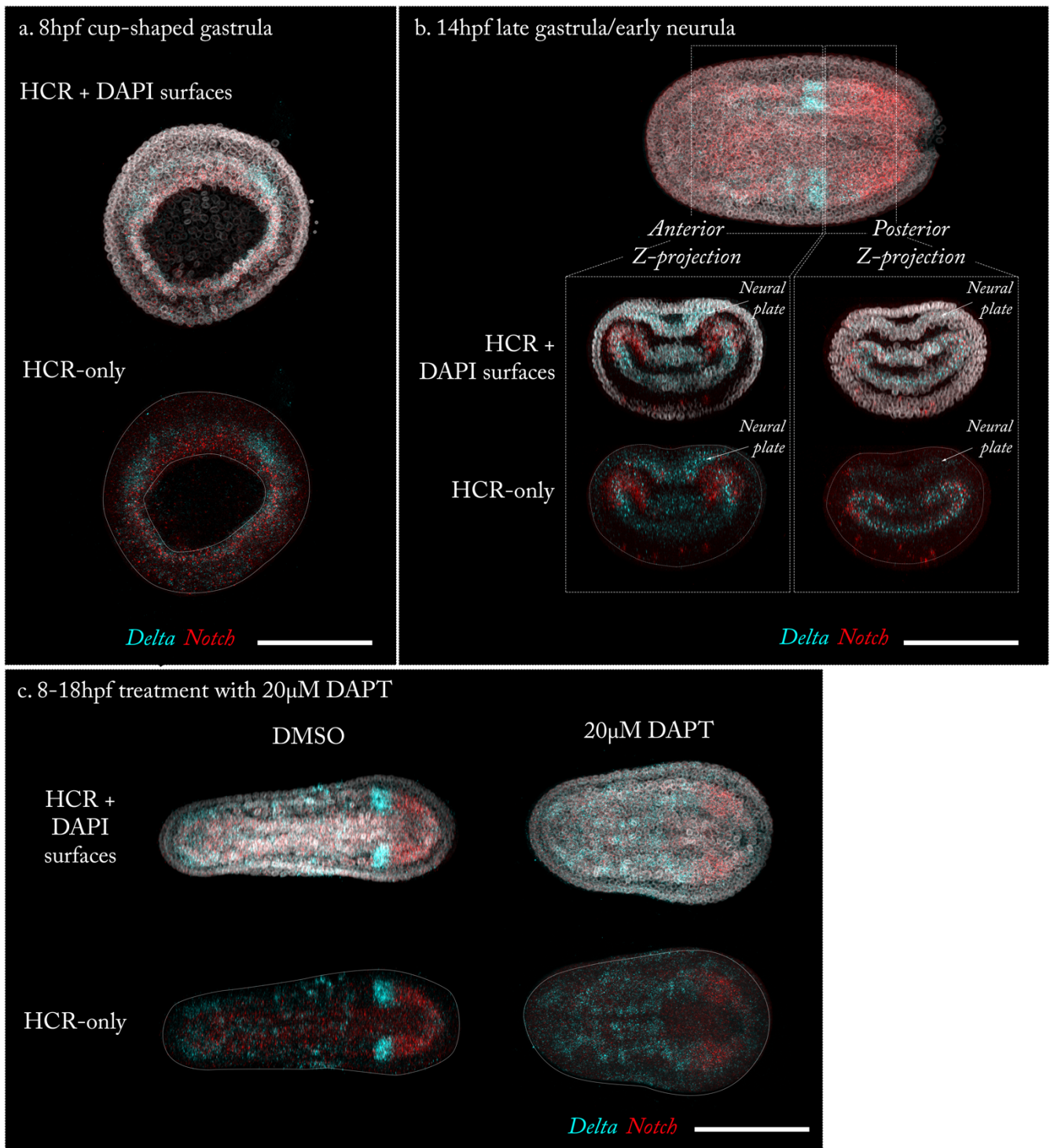


Figure. S2. Expression of *Notch* and *Delta* in normal development and a DAPT-phenotype. (a) Expression of *Notch* and *Delta* in the cup-shaped gastrula (8hpf), shown in a blastopore view, with dorsal facing up. (b) Expression in the late gastrula/early neurula (14hpf). A representative embryo is shown in dorsal view, anterior facing left. Inlays show Z-projections on a transverse plane through the regions marked with dashed boxes. Projections are shown with (top) and without (bottom) DAPI surfaces. (c) Expression at 6ss (18hpf) in embryos treated with DMSO (left) or 20µM DAPT (right) from 8hpf (shown in a), shown here in dorsal view, anterior facing left. Projections are shown with (top) and without (bottom) DAPI surfaces. All scale bars show 100µm. DAPT staining representative of over 10 embryos.

Appendix V

Andrews, T. G. R., Gattoni, G., Busby, L., Schwimmer, M. A., and Benito-Gutierrez, E. (2020). Hybridization Chain Reaction for Quantitative and Multiplex Imaging of Gene Expression in *Amphioxus* Embryos and Adult Tissues. In: Nielsen B., Jones J. (eds) *In Situ Hybridization Protocols. Methods in Molecular Biology*, vol 2148. Humana, New York, NY



Hybridization Chain Reaction for Quantitative and Multiplex Imaging of Gene Expression in Amphioxus Embryos and Adult Tissues

Toby G. R. Andrews, Giacomo Gattoni, Lara Busby,
Michael A. Schwimmer, and Èlia Benito-Gutiérrez

Abstract

In situ hybridization (ISH) methods remain the most popular approach for profiling the expression of a gene at high spatial resolution and have been broadly used to address many biological questions. One compelling application is in the field of evo-devo, where comparing gene expression patterns has offered insight into how vertebrate development has evolved. Gene expression profiling in the invertebrate chordate amphioxus (cephalochordate) has been particularly instrumental in this context: its key phylogenetic position as sister group to all other chordates makes it an ideal model system to compare with vertebrates and for reconstructing the ancestral condition of our phylum. However, while ISH methods have been developed extensively in vertebrate model systems to fluorescently detect the expression of multiple genes simultaneously at a cellular and subcellular resolution, amphioxus gene expression profiling is still based on single-gene nonfluorescent chromogenic methods, whose spatial resolution is often compromised by diffusion of the chromogenic product. This represents a serious limitation for reconciling gene expression dynamics between amphioxus and vertebrates and for molecularly identifying cell types, defined by their combinatorial code of gene expression, that may have played pivotal roles in evolutionary innovation. Herein we overcome these problems by describing a new protocol for application of the third-generation hybridization chain reaction (HCR) to the amphioxus, which permits fluorescent, multiplex, and quantitative detection of gene expression in situ, within the changing morphology of the developing embryo, and in adult tissues. A detailed protocol is herein provided for whole-mount preparations of embryos and vibratome sections of adult tissues.

Key words Amphioxus, Fluorophore-labeled, Gene expression profiling, HCR, In situ hybridization, Multiplex, Single-cell resolution

1 Introduction

In situ hybridization (ISH) methods have been utilized over the past several decades to describe spatial patterns of gene expression across tissues and across species. When combined with functional studies (e.g., gene expression inhibition) these methods have been

particularly powerful for characterizing the roles and the regulatory interactions of specific genes in particular developmental processes. ISH methods have been, for example, key for defining genes and network interactions controlling vertebrate axial patterning [1, 2], vertebrate limb development [3, 4], and segmentation of the *Drosophila* blastoderm [5, 6]. When combined with comparative developmental biology approaches, these methods have offered a means beyond morphological examination to define the homology of traits in different taxa, and therefore to define the origins of important evolutionary innovations. A remarkable discovery in this context was the observation that there is an evolutionarily conserved Hox code that patterns the anterior-posterior axis of most animals [7]. This sets the groundwork for comparisons between distantly related taxa, sharing homologous body parts (e.g., head, thorax, tail) that contain taxon-specific morphological specializations. Focusing on chordate evolution, gene expression profiling in the amphioxus has helped to resolve traits that are ancestral to the phylum, and those that are vertebrate innovations [8]. These include vertebrate traits, such as a complex brain and neural crest derivatives [9]. These studies have relied on the classic ISH protocol for amphioxus [10] which has been applied by researchers in the field for almost three decades [11].

While ISH methods have constantly evolved in other model systems to increase sensitivity, to target multiple genes simultaneously, and to achieve cellular and subcellular resolution, most of the gene expression profiling in amphioxus is still based on single-gene expression detection using nonfluorescent chromogenic methods. Chromogenic methods can be very sensitive, but they are not quantitative, as they depend on the nonlinear accumulation of a chromogenic product. Diffusion of this product can often compromise the spatial resolution of the signal, leading to loss of cellular and subcellular detail. Furthermore, chromogenic methods are limited in terms of multiplexing, usually restricted to three-color reactions (color per gene), and only two in amphioxus in very exceptional cases [12]. While possible, multiplex ISH is highly technically challenging, because it demands multiple chromogenic reactions to be performed in series without cross reaction. Many technologies have emerged recently that tackle some of these technical challenges in vertebrates and offer quantitative information by virtue of fluorescent RNA detection (e.g., TSA, RNAscope, HCR). However, because these have been inconsistently applied, reconciling gene expression dynamics between model systems is becoming increasingly challenging. Therefore, there is high demand for ISH technology that can be readily applied across model systems, and offers cellular resolution, multiplex potential, and fluorescent quantitative imaging.

To address these challenges, we have taken advantage of third-generation in situ hybridization chain reaction (HCR) technology, recently developed by Choi and collaborators [13], and adapted it to the particular requirements of amphioxus embryos and adult tissues. HCR version 3 (HCRv3) is based on the use of DNA probe pairs that bind in tandem to complementary sequences on the mRNA of interest. Split between each probe pair is an initiator sequence that triggers the focal binding and polymerization of metastable kinetically trapped DNA hairpins, each of which is conjugated to a fluorescent Alexa Fluor moiety. A complete adapter is formed where the probe pairs bind in tandem specifically to the mRNA sequence with certain separation. Only then can hairpins assemble through cooperative binding into tethered fluorescent amplification polymers, whose fluorescence intensity will scale linearly with the local density of mRNA molecules [14, 15]. Intrinsic to this design is automatic background suppression, in which the nonspecific off-site binding of a single probe will not accumulate fluorescent signal due to absence of a complete adapter sequence. This background suppression generates a significantly improved signal: noise ratio in HCRv3 imaging compared to previous versions, enabling highly sensitive imaging of even very weakly expressed genes. The specificity of adapter sequences and commercial availability of DNA hairpins conjugated to different fluorophores (Molecular Instruments) allow multiplexing probes to target up to five different genes in the same specimen per reaction [16]. The HCRv3 method is therefore multiplex, sensitive, and quantitative.

Here we describe a method for application of the HCRv3 technology to multiplex and quantitatively analyze gene expression in the amphioxus, both in embryos and adult sections. This protocol can be executed in 3 days in embryos or adult sections that had been previously fixed and dehydrated in methanol or ethanol. The sample preparation is, unsurprisingly, specific for amphioxus, but the hybridization and the amplification steps are essentially as described by Choi and colleagues [13], with some minor modifications. Below we briefly outline several key developments that have facilitated optimization of our protocol in relation to that described by Choi and colleagues [13], and the classic amphioxus ISH protocol from Holland and Holland [10]:

1. We have updated the protocol for amphioxus embryo fixation to improve the quality of the starting material (Subheading 3.1), thereby increasing the specificity and sensitivity of the HCR signal. In particular, the protocol described below differs from that previously published with respect to the fixative amount and the length of fixation [17, 18]. The handling of the embryos also differs since we do not include any centrifugation steps and all pipette tips and plates are siliconized. This

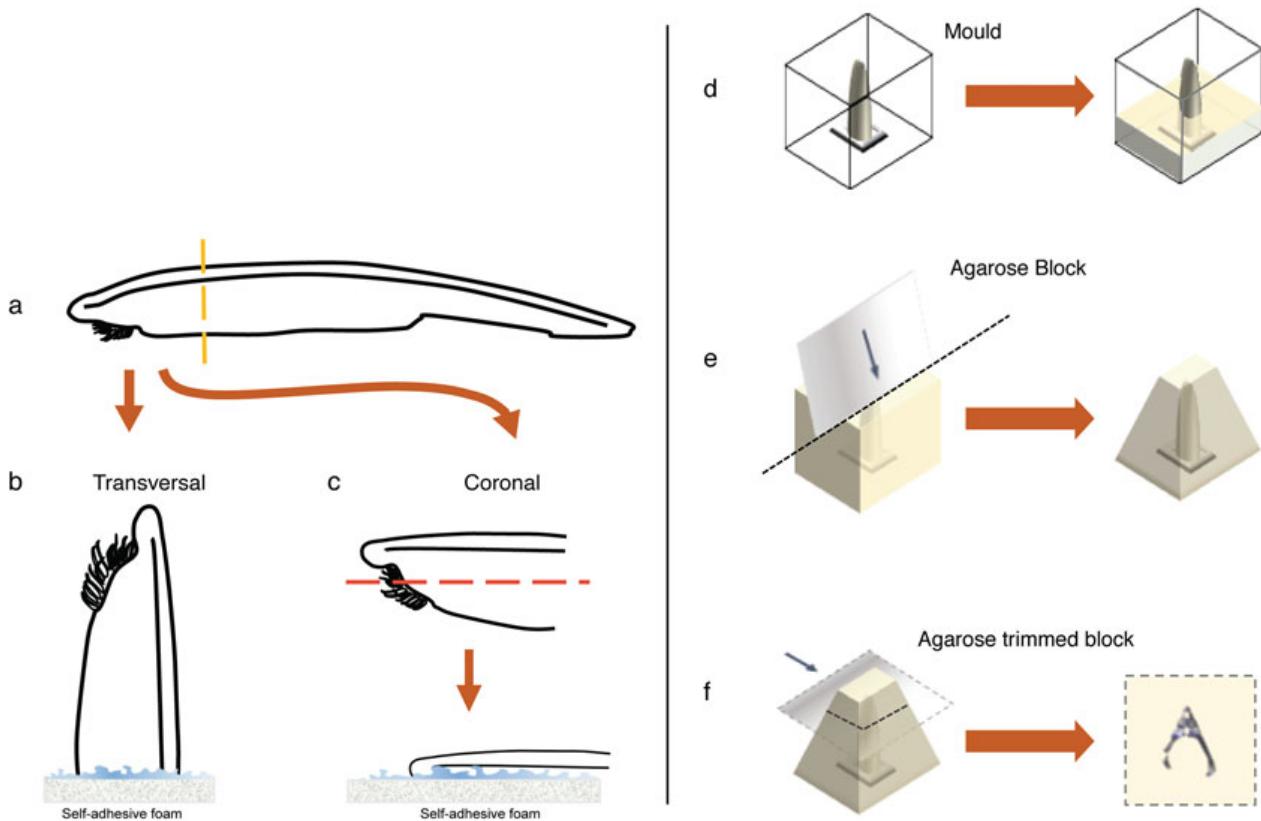


Fig. 1 Embedding and vibratome sectioning of adult amphioxus brain tissues. Once the specimen has been anesthetized (a) the head is separated from the rest of the body and fixed for 24 h as indicated in Subheading 3.3, **step 3**. The separated head is then washed and glued into the self-adhesive foam either vertically (b) or horizontally (c), depending on the orientation needed. For coronal sections further dissection of the ventral side is recommended to properly align brain and neural tube in a same section. The foam with the attached head is then transferred into a peel-a-way square embedding mold and filled up with liquid low-melting agarose (d). Once the agarose has solidified the block is extracted from the mold and trimmed as a pyramid to provide better grip while sectioning (e). The wider part of the pyramid is then glued to the vibratome holder and the head is sectioned with the dorsal fin facing the blade (f)

latter step is motivated by our observation that amphioxus embryos are very sticky, especially at the early steps of fixation and at the beginning of the HCR protocol, meaning that they can get damaged very easily or lost during handling.

2. We describe a completely new protocol for generating thick vibratome sections of adult tissues (Subheading 3.2), which we illustrate using brain tissue (Fig. 1). This represents an improvement on methods for analyzing gene expression in adult amphioxus tissues, which to date were mostly dependent on paraffin embedding and on a very lengthy protocol for chromogenic detection [19, 20]. The classic protocol adopted these strategies since the high hybridization temperatures of the traditional amphioxus ISH protocol (60–63 °C) meant that the tissue would curl unless attached to the slide. By contrast, the milder hybridization conditions of the HCR protocol are permissive enough so the technique can be applied to thick

floating vibratome sections with no curling or noticeable shrinkage. Consequently, we have been able to produce a protocol that can be applied more rapidly than the previous ISH on paraffin sections that allows a finer tuning depending on the gene of interest, and that is in general more robust (Fig. 1).

3. We introduced a bleaching step at the beginning of the HCR protocol (Subheading 3.4, step 3). Bleaching is a common step in the ISH protocols of many model systems, including flatworms and most vertebrates [21–23]. In amphioxus, we have found that this step reduces the inherent autofluorescence of the tissue and completely eliminates the natural pigmentation of the eye and other photoreceptive spots. Thereafter, the tissue becomes more transparent, which permits imaging of entire embryos at single-cell resolution (Fig. 2).
4. We found that pretreatment with proteinase K is not necessary for HCR in amphioxus (Fig. 1), unlike when using DIG-labeled riboprobes, and indeed might only be useful when hybridizing very thick sections (Fig. 3). This is a major step forward, as imaging of gene expression is now possible in undigested tissues, showing a more normal morphology. Indeed, this protocol can be readily combined with immunohistochemistry for morphological landmarks.
5. We propose a novel imaging approach for fluorescent labeling in amphioxus tissues using inverted confocal microscopy. This ensures that the specimens lie flat and within the working distance of the objective throughout the imaging process, even up to 100× optical magnification. Thus, Z-stacks can be acquired of entire specimens at single-cell resolution. This configuration is compatible with tile scanning of a large field of specimens in a multi-area time lapse, but also permits adjustment of orientation to acquire the same specimen from multiple views, or to repair small deviations of position after the initial mounting process. In principle, individual specimens can be retrieved after imaging with this method, bleached, and re-stained to further increase the number of channels in the HCR.

2 Materials

2.1 Reagents

1. Ethanol/methanol (for sample storage).
2. Split-initiator probe pairs (Molecular Instruments).
3. Fluorophore-labeled metastable DNA HCR hairpins (Molecular Instruments).
4. Probe hybridization buffer (Molecular Instruments).
5. Probe wash buffer (Molecular Instruments).

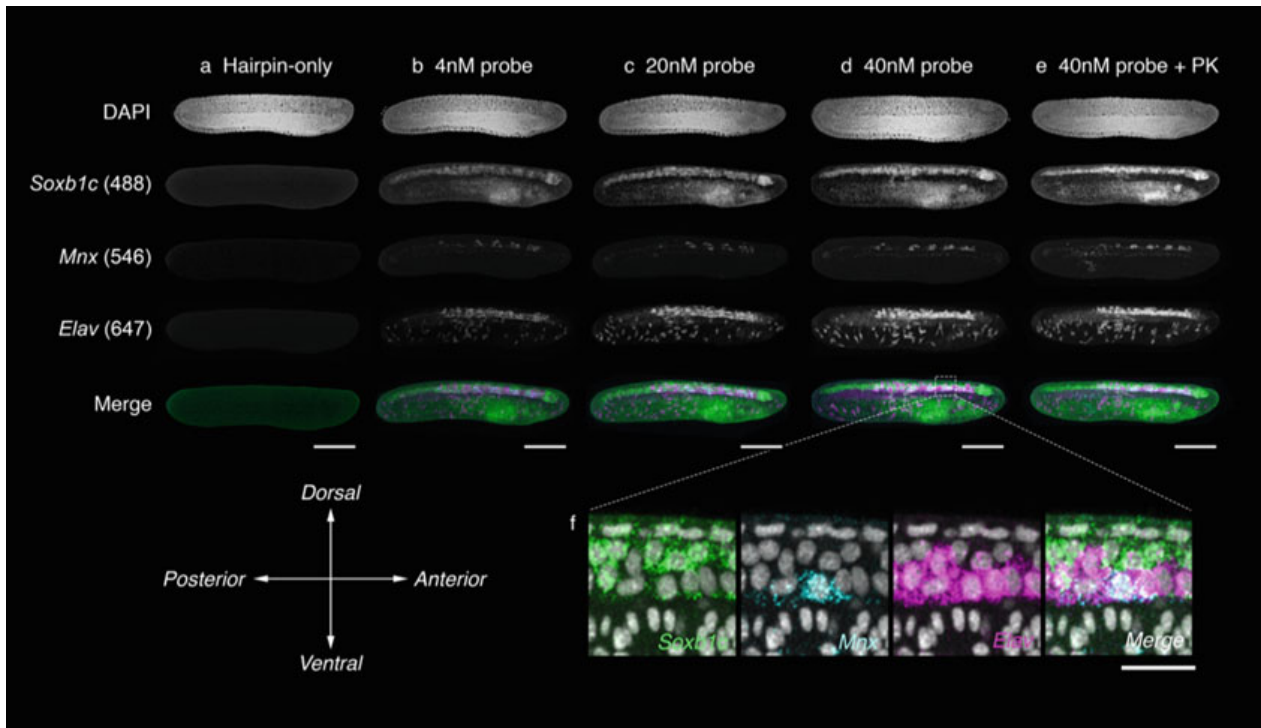


Fig. 2 Triple HCR in whole-mount embryos of *B. lanceolatum*. HCR staining was performed on whole amphioxus embryos reared in our facility [24] to 24 hpf at 21 °C with varying concentrations of probe, and in the presence and absence of proteinase K digestion. For this combination, 20-pair probe sets were designed against *Soxb1c* for broad labeling of the neural tube, *Mnx* for labeling of motor neuron progenitors, and *Elav* for postmitotic neurons. Exposure to hairpins in the absence of probes generates channel-specific background fluorescence profiles (a). This is conspicuous in all channels, but most severe following excitation at a 488 nm wavelength. A 4 nM probe concentration, as suggested for use on zebrafish embryos, generates specific signal but with a poor signal:noise ratio, even after extensive washing (b). In the 488 channel, signal can be difficult to distinguish from background. Signal:noise is greatly improved with exposure to 20 nM (c) and 40 nM (d) probe concentrations for common incubation times. At 40 nM, signal can readily be resolved from background. Proteinase K (PK) treatment is common in amphioxus ISH protocols to enhance embryo permeability. However, treatment with PK did not enhance HCR signal beyond that achieved with only permeabilization in TritonX-100 and DMSO (e). (f) Magnified view of parasagittal section through anterior neural tube of embryo in (d), revealing regional differences in expression profiles for each gene, and a single triple-positive cell. Scale bars measure 100 μ m (a–e) and 20 μ m (f)

6. Amplification buffer (Molecular Instruments).
7. RNase AWAY (Ambion).
8. Proteinase K.
9. Glycerol or Aqua-Polymount (Polysciences).

2.2 Equipment

1. Siliconized or gelatinized p200 tips.
2. Sterile filter tips.
3. Siliconized or gelatinized 1.5 mL tubes.
4. Nunc untreated 4-well plates or siliconized/gelatinized 24-well plates.
5. Hybridization oven (e.g., Hybaid Shake ‘n’ Stack).

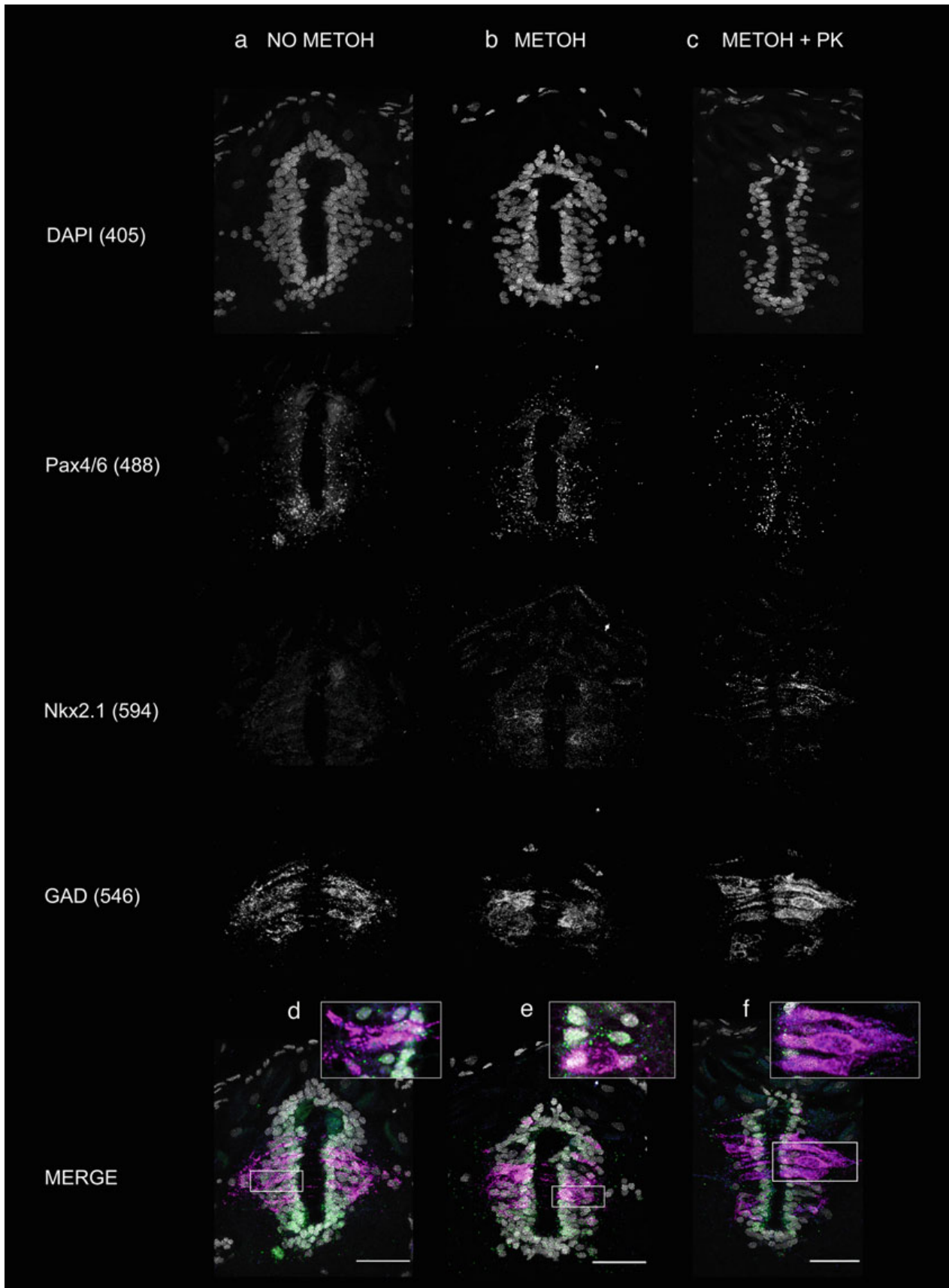


Fig. 3 Triple HCR in *B. lanceolatum* brain vibratome sections. HCR staining was performed on floating vibratome sections of adult amphioxus maintained in our amphioxus facility [24]. Sections were stained

6. Orbital shaker.
7. Water bath.
8. Heat block.
9. Stereomicroscope.
10. Vibratome (Leica).
11. Vibratome blades.
12. Dissection Instruments (for adult tissues).
13. Peel-a-way square embedding molds (Sigma).
14. Self-adhesive foam stripes for window sealing.
15. Superglue (Loctite or Gorilla).
16. Parafilm.
17. 0.2 μm pore size filters.
18. Glass-bottom dishes.

2.3 Buffers and Solutions

1. Tricaine solution: Tricaine, double-distilled water, 1 M Tris-HCl pH 9. Weigh 400 mg of tricaine and add this to 90 mL of double-distilled water. Once the tricaine has dissolved completely adjust the pH to 8.0–8.2 with 1 M Tris-HCl pH 9. Top up the solution to 100 mL with double-distilled water, filter through a 0.2 μm pore size filter, and aliquot in 2 mL doses. Store at $-20\text{ }^{\circ}\text{C}$.
2. $2\times$ MOPS buffer pH 7.5–7.6: 0.1 M MOPS (free acid), 2 mM MgSO_4 , 1 mM EGTA, 0.5 M NaCl. Weigh all in powder and dissolve in DEPC-treated water or nuclease-free water. Adjust with NaOH pellets to a pH of 7.5–7.6 (for a volume of 250 mL add approximately 8 pellets). Filter through a 0.2 μm pore size filter and store at $4\text{ }^{\circ}\text{C}$. Discard after a month.
3. 3.7% PFA-MOPS pH 7.5–7.6: Paraformaldehyde, $2\times$ MOPS buffer pH 7.5–7.6. Weigh 1.85 g of paraformaldehyde and reserve in a 50 mL tube. Bring some DEPC-treated water or nuclease-free water to the boil in a microwave and add 20 mL of this to the paraformaldehyde reserved in the 50 mL tube. To the paraformaldehyde in water add approximately 50 μL of



Fig. 3 (continued) with 20-pair probe sets designed against *Pax4/6*, used here as a neuronal marker, *Nkx2.1*, used here as a specifier of GABAergic fate and *GAD*, used here as a marker of GABAergic neurons. All probes were used at a concentration of 40 nM, as it was found to show the best signal:noise ratio for most of the genes in whole-mount preparations of embryos (see Fig. 2). Sections that had been preincubated in methanol after fixation (**b**) (see Note 1) showed a better signal:noise ratio than those that were not exposed to methanol (**a**). Low-expressed genes such as *Nkx2.1* are for example hardly visible when sections are not preincubated in methanol (compare **a** and **b**). Additional pretreatment with proteinase K (**c**) improves the sharpness of the signal for all genes, including the low-level-expressing *Nkx2.1*, the mid-level-expressing *Pax4/6*, and the highly expressed *GAD*. Magnified views of merged images in d, e, and f show co-localization of the transcripts at a single-cell resolution

NaOH 10 M. Vortex until all paraformaldehyde is dissolved. If there are still particles of paraformaldehyde in suspension, leave the 50 mL tube in a water bath at 65 °C until everything is completely dissolved. Thereafter, add 25 mL of 2× MOPS buffer and confirm that pH is 7.5–7.6. Adjust the pH if it is not within range. Top up with DEPC-treated water or nuclease-free water to 50 mL. Filter through a 0.22 µm pore size filter and store at 4 °C. For health and safety reasons it is recommended to perform all these steps, including weighing the paraformaldehyde, in a fume hood wearing protective goggles and gloves.

4. 5× Gelatine stock for coating tips and plates: Gelatine, DEPC-treated water, formaldehyde 37%. For a volume of 50 mL of stock, weigh 0.25 g of gelatine. Dissolve by autoclaving in DEPC-treated water. Allow the solution to cool and add 250 µL of formaldehyde (37%). For health and safety reasons it is recommended to add the formaldehyde in a fume hood and wear protective goggles and gloves, as the solution might still be warm. To coat tips and plates, dilute the stock to 1× with DEPC-treated water or nuclease-free water. After coating, dry plates and tips on a 65 °C oven before using them.
5. 10× NPBS: 200 mM Phosphate buffer pH 7.4, 9% NaCl. Filter through a 0.22 µm pore size filter and store at room temperature. If stocked for long, filter before use.
6. NPBST: NPBS, 0.1% Tween 20.
7. Bleaching buffer: 5% Deionized formamide, 1.5% H₂O₂, 0.2× SSC in DEPC-treated water or nuclease-free water. Prepare fresh when needed. For health and safety reasons it is recommended to wear protective goggles and gloves while preparing this buffer.
8. 3% LM-agarose: LM-agarose, DEPC-treated water or nuclease-free water. Weight 3 g of low-melting agarose for every 100 mL of DEPC-treated water or nuclease-free water. Add the 3 g of LM agarose to 80 mL of DEPC-treated water or nuclease-free water and boil in a microwave until completely dissolved. Add 10 mL of 10× NPBS and top up to 100 mL, if volume has decreased while boiling, with DEPC-treated water or nuclease-free water. The agarose can be kept at 4 °C and remelted when needed.
9. Permeabilization solution: 1% DMSO, 1% Triton. Dissolve in NPBS. Store at room temperature.
10. 5× SSCT [13]: 5× SSC (pH 7), 0.1% Tween 20. For best results, filter just before use with a 0.22 µm pore size filter. Store at room temperature.
11. DAPI counterstain solution: 1 µg/mL DAPI, NPBST. Dilute DAPI (1 µg/mL) to 1:500 in NPBST.

3 Methods

Before starting it is recommended to clean all surfaces and equipment with RNase AWAY (Ambion). This is particularly relevant for the vibratome holder and tray, as the tissue can be especially vulnerable to RNases while sectioning. It is also recommended to autoclave all glassware and other autoclavable instruments used in the procedure. Use gloves throughout the entire procedure to protect yourself and to protect the samples from RNases.

3.1 Embryo Collection and Fixation

1. Collect the embryos in the center of the dish by concentrically moving the dish. Amphioxus embryos are very small, so it is necessary to observe this process under the stereomicroscope.
2. Pipette the embryos with a siliconized or gelatinized wide orifice p200 tip into siliconized 1.5 mL tubes.
3. Transfer the 1.5 mL tubes to an ice-cold rack and leave the embryos to pellet by gravity. When the pellet is formed, remove as much seawater as possible and fill the tube with ice-cold 3.7% PFA-MOPS buffer.
4. Leave the embryos to pellet by gravity. When the pellet is formed, remove as much liquid as possible and refill the tube with ice-cold 3.7% PFA-MOPS buffer.
5. Repeat **step 4** and fix for 8–10 h (depending on the stage) at 4 °C.
6. Wash the embryos with 1× MOPS buffer by pelleting the embryos by gravity, as indicated above, at least two times.
7. Wash the embryos in either ethanol or methanol, by pelleting the embryos by gravity, as indicated above, at least twice.
8. Store the embryos in either ethanol or methanol at –20 °C, or proceed to the amphioxus HCR ISH protocol (Subheading [3.3](#), **step 2**).

3.2 Adult Tissue Fixation, Embedding, and Sectioning

1. Anesthetize adult amphioxus for 30 min using 2 mL of tricaine solution per 50 mL of seawater.
2. Make a series of cuts to divide the animal into four segments of equal length. Remove excess seawater from the tissues and transfer into ice-cold 3.7% PFA-MOPS buffer.
3. Fix for 24 h at 4 °C.
4. Wash tissues with 1× MOPS at least twice. The samples can at this point be archived for long-term storage in either ethanol or methanol at –20 °C. Otherwise, proceed to the following step to prepare samples for embedding.
5. Wash tissues with 1× NPBS at least two times.

6. Transfer the tissues into pre-warmed low-melting agarose in a water or dry bath at 45 °C and leave to equilibrate for 30 min.
7. Embedding: Cut a small rectangle of self-adhesive foam, large enough to hold the sample in the middle. Peel off the upside of the foam and add a small drop of superglue on top. With forceps extract the tissue that was equilibrating at 45 °C from the tube and place it in a suitable orientation on the top of the foam. Gently press the tissue so it gets properly attached to the foam. Transfer the foam rectangle with the attached tissue into the center of a peel-a-way square embedding mold. Fill the mold up with pre-warmed low-melting agarose (Fig. 1). Leave to cool and solidify at 4 °C.
8. Sectioning: Peel away the mold and glue the agarose block to the vibratome holder plate with superglue. Place at 4 °C while preparing the vibratome. Fill the tray of the vibratome with ice-cold RNase-free NPBS and the outer tray with ice. Assemble the vibratome blade following the instructions of the vibratome manufacturer. Attach the reserved holder plate containing the sample into the vibratome tray as indicated by the vibratome manufacturer. Place the hardest part of the tissue facing the blade (Fig. 1). If using a Leica VT100S the best sectioning conditions for amphioxus heads and trunks are as follows: speed 0.26 mm/s, frequency 50 Hz, and minimum thickness 50 µm. Collect the samples in gelatinized 24- or 96-well plates, to keep track of the sectioning order.
9. Sections can be stored at this point in either ethanol or methanol at –20 °C (*see Note 1*). Otherwise, proceed to the amphioxus HCR ISH protocol (Subheading 3.3, step 2).

3.3 Amphioxus HCR In Situ Hybridization (ISH) Steps

1. Embryo/section rehydration: If the embryos or sections are stored in ethanol it is best to transfer them to methanol for the rehydration steps. Thereafter, rehydrate through a methanol/water series, decreasing by 20% the proportion of methanol every 15 min. Perform all steps in gelatinized 4-well plates.
2. Wash embryos/sections twice in NPBST. Start the HCR protocol at this step if embryos and sections are already in NPBS or 1× MOPS buffer.
3. Bleaching: Replace NPBST with 500 µL of bleaching solution. Incubate for 30–60 min, or as long as needed to remove the pigment spots, with light and reflective foil at the base of the plate. When embryos and tissues have reached translucency, wash twice in NPBST (*see Note 2*).
4. Permeabilization: Replace NPBST with 500 µL of permeabilization solution. Incubate for 3 h at room temperature (*see Note 3*).

5. Pre-hybridization: Remove permeabilization solution or NPBST (in case of the sections) and wash the embryos/sections in $5\times$ SSCT for 5 min at room temperature. Wash the embryos/sections in pre-warmed hybridization buffer (without probes) at $37\text{ }^{\circ}\text{C}$ to equilibrate the tissues. Replace with fresh pre-warmed hybridization buffer and pre-hybridize for at least 1 h at $37\text{ }^{\circ}\text{C}$ (best results are obtained with longer pre-hybridization times).
6. Hybridization: Prepare the probe solution by diluting 1–10 μL of 2 μM probe mixed stock of each gene in 500 μL of pre-warmed hybridization solution. Replace the pre-hybridization buffer with the freshly made probe solution and incubate overnight at $37\text{ }^{\circ}\text{C}$. For adult sections, a minimum of 18-h incubation is recommended to ensure homogeneous probe binding. For best results wrap the plate in parafilm to prevent evaporation during the hybridization time (*see Note 4*).
7. Pre-amplification: Remove the probe solution and wash the embryos/sections with pre-warmed probe wash buffer at $37\text{ }^{\circ}\text{C}$. Wash for a minimum of 20 min. In the last of the washes the plate can be transferred to an orbital shaker at room temperature, as the following steps are performed at room temperature. Replace the probe wash buffer with $5\times$ SSCT and thoroughly wash embryos/sections three or four times, with each wash for a minimum of 1 h. Thereafter, pre-amplify by replacing the SSCT with 500 μL of pre-warmed amplification buffer at room temperature. Incubate in an orbital shaker at room temperature for a minimum of 1 h.
8. Preparation of the hairpins: Pipette 1 μL of each fluorescently labeled hairpin (of a 3 μM stock), per every 100 μL of amplification buffer to be used, into a fresh 1.5 mL tube. Heat up the hairpins by placing the 1.5 mL tube into a heat block at $95\text{ }^{\circ}\text{C}$ for 90 s. Cool the hairpins on ice, in the dark, for 30 min (*see Note 5*).
9. Amplification: In this step embryos and sections are transferred from the well plates to 1.5 mL tubes. In order to do this, concentrate the embryos/sections in the center of the well and use a wide-orifice siliconized p200 tip to collect them in no more of 20 μL of volume. Transfer the embryos/sections to a 1.5 mL tube containing 1 μL of each pre-cooled hairpin topped up to 80 μL with fresh amplification buffer. Protect the tubes from the light and incubate overnight in an orbital shaker at room temperature.
10. Washing: In this step embryos and sections are transferred back to a 4-well plate, so the washing volumes are bigger and therefore the excess of hairpins in the solution is removed more efficiently. To this aim, add 400 μL of $5\times$ SSCT to the

1.5 mL tube containing the embryos/sections and transfer the total volume of 500 μL to a 4-well plate. Add another 500 μL of 5 \times SSCT to the tube, to ensure that all embryos and sections are recovered, and transfer these 500 μL to the 4-well plate. Wash three times at room temperature in 5 \times SSCT by replacing the buffer every 30 min. Wash a further four to five times at 4 °C in 5 \times SSCT, by replacing the buffer every hour. Best results are obtained with overnight washes at 4 °C (*see* **Notes 6** and **7**).

11. DAPI staining: Wash the embryos/sections twice in NPBST. Replace with fresh DAPI counterstain solution. Incubate overnight protected from light at 4 °C (*see* **Note 8**).
12. Wash four to five times in NPBST, replacing the buffer every 15 min.

3.4 Whole-Mount Imaging

1. Replace NPBST with 100% glycerol and allow the embryos/sections to equilibrate.
2. Fill the base of a glass-bottomed dish suitable for imaging on an inverted confocal microscope with 100% glycerol.
3. Transfer the embryos/sections to the glass-bottomed dish using a wide-orifice siliconized p200 pipette tip. Use an eyelash wand to push the specimens to the bottom of the dish, such that they lie flat in direct contact with the glass in the correct orientation for imaging. Embryos can be organized into rows and columns based on variations in state, treatment, and HCR gene combination. Adult sections should be manually flattened against the glass with the eyelash wand to remove folds and curvatures (*see* **Note 9**).
4. Leave the glass-bottomed dish in the dark at 4 °C for at least half an hour prior to imaging to prevent drifting during the imaging process.
5. Image whole embryos and sections using a multi-area time-lapse function on an inverted confocal microscope (*see* **Note 10**).
6. After imaging, retrieve specimens from the glass-bottomed dish for long-term storage in PBS.

4 Notes

1. *Methanol incubation.* To maximize signal-to-background ratio in adult sections an incubation of at least 12 h in 100% MeOH is strongly recommended. This step has proved to be particularly useful for transcripts present at low levels, while patterns of highly expressed genes can be identified even in sections that are not treated with MeOH (*see* Fig. 3).

2. *Bleaching solution.* This solution can also be used to remove the chorion of early amphioxus embryos.
3. *Pretreatment with proteinase K.* For very thick sections incubate with proteinase K (PK) at a concentration of 1 $\mu\text{g}/\text{mL}$, for up to 8 min at 37 °C. Thereafter, thoroughly wash in NPBST and postfix with 3.7% PFA-PBS for 30 min at room temperature. Then wash thoroughly at least three times in NPBST.
4. *Hybridization time.* Hybridization time is critical for thick sections, as probes take longer to penetrate in the tissue. At least 18 h of incubation is recommended.
5. *Amplifier label.* Even with bleaching, endogenous autofluorescence in amphioxus is still particularly visible at 488 nm. We therefore advise using Alexa Fluor 488 hairpins (Molecular Instruments) for strongly expressed genes, where signal intensity is expected to exceed the autofluorescence levels. If this is not possible, background subtraction might be required during image acquisition or registration to enhance the signal of the probes.
6. *Background removal.* Although the V3 method ensures a high signal:noise ratio by preventing off-site binding, in amphioxus we find that background can still be an issue, particularly for weakly expressed genes where laser powers must be high to visualize the signal. However, we have found background to be reduced by extending probe washes and hairpin washes overnight at 4 °C. If after an overnight wash background is still high, washes can be extended for a further 2–3 days at 4 °C.
7. *Combined immunohistochemistry.* HCR imaging can be readily coupled to immunohistochemistry to label specific subcellular structures or morphological landmarks. For this, wash specimens out of the hairpin solution and then proceed directly to the immunoblock and subsequent steps of primary and secondary antibody incubation. All steps from here on should be in the dark at 4 °C to preserve HCR fluorescence. However, this is very robust, and we find no severe quenching during the immunohistochemistry protocol.
8. *Dapi staining.* This step can also be done by incubating at a higher concentration (1:200) for 3 h at 4 °C.
9. *Vibratome sections mounting for microscopy.* The use of Aqua Polymount might be more appropriate for vibratome sections of big specimens. This mounting media solidifies at application, thereby preventing the sections from moving or bend during image acquisition. This mounting media can also be used for embryos if high magnification objectives, with a shorter working distance, are used (e.g., 40 \times , 60 \times , 100 \times). In this case, use a wide-orifice siliconized p200 pipette tip to transfer sections to a glass-bottom dish, then remove NPBST, and apply Aqua-

Polymount to fill the dish. Use tungsten needles to gently arrange sections ensuring that they are completely flat and lying at the bottom of the dish, and then leave to harden at 4 °C for at least 30 min.

10. *Cross-talk suppression.* This method permits imaging five fluorophores simultaneously in the same specimen. However, we have found cross-talk between fluorophores when detection windows are too wide. To compensate for this, detection windows for each channel should be narrowed to sit exclusively on the emission peak of the fluorophore of interest.

Acknowledgments

The authors would like to thank Ben Steventon for encouraging us to develop the HCR protocol in amphioxus; to Christo Christov for technical support to our lab and amphioxus facility, the latter supported by a Sir Isaac Newton Trust Research Grant (Ref. 15.07(r)); to everybody in the histopathology and imaging facilities at the CRUK-CI; and to Matt Wayland in the imaging facilities at the Department of Zoology, which are supported by a Sir Isaac Newton Trust Research Grant (Ref. 18.07ii(c)). We also acknowledge support from CRUK (C9545/A29580) to EBG, Wellcome Trust Grant (203806/Z/16/A) to TGA, and the Claire Barnes Trust to GG.

References

1. Graham A, Papalopulu N, Krumlauf R (1989) The murine and Drosophila homeobox gene complexes have common features of organization and expression. *Cell* 57(3):367–378
2. Dubrulle J, Pourquié O (2004) fgf8 mRNA decay establishes a gradient that couples axial elongation to patterning in the vertebrate embryo. *Nature* 427:419–422
3. Riddle RD, Johnson RL, Laufer E et al (1993) Sonic Hedgehog mediates the polarizing activity of the ZPA. *Cell* 75(7):1401–1416
4. Nelson C, Morgan B, Burke AC et al (1996) Analysis of Hox gene expression in the chick limb bud. *Development* 122:1449–1466
5. Akam M, Martinez-Arias A (1985) The distribution of Ultrabithorax transcripts in Drosophila embryos. *EMBO* 4:1689–1700
6. Baker NE (1987) Molecular cloning of sequences from wingless, a segment polarity gene in Drosophila: the spatial distribution of a transcript in embryos. *EMBO* 6:1765–1773
7. McGinnis W, Krumlauf R (1992) Homeobox genes and axial patterning. *Cell* 68:283–302
8. Benito-Gutiérrez È (2011) Amphioxus as a model for mechanisms in vertebrate development. In: eLS (ed). <https://doi.org/10.1002/9780470015902.a0021773>
9. Meuleman D, Bronner-Fraser M (2004) Gene-Regulatory Interactions in neural crest evolution and development. *Dev Cell* 7:291–299
10. Holland ND, Holland LZ (1993) Embryos and larvae of invertebrate deuterostomes. In: Stern CD, Holland PWH (eds) *Essential developmental biology, a practical approach*. IRL Press, Oxford, pp 21–32
11. Holland PW, Holland LZ, Williams NA et al (1992) An amphioxus homeobox gene: sequence conservation, spatial expression during development and insights into vertebrate evolution. *Development* 116:653–661
12. Irimia M, Piñeiro C, Maeso I et al (2010) Conserved developmental expression of Fezf

- in chordates and *Drosophila* and the origin of the Zona Limitans Intrathalamica (ZLI) brain organizer. *EvoDevo* 1:7
13. Choi HMT, Schwarzkopf M, Fornace ME et al (2018) Third-generation in situ hybridization chain reaction: multiplexed, quantitative, sensitive, versatile, robust. *Development* 145: dev165753
 14. Choi HMT, Chang JY, Trinh LA et al (2010) Programmable in situ amplification for multiplexed imaging of mRNA expression. *Nat Biotechnol* 28:1208–1212
 15. Choi HMT, Beck VA, Pierce NA (2014) Next-generation in situ hybridization chain reaction: higher gain, lower cost, greater durability. *ACS Nano* 8:4284–4294
 16. Choi HMT, Calvert CR, Husain N et al (2016) Mapping a multiplexed zoo of mRNA expression. *Development* 143:3632–3637
 17. Yu JK, Holland LZ (2009) Amphioxus whole-mount in situ hybridization. *Cold Spring Harb Protoc* 2009:pdb.prot5286
 18. Yu JK, Holland LZ (2009) Amphioxus (*Branchiostoma floridae*) spawning and embryo collection. *Cold Spring Harb Protoc* 2009:pdb.prot5285
 19. Benito-Gutiérrez E, Nake C, Llovera M et al (2005) The single Amphitrk receptor highlights increased complexity of neurotrophin signalling in vertebrates and suggests an early role in developing sensory neuroepidermal cells. *Development* 132:2191–2202
 20. Benito-Gutiérrez E, Stemmer M, Rohr SD et al (2018) Patterning of a telencephalon-like region in the adult brain of amphioxus. *bioRxiv*. 307629
 21. Rybak-Wolf A, Solana J (2014) In: Nielsen BS (ed) Whole-Mount in situ hybridization using DIG-labelled probes in planarian in situ hybridization protocols, methods in molecular biology, vol 1211. Springer, New York, pp 41–50
 22. Fuentes R, Fernández J (2014) Fixation/permeabilization procedure for mRNA in situ hybridisation of zebrafish whole-mount oocytes, embryos and larvae. In: Nielsen BS (ed) In situ hybridization protocols, methods in molecular biology, vol 1211. Springer, New York, pp 1–12
 23. Saint-Jeannet JP (2017) Whole-mount in situ hybridization of xenopus embryos. From the xenopus collection, edited by Hazel L. Sive. *Cold Spring Harb Protoc*. <https://doi.org/10.1101/pdb.prot097287>
 24. Benito-Gutiérrez E, Weber H, Bryant DV et al (2013) Methods for generating year-round access to amphioxus in the laboratory. *PLoS One* 8:e71599

Appendix VI

Andrews, T. G. R., Pönisch, W., Paluch, E. K., Steventon, B. J., and Benito-Gutierrez, E. (2020).
Single-cell morphometrics reveals ancestral principles of notochord development. *Biorxiv, in review*

* Supplementary figures and appendix can be found in Appendices II and III

Single-cell morphometrics reveals ancestral principles of notochord development

Toby G R Andrews¹, Wolfram Pönisch², Ewa Paluch², Benjamin J Steventon³, Elia Benito-Gutierrez^{1*}

¹Department of Zoology, University of Cambridge, United Kingdom

²Department of Physiology, Development and Neuroscience, University of Cambridge, United Kingdom

³Department of Genetics, University of Cambridge, United Kingdom

*Corresponding author: eb647@cam.ac.uk

ABSTRACT

During development, embryonic tissues are formed by the dynamic behaviours of their constituent cells, whose collective actions are tightly regulated in space and time. To understand such cell behaviours and how they have evolved, it is necessary to develop quantitative approaches to map out morphogenesis, so comparisons can be made across different tissues and organisms. With this idea in mind, here we sought to investigate ancestral principles of notochord development, by building a quantitative portrait of notochord morphogenesis in the amphioxus embryo – a basally-branching member of the chordate phylum. To this end, we developed a single-cell morphometrics pipeline to comprehensively catalogue the morphologies of thousands of notochord cells, and to project them simultaneously into a common mathematical space termed morphospace. This approach revealed complex patterns of cell-type specific shape trajectories, akin to those obtained using single-cell genomic approaches. By spatially mapping single-cell shape trajectories in whole segmented notochords, we found evidence of spatial and temporal variation in developmental dynamics. Such variations included temporal gradients of morphogenesis spread across the anterior-posterior axis, divergence of trajectories to different morphologies, and the convergence of different trajectories onto common morphologies. Through geometric modelling, we also identified an antagonistic relationship between cell shape regulation and growth that enables convergent extension to occur in two steps. First, by allowing growth to counterbalance loss of anterior-posterior cell length during cell intercalation. Secondly, by allowing growth to further increase cell length once cells have intercalated and aligned to the axial midline, thereby facilitating a second phase of tissue elongation. Finally, we show that apart from a complex coordination of individual cellular behaviours, posterior addition from proliferating progenitors is essential for full notochord elongation in amphioxus, a mechanism previously described only in vertebrates. This novel approach to quantifying morphogenesis paves the way towards comparative studies, and mechanistic explanations for the emergence of form over developmental and evolutionary time scales.

INTRODUCTION

A major challenge in biology is to understand how individual cells coordinate their behaviours during embryogenesis to generate tissues of the correct geometry and size, and how these behaviours are modified through evolution to generate morphological novelty. The notochord is a pivotal case study

in this context. It is a defining feature of the chordate body plan with diverse contributions to axial development. The notochord also has a simple geometry, as an elongate rod of mesodermal tissue occupying the embryonic axial midline (Stemple, 2005). During its development, the notochord exerts essential roles in body plan formation, including contributions to axis elongation and mechanical stabilisation of the body axis (Stemple 2005; Segade et al., 2016; Xiong et al., 2018), and the secretion of organising signals that provide dorsoventral patterning information to the adjacent neural tube and somites (Placzek et al., 1991; Pourquié et al., 1993; Yamada et al., 1993). Once formed, the notochord also provides structural support to the embryo prior to the development of a complete skeletal system. With central roles in body plan morphogenesis, innovation of the notochord likely imposed radical change in the pattern and geometry of chordate embryos. However, while notochord development has been well characterised in outgroups (ascidians + vertebrates), the cell behaviours responsible for its formation in the first chordates remain unknown. The invertebrate chordate amphioxus, representing the most basally branching chordate subphylum (Delsuc et al., 2006), provides a unique opportunity to infer which morphogenetic principles might be ancestrally linked to notochord development, and which of these represent species-specific traits.

In vertebrates and ascidians, the notochord develops from an initially broad field of mesodermal progenitors (termed chordamesoderm) that progressively organise into an elongated rod of tissue by changing their shapes and spatial organisation. Notochord cells actively change their shape, and crawl between adjacent neighbours to intercalate and generate a single-file row. As a result, neighbouring cells are forced apart along the anteroposterior (AP) axis, resulting in tissue extension (Glickman et al., 2003; Munro and Odell, 2002; Shih and Keller, 1992). This process is termed convergent extension, in which tissue length is established at the expense of width (Keller et al., 2000). To variable degrees in each of the species studied, convergent extension synergises with cell growth and proliferation to define total notochord length. This ranges from ascidians, where notochord morphogenesis occurs in a population of exactly 40 post-mitotic cells (Miyamoto and Crowther, 1985; Veeman and Smith, 2013), to amniotes that extensively elongate the notochord primordium after gastrulation through proliferation of posterior axial progenitors, and widespread intercalatory cell division (Cambray and Wilson, 2002; Catala et al., 1996; Selleck and Stern, 1991). Intercalation is generally followed by vacuolation of individual notochord cells, which expands their volume and increases notochord length and rigidity (Adams et al., 1990; Bagnat and Gray, 2020; Bancroft and Bellairs, 1976; Ellis et al., 2013).

In amphioxus, the chordamesoderm is specified at the dorsal midline of the archenteron, the primitive gut cavity formed during gastrulation (Zhang et al., 1997). After gastrulation, the chordamesoderm evaginates to generate a longitudinal groove, and cells on either side interdigitate. This establishes a single file row of cells that ultimately stabilises in a trilaminar arrangement along the dorsoventral (DV) axis, described as a central row of flattened cells in a stack-of-coins pattern, flanked dorsally and ventrally by single-file rows of rounded Müller cells (Conklin, 1934). The central stack-of-coins is a feature shared with other chordates. In contrast, the Müller cells are unique to amphioxus. While their function is unknown, roles have been proposed in secretion of the notochord sheath and mechanical axial support (Bočina and Saraga-Babić, 2006; Holland and Holland, 1990; Flood, 1975). During amphioxus development, little proliferation has been reported in the notochord, except for cells at its posterior tip (Holland and Holland, 2006). Cell growth has also been described, and attributed to vacuolation (Hatschek, 1893). However, beyond these studies, a detailed understanding of the cellular behaviours collectively contributing to the formation and elongation of the amphioxus notochord remains lacking (Annona et al., 2015). This is in part due to the challenge of imaging amphioxus

embryos *in vivo*. Although their simple morphology, small size and optical transparency make them an ideal system for high-resolution confocal imaging, their epidermis is covered in motile cilia, which currently prevents them being kept stationary for live imaging. This means other methods need to be developed to infer cell behaviour.

To build a complete picture of cell shape changes during amphioxus notochord development, we use large-scale morphometric techniques, that have been previously used to compare biological shapes ranging from single cells in culture to entire organisms. Approaches for shape quantification have included standard geometric measures (Mingqiang et al., 2008; Pincus and Theriot, 2007; Tassy et al., 2006), landmark-based morphometrics (Watanabe et al., 2019; Webster and Sheets, 2010), and Fourier descriptors (Boehm et al., 2011; Medyukhina et al., 2020; Tweedy et al., 2013). The resulting high-dimensional datasets are often visualised in lower-dimensional spaces, termed morphospaces, by applying dimensionality reduction approaches such as Principal Component Analysis (PCA) (Bhullar et al., 2012; Ruan et al., 2020; Tweedy et al., 2013). In morphospace, short distances between specimens reflect morphological similarity between different shapes, whereas large distances represent disparity. These distributions can expose specific transitions in form over developmental and evolutionary timescales (Morris et al., 2019; Yin et al., 2014; Young et al., 2014). Here, we reason that this approach can be used to define trajectories of cell shape change underpinning tissue morphogenesis, when applied to morphometric data for thousands of cells, from embryos at different developmental stages, across the whole spatial extent of a developing tissue. This analysis offers a systems-level view of tissue morphogenesis. From here on, we refer to such a descriptions of developmental transformations in cell shape as ‘trajectories’, akin to the description of cell state trajectories in single cell transcriptomic analyses.

Here, we define trajectories of shape change for cells of the amphioxus notochord during its elongation, by projecting them into a single-cell morphospace. We find that cells in morphospace cluster into a series of branching cell type-specific trajectories, which all emerge from a common progenitor morphology. We next make use of geometric modelling, applied to mean progenitor cell shapes, to determine how specific geometric transformations contribute to the global cell shape transitions measured along each trajectory. This analysis suggests that volumetric growth enables convergent extension in the notochord in two steps: Firstly, by counterbalancing loss of AP length as cells increase their surface area during intercalation. Secondly, by directly increasing cell AP length after they have intercalated and become distributed along axial midline. Since our approach also captures each cell’s position within the embryo, we further show that cells at different positions along the AP axis progress towards common morphologies at different times, and through different morphogenetic paths. Finally, we use cell labelling strategies and pharmacological cell cycle arrest to test the role of cell division in notochord elongation and expose a novel role for posterior progenitors in regulating the number of cells available for each morphogenetic trajectory. Overall, our approach reveals the notochord of amphioxus to be morphologically more complex and heterogenous than previously thought, and identifies a conserved repertoire of morphogenetic processes ancestrally linked to notochord development.

RESULTS

A single-cell morphospace captures branching trajectories of shape differentiation specific to cell type

In amphioxus, notochord formation involves a complete restructuring of cellular organisation from a seemingly disorganised array of rounded cells at the 6-somite stage (ss), to a regular trilaminar array at the 14ss. This consists of central cuboidal cells in a stack-of-coins pattern sandwiched between two rows of Müller cells (*Fig. 1a, insets*) (Hatschek, 1893; Conklin, 1924). Assuming that cells gradually transition towards their final morphologies, cell shapes in fixed specimens will reflect snapshots of differentiation. With this logic, we sought to reconstruct dynamic trajectories of single-cell shape change by assembling 3D single-cell morphometric data into a developmental morphospace. To achieve this, we built a dataset of manually-segmented notochord cells at successive stages of elongation, using embryos stained with phalloidin, to mark cortical actin, from 6-14ss (*Fig. 1a, b*). In total 3,796 cells were segmented, from 15 notochords across 5 developmental stages. We next quantified a series of geometrical parameters for each cells, relating to their shape, size and orientation (*Fig. 1c*; itemised in *Materials and Methods*). To identify the major axes of shape variation between cells, we then performed a principal component analysis (PCA) on these measurements (*Fig. S1*). In doing so, we found that 86.2% of cell shape variability was explained by 5 eigenvectors (*Fig. S1a*); anisotropic elongation along the AP axis (PC1, 36.7% variation; *Fig. S1d*), transverse elongation and orientation (PC2, 20.9% variation; *Fig. S1e*), volume and surface smoothness (PC3, 14.1% variation; *Fig. S1f*), surface convolution (PC4, 9.7% variation; *Fig. S1g*), and nuclear displacement from the centre of homogenous mass (PC5, 4.8% variation; *Fig. S1h*) (*Fig. 1c, S1*). These components now offered a framework to visualise geometric variation in low-dimensional space.

We next plotted cells against the first three PCs to construct a developmental morphospace. In morphospace, cells organised in a continuous and highly-structured branching pattern (*Fig. 1d*), with three primary branches linking the diversity of cell shapes that emerge during notochord development (*Fig. 1d*). This pattern was reproducible across the three embryos analysed per stage (*Fig. S2*). To ask how cells traverse this morphospace during their development, we subdivided the data by developmental stage. At 6ss, all cells occupied the central branch of morphospace, with tall DV-elongated morphologies (*Fig. 1e, 6ss*). Over time, these morphologies were lost, and cells flowed from the central branch of morphospace into a bifurcation at the base of the plot (at the level of -1.5 on PC1) to form two distinct trajectories of shape change (*Fig. 1e, asterix*). Although cells from later somite stages populated more distal positions in morphospace, with respect to this bifurcation, a continuum was present at each stage between immature and differentiated states. This suggests that not all cells undergo the same shape transitions at the same time. By additionally categorising cells based on relative DV position, we found the bifurcation event to yield independent trajectories for the two main cell types in the notochord: the central cells and Müller cells (*Fig. 1e, 8ss – 14ss*). While the Müller cells became elongated along the AP axis at the expense of their transverse area (decreasing on PC1, anti-correlated with AP anisotropy), the central cells spread out on a transverse plane at the expense of their length (increasing on PC1). The trajectory followed by Müller cells was further divided in sub-trajectories for the dorsal and ventral rows, based on distinctive levels of AP anisotropy (*Fig. 1e, yellow and blue points*). Overall, morphospace embedding approach reveals a progressive diversification of cell morphology during notochord development, in which a common progenitor morphology is remodelled to generate a diversity of cell morphologies.

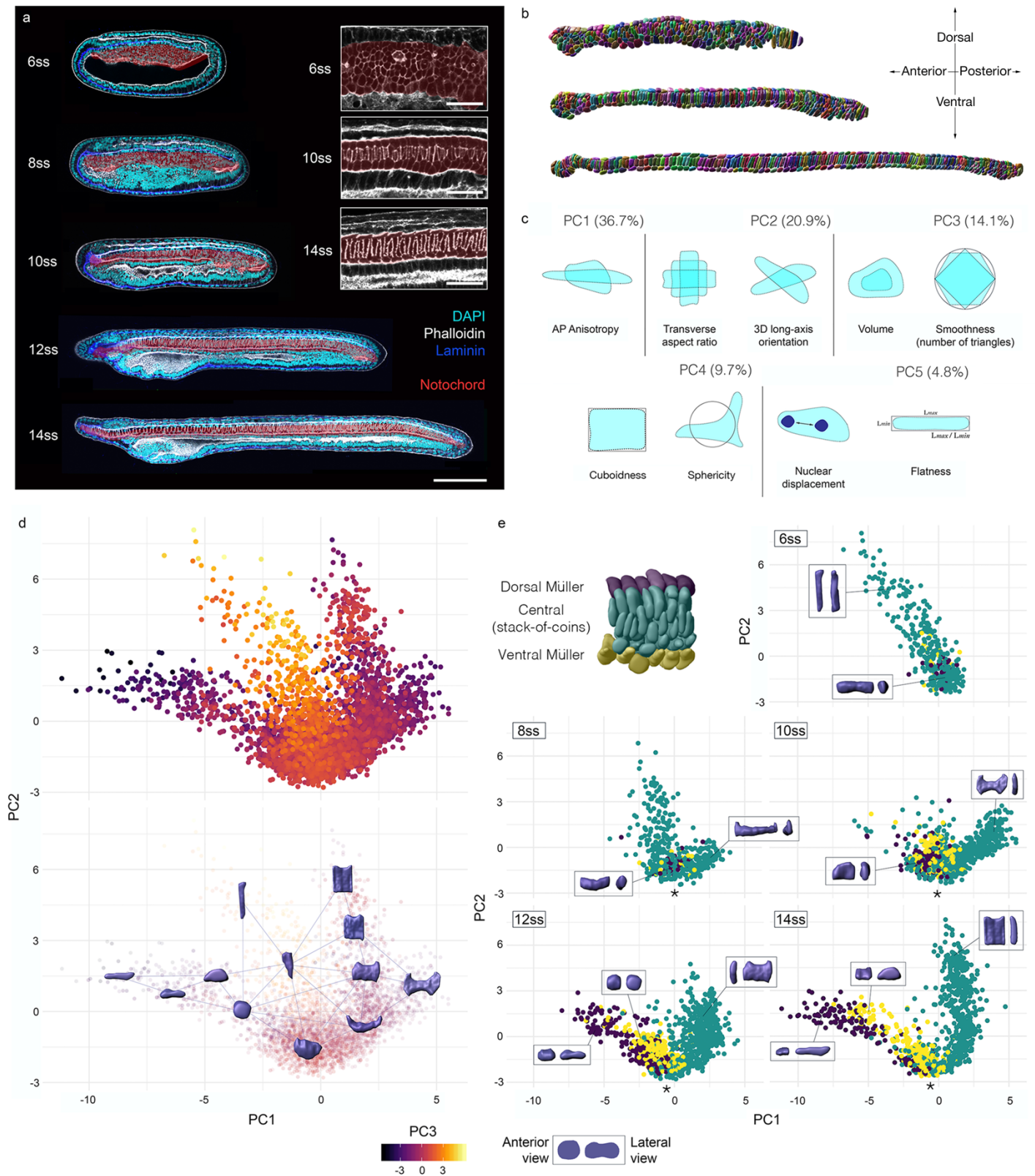


Figure 1. A single-cell morphospace captures notochord cell shape diversity. (a) Successive stages of amphioxus embryo spanning axis extension, stained for phalloidin, and immunostained for laminin. (b) Fully segmented notochords from the 8-, 10- and 12-somite stages. (c) Major geometric correlates of the first five principal components. (d top) Active notochord morphospace for all cells and stages, with colour code for PC3. (d bottom) Notochord morphospace illustrated with representative surfaces from segmentation data. (e) Morphospace filtered by developmental stage and colour-coded for position along the DV axis, where Müller and stack-of-coins cell types become resolved. Representative cells for each domain shown in inlays, in anterior (left) and lateral (right) views. 3,796 individually-segmented cells, 5 stages, 3 embryos per stage.

Single-cell morphometrics highlights two major shape transitions in central notochord cells

From this global view of shape differentiation, we next sought to refine a single shape trajectory for notochord cells by selecting those at a specific position along the anteroposterior axis and mapping their changing distribution in morphospace over time (*Fig. 2a*). Collectively, we found central layer cells from the 40-60% level of the anteroposterior axis to exhibit a continuous distribution across morphospace. This is illustrated by a partial overlap of the point clouds for cells of successive somite stages, suggesting that cells from each stage are heterogenous in their extent of shape differentiation (*Fig. 2a*). We next used the trajectory inference method, Slingshot, to order cells along a pseudotemporal axis (Street et al., 2020). This was performed in a semi-supervised manner, guided by prior information on temporal transitions from somite stages. The inferred pseudotemporal axis passed through the point clouds for each somite stage in correct temporal sequence, and fit closely to their mean PC coordinates (*Fig. 2a*, compare blue and black lines). By plotting the frequency of cells across pseudotime for each somite stage, we found cell shape transitions to be tightly controlled across developmental time, as measured by somite stage (*Fig. 2b*). Furthermore, we identified a strong positive correlation between pseudotime and somite stage (Pearson correlation = 0.94), showing that pseudotime is linearly related to developmental time (*Fig. 2c*). This validated the inferred pseudotemporal axis as a vector for expressing both the directionality and temporal progression of cell shape changes through morphospace.

We next asked how cell shape changes across the 40-60% central cell trajectory. We examined this both qualitatively, by selecting cells from evenly-spaced intervals across pseudotime, that represent shapes acquired sequentially along the trajectory (*Fig. 2d*), and quantitatively, by analysing changes in the major correlates of each principal component (*Fig. 2e - h*). Together, the results we obtained highlight two major shape transitions that occur sequentially in central notochord cells:

In the first major shape transition ('ST1', 6ss – 10ss), cells transition from a ML-elongated morphology that is rounded in lateral view, to a flattened morphology spread across the transverse plane, with distinct flared margins, similar in shape to a bowtie (*Fig. 2di - diii*). In this process, notochord cells decline in AP-oriented anisotropy (anti-correlated with PC1; *Fig. 2e, S1b, S3f*), accounted for by an increase in transverse cross-sectional area at the expense of AP length (*Fig. 2e*). In parallel, the transverse shape of each cell changes, with an increase in DV:ML ratio (positively correlated with PC2, *Fig. 2a, f, S3l*). Cells elongate on both the ML and DV axes during this period, but the earlier plateauing of ML length at 8ss leads to an anisotropic elongation along the DV axis (*Fig. 2f*). During the first transition, we also found an increase in volume (anti-correlated with PC3, *Fig. 2g, S1c*), and a decline in cuboidness, which reflects how faithfully the cell fits its object-oriented bounding box (anti-correlated with PC4, *Fig. 2h*). This means that the total spreading area of the cell is increased beyond its cross-sectional area through convolution of its surface, which we quantify in a scaling factor, γ (*Fig. 2h; see Appendix I*). When cuboidness reaches its minimum value at 10ss, γ reaches its maximum value (*Fig. 2h*). Collectively, these geometric transitions describe formation of a bowtie morphology at 10ss, which occupies a distinct domain in morphospace that we term the 'bowtie domain' (*Fig. 2a, diii*).

During the second major shape transition ('ST2', 10ss – 14ss), cells lose their bowtie morphology, and acquire tall cuboidal shapes (*Fig. 2diii - dvi*). Underlying these global changes, AP-oriented

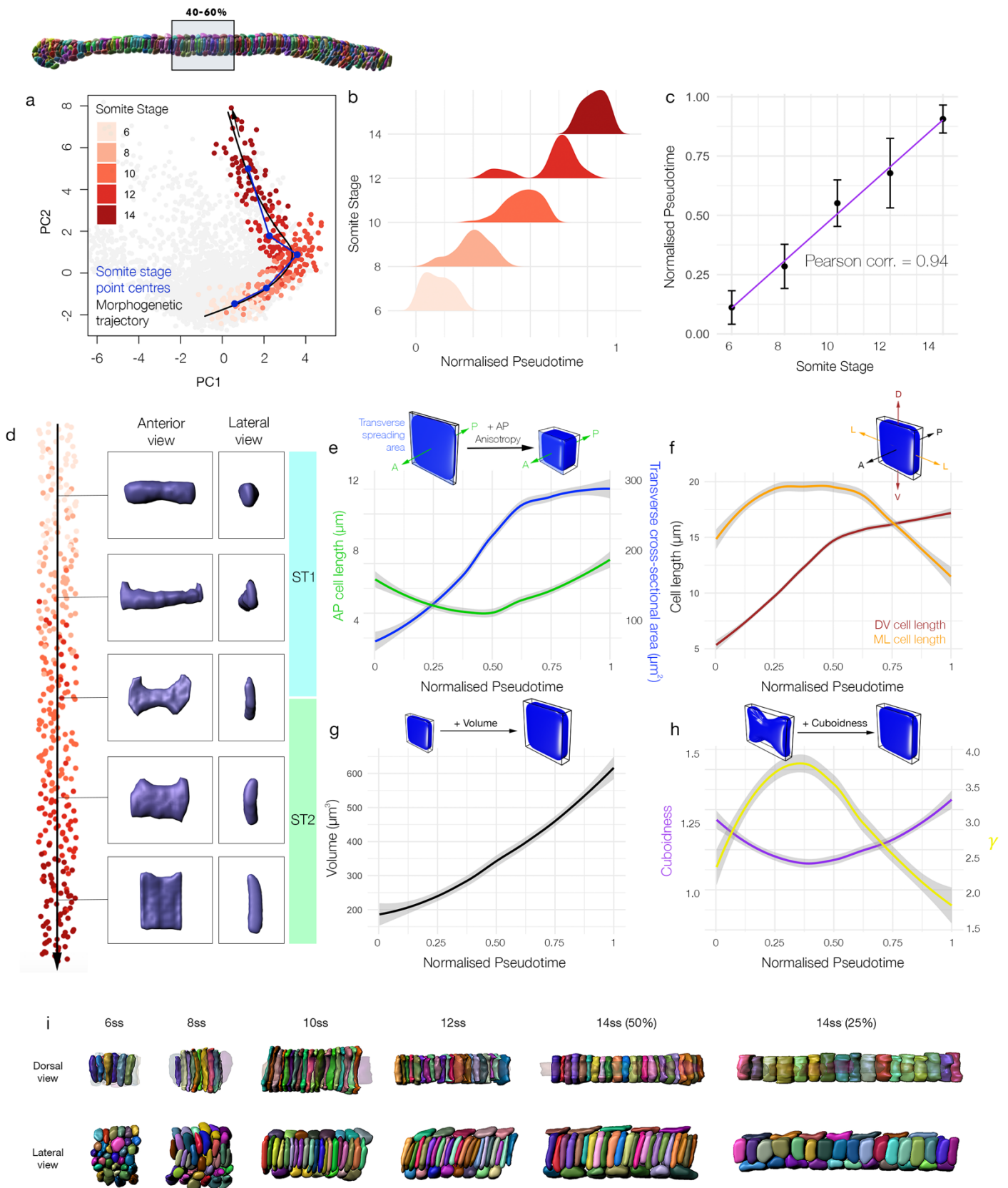


Fig. 2. **The 40-60% central notochord cell shape trajectory.** (a) Notochord cells from the central layer at the 40-60% level of the AP axis projected into morphospace, coloured by somite stage. Blue segmented line connects point cloud centres for each stage, black curve defines the inferred Slingshot trajectory. (b) Density plots showing frequency of cells across pseudotime for each somite stage. (*continued overleaf*)

anisotropy increases, in this case due to an increase in AP length without further change in cross-sectional area (Fig. 2e, S3f). Meanwhile, DV:ML ratio continues to increase due to a further slow increase in DV length, coupled to an almost 2-fold decline of ML length (Fig. 2f, S3l). Volume continues to increase during the second major transition (Fig. 2g). However, cuboidness and sphericity now increase, thereby reflecting a decline in cell surface convolution (Fig. 2h, S3g, h). In turn, γ also declined, corresponding to a lesser spread of the cell beyond its transverse cross-sectional area and loss of the bowtie morphology (Fig. 2diii – dvi, 2h). In sum, decomposition of the PCs exposed dynamic profiles of AP anisotropy, DV:ML ratio, volumetric growth and surface convolution as the primary geometric transformations underlying both major shape transitions of the central cell trajectory: First, an expansion of transverse cell spreading area at the expense of AP length, enhanced by surface convolution and formation of a bowtie morphology. Second, collapse of the bowtie morphology and an increase in AP length associated with ongoing cellular growth.

The sequence of cell shape transitions we identified in central notochord cells define a unique trajectory through morphospace (Fig. 2a). The next question is how these behaviours correspond to changes in multicellular organisation. To address this question, we segmented neighbourhoods of 35 adjacent cells at the 40 – 60% level, and aligned changes in their organisation with the transitions in cell shape defined above (Fig. 2i). At 6ss, all cells were elongated along their ML axes, with bipolar contacts with both the left and right margins of the chordamesoderm (Fig. 2i, Dorsal view, 6ss). Because this stage precedes most of notochord AP elongation (Fig. 1a), ML intercalation cannot generate further tissue length. Instead, we noted an increase in the number of cell layers on the DV axis between 3ss and 6ss, suggesting that ML intercalation might drive an early convergent thickening (Fig. 2i Lateral view, Fig. S4 compare 3ss and 6ss). During the first shape transition in central cell progenitors (6ss – 10ss), in which they increase their transverse spread and adopt a bowtie morphology, we observed a process of intercalation oriented along the DV axis, that reduces the number of cell layers from 6 to 3 (Fig. 2i, Lateral view, 6ss – 10ss). During this DV intercalation, we found that cell neighbourhoods elongated, despite the AP shortening of individual cells (Fig. 2e, 2i). We found that DV intercalation was followed by a latter phase of neighbourhood elongation in the absence of further cell rearrangement, coincident with the second major transition in cell shape, in which cells increased in AP length and

Fig 2 (continued). (c) Mean pseudotime distance for cells of each somite stage, +/- standard deviation. Blue line shows a linear regression, with a Pearson correlation coefficient of 0.94. (d) All 40-60% central layer notochord cells ordered across the inferred trajectory from (a). Segmented cells sampled from each marked position are shown in anterior and lateral view. The two major transitions of cell shape observed are indicated as T1 and T2. (e – h) Changes in specific geometric parameters along the 40-60% central cell trajectory. (e) PC1 is anti-correlated with AP anisotropy, derived from transitions in cell AP length and cross-sectional area. (f) PC2 is positively correlated with DV:ML aspect ratio, influenced by transitions in DV and ML cell length, inferred from bounding box dimensions. (g) PC3 is anti-correlated with cell volume. (h) PC4 is positively correlated with cell surface convolution, quantified here by cuboidness. This affects the discrepancy between cell and bounding box cross-sectional area, which we quantify as γ . (i) Segmented cells from the 40-60% level, shown in dorsal and lateral views across somite stages. In dorsal view, the Müller cells are transparent, enabling visualisation of the central layer. In lateral view, both the central and Müller cells are shown. $n = 344$ cells for 40-60% level central layer cells, $n = 360$ for 25 – 40% cells.

volume (*Fig. 2e, g, i 10 – 14ss*). This latter elongation phase was most pronounced in the pharyngeal region (*2i, compare 14ss 40 – 60% and 25 – 40%*). In sum, the sequential shape changes of the central cell trajectory aligned with distinct phases of notochord elongation, mediated first by DV cell intercalation, and second by cell elongation.

Geometric modelling reveals a requirement for growth in coupling convergence and extension

By deconstructing notochord development in morphospace, we have shown that AP anisotropic elongation, DV:ML ratio, growth and surface convolution are key geometric transformations underpinning central cell differentiation (*Fig. 2, 3a*). Therefore, we infer that changes in cell length should be the summed effect of change in AP anisotropy, which we know has an adverse effect on cell length, and growth acting together. We next set out to investigate the effect of each transformation on the lengths of single cells, and groups of cells undergoing intercalation, when applied individually. To this end, we devised a simplified mathematical framework to model the effect of each transformation on a mean cell from the 6-somite stage notochord at the 40 – 60% level (*Appendix I*). This cell is defined by its AP length $l_{AP}^{(cell)}$, volume $V^{(cell)}$, and cross-sectional area $A^{(cell)}$. Where s denotes stage, AP length can be calculated as

$$l_{AP}^{(cell)}(s) = \frac{V^{(cell)}(s)}{A^{(cell)}(s)}.$$

We can now measure change in cell length when change in either volume or cross-sectional area occur independently, with the other fixed at their 6ss value.

As we have shown, central notochord cells in the 40 – 60% region undergo an early phase of shortening on the AP axis linked to intercalation (6-10 somites), followed by a late phase of elongation in which AP length is restored (10-14 somites) (*Fig. 2e, 3b black line*). We first set out to investigate how cell length would change if governed only by AP anisotropy, in the absence of growth. Here, we allowed cell length to change in accordance with measured change in cross-sectional area, while maintaining the cell at constant volume (*Fig. 3b, blue line*). Under these modelled conditions, cross-sectional area increases at the expense of length, such that cells undergo a 2.16-fold shortening between 6ss and 10ss. Thereafter, instead of restoring length, cells continued to shorten at a slower rate, by an additional 1.17-fold change. This suggests that, during intercalation, transverse cell spreading has a sustained negative effect on length. Without prior knowledge of growth dynamics, we envisaged two scenarios for its effect on shape. First, we considered a scenario in which cells maintain their shape at 6ss, and the growth that we measure (*see Fig. 2g*) acts isotropically to expand cell geometry proportionally in all directions. In this case, cells underwent a progressive increase in length by a total of 1.37-fold, thereby exceeding the 1.02-fold net length change measured during normal development (*Fig. 3b, grey line*). This change was more pronounced in the second scenario of anisotropic growth, in which we prevented radial cell expansion and forced growth to act unidirectionally on AP length. In this case, we measured a 2.59-fold elongation (*Fig. 3b, orange line*), again far exceeding the measured change. Collectively, these calculations suggest that transverse cell spreading behaviour and growth have antagonistic contributions to cell AP length, and the real profile of length change is a dynamic balance between the two transformations. We therefore infer that, up to the 10-somite stage, the rate of transverse cell spreading outweighs that of growth, leading to a net cell shortening during intercalation.

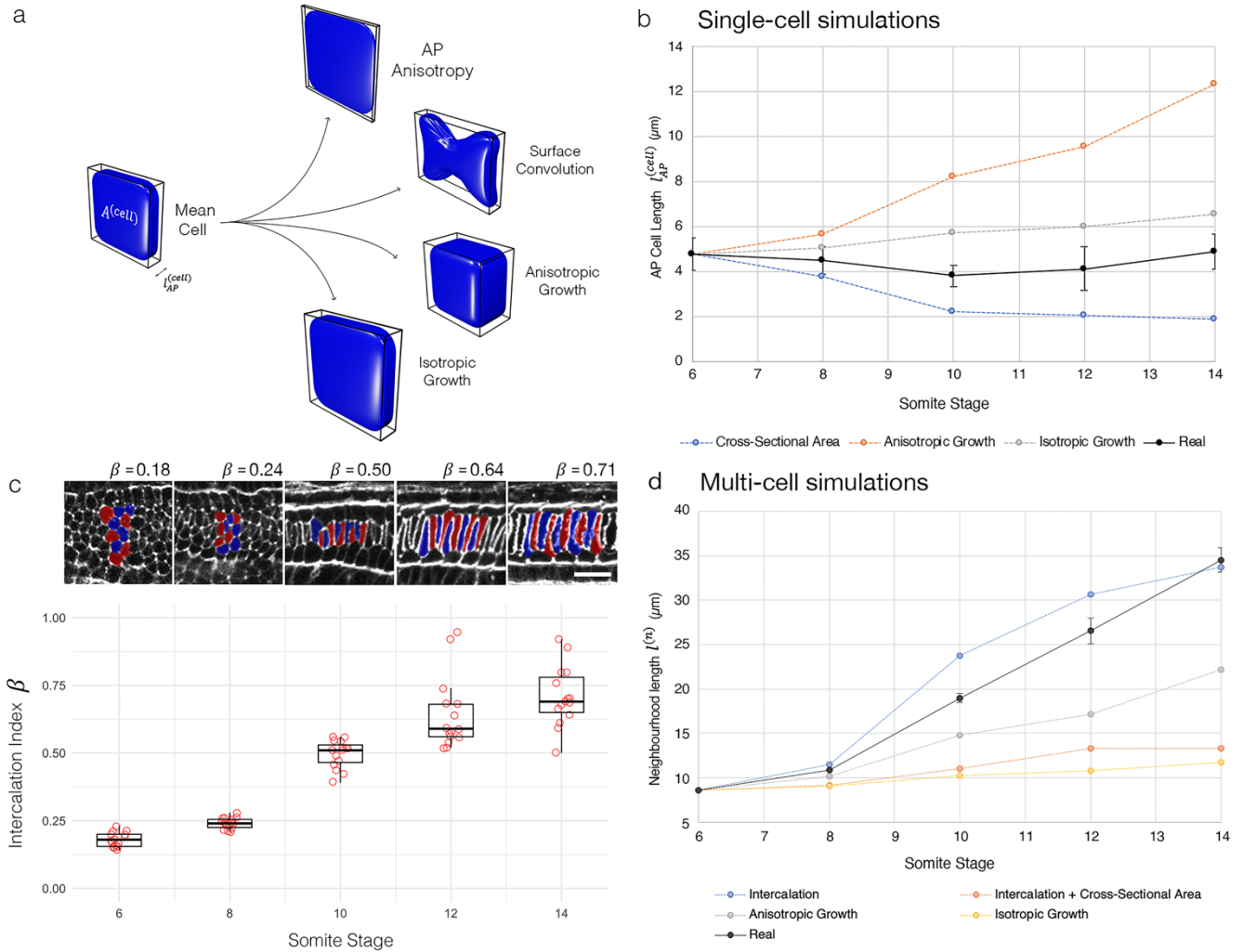


Figure 3. Geometric modelling predicts contributions of shape and size to major transitions of the central cell trajectory (a) Visual renderings of transformations identified in the central cell trajectory. (b) Results of geometric perturbations applied to a mean central cell from the 6-somite stage, over a developmental time course, illustrating predicted change in cell length. Coloured lines represent modelled scenarios, black line represents real measured change with measured standard error. (c) Quantification of intercalation index across developmental time, with representative groups of 10 cells per stage. Scale bar shows $20\mu\text{m}$. (d) Predicted change in the length of a neighbourhood of 10 6-somite central cells, integrating both intercalation and changes in single-cell shape and size. Black line shows real measured length changes, with standard error.

When cross-sectional area stabilises at 10ss (*Fig. 2e*), growth then dominates to translate a programme of transverse cell spreading into one of elongation.

We next sought to test how this relationship between shape and size in single cells affects the rate of elongation in a group of neighbouring cells undergoing intercalation. We tested this in groups of 10 cells from the 40 - 60% region of the notochord. To investigate the effect of intercalation, we defined an intercalation factor, β , which allows calculation of extended AP group length $l^{(n)}$ from cell

number n and mean AP cell length $l_{AP}^{(cell)}$ for a given stage (*Fig. 3c, appendix I*);

$$l^{(n)} = n \beta l_{AP}^{(cell)}.$$

We made use of values for $l^{(n)}$ obtained from groups of 10 adjacent cells measured in the embryo at each stage. When $\beta = 1$, group length equates to the summed lengths of all cells, whereas when $\beta < 1$ cells are displaced from the midline and so their individual lengths are not additive in the same plane (*Fig. 3c, Appendix I Fig. 2*). We used these metrics to drive intercalation either independently, or in combination with transformations in cell shape and size. We first tested how intercalation alone contributes to length by applying experimentally obtained intercalation index values (β values, *Fig. 3c*) to groups of mean 6ss progenitors. Here, we found that intercalation can drive a 3.49-fold AP elongation, occurring at its greatest rate between the 8-somite and 12-somite stages (*Fig. 3d, blue line*). This is the effect of simply aligning cells into a single-file array, with no accompanied shape change. To then factor in cell shape changes, we applied measured changes in both cross-sectional area (as for *Fig. 3b*) and intercalation index, while keeping volume constant (*Fig. 3d, orange line*). In this growth-free scenario, intercalation did increase neighbourhood length, despite the shortening of individual cells, but only to a maximum 1.55-fold extension, measured at the 12ss. This falls significantly short of real measured values, therefore suggesting that the ability of cell intercalation to drive AP tissue elongation is counteracted by cell spreading behaviours that reduce cell length. We therefore hypothesised that growth should account for most of AP elongation. By itself, isometric growth achieved only a 1.76-fold elongation (*Fig. 3d, yellow line*), whereas anisotropic growth was more effective, driving a 2.59-fold increase (*Fig. 3d, grey line*). This means that growth is also insufficient to drive full tissue elongation, unless coupled to intercalation. In sum, our geometric modelling suggests that growth enables convergent extension in two manners. First, by counteracting loss of cell AP length during intercalation due to cell spreading (6ss – 10ss). Second, by further increasing cell length after intercalation, once the stack-of-coins is formed (10ss – 14ss).

Spatial mapping reveals bidirectional gradients of shape maturation

Having previously identified heterogeneity in the extent of shape maturation for cells of the same somite stage (*Fig. 1e*), we next sought to test whether this temporal variation is spatially organised. To this end, we isolated all cells in the central notochord layer, this time regardless of position, and used Slingshot to infer a pseudotemporal axis passing through all points. In this case, cells from successive somite stages were strongly overlapping in morphospace, although dispersal across the central cell branch of morphospace increased progressively over time (*Fig. 4a*). Here, we therefore used k means clustering to construct the minimal spanning tree, and again prior information on temporal transitions from somite stages to define the trajectory start and end points. The inferred trajectory initiated in the central branch of cells in morphospace, passed through the bifurcation from Müller cells at the base of the plot, and extended through the central cell branch (*Fig. 4b*). We next quantified spatial variation in pseudotemporal progression by calculating the mean position in pseudotime for 10 non-overlapping bins of normalised AP notochord length (*Fig. 4c*). This was performed for notochords between 8ss and 14ss, when shape heterogeneity becomes explicit across the notochord. By this method, we found for each stage that the most advanced cells in pseudotime concentrated in the middle of the notochord, and the distance in pseudotime progressively decreases in each bin towards the most anterior and

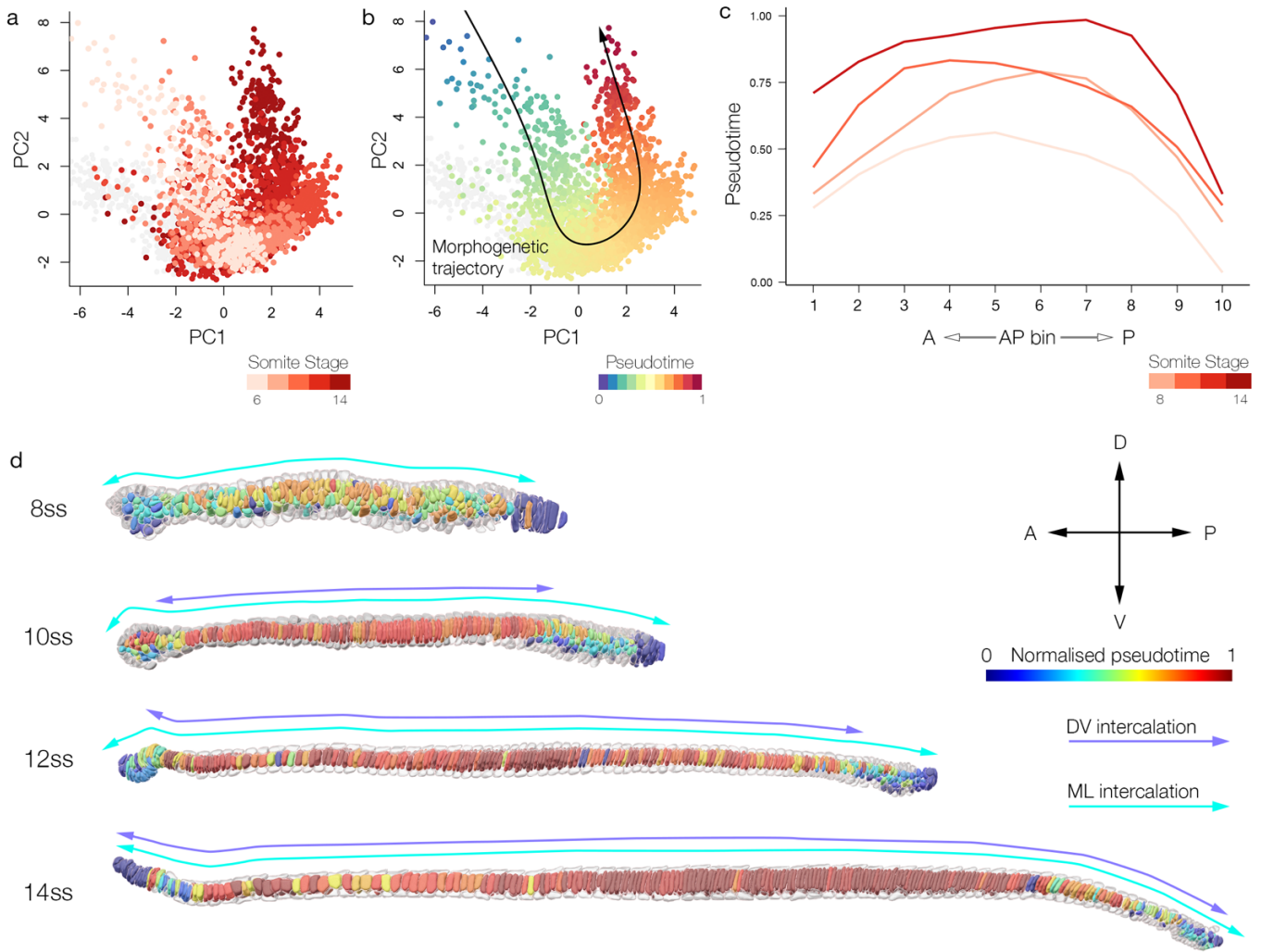


Figure 4. Temporal variation is spatially organised in bidirectional maturation gradients (a) All central layer notochord cells, regardless of spatial position on the AP axis, projected into morphospace. Colour-code reflects somite stage. (b) Central notochord cells ordered across an inferred pseudotemporal axis, guided by prior information on temporal transitions (a). (c) Mean pseudotemporal distance for cells in each of 10 evenly-sized bins of the AP axis, in embryos between 8ss and 14ss. 1 is most anterior, 10 is most posterior. (d) Colour-coding of the central notochord layer by pseudotemporal distance, aligned with the progression of ML and DV intercalation events inferred from transitions in cell topology. The progress of ML and DV intercalation is marked by cyan and purple bidirectional arrows.

posterior tips (*Fig. 4c*). In morphospace, the most advanced cells lie at the leading edge of a shape continuum that extends back to the most immature morphologies towards the posterior tip of the embryo, in which shape maturation correlates strongly with AP position (*Fig. S5 aii – dii*). Cells of the anterior tip also lie proximal to the leading cells in morphospace (*Fig. S5 ai – di*). At 10ss, cells of the 0 – 15% region occupy the same position as 40 – 60% cells at 8ss (*Fig. S5 a, b*), and at 14ss they overlap with 40 – 60% cells at 12ss (*Fig. S5 c, d*). In sum, this analysis reveals temporal variation in cell shape transitions to be spatially organised into bidirectional gradients across the AP axis.

To further illustrate the spatial structure of temporal variation *in situ*, we colour-coded whole notochords by pseudotime (Fig. 4d). This confirmed the enrichment of leading cells in pseudotime in the middle part of the notochord, and a delay towards the anterior and posterior tips. It additionally revealed a correlation between the extent of shape maturation and changes in multi-cellular topology. Cells in the middle of the notochord were the first to undergo dorsoventral intercalation, as inferred from the local transition from a multi-layered organisation to a trilaminar organisation (Fig. 4d, 10ss). Unlike the 40-60% level, that undergo DV intercalation between 6ss and 10ss (Fig. 2j), cells in the anterior tip remained stratified on the dorsoventral axis until 10ss, and reduced to a single layered organisation by 14ss (Fig. 4d, 10ss – 14ss, Fig. S5e). This represents a 4-somite delay compared to the trunk region (Fig. 4d, 10ss – 14ss). We additionally found the posterior notochord to exhibit delayed intercalation. At all stages analysed, progenitors in the most posterior notochord remained stratified on the dorsoventral axis (Fig. 4d, S5e). Up to 12ss, we also found the persistence of tall columnar cells lacking bipolar left-right contacts at the extreme posterior tip of the notochord (Fig. 4d, S5e). This is characteristic of the monolayered archenteron roof prior to mediolateral cell intercalation (Fig. S4a). Over developmental time, cells organised in both of these topologies were depleted and restricted further towards the posterior tip of the embryo (Fig. 4d, S5e). This is also reflected in a gradual decline in occupancy of the central branch of the notochord morphospace between 6ss and 10ss (Fig. 1e). In sum, the middle-to-tips dynamic of cell shape maturation in the notochord spatially and temporally mirrors bidirectional waves of ML and DV intercalation that establish a distinctive stack-of-coins pattern in the central notochord layer.

Spatial variants in trajectory structure demonstrate divergent and convergent paths to specific cell morphologies

Having identified spatial variation in developmental timing across the AP axis, we sought to test whether the structure of the central cell trajectory is shared by all cells, regardless of spatial position. We investigated this by constructing region-specific shape trajectories for four candidate regions sampled across the AP axis (Fig. 5a); anterior (0-15% AP position), pharynx (15-40% AP), trunk (40-60% AP) and posterior (60-100% AP). In each sampled region of the AP axis, we performed trajectory inference as described previously, guided by the temporal information in somite stages. We then analysed variation between regions in trajectory topology and its correlation with developmental time:

In anterior progenitors, the trajectory we inferred involved similar geometric transitions to the trunk (40-60%) level (compare Fig. 5bi and biii, ci and ciii). This included a transient loss of AP length during intercalation (Fig. S6a), and continuous increases in cross-sectional area (Fig. S6d), volume (Fig. S6i) and DV:ML aspect ratio (Fig. S6l). Maturation additionally involved a decline in the coefficient of variation for cuboidness, although the mean values remained constant (Fig. S6g), and a progressive decline in sphericity (Fig. S6h). In accordance with its temporal delay compared to the pharynx and trunk, the anterior trajectory extended least far into the central cell branch of morphospace (Fig. 5bi, ci). In addition, and unlike the more posterior regions, there is a poor separation of cells over pseudotime between somite stages, reflecting loose temporal control of shape transitions in this region (Fig. 5di). Considered together, the anterior region shares common shape transitions to other regions, but is unique in its heterogeneity, with extensive variation in developmental timing between adjacent cells as they progress to their final morphologies.

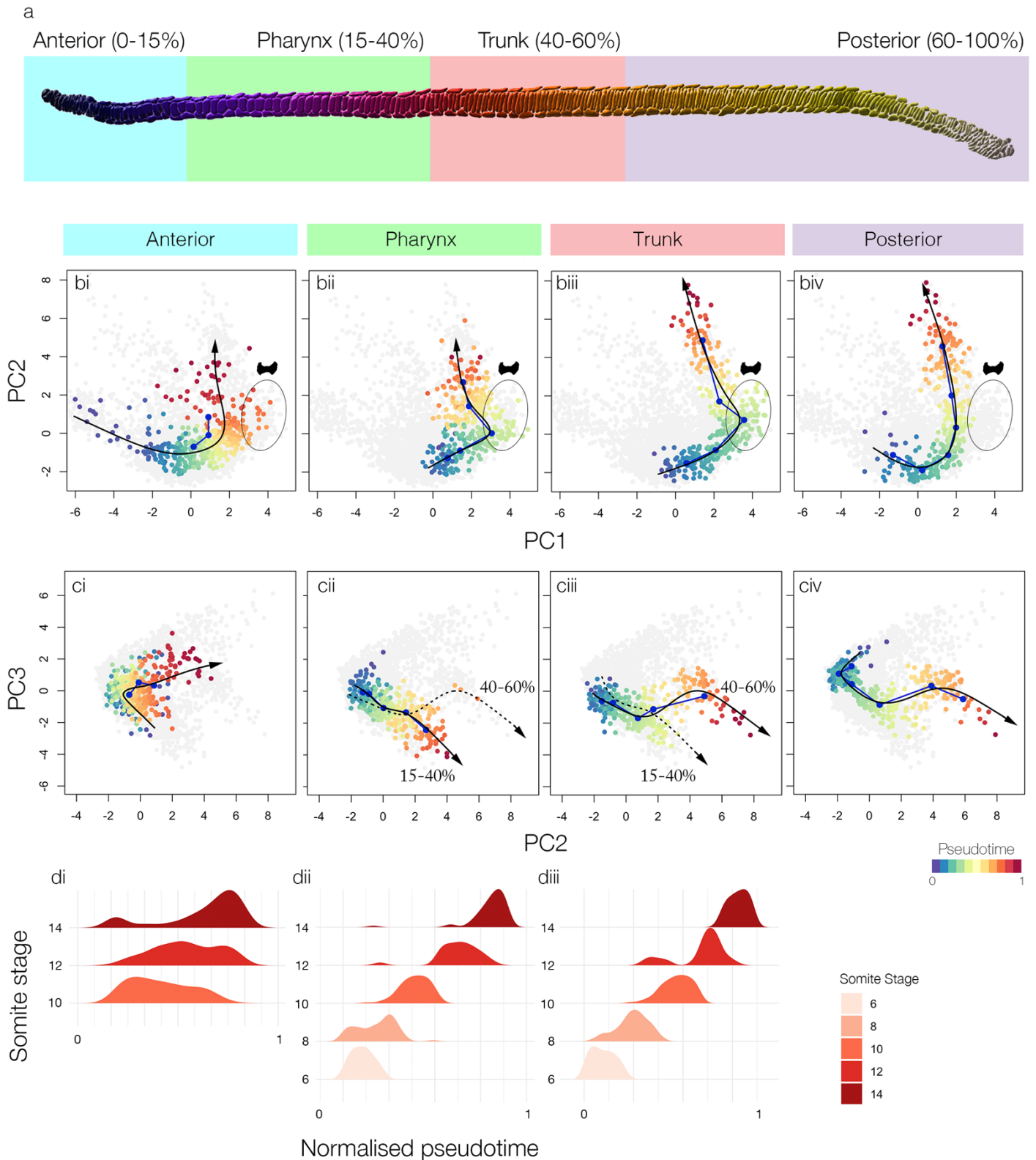


Figure 5. **Variation in cell shape trajectory topology and temporal control across the AP axis.** (a) A sample 14ss notochord showing sampled regions on the AP axis for trajectory comparison; anterior (0 – 15%), pharynx (15 – 40%), trunk (40 – 60%) and posterior (60 – 100%). (bi – iv) Cells from each region defined in (a) now projected in morphospace against PC1 and PC2, with a segmented line connecting point cloud centres for each stage, and an inferred Slingshot trajectory. For the posterior trajectory, 6 bins of AP length at the 14ss are used instead of somite stage. Colour-code is for pseudotemporal position. (ci – iv) Projections of the same cells as (bi – iv), now against PC2 and PC3. For the 15 – 40% and 40 – 60% levels, both trajectories are highlighted to highlight late shape bifurcation. (di – iv) Density plots showing the frequency of cells across pseudotime for each somite stage in the anterior (di), pharyngeal (dii) and trunk (diii) regions. Anterior, $n = 396$; pharynx, $n = 360$; trunk, $n = 344$; posterior, $n = 408$

The shape trajectories of the pharyngeal and trunk levels are similar to one another in that they display the two major transitions observed at the 40 – 60% level, including entry to the ‘bowtie domain’ at the 10-somite stage (*Fig. 5bii - iii, cii - iii*). In both cases, and unlike in the anterior notochord (*Fig. 5bi*), cell shape changes were tightly controlled in developmental time (*Fig. 5dii - iii*). However, the pharyngeal trajectory was contracted on PC2 compared to the trunk trajectory, reflecting a lesser increase in DV:ML ratio, and therefore a stabilisation of a square transverse profile (mean DV:ML ratio of 1.035 at 14ss) rather than further elongating along the DV axis like cells in the trunk region (mean DV:ML ratio of 1.283 at 14ss) (*compare Fig. 5bii and biii, Fig. S3l, S7l*). The pharyngeal trajectory also involves greater and more rapid increases in length and volume between the 12- and 14-somite stages (*compare Fig. 2e, g with Fig S7a, i*). Combined, these variations lead to a second bifurcation event in morphospace across PC2 and PC3 between 12ss and 14ss, yielding two unique cell morphologies that are spatially resolved along the AP axis in the pharynx and trunk (*compare Fig. 5cii and ciii*).

To predict the trajectory of remaining posterior progenitors (60 – 100% AP position), which continue to differentiate beyond the final timepoint of the analysis here, we used relative AP position to guide trajectory inference. This was justified by the correlation we identified previously between axial position and developmental maturity in this posterior region (*Fig. 3, S5*). In this region, cells were similar in initial and final morphologies to the trunk region, but appeared to circumvent the distinctive bowtie morphology, as shown by failure to populate the ‘bowtie domain’ occupied by pharyngeal and trunk cells at 10ss (*compare Fig. 5biii and biv*). This implies a shortcut in their trajectories, such that maturation involves a continuous elevation of transverse area (increase in PC1), that is not enhanced by surface convolution. In sum, this analysis reveals discontinuity in shape transitions across the AP axis, in which some trajectories split over time to generate morphological diversity, while others take divergent paths to common morphologies.

Posterior axial progenitors accelerate notochord elongation by increasing cell number

Our morphometric analysis decomposes notochord morphogenesis into a branching series of cell shape trajectories. Our final objective was to test whether the behaviours we identify at this scale are sufficient to account shape change at the tissue-scale. We therefore compared the dynamics of elongation at the neighbourhood level with that at the tissue level, using direct measurements of total notochord length (*Fig. 6a*). Here, we found the amount of whole notochord elongation to exceed that of local cell neighbourhoods, due to a specific acceleration in rate between 8ss and 10ss (*Fig. 6b*). This discrepancy indicated that some other factors apart from change in cell shape and size must be affecting the rate of tissue elongation. We therefore hypothesised that addition of new cells through cell division might be required to explain full notochord elongation at the tissue-scale.

To test our hypothesis that cell division modifies the notochord elongation curve by increasing cell number, we first set out to generate a map of cell division dynamics in the notochord during its elongation. With this objective, we first labelled embryos at successive somite stages with markers for nuclei in two cell cycle phases; EdU, to cumulatively label cells passing through S-phase in the time window of exposure (applied 2-hours before fixation), and immunostaining for phosphorylated histone

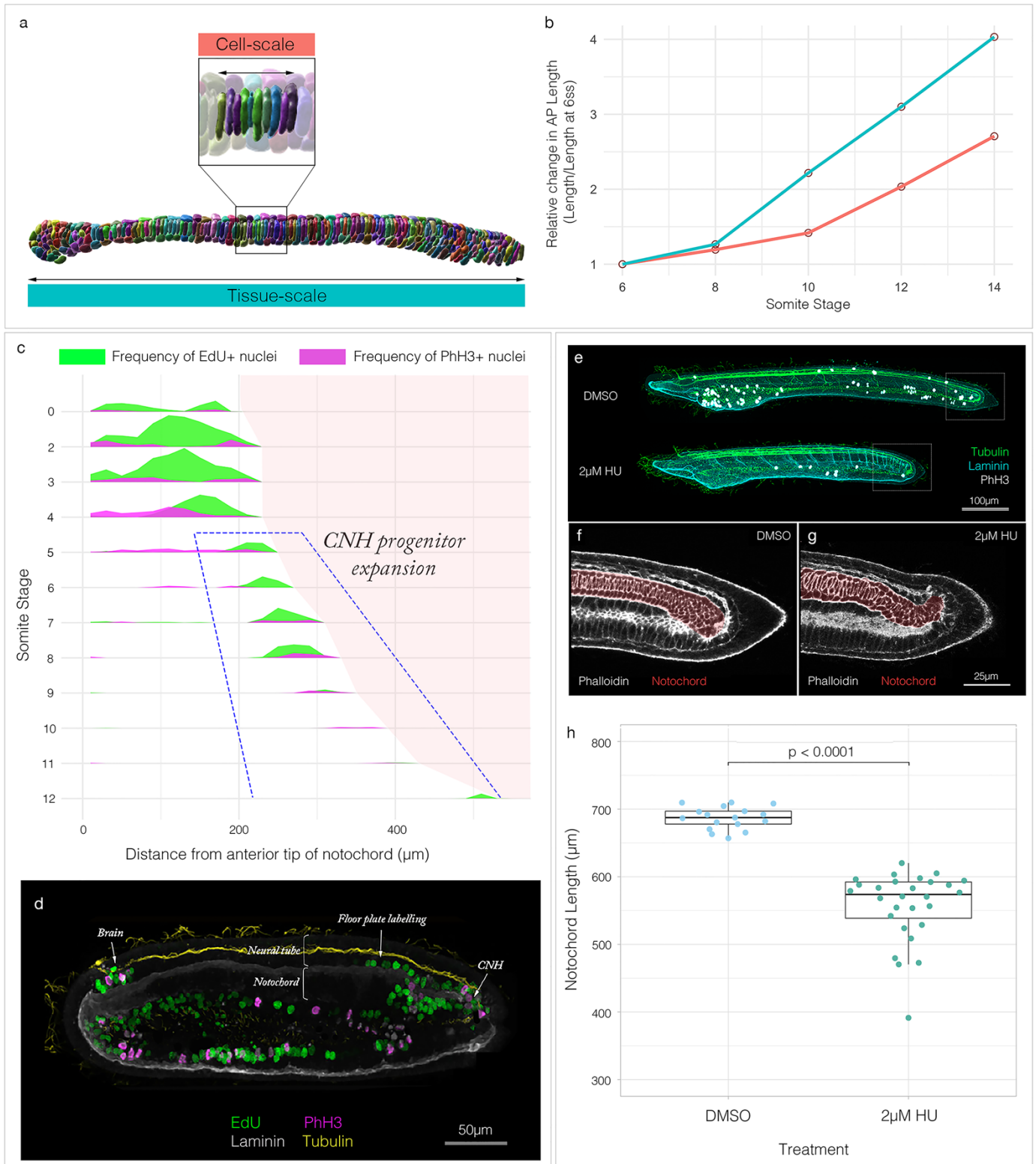


Figure 6. Posterior addition is required for full extension of the body axis. (a) 10ss segmented notochord illustrating cell-scale (top) and tissue-scale (bottom) measurements of AP length. (b) Graph showing relative change in AP length at the cell-scale (neighbourhoods of 10 adjacent cells) and tissue-scale (whole notochords). (c) Tissue-specific proliferation landscape for the notochord, showing mean frequency of EdU and PhH3 staining in embryos at successive somite stages, with length scaled to mean per stage ($n = 102$). (d) Raw staining for EdU and PhH3 at the 8-somite stage in a sagittal section. During elongation, proliferation restricts to the anterior neural plate, and chordoneural hinge in dorsal tissues, and continues in the ventral endoderm. Staining around the chordoneural hinge (CNH) extends into the posterior floor plate and notochord. (e) Effect of 2 μM hydroxyurea on axial length from the 6-somite stage. (f, g) Phalloidin staining in a sagittal section through tails of DMSO and HU-treated specimens, notochord highlighted in red. (h) Quantification of total axial length in DMSO and HU-treated specimens ($n = 17$ DMSO, 27 HU).

in the notochord, which become sequentially enriched with EdU and PHH3, thereby capturing cell cycle progression. Prior to elongation, these data reveal broad cell division throughout the notochord (*Fig. 7c, 0 – 5ss*). However, at the onset of elongation (*Fig. 6c, 6ss*), this transitions to a specific proliferative domain at the posterior tip, which is active until the 8-somite stage (*Fig. 6c 8ss, 6d*). Therefore, we can infer that cells developing along shape trajectories defined for the anterior, pharyngeal and trunk regions of the notochord are in a post-mitotic state during tissue elongation (not labelled with EdU or PhH3, *Fig. 6c*), whereas the posterior trajectory is continually fuelled by cell division. To functionally test the contribution of posterior proliferative progenitors to tissue elongation, we treated embryos with hydroxyurea (HU) at 6ss, when proliferation becomes specifically restricted to the posterior tip. We observed that HU-treated embryos elongated, but to only 81% of their expected length by the 14-somite stage (*Fig. 6e – h*), and this was coupled to disorganisation of the posterior notochord, which lost its regular stack-of-coins pattern (*Fig. 6f, g*). In sum, while notochord length is primarily generated by cell rearrangement and growth, these data reveal a further role for posterior notochord progenitors in providing additional cellular material required for full tissue elongation.

DISCUSSION

Here, we decompose the development of an entire tissue - the amphioxus notochord - by embedding it in a single-cell morphospace. In this environment, morphogenesis is unravelled into a branching portrait of shape differentiation, in which cells transit along trajectories specific to cell type to form a stereotypical diversity of morphologies. When spatially mapped in the embryo, these trajectories organise into temporal gradients of shape differentiation, which in turn align with stepwise changes in multicellular topology. By carrying spatial coordinates into the morphospace, our approach exposes both predictable variation in cell morphology across the AP axis, and the convergence of cells on common morphologies through variable morphogenetic routes. Furthermore, because our approach allows extraction of dynamic information from static imaging data, it enables the inference of cell behaviour where *in vivo* imaging is not yet possible. This also makes the approach widely applicable in a range of non-model organisms where genetics and live imaging are challenging.

Our findings also suggest that cell morphology may contain a much richer body of information than is typically assumed, to the point of being predictive of cell identity, spatial position, and developmental time. Single-cell morphometrics therefore stands to complement single-cell genomics as a rich resource for building multiscale definitions of cell types, and defining their roles in the emergence of embryonic form (Briggs et al., 2018; Ibarra-Soria et al., 2018; Sebé-Pedrós et al., 2018; Wagner et al., 2018). In this case study, we have uncovered remarkable complexity in the trajectories of cell shape change responsible for amphioxus notochord formation, offering a unique window into emergence of a morphological novelty at the base of the chordate phylum. Further studies will take advantage of developments in automated image segmentation and multivariate shape quantification to dissect morphogenesis in a diversity of systems, and integrate these data to define patterns of morphogenetic variation over both developmental and evolutionary time scales. In this respect, single-cell morphometrics will offer a quantitative framework for comparative morphogenesis.

An unexpected finding in our study was regional variation of cellular behaviour across the AP axis, within a tissue that appears to be morphologically continuous: In the anterior we find a highly variable morphogenesis, perhaps characterised by asynchronous maturation between neighbours; in the

pharynx and trunk we find a unique dynamic in which a bowtie morphology disproportionately expands cell spreading area during intercalation; and in the posterior we find a simplified shape trajectory fuelled by cell division. These variations may arise due to a common programme of differentiation occurring under unique mechanical conditions or be the effect of region-specific signalling and genetic regulation. Such correlation is supported by the explicit notochord regionalisation found across vertebrates. In the mouse, live imaging has revealed marked differences in morphogenesis between the anterior head process (AHP), trunk and tail notochord (Yamanaka et al., 2007). Unlike the trunk, AHP progenitors derive from the early- and mid-gastrula organiser without passing through the node (Kinder et al., 2001; Yamanaka et al., 2007), and accordingly are uniquely sensitive to loss of Nodal signalling, but are insensitive to loss of Noto expression (Vincent et al., 2003). In contrast, the tail progenitors are unique in their active migration to move posteriorly to the node late in axis elongation (Yamanaka et al., 2007). Another example of regionalisation is the prechordal plate (PrCP) in all vertebrates, which shares with the AHP its developmental origin from the most anterior axial mesoderm, and forms through anteriorly-directed collective cell migration (Tada and Heisenberg, 2012). Evidence for regionalised behaviour aligns with nested expression of Hox genes in the vertebrate notochord (Prince et al., 1998). Previous work has also identified regionalised gene expression in the amphioxus notochord, and the data presented here adds to this in hinting at readout of these variations as discrete cell behaviours (Albuixech-Crespo et al., 2017). In evolution, the striking variations in vertebrates – the PrCP, AHP, trunk and tail regions – may have emerged within semi-discrete morphogenetic fields that were already defined in the first chordates.

By deconstructing and reconstructing the trajectory for central notochord cells, we elucidate a balance of cell shape, size and topology that dictates the length of small cell neighbourhoods. First, we infer that mediolateral intercalation does not contribute directly to notochord elongation. Rather, it drives a convergent thickening, that increases the number of cell layers stratified across the dorsoventral axis. This multi-layered organisation is then reduced to a trilaminar pattern through dorsoventral intercalation, which is linked to convergent extension and tissue elongation at the tissue level. In this second process, we find that individual notochord cells increase their transverse spreading area at the expense of their AP length. While transverse cell spreading may facilitate intercalation between neighbouring cells, our geometric modelling suggests that the coupled loss of cell length almost entirely abrogates the contribution of intercalation to tissue elongation. In turn, we find that cell growth is required to counterbalance cell length. As a result, we predict that cell growth is required in this system to ensure tissue elongation. During intercalation, cell growth buffers the loss of cell AP length due to cell spreading, thereby enabling cell intercalation to generate tissue length. This accounts for the first phase of notochord elongation. After intercalation, cell growth plays an additional role in further increasing cell length, once cross-sectional area is stabilised. This enables tissue length to further increase, without any ongoing changes in cell topology, at a constant rate. At this scale, we therefore predict that a tight spatiotemporal coordination of growth is required in the notochord to modulate cell shape and in turn control tissue shape and size. Conversely, the effect of growth on form is equally controlled by active changes in cell shape and topology.

Our investigation also revealed an important role for cell division in posterior axial progenitors for defining notochord length at full extension. Indeed, neighbourhood elongation dynamics alone are insufficient to account for those at the tissue scale. We show that this discrepancy may be explained by cell division during notochord elongation, which generates cells for its posterior 20%. It is important to note that the programme of cell shape morphogenesis that generates length operates only after cell

division arrest, when waves of intercalation and growth propagate across the tissue. As such, cell division, intercalation and growth are temporally separated, but ultimately act cumulatively to generate tissue length. Our data suggests that cell division is not necessarily a length-generating process, rather it dictates the number of cells available to fuel length-generating mechanisms that act later in development. This stresses the importance of studying morphogenesis over broad developmental time scales. The amount of cell division we find in amphioxus, and its contribution to length, is relatively small compared to vertebrate systems like mouse and chick (Bénazéraf et al., 2017; Steventon et al., 2016). However, its presence in amphioxus is important in offering an evolvable node for evolutionary change. This is supported by an increase in the role of cell division in the notochord elongation throughout vertebrate evolution, contributing to an increase in its size and length. In amniotes, extensive cell division and growth in posterior progenitors dramatically expand the size of the notochord field when it is established during gastrulation (Catala et al., 1996; Krol et al., 2011; Mugele et al., 2018). Our data suggest that these dynamics are not inherently novel, rather they have arisen through changes in the magnitude of cell division in cell types already present in the first chordates.

The approaches presented here offer a new way of seeing in the study of tissue morphogenesis, that enables holistic analysis of cell behaviours defining tissue geometry and lends itself to cross-species comparisons. In this case study, we use single-cell morphometrics to define a new model for notochord morphogenesis in the amphioxus, and in doing so shine light on principles of morphogenesis at the base of the chordate phylum. We find a conserved role for cell intercalation and growth in generating notochord length that complements previous studies in vertebrates, and also identify a number of evolvable nodes that predict the diversity of developmental dynamics found in vertebrate model systems. This includes evidence for spatial variation in developmental timing across the anteroposterior axis, localised differences in single-cell shape trajectories within a morphological continuum, and a role for axial progenitor cells in accelerating notochord elongation through cell division. As a result, we propose that the diversification of notochord form and developmental dynamics in vertebrates has depended more on tweaks in the magnitude of morphogenetic processes already present in the first chordates, rather than their innovation *de novo*.

MATERIALS AND METHODS

Animal husbandry, spawning and fixation

Wild catch collections of amphioxus, *B. lanceolatum*, were made in Banyuls-sur-Mer, France, and transported to a custom-made amphioxus facility in Cambridge, UK. Adult amphioxus were maintained, bred and the progeny raised as described in Benito-Gutierrez et al (2013). All embryos were fixed in 3.7% PFA + MOPS buffer for 12 hours, then stored in sodium phosphate buffered saline (PBS) + 0.1% sodium azide at 4°C.

Embryo staining and imaging

Embryos were first permeabilised overnight in PBS + 1% DMSO + 1% Triton. They were then blocked in PBS + 0.1% Triton + 0.1% BSA + 5% NGS, and incubated overnight in primary antibodies as follows: rabbit anti-laminin (Sigma, L9393) at 1:50, rabbit anti-PhH3(Abcam, ab5176) at 1:500, mouse anti-acetylated tubulin(T 6793, Sigma) at 1:250.

Primary wash was performed in PBS + 0.1% Triton + 0.1% BSA, before a secondary block in PBS + 0.1% Triton + 0.1% BSA + 5% NGS, and overnight incubation in goat anti-rabbit and/or goat anti-mouse secondary antibodies at 1:250. Staining with DAPI at 1:500 and rhodamine phalloidin at 1:250 was performed with the secondary incubation. Embryos were washed thoroughly with PBS + 0.1% Triton and mounted for confocal imaging on glass-bottomed dishes in 80% glycerol. All imaging was performed on an Olympus V3000 inverted confocal microscope at 30X optical magnification.

For EdU labelling, EdU was applied to live embryos in seawater at a final concentration of 20 μ M for 2 hours prior to fixation. Fluorescent detection of incorporated EdU was performed following the manufacturer's instructions using a Click-it EdU Alexa Fluor 647 Imaging Kit (Invitrogen) prior to primary antibody incubation.

Drug treatment

Live amphioxus embryos were treated with 2 μ M hydroxyurea (Sigma, H8627) or dimethylsulfoxide (DMSO; Sigma, 276855) continuously between the 6-somite and 14-somite stages (18-34hpf at 21°C). They were then fixed immediately for imaging.

Image segmentation and shape quantification

Z-stacks of embryos immunostained for tubulin and laminin, and stained for actin with phalloidin, were imported to Imaris 9.2.1 for segmentation.

Cells were segmented manually, using phalloidin staining to delineate cell outlines. Splines were drawn around each cell every 2 slices in parasagittal section. Cell surfaces were validated by false colouring the contents and checking its faithful fit to the phalloidin stain. Cells were excluded if contours could not confidently be drawn using the phalloidin stain. Most shape metrics were obtained directly from Imaris (raw xyz position for centre of surface homogenous mass, 3D orientation of the long ellipsoid axis, area, axis-aligned/object-oriented bounding box dimensions, centre of homogenous mass for the DAPI channel masked within each surface, number of triangles, volume). The remainder were calculated manually as stated, where l represents length, x , y , and z represent positions in space, bb refers to bounding box-derived metrics, and $cell$ refers to cell-derived metrics. Position along the AP axis was also maintained for all cells.

Quantity	Calculation
AP:DV ratio	$l_{AP}^{(bb)} / l_{DV}^{(bb)}$
AP:ML ratio	$l_{AP}^{(bb)} / l_{ML}^{(bb)}$
DV:ML ratio	$l_{DV}^{(bb)} / l_{ML}^{(bb)}$

Mean cell diameter $d^{(cell)}$	$\frac{l_{DV}^{(bb)} + l_{ML}^{(bb)}}{2}$
AP anisotropy	$\frac{l_{AP}^{(bb)}}{d^{(cell)}}$
Transverse spreading area	$l_{DV}^{(bb)} \times l_{ML}^{(bb)}$
Cross-sectional area $A^{(cell)}$	$\frac{V^{(cell)}}{l_{AP}^{(bb)}}$
Cuboidness	$\frac{Vol}{(l_{AP}^{(cell)} \times l_{DV}^{(cell)} \times l_{ML}^{(cell)})}$
Sphericity	$\frac{\pi^{\frac{1}{3}} (6V^{(cell)})^{\frac{2}{3}}}{A^{(cell)}}$
Flatness	$\frac{l_{max}^{(cell)}}{l_{min}^{(cell)}}$
Nuclear displacement from centre of homogenous mass (x, y, z)	$ABS(x^{(cell)} - x^{(DAPI)})$ $ABS(y^{(cell)} - y^{(DAPI)})$ $ABS(z^{(cell)} - z^{(DAPI)})$
Transverse surface convolution	$\frac{A^{(cell)}}{l_{DV}^{(cell)} \times l_{ML}^{(cell)}}$

Principal component analysis

Principal component analysis (PCA) was performed using the Factoextra package in R on the following geometric variables;

- Angle of major ellipsoid axis relative to x, y, z coordinate system
- Number of triangles
- Volume
- Relative AP, DV, ML dimensions
- AP anisotropy
- Nuclear displacement from centre of homogenous mass on x, y and z planes
- Cuboidness
- Flatness
- Compactness

The ‘scale’ function was used to standardise the data across all cells, giving them a standard deviation of 1 and mean of 0. The PCA coordinates were merged with the raw dataset to allow colour-coding and filtering for specific groups. For stage, we filtered based on the number of somites counted along the AP axis using phalloidin, and laminin immunostaining. For region on the AP axis, we sampled four

broad domains; the anterior (0-15% axial length), pharynx (15-40% axial length), trunk (40-60% axial length) and posterior (60-100% axial length), where 0% is the anterior tip of the notochord and 100% is the posterior tip. For cell layer on the DV axis, the prospective Müller cells were filtered out as the most dorsal and ventral rows of notochord cells at each stage, regardless of morphology. All remaining cells were classified as 'central' cells. Morphospace graphs were constructed using *ggplot2*.

Morphospacial trajectories were constructed by connecting the centre point for point clouds at successive developmental stages, calculated as the mean position on each PC shown in the graph. For the posterior 40% of the notochord, which continues differentiating at 14ss, the trajectory was constructed by connecting the centre points for point clouds from five evenly-sized bins of the AP axis, from posterior to anterior. Here, relative AP position is used as a proxy for developmental maturity

Morphogenetic trajectory inference

Trajectory inference was performed using the Slingshot package in R (Street et al., 2018), which uses clustering information on dimensionally-reduced data to build a minimum spanning tree, and identify one or more principal curves. The data input to Slingshot was the coordinates of the first three principal components, and somite stage was used as a clustering input to guide assembly of the minimum spanning tree by prior information on temporal transitions. The start and end points of the trajectory were also defined as the first and final somite stages included in the analysis. For studying spatial variation, a single principal curve was identified for all regions, representing a mean trajectory. To study spatial variation, the coordinates for each region were passed to Slingshot individually, and the resulting principal curves were compared. The directionality of the trajectory, as marked with an arrow in relevant figures, was inferred from prior information on transitions between somite stages. For the posterior trajectory, clusters were defined as 6 bins of equal length across the AP axis of the 14ss notochord. For trajectory inference regardless of AP position, k means clustering was used, and the resulting clusters were ordered based on known temporal transitions between stages.

Cell position mapping

To construct proliferation landscapes, the point selection tool in FIJI/ImageJ was used to identify a coordinate position for each nucleus positive for EdU or PHH3, and the most anterior and posterior nuclei in the embryo. The position for each labelled nucleus was then quantified across a normalised AP axis. Data was then pooled for embryos at each somite stage, and normalised length was scaled to the mean per stage. Mean frequency of EdU+ and PHH3+ nuclei was then plotted using the *ggridges* package in R to generate proliferation landscapes.

Funding

This work was supported by a Wellcome Trust PhD Studentship in Developmental Mechanisms (T.A), a Herchel Smith Postdoctoral Fellowship (W.P.), a Leverhulme Trust grant (E.K.P. and W.P.), a Sir Henry Dale Fellowship (BS), by CRUK and the Isaac Newton Trust (EBG).

Conflicts of interest

Authors declare no competing interest

Acknowledgements

We thank Michael Akam, Andrew Gillis, John Marioni, Berta Verd and the EBGLab for critical reading of the manuscript and feedback. We also thank Matt Wayland in the Imaging Facilities at the Department of Zoology and the Cambridge Advanced Imaging Centre for their support and assistance.

References

- Adams, D. S., Keller, R. and Koehl, M. A. R. (1990). The mechanics of notochord elongation, straightening and stiffening in the embryo of *Xenopus laevis*. *Development* **110**, 115–130.
- Albuixech-Crespo, B., López-Blanch, L., Burguera, D., Maeso, I., Sánchez-Arrones, L., Moreno-Bravo, J. A., Somorjai, I., Pascual-Anaya, J., Puellas, E., Bovolenta, P., et al. (2017). *Molecular regionalization of the developing amphioxus neural tube challenges major partitions of the vertebrate brain*.
- Annona, G., Holland, N. D. and D’Aniello, S. (2015). Evolution of the notochord. *Evodevo* **6**, 1–13.
- Bagnat, M. and Gray, R. S. (2020). Development of a straight vertebrate body axis.
- Bancroft, M. and Bellairs, R. (1976). The development of the notochord in the chick embryo, studied by scanning and transmission electron microscopy. *J. Embryol. Exp. Morphol.* **35**, 383–401.
- Bénazéraf, B., Beaupeux, M., Tchernookov, M., Wallingford, A., Salisbury, T., Shirtz, A., Shirtz, A., Huss, D., Pourquié, O., François, P., et al. (2017). Multiscale quantification of tissue behavior during amniote embryo axis elongation. *Development* **144**, 4462–4472.
- Benito-Gutiérrez, È., Weber, H., Bryant, D. V. and Arendt, D. (2013). Methods for Generating Year-Round Access to Amphioxus in the Laboratory. *PLoS One* **8**,
- Bhullar, B. A. S., Marugán-Lobón, J., Racimo, F., Bever, G. S., Rowe, T. B., Norell, M. A. and Abzhanov, A. (2012). Birds have paedomorphic dinosaur skulls. *Nature* **487**, 223–226.
- Bijtel, J. H. (1956). The growth of the tail in urodele larvae. *Experientia* **12**, 259.
- Bočina, I. and Saraga-Babić, M. (2006). The notochordal sheath in amphioxus - An ultrastructural and histochemical study. *Coll. Antropol.* **30**, 361–367.
- Boehm, B., Rautschka, M., Quintana, L., Raspopovic, J., Jan, Ž. and Sharpe, J. (2011). A landmark-free morphometric staging system for the mouse limb bud. *Development* **138**, 1227–1234.
- Briggs, J. A., Weinreb, C., Wagner, D. E., Megason, S., Peshkin, L., Kirschner, M. W. and Klein, A. M. (2018). The dynamics of gene expression in vertebrate embryogenesis. *Science (80-)*. **5780**, 1–17.
- Cambray, N. and Wilson, V. (2002). Axial progenitors with extensive potency are localised to the mouse chordoneural hinge. *Development* **129**, 4855–66.
- Catala, M., Teillet, M. A., De Robertis, E. M. and Le Douarin, N. M. (1996). A spinal cord fate map in the avian embryo: While regressing, Hensen’s node lays down the notochord and floor plate thus joining the spinal cord lateral walls. *Development* **122**, 2599–2610.
- Conklin, E. G. (1934). The embryology of amphioxus. *J. Morphol.* **54**, 69–151.
- Delsuc, F., Brinkmann, H., Chourrout, D. and Philippe, H. (2006). Tunicates and not

- cephalochordates are the closest living relatives of vertebrates. *Nature* **439**, 965–968.
- Ellis, K., Bagwell, J. and Bagnat, M. (2013). Notochord vacuoles are lysosome-related organelles that function in axis and spine morphogenesis. *J. Cell Biol.* **200**, 667–679.
- Glickman, N. S., Kimmel, C. B., Jones, M. A. and Adams, R. J. (2003). Shaping the zebrafish notochord. *Development* **130**, 873–87.
- Halpern, M. E., Thisse, C., Ho, R. K., Thisse, B., Riggleman, B., Trevarrow, B., Weinberg, E. S., Postlethwait, J. H. and Kimmel, C. B. (1995). Cell-autonomous shift from axial to paraxial mesodermal development in zebrafish floating head mutants. *Development* **121**, 4257–4264.
- Hatschek, B. (1893). *The amphioxus and its development*. Swan Sonnenschein & Co, London.
- Holland, N. D. and Holland, L. Z. (1990). Fine Structure of the Mesothelia and Extracellular Materials in the Coelomic Fluid of the Fin Boxes, Myocoels and Sclero-coels of a Lancelet, *Branchiostoma floridae* (Cephalochordata = Acrania). *Acta Zool.* **71**, 225–234.
- Holland, N. D. and Holland, L. Z. (2006). Stage - and tissue - specific patterns of cell division in embryonic and larval tissues of amphioxus during normal development. *Evol. Dev.* **8**, 142–149.
- Ibarra-Soria, X., Jawaid, W., Pijuan-Sala, B., Ladopoulos, V., Scialdone, A., Jörg, D. J., Tyser, R. C. V., Calero-Nieto, F. J., Mulas, C., Nichols, J., et al. (2018). Defining murine organogenesis at single-cell resolution reveals a role for the leukotriene pathway in regulating blood progenitor formation. *Nat. Cell Biol.*
- Keller, R., Davidson, L., Edlund, A., Elul, T., Ezin, M., Shook, D. and Skoglund, P. (2000). Mechanisms of convergence and extension by cell intercalation. *Philos. Trans. R. Soc. B Biol. Sci.* **355**, 897–922.
- Kinder, S. J., Tsang, T. E., Wakamiya, M., Sasaki, H., Behringer, R. R., Nagy, A. and Tam, P. P. L. (2001). The organizer of the mouse gastrula is composed of a dynamic population of progenitor cells for the axial mesoderm. *Development* **128**, 3623–3634.
- Krol, A. J., Roellig, D., Dequéant, M. L., Tassy, O., Glynn, E., Hattem, G., Mushegian, A., Oates, A. C. and Pourquié, O. (2011). Evolutionary plasticity of segmentation clock networks. *Development* **138**, 2783–2792.
- Medyukhina, A., Blickensdorf, M., Cseresnyés, Z., Ruef, N., Stein, J. V. and Figge, M. T. (2020). Dynamic spherical harmonics approach for shape classification of migrating cells. *Sci. Rep.* **10**, 1–12.
- Mingqiang, Y., Kidiyo, K. and Joseph, R. (2008). *A Survey of Shape Feature Extraction Techniques*.
- Miyamoto, D. M. and Crowther, R. J. (1985). Formation of the notochord in living ascidian embryos. *J. Embryol. Exp. Morphol.* **VOL. 86**, 1–17.
- Morris, Z. S., Vliet, K. A., Abzhanov, A. and Pierce, S. E. (2019). Heterochronic shifts and conserved embryonic shape underlie crocodylian craniofacial disparity and convergence. *Proc. R. Soc. B Biol. Sci.* **286**,.
- Mugele, D., Moulding, D. A., Savery, D., Molè, M. A. and Nicholas, D. E. (2018). Genetic approaches in mice demonstrate that neuro-mesodermal progenitors express T / Brachyury but not Sox2.
- Munro, E. M. and Odell, G. M. (2002). Polarized basolateral cell motility underlies invagination and convergent extension of the ascidian notochord. *Development* **129**, 13–24.
- Pincus, Z. and Theriot, J. A. (2007). Comparison of quantitative methods for cell-shape analysis. *J. Microsc.* **227**, 140–156.
- Placzek, M., Yamada, T., Tessier-Lavigne, M., Jessell, T. and Dodd, J. (1991). Control of dorsoventral pattern in vertebrate neural development: Induction and polarizing properties of the floor plate. *Development* **113**, 105–122.

- Pourquié, O., Coltey, M., Teillet, M. A., Ordahl, C. and Le Douarin, N. M. (1993). Control of dorsoventral patterning of somitic derivatives by notochord and floor plate. *Proc. Natl. Acad. Sci. U. S. A.* **90**, 5242–5246.
- Prince, V. E., Price, A. L. and Ho, R. K. (1998). Hox gene expression reveals regionalization along the anteroposterior axis of the zebrafish notochord. *Dev. Genes Evol.* **208**, 517–522.
- R. Flood (1975). Fine structure of the notochord of amphioxus. *Symp. zool. Soc. L.* **36**, 81–104.
- Ruan, X., Johnson, G. R., Bierschenk, I., Nitschke, R., Boerries, M., Busch, H. and Murphy, R. F. (2020). Image-derived models of cell organization changes during differentiation and drug treatments. *Mol. Biol. Cell* **31**, 655–666.
- Sebé-Pedrós, A., Saudemont, B., Chomsky, E., Plessier, F., Mailhé, M. P., Renno, J., Loe-Mie, Y., Lifshitz, A., Mukamel, Z., Schmutz, S., et al. (2018). Cnidarian Cell Type Diversity and Regulation Revealed by Whole-Organism Single-Cell RNA-Seq. *Cell* **173**, 1520–1534.e20.
- Segade, F., Cota, C., Famiglietti, A., Cha, A. and Davidson, B. (2016). Fibronectin contributes to notochord intercalation in the invertebrate chordate, *Ciona intestinalis*. *Evodevo* **7**, 1–16.
- Shih, J. and Keller, R. (1992). Cell motility driving mediolateral intercalation in explants of *Xenopus laevis*. *Development* **116**, 901–914.
- Stemple, D. L. (2005). Structure and function of the notochord: an essential organ for chordate development. *Development* **132**, 2503–2512.
- Steventon, B., Duarte, F., Lagadec, R., Mazan, S., Nicolas, J.-F. and Hirsinger, E. (2016). Species-specific contribution of volumetric growth and tissue convergence to posterior body elongation in vertebrates. *Development* **1732–1741**.
- Street, S., Risso, D., Fletcher, R., Das, D., Ngai, J., Yosef, N., Purdom, E. and Dudoit, S. (2018). Slingshot: cell lineage and pseudotime inference for single-cell transcriptomics. *BMC Genomics* **19**,
- Sugiyama, M., Sakaue-Sawano, A., Iimura, T., Fukami, K., Kitaguchi, T., Kawakami, K., Okamoto, H., Higashijima, S. and Miyawaki, A. (2009). Illuminating cell-cycle progression in the developing zebrafish embryo. *Proc. ...* **106**, 20812–20817.
- Tada, M. and Heisenberg, C.-P. (2012). Convergent extension: using collective cell migration and cell intercalation to shape embryos. *Development* **139**, 3897–3904.
- Tassy, O., Daian, F., Hudson, C., Bertrand, V. and Lemaire, P. (2006). A quantitative approach to the study of cell shapes and interactions during early chordate embryogenesis. *Curr. Biol.* **16**, 345–358.
- Tweedy, L., Meier, B., Stephan, J., Heinrich, D. and Endres, R. G. (2013). Distinct cell shapes determine accurate chemotaxis. *Sci. Rep.* **3**, 1–7.
- Veeman, M. T. and Smith, W. C. (2013). Whole-organ cell shape analysis reveals the developmental basis of ascidian notochord taper. *Dev. Biol.* **373**, 281–289.
- Vincent, S. D., Dunn, N. R., Hayashi, S., Norris, D. P. and Robertson, E. J. (2003). Cell fate decisions within the mouse organizer are governed by graded Nodal signals. *Genes Dev.* **17**, 1646–1662.
- Wagner, D. E., Weinreb, C., Collins, Z. M., Briggs, J. A., Megason, S. G. and Klein, A. M. (2018). Single-cell mapping of gene expression landscapes and lineage in the zebrafish embryo. *Science (80-)*. **4362**,
- Watanabe, A., Fabre, A. C., Felice, R. N., Maisano, J. A., Müller, J., Herrel, A. and Goswami, A. (2019). Ecomorphological diversification in squamates from conserved pattern of cranial integration. *Proc. Natl. Acad. Sci. U. S. A.* **116**, 14688–14697.
- Webster, M. and Sheets, H. D. (2010). A practical Introduction to Landmark-Based Geometric

- Morphometrics. *Paleontol. Soc. Pap.* **16**, 163–188.
- Xiong, F., Ma, W., Benazeraf, B., Mahadevan, L. and Pourquie, O. (2018). Mechanical Coupling Coordinates the Co-elongation of Axial and Paraxial Tissues in Avian Embryos. *bioRxiv* 412866.
- Yamada, T., Pfaff, S. L., Edlund, T. and Jessell, T. M. (1993). Control of cell pattern in the neural tube: Motor neuron induction by diffusible factors from notochord and floor plate. *Cell* **73**, 673–686.
- Yamanaka, Y., Tamplin, O. J., Beckers, A., Gossler, A. and Rossant, J. (2007). Live Imaging and Genetic Analysis of Mouse Notochord Formation Reveals Regional Morphogenetic Mechanisms. *Dev. Cell* **13**, 884–896.
- Yin, Z., Sailem, H., Sero, J., Ardy, R., Wong, S. T. C. and Bakal, C. (2014). How cells explore shape space: A quantitative statistical perspective of cellular morphogenesis. *BioEssays* **36**, 1195–1203.
- Young, N. M., Hu, D., Lainoff, A. J., Smith, F. J., Diaz, R., Tucker, A. S., Trainor, P. A., Schneider, R. A., Hallgrímsson, B. and Marcucio, R. S. (2014). Embryonic bauplans and the developmental origins of facial diversity and constraint. *Dev.* **141**, 1059–1063.
- Zhang, S., Holland, N. D. and Holland, L. Z. (1997). Topographic changes in nascent and early mesoderm in amphioxus embryos studied by DiI labeling and by in situ hybridization for a Brachyury gene. *Dev. Genes Evol.* **206**, 532–535.